

PHASE EQUILIBRIA AND MAGNETIC
CHARACTERIZATION STUDIES IN THE
RE-Co-Fe-Cu-Zr, RE-Fe-B AND RE-Fe SYSTEMS

BY

M. UMA DEVI

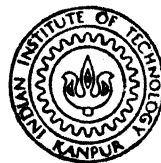
ME

1992

D

DEV

PHA



DEPARTMENT OF METALLURGICAL ENGINEERING
INDIAN INSTITUTE OF TECHNOLOGY KANPUR
MAY, 1992

PHASE EQUILIBRIA AND MAGNETIC
CHARACTERIZATION STUDIES IN THE
RE-Co-Fe-Cu-Zr, RE-Fe-B AND RE-Fe SYSTEMS

*A Thesis Submitted
In Partial Fulfilment of the Requirements
for the Degree of*
DOCTOR OF PHILOSOPHY

BY
M. UMA DEVI

to the
**DEPARTMENT OF METALLURGICAL ENGINEERING
INDIAN INSTITUTE OF TECHNOLOGY KANPUR**
MAY, 1992

15/5/92

CERTIFICATE

It is certified that the work contained in the thesis entitled " Phase Equilibria and Magnetic Characterization Studies in the RE-Co-Fe-Cu-Zr, RE-Fe-B and RE-Fe Systems " by M. Uma Devi has been carried out under my supervision and this work has not been submitted elsewhere for a degree.

May, 1992


(K.P. Gupta)

Professor
Department of Metallurgical Engineering
Indian Institute of Technology
Kanpur

ME-1992-D-DEV-PHA

20 OCT 1993 MET

CE LIBRARY
KAPUR

Doc. No. **116573**

Dedicated to my father
Late M. Gopala Krishna Reddy

LIST OF CONTENTS

	Page
LIST OF FIGURES	x
LIST OF TABLES	xx
SYNOPSIS	xxiii
 CHAPTER	
I INTRODUCTION	1
II REVIEW OF LITERATURE	6
2.1 General Overview	9
2.1.1 4f-3d Compounds	9
2.1.1.1 Binary and Ternary Compounds	10
2.1.1.2 Effect of Substitution	13
2.1.2 Microstructure and Coercivity	21
2.2 Phase Equilibria and Crystal Structure	22
2.2.1 R-Co Systems	22
2.2.1.1 Binary Systems	24
2.2.1.2 Multicomponent Systems	24
2.2.2 R-Fe and R-Fe-B Systems	36
2.2.2.1 Binary R-Fe Systems	36
2.2.2.2 R-Fe-B Systems	41
2.2.3 Crystal Structure	46
2.2.3.1 RT_5 and R_2T_{17} Compounds	46
2.2.3.2 $R_2Fe_{14}B$ and RFe_4B_4 Compounds	48
2.3 $Sm_2(Co, Fe, Cu, Zr)_{17}$ and Nd-Fe-B Magnets	48
2.3.1 $Sm_2(Co, Fe, Cu, Zr)_{17}$ Magnets	48
2.3.1.1 Chemical Composition and Magnetic Features	50
2.3.1.2 Heat Treatment and Microstructure	55
2.3.1.3 Role of Zirconium	58
2.3.2 Nd-Fe-B Magnets	59
2.3.2.1 Chemical Composition and Magnetic Features	59
2.3.2.2 Effect of Substitution	60
2.3.2.3 Heat Treatment, Microstructure and Coercivity	63
2.4 Magnet Fabrication Methods	67
2.4.1 Powder-Orient-Press-Sinter-Process	67
2.4.1.1 Alloy Preparation	70

CHAPTER	Page
2.4.1.2 Pre-Milling	71
2.4.1.3 Milling	72
2.4.1.4 Composition Control and Adjustment	72
2.4.1.5 Particle Alignment and Pressing	74
2.4.1.6 Sintering and Heat Treatment	74
2.4.1.7 Finishing and Magnetizing	75
2.4.2 Other Processes	77
2.5 Concluding Remarks : Samarium versus Neodymium Magnets	78
III STATEMENT OF THE PROBLEM	79
3.1 Phase Equilibria	80
3.1.1 RE-Co-Fe-Cu-Zr System	80
3.1.2 RE-Fe-B System	80
3.1.3 Research Strategy	81
3.2 Magnetic Characterization and Fabrication	82
3.2.1 Bulk Alloys	82
3.2.2 Resin Bonded Magnets	82
3.2.3 Sintered Magnets	83
IV MATERIALS AND EXPERIMENTAL PROCEDURES	85
4.1 Alloy Preparation	85
4.1.1 Materials	85
4.1.2 Melting of Alloys	85
4.1.3 Annealing of Alloys	86
4.2 Phase Analysis	86
4.2.1 Metallography	87
4.2.2 X-ray Diffraction	87
4.2.3 Thermomagnetic Analysis	89
4.2.4 Differential Scanning Calorimetry	96
4.2.5 SEM-EDS Microanalysis	96
4.3 Magnet Fabrication and Characterization	97
4.3.1 Aging Studies on Bulk Alloys	97
4.3.2 Magnet Fabrication	98
4.3.2.1 Communiton	98
4.3.2.2 Resin Bonded Magnet	99
4.3.2.3 Sintered Magnets	100
4.3.3 Physical and Magnetic Characterization Techniques	102

CHAPTER		Page
	4.3.3.1 Physical Characterization Techniques	102
	4.3.3.2 Magnetic Characterization Using VSM	103
V	PHASE EQUILIBRIA IN THE RE-Co-Fe-Cu-Zr SYSTEM AT 1100°C	105
5.1	Results	105
5.1.1	Metallography and Microhardness Measurements	107
5.1.1.1	Metallographic Analysis	107
5.1.1.2	Microhardness Measurements	110
5.1.2	X-Ray Diffraction Analysis	110
5.1.3	Scanning Electron Microscopy (SE-Mode) and X-Ray Microanalysis	117
5.1.4	Thermomagnetic Analysis	121
5.2	Discussion	124
5.2.1	Phases Present in the System	124
5.2.1.1	The U and N Phases	125
5.2.1.2	The γ Phase	130
5.2.1.3	The Δ Phase	130
5.2.2	Phase Equilibria	131
5.2.2.1	Assumptions	131
5.2.2.2	The Phase Diagram	132
5.3	Summary	139
VI	PHASE EQUILIBRIA IN THE RE-Fe-B SYSTEM AT 1000 °C	140
6.1	Results	140
6.1.1	Metallographic Analysis	140
6.1.2	X-Ray Diffraction Analysis	146
6.1.3	Thermomagnetic Analysis	153
6.2	Discussion	158
6.2.1	Γ , Δ , α and β Phases	158
6.2.1.1	The Γ Phase	158
6.2.1.2	The Δ Phase	159
6.2.1.3	The α Phase	161
6.2.1.4	The β Phase	162
6.2.2	Phase Equilibria	164
6.3	Summary	171

CHAPTER		Page
VII	PHASE EQUILIBRIA IN THE RE-Fe SYSTEM	172
7.1	Results	172
7.1.1	Metallographic Analysis	174
7.1.2	X-Ray Diffraction Analysis	178
7.1.3	Thermomagnetic Analysis	186
7.1.4	Differential Scanning Calorimetry	186
7.2	Discussion	190
7.2.1	Phases	190
7.2.2	Phase Equilibria	194
7.3	Summary	199
VIII	MAGNETIC CHARACTERIZATION IN THE RE-Co-Fe-Cu-Zr AND THE RE-Fe-B SYSTEMS	200
8.1	Magnetic Characterization of RE-Co-Fe-Cu-Zr Alloys	200
8.1.1	Results	201
8.1.1.1	Selection of Alloy Composition for Processing	201
8.1.1.2	Aging Behaviour of N Phase Alloys	203
8.1.1.3	Intrinsic Magnetic Properties of the N Phase	205
8.1.1.4	Resin Bonded Magnets	211
8.1.1.5	Sintered Magnets	217
8.1.2	Discussion	234
8.1.2.1	Aging Behaviour of the N Phase Alloys	234
8.1.2.2	Intrinsic Magnetic Properties of the N Phase	235
8.1.2.3	Resin Bonded Magnets	236
8.1.2.4	Sintered Magnets	238
8.1.2.5	Future Prospects	240
8.2	RE-Fe-B System	241
8.2.1	Results	242
8.2.1.1	Effect of Aging Treatment on the Magnetic Hardenability of Bulk Alloy	242
8.2.1.2	Resin Bonded Magnets	242
8.2.1.3	Sintered Magnets	246
8.2.2	Discussion	249
8.2.2.1	Intrinsic Magnetic Properties of the Γ Phase	249
8.2.2.2	Aging Behaviour	251
8.2.2.3	Resin Bonded Magnets	251
8.2.2.4	Sintered Magnets	252

CHAPTER	Page
8.2.2.5 Further Prospects	253
IX CONCLUSIONS AND SCOPE FOR THE FUTURE WORK	255
9.1 Conclusions	255
9.1.1 Phase Equilibria Studies	255
9.1.2 Magnetic Characterization and Fabrication	257
9.2 Scope for the Future Work	259
REFERENCES	261
APPENDIX	275

LIST OF FIGURES

FIGURE	TITLE	Page
I.1	Progress in permanent magnetic materials (after Warlimont [6])	3
I.2	Estimated market development of permanent magnetic materials (after Warlimont [6])	3
I.3	Natural abundance of rare-earth elements in the earth crust [3]	4
II.1	General hysteresis curve for permanent magnets [4]	7
II.2	(a) Curie temperatures of 4f-3d compounds in the isostructural families of interest for magnets (b) room temperature saturation induction of 4f-3d compounds of interest for magnets (after Strnat [3])	11
II.3	Anisotropy field H_A of 4f-3d compounds of interest for magnets : (a) RCo_5 ; (b) R_2Co_{17} ; and (c) $Nd_2Fe_{14}B$ (compiled from reference 1,2,37, 60-64)	12
II.4	(a) Temperature dependence of the spontaneous magnetization in $R_2Fe_{14}B$ compounds (b) temperature dependence of the anisotropy field H_A of $R_2Fe_{14}B$ compounds (after Sagawa et.al.[65])	14
II.5	Rare-earth elements used in REPM and some of their effects on magnetic properties (after Strnat [3])	15
II.6	Variation of anisotropy field H_A as a function of x in $Ce_2Co_{17-x}T_x$, open circle indicate the data at 295 K and closed ones at 77 K (after Wallace et.al.[75])	17
II.7	Composition dependence of Curie temperature in various $Nd_2(Fe_{1-x}M_x)_{14}B$ compounds (after Buschow [72])	19

FIGURE	TITLE	Page
II.8	Hysteresis loops and H_c as a function of maximum applied field : (a),(b) $\text{Sm}(\text{Co,Fe,Cu,Zr})_{7.6}$; and (c),(d) $\text{Nd}_2\text{Fe}_{14}\text{B}$ based magnets (after Durst and Kronmüller [52])	23
II.9	Intermediate phases found in the various R-Co binary systems (after Gupta [101])	25
II.10	(a) Initial phase diagram of the Sm-Co system (after Buschow and Van der Goot [117]) (b) Co-rich portion of the Sm-Co phase diagram (after den Broeder and Zijlstra [119])	26
II.11	Ce-La-Co ternary system (after Khan and Feldman [122] and Khan [123])	28
II.12	MM-Co phase diagram (after Schäfer and Spyra [126,127])	29
II.13	RE-Co-Fe phase diagram (after Mittal et.al. [131])	31
II.14	Sm-Co-Fe-Cu phase equilibria : (a) Sm-Co-13.0 at.pct. Cu-10.0 at.pct. Fe (Cu > Fe) section of phase diagram; and (b) Sm-Co-7.0 at.pct. Cu-22.0 at.pct. Fe (Cu < Fe) section of phase diagram (after Morita et.al.[133])	33
II.15	Relationship between crystal structure of 2:17 phase obtained after homogenizing and Cu and Fe contents for various alloys (after Morita et.al.[133])	34
II.16	Sm-Co-7.0 at.pct. Cu-22.0 at.pct. Fe-2.0 at.pct. Zr section of Sm-Co-Fe-Cu-Zr phase diagram (after Morita et.al.[133])	35
II.17	(a) Phase diagram section (Cu,Zr)-(Sm,Co,Fe) with fixed 11.9 at.pct. Sm, 60.0 at.pct. Co, 18.9 at.pct. Fe and Cu+Zr = 9.2 at.pct. (b) phase diagram section Sm-(Co,Fe,Cu,Zr) (after Chin et.al.[134])	37

FIGURE	TITLE	Page
II.18	(a) Ce-Fe binary phase diagram, (b) iron-rich portion of the Ce-Fe phase diagram (after Chaung et.al.[137])	39
II.19	Selected R-Fe binary phase diagrams : (a) Nd-Fe (after Landgraf et.al.[136]); (b) Pr-Fe, (c) Sm-Fe, and (d) La-Fe (compiled from Kubaschewski [135])	42
II.20	Ternary section of Nd-Fe-B : (a) data pertain to 900 °C for the Nd poor alloys and 700 °C for Nd rich alloys (after Buschow et.al.[153]); (b) data pertain to 1000 °C (after Schneider et.al.[150])	44
II.21	Crystal structure of (a) RT_5 and (b),(c) R_2T_{17} (rhombohedral and hexagonal) compounds (after Hadjipanayis [167])	47
II.22	(a) Schematic representation of $Nd_2Fe_{14}B$ ($P4_2/mnm$ space group) (after Herbst et.al.[156]) (b) projection of crystallographic structure of $NdFe_4B_4$ onto the (110) plane (after Givord et.al.[161])	49
II.23	$(BH)_{max}$ values for 2:17 type magnets as a function of Cu and Fe contents (after Tawara and Kaneko [173])	53
II.24	Relationship between intrinsic coercive force, H_c , and Sm content for Sm-Co-7.0 at.pct. Cu-22.0 at.pct. Fe-0 to 3.5 at.pct Zr alloys (after Morita et.al.[133])	54
II.25	Schematic diagram showing (a) the typical ragged arrangement of the cellular microstructure, and (b) the different phases within the rhombic cells (after Fidler and Skalicky [177])	57
II.26	Schematic drawing of the multiphase micro-structure found in the sintered Nd-Fe-B magnets (after Fidler [34])	64

FIGURE	TITLE	Page
II.27	Schematic diagram illustrating possible micro structural and compositional changes during post sintering heat treatment of Nd-Fe-B magnets : (a) $\text{Nd}_2\text{Fe}_{14}\text{B}$ grain before heat treatment; and (b) after heat treatment (after Elbicki et.al.[226])	68
II.28	Schematic representation of the various process steps for the manufacturing of sintered rare-earth permanent magnets (after Ormerod [11])	69
II.29	Effect of milling time on particle size (right scale) and on oxygen pick up (left scale) during ball milling in freon of Nd-Fe-B (full lines) and $\text{Sm}(\text{Co,Fe,Cu,Zr})_2$ (broken lines) alloys [2,11]	73
II.30	Typical sintering and heat treatment cycle for (a) $\text{Sm}(\text{Co,Fe,Cu,Zr})_{7.4}$ and similar "2-17" magnets, (after Kumar [4]) (b) $\text{Nd}_2\text{Fe}_{14}\text{B}$ based magnets (after Okada and Homa [233])	76
IV.1	Magnetic moment vs. temperature curve for Ni using a vibrating sample magnetometer in the residual field (about 40 Oe) of an electromagnet	91
IV.2	Magnetic permeability testing apparatus used for thermomagnetic analysis	92
IV.3	(a) Transducer (schematic) and (b) detection system (block diagram) used in the permeability testing apparatus	94
IV.4	Permeability vs. temperature traces for Ni and Fe samples	95
V.1	Representative optical micrographs of RE-Co-Fe-Cu-Zr alloys (homogenized at 1100 °C): (a) alloy C_7 ; (b) alloy C_{15} ; (c) alloy C_{20} ; (d) alloy C_{16} ; (e) alloy C_{17} ; and (f) alloy C_{19} (Magnification 500x)	108

FIGURE	TITLE	Page
V.2	XRD patterns of typical RE-Co-Fe-Cu-Zr alloys (homogenized at 1100 °C) containing U, N or mixture of U and N phases : (a) alloy C ₁₈ (U phase); (b) alloy C ₁₇ (U+N phases); and (c) alloy C ₁₆ (N phase)	112
V.3	XRD pattern of an alloy (C ₇) containing solidified liquid phase (L')	116
V.4	SEM (SE-mode) micrographs of RE-Co-Fe-Cu-Zr alloys used for the X-ray microanalysis of different phases	118
V.5	X-ray spectra (SEM-EDS) of (a) U phase, and (b) N phase grains	119
V.6	X-ray spectra (SEM-EDS) of (a) γ phase, and (b) Δ phase grains	120
V.7	X-ray spectra (SEM-EDS) of solidified liquid (L') regions	122
V.8	TMA plots of some typical RE-Co-Fe-Cu-Zr alloys obtained using high temperature permeability testing apparatus (C _{19(D)} is the ductile phase separated from the powders of alloy C ₁₉) (compiled from Devi (1985)[245])	123
V.9	1100 °C isothermal section of RE-Co-Fe-Cu-Zr system at fixed Cu (8.0 at.pct.) and Zr (2.0 at.pct.) contents	133
V.10	Variation of lattice parameters as a function of chemical composition : (a) N phase; and (b) U phase	135
V.11	Variation of lattice parameter of the γ phase as a function of chemical composition	137
VI.1	Representative optical micrographs of RE-Fe-B alloys having composition close to the expected Γ phase region : (a) alloy E ₃₀ ; (b) alloy E ₂₈ ; (c) alloy E ₄ ; (d) alloy E ₃₄ ; (e) alloy E ₂₀ ; (f) alloy E ₂₇ ; (g) alloy E ₃₁ ; and (h) alloy E ₂₉ (Magnification 500x)	143

FIGURE	TITLE	Page
VI.2	Optical micrographs of typical RE-Fe-B alloys located away from the expected L' phase region : (a) E_{33} ; (b) E_{35} ; (c) E_8 ; and (d) E_{32} (Magnification 500x)	145
VI.3	XRD patterns of some RE-Fe-B alloys : (a) alloy E_{30} [single phase $RE_2Fe_{14}B$ (Γ)]; (b) alloy E_{19} [major phase $REFe_4B_4$ (Δ)]	147
VI.4	XRD pattern of the Fe_2B (β) phase (alloy E_{32}) (the peaks marked as Δ corresponds to the $REFe_4B_4$ phase)	151
VI.5	XRD patterns of some RE-Fe-B alloys containing solidified liquid (L') : (a) alloy E_{18} , ($\Delta+L'$) ; (b) alloy E_{14} ($\Gamma+\Delta+L'$); and (c) alloy E_{11} ($\Gamma+\Delta+L'$)	152
VI.6	TMA traces of some typical RE-Fe-B alloys : (a) alloy E_1 , E_2 , E_{24} , E_{27} , E_4 , E_5 , E_{30} and X; (b) alloy E_{26} , E_{17} , E_{19} , E_{16} , E_{25} , E_{12} and A (alloy X and A are Nd-Fe-B alloys and correspond to the 2:14:1 and 1:4:4 compositions, respectively)	154
VI.7	Magnetic moment vs. temperature curves for alloy E_{19} , E_{35} , E_{30} , and A (alloy A is a Nd-Fe-B alloy and corresponds to the 1:4:4 composition)	156
VI.8	DSC trace of alloy E_{33} annealed at 1000 $^{\circ}C$ for 3 days	163
VI.9	RE-Fe-B isothermal section at 1000 $^{\circ}C$	167
VII.1	Optical micrographs of alloy D_1 annealed at (a) 700 $^{\circ}C$, and (b) 900 $^{\circ}C$ (Magnification 500x)	175
VII.2	Typical optical micrographs of some high RE containing RE-Fe alloys (a) D_3 (annealed at 700 $^{\circ}C$); (b) D_5 (annealed at 700 $^{\circ}C$); and (c) D_4 (annealed at 900 $^{\circ}C$)	176
VII.3	Typical optical micrographs of some high Fe containing RE-Fe alloys annealed at 1000 $^{\circ}C$ or 1100 $^{\circ}C$: (a) D_{000} (annealed at 1000 $^{\circ}C$); (b) D_0 (1000 $^{\circ}C$); (c) D_1 (1000 $^{\circ}C$); and (d) D_0 (1100 $^{\circ}C$) [Magnification (a)-(c) 500x and (d) 200x]	177

FIGURE	TITLE	Page
VII.4	XRD patterns of some RE-Fe alloys homogenized at 700 °C : (a) D ₁ ; (b) D ₂ ; (c) D ₃ ; (d) D ₄ ; and (e) D ₅	179
VII.5	XRD patterns of some RE-Fe alloys homogenized at 900 °C : (a) D ₀₀ ; (b) D ₀ ; (c) D ₁₂ ; (d) D _{1A} ; (e) D _{1C} (f) D ₂ ; and (g) D ₄	180
VII.6	XRD patterns of some RE-Fe alloys homogenized at 1000 °C : (a) D ₀₀₀ ; (b) D ₀₀ ; (c) D ₀ ; (d) D ₁ ; and (e) D _{1C} (f) D ₂ ; and (g) D ₄	181
VII.7	XRD patterns of some RE-Fe alloys homogenized at 1100 °C : (a) D ₁ ; (b) D ₀ ; and (c) D ₀₀₀	182
VII.8	TMA curves of a few RE-Fe alloys obtained using high temperature magnetic permeability testing apparatus : (a) D ₁ (900 °C); (b) D ₁ (1000 °C); and (c) D ₄ (1000 °C)	187
VII.9	TMA curves of a few RE-Fe alloys obtained using a vibrating sample magnetometer (measured in the residual field of 40 Oe) : (a) D ₁ (700 °C); (b) D ₁ (900 °C); and (c) D ₁₂ (900 °C)	188
VII.10	DSC traces of a few RE-Fe alloys	189
VII.11	(a) Phase equilibria in the RE-Fe system	196
	(b) schematic phase diagram of the RE-Fe system showing a possible peritectoid type reaction at the Fe-end	197
VIII.1	Effect of aging time on the intrinsic coercivity (H_c) for RE(Co _{0.89-x} Fe _x Cu _{0.09} Zr _{0.02}) ₂ alloys at 675 °C (data from Devi (1985) [245])	202
VIII.2	Aging behaviour of solid annealed specimens of alloy C ₁₁ [RE(Co _{0.76} Fe _{0.13} Cu _{0.09} Zr _{0.02}) ₆] at different temperatures (C ₁₁ (A), C ₁₁ (B) and C ₁₁ (C) indicates different batch of alloy C ₁₁)	204
VIII.3	Magnetization (σ) vs. applied field (H) curves for a resin bonded pellet of alloy C ₁₁ (C)	207

FIGURE	TITLE	Page
VIII.4	Magnetization (σ) vs. applied field (H) curves for a resin bonded pellet of alloy $C_{11}(C)$ (at room temperature) measured parallel and perpendicular to the magnetic alignment direction	208
VIII.5	XRD patterns of alloy $C_{11}(C)$: (a) randomly oriented powder sample; and (b) magnetically aligned cylindrical resin bonded sample (XRD pattern from the surface perpendicular to the magnetic alignment direction)	210
VIII.6	Effect of milling time on the magnetic properties of two different batches of alloy C_{11} (annealed at 1100°C for 48 hours)	214
VIII.7	Particle size distribution at different milling periods for alloy $C_{11}(B)$	215
VIII.8	SEM (SE-mode) micrographs of 5 hours milled powder of alloy $C_{11}(B)$: (a) milled powder; and (b) milled powder after magnetic alignment and setting in epoxy resin (photomicrograph in (b) is recorded from the sample surface perpendicular to the magnetic alignment direction)	216
VIII.9	Effect of milling time on the magnetic properties of resin bonded magnets prepared from alloy $C_{11}(C)$ (annealed at 1100°C for 48 hours) after different aging schemes : (a) milling followed by aging at 620°C for 200 hours; (b) aging at 620°C for 200 hours followed by milling	218
VIII.10	Particle size distribution for 1 hr and 5 hours milled powders of alloy $C_{11}(C)$: (a),(c) SEM micrographs; and (b),(d) image analyzer statistical particle count data	219
VIII.11	Heat treatment cycle for some of the sintering operations used in the RE-Co-Fe-Cu-Zr system	221

FIGURE	TITLE	Page
VIII.12	X-ray powder diffraction patterns for alloy C ₁₁ : (a) green pellet; and (b) 1100 °C sintered pellet	223
VIII.13	Schematic representation of alloy compositions chosen for the fabrication of magnets in the RE-Co-Fe-Cu-Zr system with Cu and Zr contents fixed at 8.0 at.pct. and 2.0 at.pct., respectively	224
VIII.14	Aging behaviour of 1100 °C sintered pellets of alloy C ₁₅ , C ₃₀ , C ₃₂ , C ₃₃ , C _{33(b)} , C _{34(b)} and C _{35(b)} at 620 °C	227
VIII.15	Aging behaviour of 1000 °C sintered pellets of alloy C ₂₉ and C _{34(b)} at different temperatures	228
VIII.16	Aging behaviour of 950 °C sintered pellets of alloy C ₂₈ and C ₁₁ at different temperatures	229
VIII.17	Variation of magnetic properties with aging time (at 620 and 600 °C) for the sintered pellets of alloy C ₃₃ after sintering at different temperatures	230
VIII.18	Optical micrographs illustrating formation of liquid phase during sintering of green pellets of alloy C _{34(b)} at different temperatures : (a) 1100 °C; and (b) 1000 °C	231
VIII.19	XRD patterns of the 950 °C sintered pellets of (a) alloy C ₂₈ and (b) alloy C ₁₁ illustrating relative amounts of the N and U phases	232
VIII.20	XRD patterns of the 1000 °C sintered pellets of (a) alloy C ₂₉ and (b) alloy C _{34(b)} illustrating relative amounts of the N and U phases	233
VIII.21	XRD patterns of sintered pellets of alloy C ₃₃ : (a) sintered at 1000 °C for 0.5 hour; and (b) sintered at 1000 °C for 0.5 hour and annealed at 1100 °C for 0.25 hour	239
VIII.22	Effect of aging time on μH_c and σ_s of alloy E ₂₆ (RE ₁₅ Fe ₇₇ B ₈) at different aging temperatures	243

FIGURE	TITLE	Page
VIII.23	Effect of milling time on the magnetic properties of alloy E_{26} (measured on resin bonded oriented powder samples)	244
VIII.24	Half of the Hysteresis loop of a typical resin bonded pellet prepared from the 3 hours milled powder of alloy E_{26}	245
VIII.25	Optical micrographs of sintered pellets of $RE_xFe_{92-x}B_8$ alloys : (a) alloy E_{26} ($x = 15$) sintered at $1100^\circ C$ for 0.5 hour; (b) E_{36} ($x = 17$); and (c) E_{38} ($x = 19$) [both (b) and (c) sintered at $1050^\circ C$ for 1 hour]	248
VIII.26	XRD patterns of $1050^\circ C$ sintered pellets of alloy (a) E_{38} and (b) E_{36}	250

LIST OF TABLES

TABLE	TITLE	Page
II.1	Comparison of the magnetic properties of several commercially available rare-earth permanent magnets [2].	8
II.2	Intrinsic properties of MM bearing compounds as compared to the corresponding Ce, Sm, or Nd compounds.	20
II.3	Lattice parameters of RE containing phases observed in the RE-Co-Fe system at 900°C [131,132].	30
II.4	Structural data of phases in Ce-Fe system [135].	40
II.5	Structural and magnetic characteristics of binary and ternary phases in Nd-Fe-B system.	45
II.6	Some typical $\text{Sm}(\text{Co}_{\text{bal.}}\text{Fe}_u\text{Cu}_v\text{T}_w)_z$ (precipitation hardenable) magnet alloys and their magnetic properties.	51
II.7	Magnetic properties of $(\text{Nd}_{1-x}\text{R}_x)_p(\text{Fe}_{\text{bal.}}\text{X}_u\text{Y}_v\text{Z}_w)_q\text{B}_r$ sintered magnets.	61
II.8	Powder-Orient-Press-Sinter process [40].	70
II.9	(a) Bonded particle magnet technology [40].	77
	(b) Rapid solidification techniques [40].	77
IV.1	Operating conditions for tracing XRD patterns using Seifert Iso-Debyeflex 20020 diffractometer.	89
V.1	Chemical composition and phase analysis of the RE-Co-Fe-Cu-Zr alloys [all the alloys contained fixed amounts of Cu (8 at.pct.) and Zr (2 at.pct.)].	106
V.2	Powder X-ray diffraction data of the U phase in alloy C ₁₈ .	113
V.3	Powder X-ray diffraction data of the N phase in alloy C ₁₆ .	114

TABLE	TITLE	Page
V.4	Powder X-ray diffraction data of the γ phase in alloy C ₁₄ .	115
V.5	Comparison of lattice parameters of the U and N phases with the phases observed in RE-Co, RE-Co-Fe and RE-Co-Fe-Cu systems.	126
V.6	Comparison of Curie temperatures of the U and N phases with the phases observed in RE-Co, RE-Co-Fe and RE-Co-Fe-Cu systems.	127
VI.1	Chemical composition and phase analysis of the investigated RE-Fe-B alloys.	141
VI.2	Powder X-ray diffraction data of the RE ₂ Fe ₁₄ B (Γ) phase (alloy E ₃₀).	148
VI.3	Powder X-ray diffraction data of the REFe ₄ B ₄ (Δ) phase (alloy E ₁₉).	149
VI.4	Powder X-ray diffraction data of the β phase (Fe ₂ B) in alloy E ₃₂ .	150
VI.5	Lattice parameters and Curie temperature of the Γ phase in alloys of different chemical compositions.	169
VII.1	Chemical composition and phase analysis of the RE-Fe alloys.	173
VII.2	Powder X-ray diffraction data of RE ₂ Fe ₁₇ phase (alloy D ₁ , annealed at 700°C for 30 days).	183
VII.3	Powder X-ray diffraction data of REFe ₂ phase (alloy D ₄ , annealed at 700°C for 30 days).	184
VII.4	Lattice parameters and Curie temperatures of RE-Fe compounds found in this investigation and the R-Fe compounds in the Ce-Fe and Nd-Fe systems.	192
VIII.1	Chemical composition, phases and initial magnetic properties of the [RE(Co _{0.89-x} Fe _x Cu _{0.09} Zr _{0.02}) ₂] used for low temperature aging treatment studies.	203
VIII.2	H_c and σ_s values for different batch of alloy C ₁₁ after aging at 620 °C.	205

TABLE	TITLE	Page
VIII.3	Magnetic properties of oriented resin bonded coarse powders of alloy $C_{11}(B)$ (annealed at 1100°C , 48 hrs) before and after aging at 620°C for 200 hrs.	212
VIII.4	Physical and magnetic properties of the sintered pellets of RE-Co-Fe-Cu-Zr alloys.	222
VIII.5	Magnetic properties of the sintered RE-Fe-B pellets prepared under different experimental conditions.	247

SYNOPSIS
OF
PH.D. DISSERTATION
ON
PHASE EQUILIBRIA AND MAGNETIC CHARACTERIZATION STUDIES
IN THE RE-CO-Fe-CU-Zr, RE-Fe-B AND RE-Fe SYSTEMS
BY
M. UMA DEVI (ROLL No 8510665)
DEPARTMENT OF METALLURGICAL ENGINEERING
INDIAN INSTITUTE OF TECHNOLOGY, KANPUR 208016 (INDIA)

In the last two to three decades, rare-earth magnets, which occupy an important place in the arsenal of modern engineering materials, have evolved from a physicist's vision into a large family of commercial materials. Precipitation hardenable $\text{Sm}(\text{Co,Fe,Cu,Zr})_2$ ($Z \sim 7$) magnets and Nd-Fe-B magnets, based on the ternary intermetallic compound $\text{Nd}_2\text{Fe}_{14}\text{B}$, have attracted special attention in the last few years because of their excellent magnetic properties. The widespread application of these magnets is restricted due to their high cost attributed to Sm and Nd. Mischmetal (MM), the natural mixture of light rare-earths (Ce, La, Nd and Pr) is abundant, 30-40 times less costly than pure Sm or Nd, and most readily available. The central idea of this thesis is to study the replacement of Sm and Nd by Mischmetal and explore the prospects of fabricating low cost magnets in MM-Co-Cu-Fe-Zr and MM-Fe-B systems. India is richly endowed with rare-earth deposits. Since at present only Mischmetal is produced in metallic form from these deposits, the present study is relevant in the Indian context. The overall contents of this thesis are arranged in nine chapters.

A brief introduction on rare-earth permanent magnets in chapter I is followed up by a critical review of rare-earth permanent magnets in chapter II with emphasis on rare-earth(R)-transition metal(T) compounds, microstructure and coercivity mechanisms, phase equilibria in the R-Co, R-Co-T, R-Fe and R-T-B systems, $\text{Sm}(\text{Co,Fe,Cu,Zr})_2$ and Nd-Fe-B magnets, substitution of Sm or Nd by Mischmetal, and fabrication methods for sintered and resin bonded magnets.

The scope and statement of the present research problem is defined in chapter III. Broadly, this investigation concerns with two distinct but related aspects: (i) phase equilibria studies in (a) MM-Co-Fe-Cu-Zr, (b) MM-Fe-B, and (c) MM-Fe systems; and (ii) some preliminary studies on magnetic characterization of phases and fabrication of sintered and resin bonded magnets in these systems. Phase equilibria work on MM-Fe system was undertaken as an extension of the MM-Fe-B system. To represent phase equilibria of the investigated multicomponent systems, the total rare-earth content (RE) of the Mischmetal has been treated as a single component.

Detailed description of materials, melting techniques, phase analysis techniques to study the phase equilibria, fabrication of sintered and resin bonded magnets and their physical and magnetic characterization etc. is presented in chapter IV. The alloys were prepared by arc melting. Phase analysis of the alloys was carried out using optical microscopy, X-ray diffraction (XRD), thermomagnetic analysis (TMA), differential scanning calorimetry (DSC) and X-ray microanalysis in a scanning electron microscope (SEM-EDS). A vibrating sample magnetometer (VSM) was used for the magnetic characterization of the bulk alloys and resin bonded and sintered magnets. Metallography and X-ray diffraction techniques were also used for the characterization of microstructure and phases present in the sintered magnets.

The results and discussion on 1100°C isothermal section of the RE-Co-Fe-Cu-Zr system, where RE represents the total

rare-earth content of mischmetal (MM), are presented in chapter V. The investigated composition region of phase equilibria, which lies around RE/T ratio of $\sim 1:7$, is bounded by 5 to 19 at.pct. RE, 55 to 75 at.pct. Co, 7 to 20 at.pct. Fe, and Cu and Zr contents fixed at 8 and 2 at.pct., respectively. The techniques used for the phase equilibria studies are metallography, XRD, SEM-EDS analysis and TMA. The intermediate phases reported to be stable in RE-Co-Fe system are not found in the RE-Co-Fe-Cu-Zr system at 1100 °C. Existence of two new phases U and N, located around RE:T ratio of $\sim 1:7$ and $1:6$ respectively have been established. The U and N phases, which appear to be structurally similar to the 2:17 and 1:5 phases, have lattice parameters (hexagonal cell) of $a = 8.452$ Å, $c = 24.57$ Å and $a = 4.940$ Å, $c = 20.42$ Å, and $T_c \sim 830$ and 740 °C, respectively. Both the U and N phases are restricted in their composition limits. The U phase appears to have small solubility range. The other phases which are found at 1100 °C include a cobalt rich fcc solid solution phase (γ) with lattice parameter $a = 3.567$ Å and $T_c \sim 1045$ °C, a Zr rich hard phase Δ and a liquid phase.

Chapter VI concerns with the results and discussion on the RE-Fe-B system. The composition region which has been found important for the fabrication of permanent magnets in Nd-Fe-B system has been investigated. 1000 °C isothermal section of the RE-Fe-B system has been established at the iron rich side, upto about 40 at.pct. RE and about 45 at.pct. B, using metallography, XRD and TMA techniques. Two ternary intermediate phases Γ and Δ , which are structurally analogous to the $R_2Fe_{14}B$ and RFe_4B_4 phases, have been identified. The Γ and Δ phases are tetragonal with lattice parameters $a = 8.784$ Å, $c = 12.177$ Å and $a = 7.106$ Å, $c = 17.011$ Å, respectively. The Curie temperature of the Γ phase is ~ 245 °C. The Δ phase also shows a peculiar magnetic transition between 240 and 440 °C and its magnetic behaviour is not well understood. Besides the ternary intermediate phases Γ and Δ , the other phases observed are a bcc Fe solid solution phase (α), a Fe_2B (β) phase and a liquid. The bcc α phase possibly arises out of the transformation of the fcc γ solid solution phase when the

alloys are quenched to room temperature after equilibration at 1000 °C. The α and β phases have practically no solubility of RE. The Γ phase appears to have a small homogeneity region. The phase equilibria at 1000 °C is quite similar to the Nd-Fe-B system except that no $\text{RE}_2\text{Fe}_{17}$ phase is observed in equilibrium with any of the ternary phases in the the RE-Fe-B system at 1000 °C.

During the phase equilibria studies on RE-Fe-B system, no ternary alloy showed the presence of the $\text{RE}_2\text{Fe}_{17}$ phase even when the B content was as low as 1.0 at.pct. The presence of a bcc α phase at 1000°C was also somewhat unusual as it is not found stable at this temperature in any of the R-Fe binaries, where R = Ce, Nd, Pr, Sm etc. No information was found available on the RE-Fe system. Hence as an extension of phase equilibria studies in RE-Fe-B system, the phase equilibria study of the RE-Fe system was taken up to explain the absence of the $\text{RE}_2\text{Fe}_{17}$ phase and the occurrence of α phase at 1000°C. Phase equilibria study has been done between 700-1150°C and in the composition range 0.5 to 33.3 at.pct. RE (i.e. the Fe rich end). The results and discussion on RE-Fe system are presented in chapter VII. In the RE-Fe system, two intermediate phases $\text{RE}_2\text{Fe}_{17}$ and REFe_2 , and a Fe solid solution phase are observed. The lattice parameters of hexagonal unit cell of $\text{RE}_2\text{Fe}_{17}$ phase, which has a Curie temperature between 40-45°C, are $a = 8.525 \text{ \AA}$, $c = 12.420 \text{ \AA}$ and c/a ratio 1.46. The REFe_2 is a cubic Laves phase with lattice parameter $a = 7.299 \text{ \AA}$. The fcc γ phase can not be retained by quenching of alloys from high temperature. The solubility of RE in Fe is less than 0.5 at.pct. The RE-Fe system is quite similar to the R-Fe systems (R = Ce, Pr) except for the opening up of the two peritectic reactions into two broad three phase regions consisting of ($\gamma + \text{RE}_2\text{Fe}_{17} + \text{Liquid}$) and ($\text{RE}_2\text{Fe}_{17} + \text{REFe}_2 + \text{Liquid}$). The results of DSC study also indicate a transformation of the α phase at temperature slightly higher than 912 °C, the transformation temperature increases with the RE content of the alloys, and it is possibly due to the transformation of the α phase into the fcc γ phase. This transformation of α phase may be interpreted as a peritectoid formation of the α phase through a very narrow three phase region

($\alpha + \gamma + \text{RE}_2\text{Fe}_{17}$). No $\text{RE}_5\text{Fe}_{17}$ phase was detected down to 700°C even after prolonged annealing upto 30 days.

The contents of Chapter VIII focus on the results and discussion of some preliminary magnetic characterization experiments which were performed to explore the possibility of fabricating hard permanent magnets using the RE-Co-Fe-Cu-Zr and the RE-Fe-B alloys. The work strategy involved systematic characterization (e.g. magnetic, metallurgical etc.) studies on bulk alloys, and resin bonded and sintered magnets.

In the RE-Co-Fe-Cu-Zr system, unaged bulk U phase alloys had higher saturation magnetization (σ_s) and intrinsic coercivity (H_{iC}) (typical values ~ 110 emu/g, 40 Oe) compared to the N phase alloys (typical values ~ 75 emu/g, 20 Oe). In the low temperature aging studies at 675°C , the N phase alloys showed a superior magnetic hardening behaviour as compared to the U phase alloys. The N phase alloy of the composition $[\text{RE}(\text{Co}_{0.76}\text{Fe}_{0.13}\text{Cu}_{0.09}\text{Zr}_{0.02})_6]$ (this alloy will be labelled as C_{11} in further description) showed remarkable increase, more than 50 fold, in coercivity due to aging at 620°C ; the coercivity was found to increase from 20 Oe to 1180 Oe after about 300 hours of aging. The composition of alloy C_{11} was selected for the characterization of the N phase, and exploratory studied on the fabrication of resin bonded and sintered magnets. The magnetic properties of alloys of C_{11} composition varied due to a small variation of composition during melting. The σ_s of N phase was found to be 88 emu/g (saturation field 10 kOe) on the basis of magnetic measurements made on a resin bonded magnet prepared from an alloy of C_{11} composition. The N phase showed a moderate H_A value of ≥ 25 kOe and also the desired uniaxial anisotropy. During the course of studies on resin bonded magnets, it was found that the aging treatment needs to be carried out on solid piece of the alloy before milling and not on the milled powder. Resin bonded pellets prepared from 2.5 hours milled powder of an aged (620°C , 200 hours) alloy showed σ_s and σ_r values comparable to the commercially available Sm based 2:17 magnets, however, H_{iC} was

6-10 times lower; the typical value of magnetic properties were as follows: $H_c = 1170$ Oe, $\sigma_s = 83$ emu/g, and $\sigma_r = 59$ emu/g. Initial efforts to fabricate sintered magnets using an alloy of C_{11} composition resulted in $4\pi M_s$ value of 9-10 kG and very low values of H_c , about 100 Oe, and $M_r/M_s (< 0.1)$. The low values of H_c and M_r/M_s were attributed to a small loss of RE, during processing, resulting in a microstructure consisting of U and N phases. Efforts to fabricate sintered magnets using alloys containing somewhat higher RE than the alloy C_{11} , to compensate for composition shift during processing, also resulted in very poor H_c and σ_r values inspite of using several combination of sintering condition (900-1100 °C, 0.2 to 1.0 hour) and post sintering aging treatment (between 580-620 °C upto 240 hours). In two of the alloys of modified composition (i.e. the alloys containing 13.0 at.pct. Fe, 18.25 at.pct. RE and 12.0 at.pct. Fe, 16.8 at.pct. RE) N phase microstructure was obtained after sintering at 1000 °C, however, even for these alloys H_c and M_r/M_s values were unexpectedly low after sintering as well as aging treatments. The highest value of H_c observed for these alloys, after 120 hours aging at 620 °C, was of the order of 700 Oe. The reasons for the poor value of magnetic properties observed for the N phase containing sintered magnets were not understood properly.

In the RE-Fe-B system, the intrinsic properties of the $RE_2Fe_{14}B$ (Γ) phase were moderate in comparison with the $Nd_2Fe_{14}B$ phase. The Γ phase was found to have the following intrinsic magnetic properties: $T_c \cong 245$ °C and $\sigma_s \cong 125$ emu/g (for magnetically oriented resin bonded magnet of an alloy of composition $RE_{15}Fe_{77}B_8$). The Γ phase also has the desired uniaxial anisotropy and H_A value of ~ 40 Oe. Since the RE-Fe-B phase equilibria is quite similar to the Nd-Fe-B system, for magnetic characterization and magnet fabrication studies an alloy of composition $RE_{15}Fe_{77}B_8$ was selected on the basis of literature available on the Nd-Fe-B magnets. The alloy of composition $RE_{15}Fe_{77}B_8$ did not show any response to the aging treatment between 600-800 °C because of the very narrow homogeneity region of Γ phase at 1000 °C and possibly its extension at lower temperatures

without change in composition. The powders of $\text{RE}_x\text{Fe}_{92-x}\text{B}_8$ alloys ($x = 15-19$) were very reactive and invariably caught fire during handling in open air atmosphere. Because of this difficulty in handling the alloy powders, the efforts to fabricate resin bonded and sintered magnets in the RE-Fe-B system were rather restricted. A resin bonded RE-Fe-B magnet, produced using 3 hours milled powder of an alloy of $\text{RE}_{15}\text{Fe}_{77}\text{B}_8$ composition, showed the following properties: $H_C = 1400$ Oe, $\sigma_s = 118$ emu/g, $\sigma_r = 97$ emu/g and $\sigma_r/\sigma_s = 0.82$. Very low value of H_C and σ_r/σ_s , less than 400 Oe and 0.1, respectively, were observed for the sintered magnets prepared using alloys of $\text{RE}_x\text{Fe}_{92-x}\text{B}_8$ ($x = 15, 17, 19$) compositions. The poor magnetic properties of sintered magnets were found to be due to the presence of reasonably large amount of the magnetically soft α phase, small amount of the Γ phase and unevenly distributed RE-rich grain boundary phase in the microstructure of sintered pellets.

The conclusions and scope for the future work are presented in the last chapter.

CHAPTER I

INTRODUCTION

Rare earth permanent magnets (REPM) can be defined as a group of permanent magnet materials containing the magnetically active components rare-earth (R) and transition metal (T), where R is one or more of the elements having atomic numbers 57 (La) to 71 (Lu) and the group IIIB element of atomic number 39 (Y). In the last two decades, rare-earth magnets, which occupy an important place in the arsenal of modern engineering materials, have evolved from a physicist's vision into a large family of commercial materials [1-4]. Offering upto five times higher energy density and ten times more intrinsic coercivity than the best magnets of the 1960's, the REPM have displaced several older types and opened up entirely new areas of applications for permanent magnets [5,6].

The development of rare-earth-metal-bearing permanent magnets began in mid-sixties when K.J. Strnat and Coworkers [7] discovered that in a number of RCo_5 compounds a pronounced magnetocrystalline anisotropy is accompanied by high saturation magnetization and Curie temperature. Fabrication of sintered magnets by Das [8], Buschow et.al.[9] and Benz and Martin [10] was a major subsequent development. Since 1970, SmCo_5 magnets [coercivity 15-40 kOe, energy product $(\langle \text{BH} \rangle_{\text{max}})$ 16-20 MGOe] are manufactured on a commercial basis [11,12]. Shortly after the development of SmCo_5 permanent magnets, alloys containing copper as well as rare-earth and cobalt emerged. These became known as the precipitation-hardened family of R-(CuCo) alloys and eventually led to the development of second group of high energy product $\text{Sm}(\text{Co,Cu,Fe,X})_Z$ magnets (where $Z = 6-8.5$, and $X = \text{Mn, Ti, Zr, Hf}$) [13-16]. On account of the relationship with the stoichiometric R_2Co_{17} compounds, these alloys are designated as the 2:17 materials. Magnets from this group of alloys, especially, $\text{Sm}(\text{Co,Cu,Fe,Zr})_Z$ type, have gained considerable technical importance on account of their higher B_r and $(\text{BH})_{\text{max}}$ values (laboratory record more than 33 MGOe [17,18] compared with SmCo_5)

and their low Sm and Co contents. The latest development in the area of rare-earth-metal-bearing permanent magnets is a third generation of materials based on rare-earth-iron-borides (prototype : $\text{Nd}_2\text{Fe}_{14}\text{B}$). The Nd-Fe-B magnets became known in 1983 following developments in Japan [19] and USA [20]. At room temperature the $(\text{BH})_{\text{max}}$ value of these magnets exceeds that of all other magnet grades (Fig.I.1). Sintered Nd-Fe-B laboratory magnets have upto 50.8 MGOe energy product [21] and magnets with 20-30 MGOe and coercivity (H_c) 10-20 kOe are commercially available. As illustrated in Fig.I.2, a strong growth for REPM, especially, Nd-Fe-B type, is expected in the last decade of this century [6].

The R-Co magnets use Sm as the principal component. But Sm is fairly scarce and expensive. Even though Nd content in common ores of rare-earth is more abundant than Sm, the cost of Nd keeps the price of Nd-Fe-B magnets much higher than desired [22]. Fig.I.3 shows the estimates for the terrestrial abundance of rare-earth elements. It is evident from the figure that for mass consumption magnets one ought to use light rare-earth (LRE) as much as possible and avoid Nd, Sm and heavy rare-earths (HRE) except where they are absolutely needed for special magnet properties [3].

Mischmetal (MM), the natural mixture of light rare-earths (Ce, La, Nd and Pr) is abundant, 30-40 times less costly than pure Sm or Nd, and most readily available. Cheaper magnets with moderate magnetic properties have been produced in Sm-Co (e.g. SmCo_5 ; $\text{Sm}(\text{Co},\text{T})$, $\text{T} = \text{Cu}, \text{Fe}$; $\text{Sm}(\text{Co},\text{Fe},\text{Cu},\text{Mg})_Z$ etc.), Nd-Fe-B and related systems, by partial or complete substitution of Sm or Nd with mischmetal [4,22,24]. The theme of this thesis centres on such cheaper magnets in $\text{MM}(\text{Co},\text{Fe},\text{Cu},\text{Zr})_Z$ ($Z \sim 7$) and MM-Fe-B systems. Broadly, the investigation concerns two distinct but related aspects: (i) phase equilibria studies in (a) MM-Co-Fe-Cu-Zr, (b) MM-Fe-B, and (c) MM-Fe systems; and (ii) some preliminary studies on magnetic characterization of phases and fabrication of magnets in these systems. Phase equilibria work on MM-Fe system was undertaken to supplement the investigation on the MM-Fe-B system. Since India is richly endowed with rare-earth

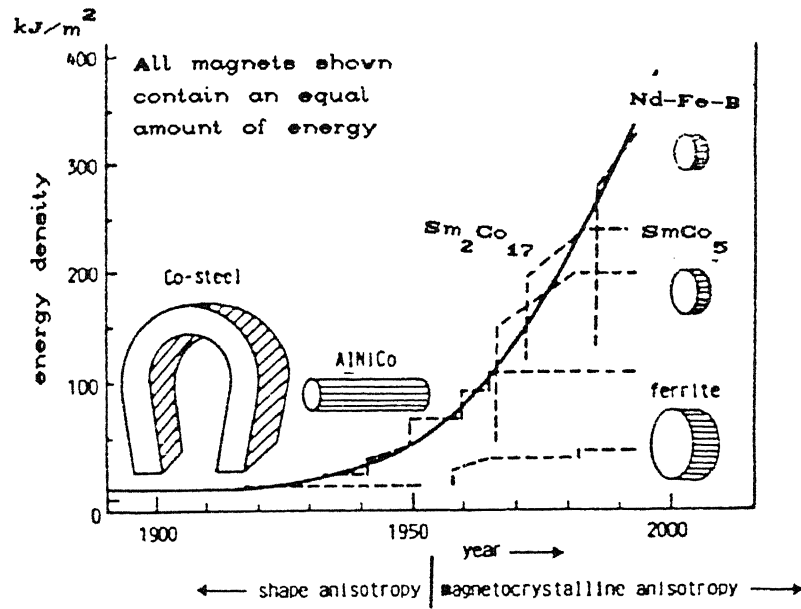


Fig.I.1 Progress in permanent magnetic materials (after Warlimont [6])

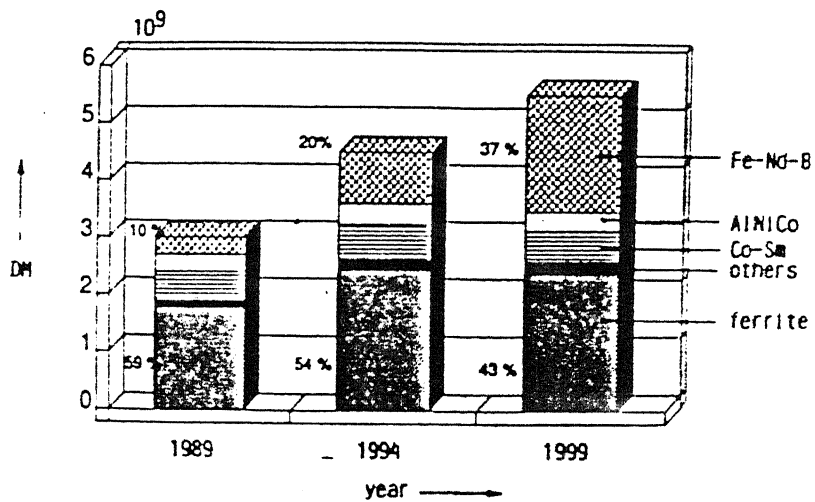


Fig.I.2 Estimated market development of permanent magnetic materials (after Warlimont [6])

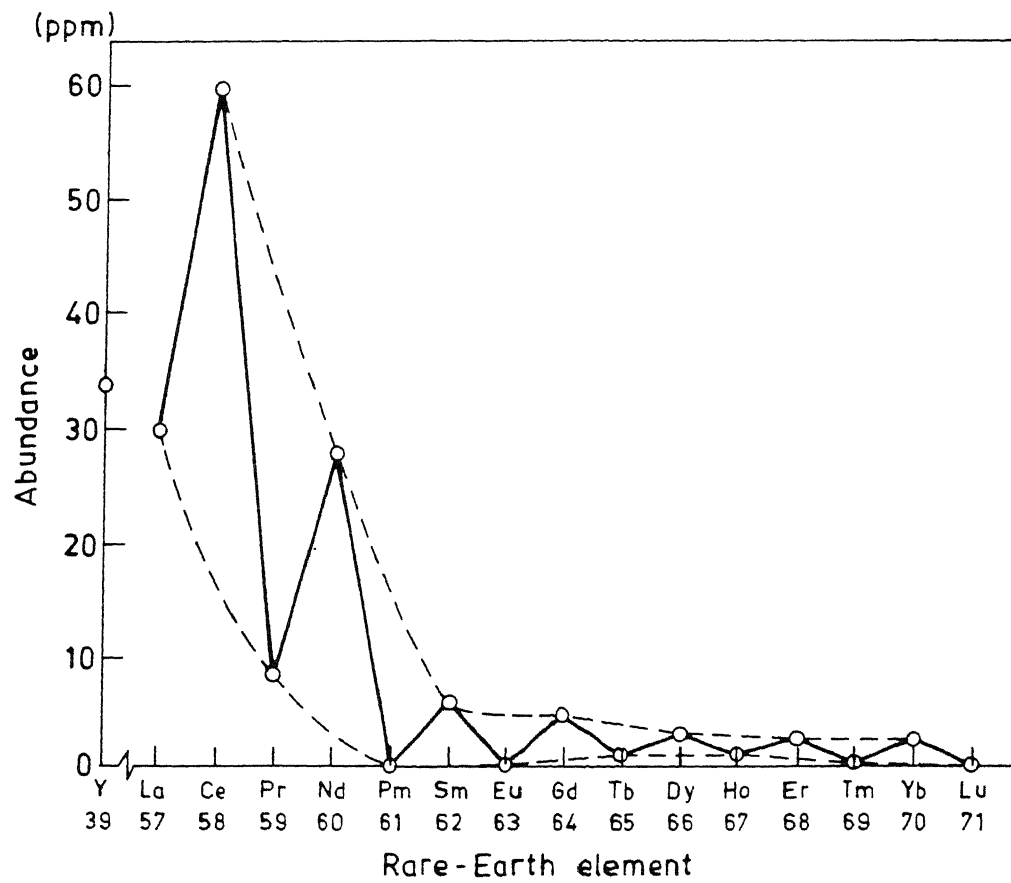


Fig.I.3 Natural abundance of rare-earth elements in the earth crust [3]

deposits [25], it makes this study relevant in Indian context.

A brief and critical review (Chapter-II) on rare-earth permanent magnets, with emphasis on $\text{Sm}(\text{Co}, \text{Fe}, \text{Cu}, \text{Zr})_2$ and Nd-Fe-B magnets, phase equilibria and fabrication methods, follows as a prelude to Chapter-III which defines precise scope and statement of present research problem. The general details regarding materials used and experimental techniques employed are presented in Chapter-IV. The main emphasis in the subsequent three chapters (Chapters V to VII) is on results and discussion of phase equilibria studies. Magnetic characterization and fabrication studies are presented in Chapter VIII. The final conclusions of this investigation and scope for the future work are highlighted in the last Chapter (Chapter-IX).

CHAPTER II

REVIEW OF LITERATURE

A magnet is fundamentally an energy storage device [26]. The special importance of permanent magnets derives from their ability to act on ferromagnetic materials, either by attraction or repulsion, and to provide a permanent magnetic flux with no operating cost. A permanent magnet is characterized by its intrinsic coercivity (H_C) (unit*: kOe or kA/m) and remanence B_r or $4\pi M_r$ (unit : KG or Tesla) (Fig.II.1). The remanence B_r determines the flux density which remains after removal of a magnetizing field, while the intrinsic coercivity H_C is a measure of a material's resistance against demagnetizing field. The maximum energy storage per unit volume $(BH)_{\max}$ (unit : MGOe or kJ/m^3) is the figure of merit often used for permanent magnetic materials. The most obvious properties for several commercially available magnetic materials are compared in Table II.1. It can be seen that rare-earth permanent magnets, especially based on Nd-Fe-B, are superior to other magnet types.

The evolution of rare-earth permanent magnets (REPM) to the current standard has involved enormous scientific and technical endeavours of diverse nature. These include search for new materials with improved magnetic properties, phase equilibria studies in the systems of potential importance, development of low cost magnets, fabrication methods etc. These efforts are periodically documented in several review papers [1-6,11,27-43], books and monographs [44-48], proceedings of international conferences (International Workshop on Rare-Earth Magnets, INTERMAG, MMM etc.) and technical journals (such as J. Appl. Phys., J. Magnetism and Magnetic Materials, J. Less Common Metals etc.) [e.g.49,50]. The objective of this Chapter is not to cover

* Vide Appendix-A for conversion factors and details of units in CGS and SI systems.

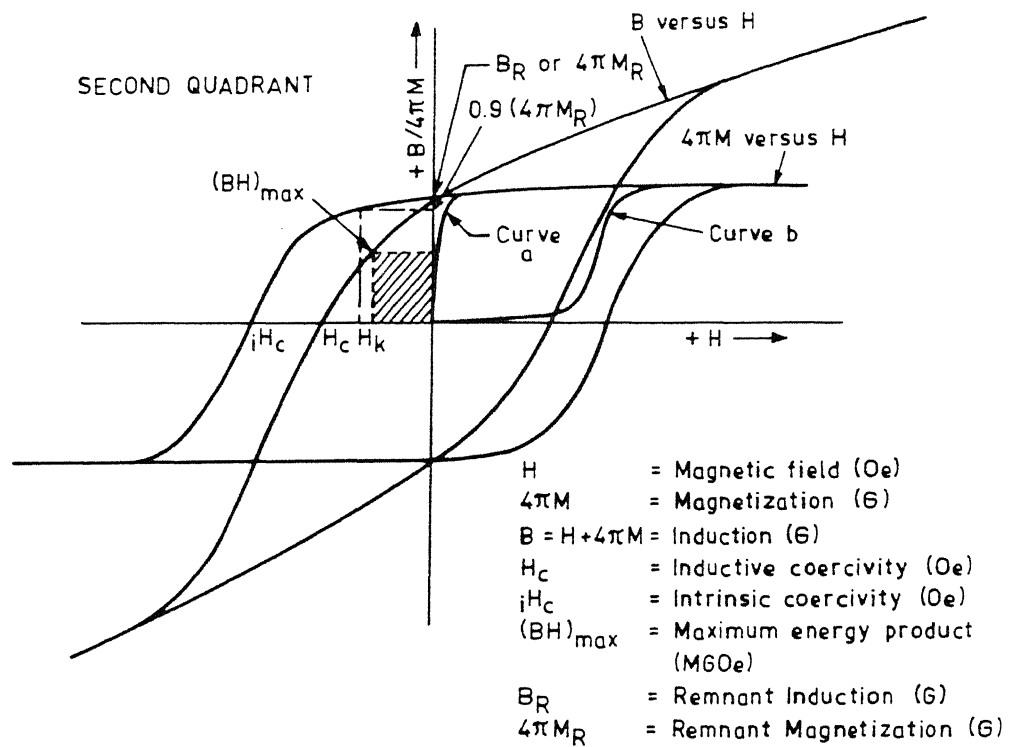


Fig.II.1 General hysteresis curve for permanent magnets [4]

Table II.1: Comparison of the Magnetic Properties of Several Commercially Available Rare-Earth Permanent Magnets [2]

Material	$(BH)_{\max}$ (kJ m ⁻³)	B_r (T)	H_c (kA m ⁻¹)	H_c (kA m ⁻¹)	Price (\$/J)
Ferroxdure 380 SrFe ₁₂ O ₁₉	28.5	0.39	275	275	1
Alnico RES 190	83.5	1.04	-	124	2
SmCo ₅	154	0.89	1100	668	10
REC 26 Sm(Co,Fe,Cu,Zr) ₇	215	1.08	800	796	8
Neomax 35 Nd ₁₅ Fe ₇₇ B ₈	279	1.22	995	891	5
Magnaquench	318	1.35	880	-	-

the whole gamut of rare-earth permanent magnets but to present a general review with emphasis on $\text{Sm}_2(\text{Co,Fe,Cu,Zr})_{17}$ and Nd-Fe-B magnets, and fabrication methods which are particularly relevant to this investigation. MM substitution for Sm or Nd is highlighted wherever data is available.

The contents of this Chapter are arranged in five sections. The first section presents a brief overview of rare earth(R)-transition metal(T) compounds (4f-3d compounds) and some general comments on microstructure and coercivity mechanisms. Phase diagrams of some R-Co, R-Fe and R-T-B systems together with crystal structure information on important phases are covered in section two. The next section elaborates on $\text{Sm}_2(\text{Co,Fe,Cu,Zr})_{17}$ and Nd-Fe-B magnets, with main emphasis on sintered magnets. The penultimate section focuses very briefly on fabrication methods. The last section compares the Samarium and Neodymium magnets.

2.1 General Overview

For an alloy (or phase) to be a potential candidate for permanent magnet fabrication, it should belong to ferro- or ferri-magnetic, especially the former, class of materials and possess the following characteristics : (a) high level of saturation magnetization ($4\pi M_s$), (b) high Curie temperature T_c , and (c) strong uniaxial magnetocrystalline anisotropy field H_A [44,51]. Saturation magnetization level determines the maximum level of flux that can be obtained from the magnet. The Curie temperature T_c also determines the obtainable flux by its effect on saturation magnetization. The Curie point should be substantially higher than the use temperature because as the operating temperature is increased the flux decrease becomes increasingly rapid [45]. Large uniaxial anisotropy field permits the attainment of high intrinsic coercivity. A large magnetocrystalline anisotropy is a necessary condition for a large H_{iC} but it is not a sufficient condition; the coercive force finally developed in a magnet is influenced by metallurgical factors involved during processing [1,11,52].

2.1.1 4f-3d Compounds

The atomic diameters of R (R: 4f element) atoms are substantially larger than T (T: 3d element) atoms [53]. According to the Hume-Rothery rules [54], this precludes any significant substitutional solid solubility between atoms from 4f and 3d groups. A series of intermetallic compounds forms in the binary R-T systems. Many of these compounds have non-cubic structure (usually hexagonal or rhombohedral) with unique crystallographic axes. Elements of very small atomic radii, e.g. B, C, N etc., have added further possibilities of having large number of ternary intermetallic compounds, many of them having immense potential as magnetic materials [1,2,55-57]. One can also substitute one rare-earth element by another rare-earth element and/or one transition metal by another transition metal, and form phases of desired magnetic properties.

2.1.1.1 Binary and Ternary Compounds

Almost all the rare-earths form hexagonal intermetallic compounds of the type R_2T_{17} , RT_5 , R_2T_7 (where $R = Co, Fe, Ni, Mn$) and several other stable and metastable phases in between these compositions [1,47]. However, the choice of compounds for use as a permanent magnetic material narrows down to the groups RCo_5 and R_2Co_{17} due to their high Curie temperature, high saturation magnetization and large uniaxial magnetocrystalline anisotropy. The first two generations of magnet families, i.e. 1:5 and 2:17, are based on these two compounds. The development of binary R-Fe based permanent magnets have been hindered for several reasons, e.g. (i) Fe forms fewer compounds with rare-earths than Co, (ii) stable compounds of RFe_5 type are absent, and (iii) compounds which are stable, such as R_2Fe_{17} , have very low Curie temperatures (Nd_2Fe_{17} has a Curie temperature of only $\sim 60^\circ C$) and do not possess uniaxial anisotropy [1,3,58]. Recent work [2,59] revealed a ternary modification, $R_2Fe_{14}B$, which has a tetragonal structure and exists with all the rare-earths. The Curie points of $R_2Fe_{14}B$ are higher by $200-300^\circ C$ than the corresponding R_2Fe_{17} compounds [2,59]. Especially, $Nd_2Fe_{14}B$ also has the desired uniaxial anisotropy at room temperature, a very high value of $4\pi M_s$ and $T_c \sim 310^\circ C$ [19]. The third generation magnets are based on this compound.

Structural and magnetic characteristics of rare-earth compounds, that form the basis of the present REPM types, have been recently reviewed by Wallace [1], Buschow [2], Strnat [3] and Livingston [37]. Fig.II.2(a),(b) and Fig.II.3(a)-(c), summarize the T_c and room temperature values of $4\pi M_s$ and H_A (with direction of easy magnetization vector) for RCo_5 , R_2Co_{17} and $R_2Fe_{14}B$ compounds. The Curie temperatures of $RE_2Fe_{14}B$ compounds are lower than the RCo_5 and R_2Co_{17} compounds [Fig.II.2(a)]. In general, the saturation magnetization is higher for the light rare-earth compounds.

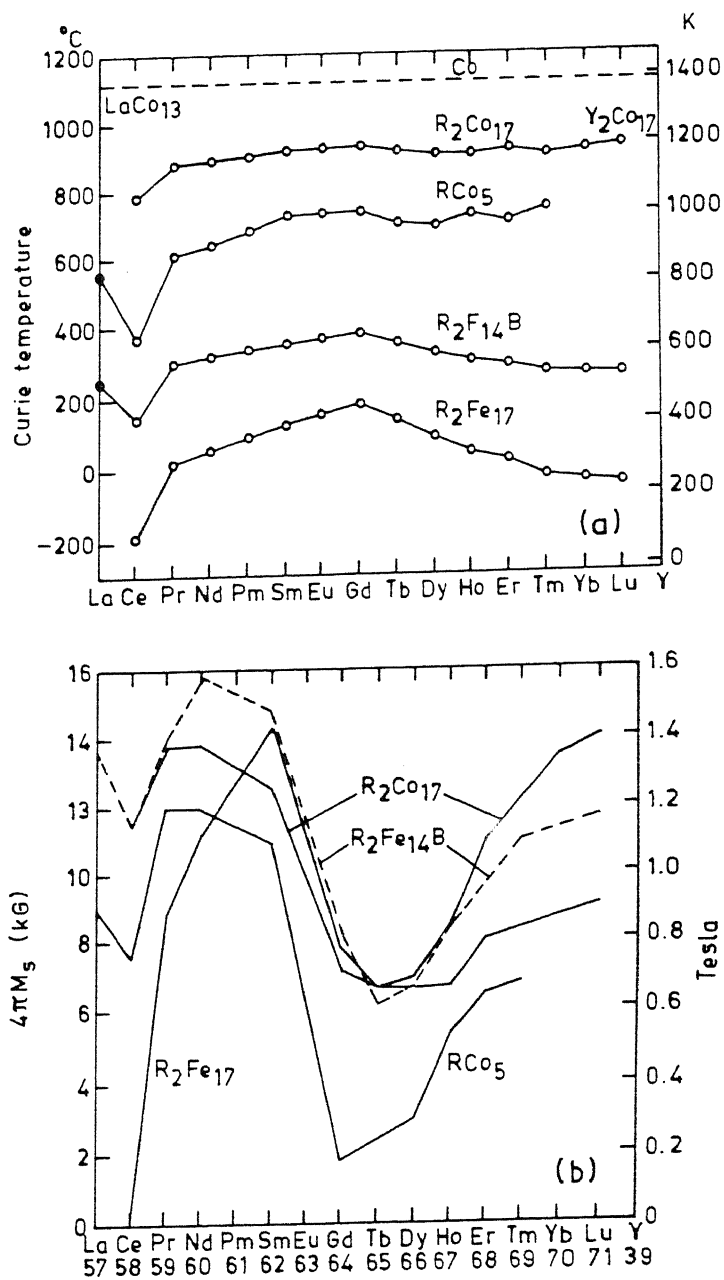


Fig.II.2 (a) Curie temperatures of 4f-3d compounds in the isostructural families of interest for magnets
 (b) Room temperature saturation induction of 4f-3d compounds of interest for magnets (after Strnat [3])

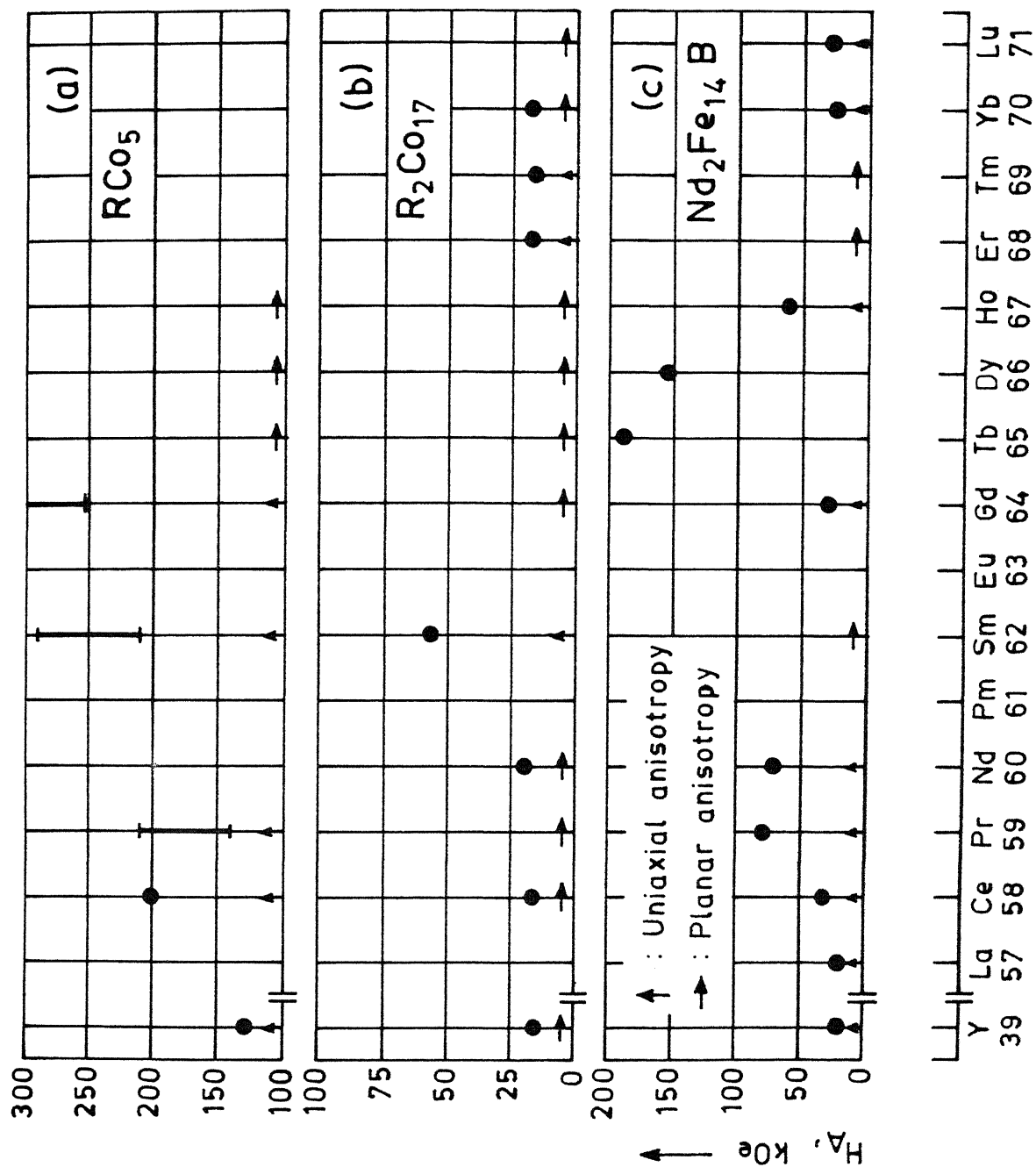


Fig.11.3 Anisotropy field H_A of 4f-3d compounds of interest for magnets : (a) RCo_5 ; (b) R_2Co_{17} ; and (c) $Nd_2Fe_{14}B$ (compiled from reference 1,2,37, 60-64)

At room temperature the magnetization vector of $R\text{Co}_5$ compounds lies along the c-axis for $R = \text{La, Ce, Sm, Pr, Gd}$ and Y , and it lies in the basal plane for the other rare-earth elements [Fig.II.3(a)]. The anisotropy field H_A for SmCo_5 (>210 kOe) is the highest. In the case of $R_2\text{Co}_{17}$ compounds, uniaxial anisotropy occurs only for $R = \text{Sm, Er}$ and Tm [Fig.II.3(b)]. With other binary 2:17 compounds, the preferred direction of the magnetic polarization vector is in the plane perpendicular to the hexagonal or rhombohedral axis. [1].

Magnetic anisotropy for the $R_2\text{Fe}_{14}\text{B}$ compounds is uniaxial for $R = \text{Y, Ce, Pr, Nd, Gd}$ and Dy , and for $R = \text{Sm, Er}$ and Tm it is planar (means magnetization vector lies in the basal plane). Low Curie temperature of these compounds have been of great concern. Temperature dependence of anisotropy field H_A and magnetization for a series of $R_2\text{Fe}_{14}\text{B}$ has been studied by Sagawa et.al.[65] (Fig.II.4) and several others [64,66-69]. Uniaxial anisotropy in Nd and Ho compounds changes to planar anisotropy at lower temperature. It is evident from Fig.II.4 that compared with light rare-earths (e.g.Ce, Nd, Pr, Sm) the compounds of Dy and Tb possess large anisotropy field and are less sensitive to the influence of temperature on magnetization.

2.1.1.2 Effect of Substitution

One can combine several rare-earths and form phases of the type $(R_1, R_2, \dots)_2\text{Co}_{17}$, e.g. $(\text{Sm, Gd})_2\text{Co}_{17}$. Transition elements can substitute for one another to a lesser extent; $R_2(T_1, T_2, \dots)_{17}$ type phases exist, such as $R_2(\text{Co, Fe})_{17}$ [70,71]. $R_2\text{Fe}_{14}\text{B}$ compounds with substitution of R and T elements, $(R_1, R_2, \dots)_2(\text{Fe, T}_1, \text{T}_2, \dots)_{14}\text{B}$, can readily form, e.g. $(\text{Nd, Dy})_2(\text{Fe, Co})_{14}\text{B}$ [1,72]. These substitutions are made for various practical reasons [3]. The rare-earth elements used in the REPM are shown in Fig.II.5 with general comments on how they affect properties and cost.

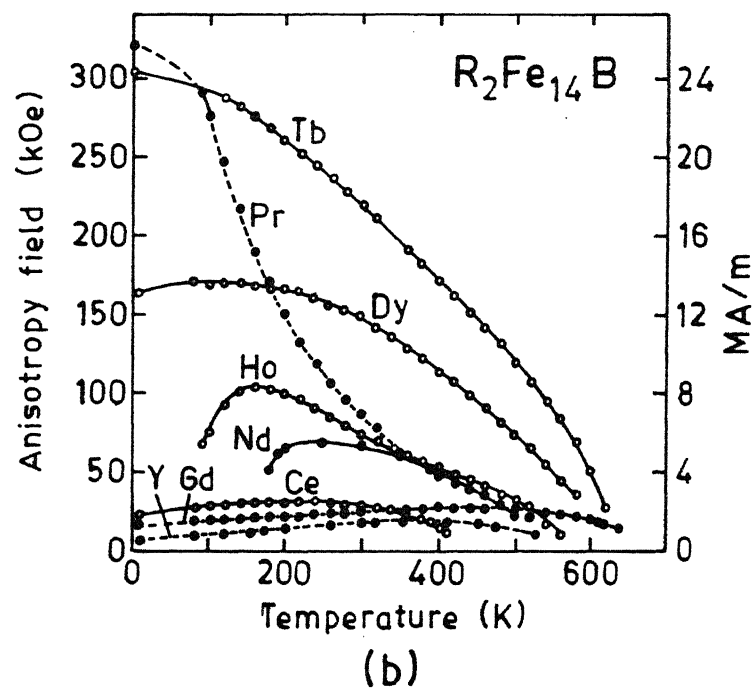
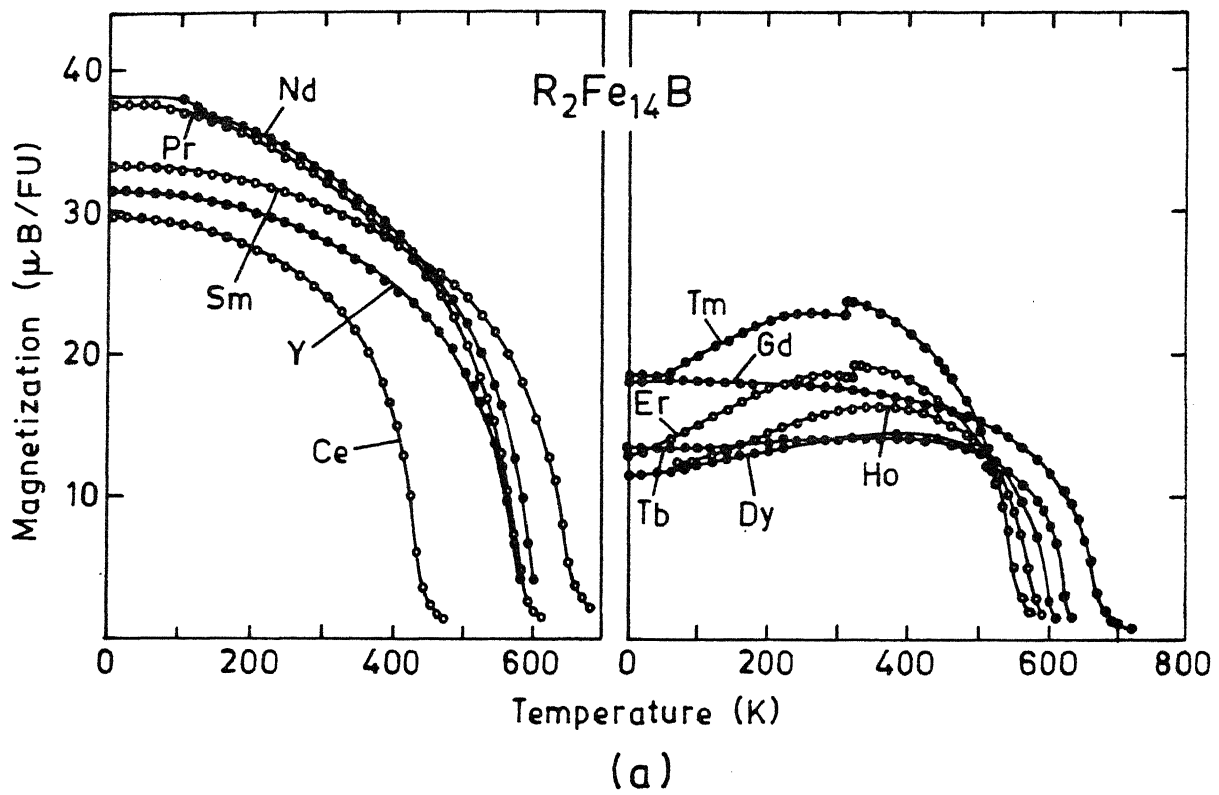


Fig.II.4 (a) Temperature dependence of the spontaneous magnetization in $R_2Fe_{14}B$ compounds
 (b) Temperature dependence of the anisotropy field H_A of $R_2Fe_{14}B$ compounds (after Sagawa et.al.[65])

PRINCIPAL CONSTITUENTS						MINORITY CONSTITUENTS				
Sm	La	Ce	Pr	Y	Nd	Gd	Tb	Dy	Ho	Er
High coercivity (in RCO_5)		Lowers B_s, T_c	Raise saturation, B_s Raise Curie Point, T_c			Reduce B_s , Raise T_c Improve temp. coefficient				
Mod.	Lowest cost		Moderate cost			Highest cost				

Fig.II.5 Rare-earth elements used in REPM and some of their effects on magnetic properties (after Strnat [3])

R_2Co_{17} Compounds

Among all the light rare-earth R_2Co_{17} compounds, a large amount of work has been performed with the Sm_2Co_{17} alloy which alone possesses an uniaxial anisotropy. Substitutions of R atom with other rare-earths have produced only marginal improvement in anisotropy of the R_2T_{17} compounds [4,73-77]. Substitution of Sm by heavy R (= Gd,Tb,Dy,Ho,Er) have been attempted to produce magnets with improved thermal coefficients [3,4,78]. The replacement of Sm by light rare-earths La, Ce, Pr, Y or mischmetal (MM) is done due to economic reasons [4,79-81].

Substantially beneficial effects are obtained by substitution of Co atoms with other elements [82]. The contributions of Ray and Strnat [83] and Schaller et.al.[84], dealing with ternary $R_2(Co_{1-x}Fe_x)_{17}$ compositions, are important in the development of R_2T_{17} type permanent magnet alloys. For $R = Sm$, the easy axis of $R_2(Co_{1-x}Fe_x)_{17}$ compound was found to be retained for x upto 0.5, with little effect on Curie temperature. Easy direction of magnetization in $R_2(Co_{1-x}Fe_x)_{17}$ compounds, with $R = Ce, Pr$, and Y , changes from planar to uniaxial for a range of x values; 0.05-0.45 for Ce, 0.2-0.6, for Pr and 0.1-0.5 for Y [83]. For the $Nd_2(Co_xFe_{1-x})_{17}$ alloys, however, the easy basal plane was retained for all values of x . Mn substitution for cobalt also produces similar effects in $Ce_2Co_{17-y}Mn_y$ ($y = 2-6$) and $Y_2Co_{17-y}Mn_y$ ($y = 2-3$) [70]. The effects of large number of other transition metal substitutions have been discussed by Narasimhan and Coworkers [85,86] and Wallace and Coworkers [75,87]. Except for Mn (upto 20% of T) and Fe-substitutions (both of which increase the saturation magnetization M_s) M_s decreases for substitution of Co by other T elements in the order $Hf > V > Cr > Mn(>20\%) > Zr > Ti > Cu$ [75]. The effect of substitution of Co, by other T elements, on strengthening the anisotropy field H_A is in the order $Zr > V > Hf > Ti > Cr > Mn > Fe > Cu$ [75]. Curie temperature decreases with all these substitutions [75]. The effect on H_A for transition metal substituents in Ce_2Co_{17} are shown in Fig.II.6. The effect of Cr on anisotropy field H_A is almost twice that of Mn; the severe penalties in M_s reduction with Cr substitution detract from its

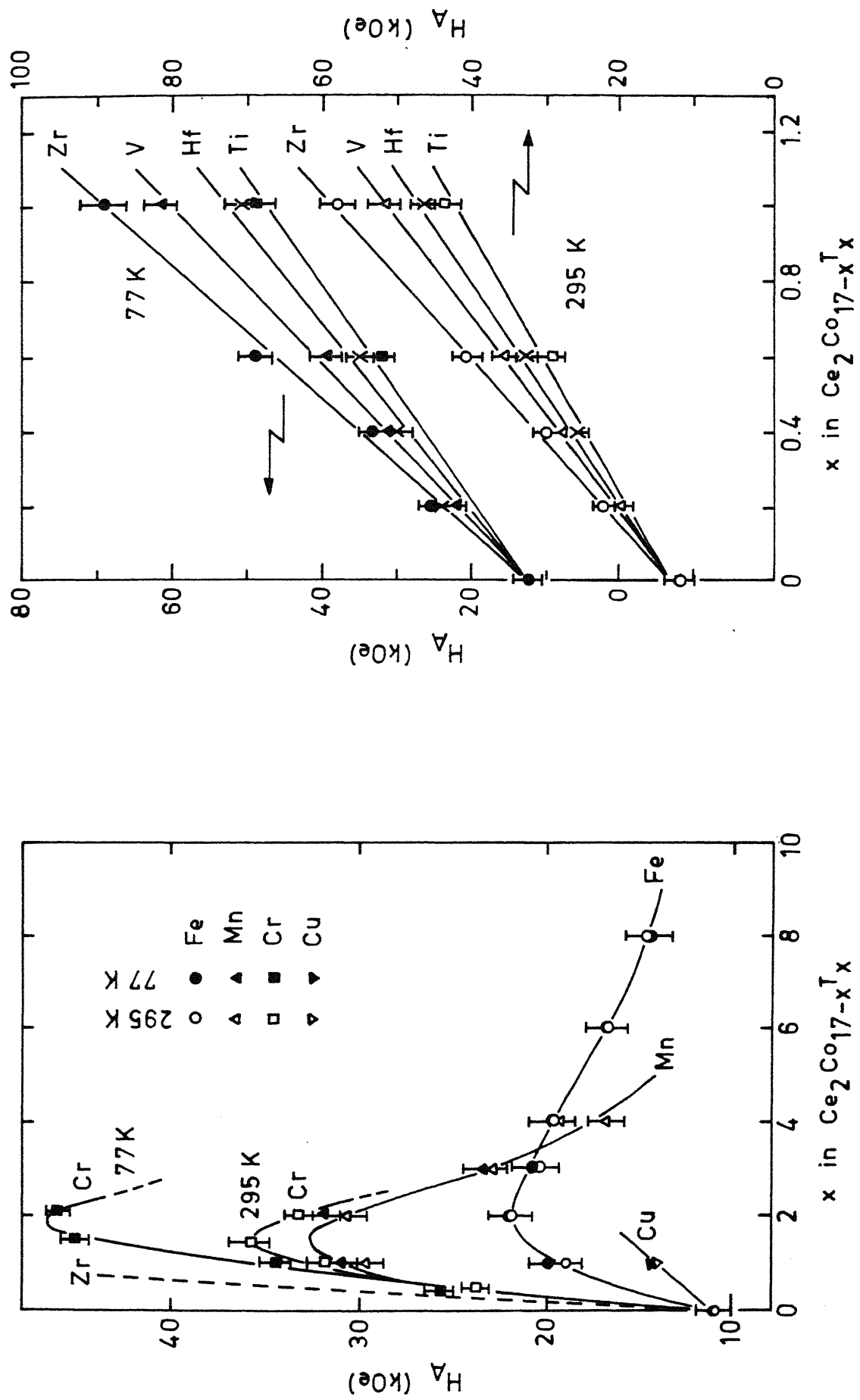


Fig.II.6 Variation of anisotropy field H_A as a function of x in $\text{Ce}_2\text{Co}_{17-x}\text{T}_x$. open circle indicate the data at 295 K and closed ones at 77 K (after Wallace et.al.[75])

use. The effect of Zr on H_A is the greatest and is two to three times more than that of Mn and Cr.

$R_2Fe_{14}B$ Compounds

Substitutions in $Nd_2Fe_{14}B$ have been most extensively studied. Substitution of Dy or Tb for Nd in $Nd_2Fe_{14}B$ results in an increase of hard magnetic properties (as expected, Fig.II.4) but it affects the Curie temperature only slightly and decreases the saturation magnetization [1,37,88]. Sun et.al.[89] found that replacement of Nd by Y, La or Ce does not have a pronounced effect on T_c . Other workers [90,91] have reported a decrease in magnetic moment and Curie temperature when substituting Nd with Ce or Mischmetal. The effect of Mischmetal on T_c has been reported to be less pronounced as compared to Ce [92].

The substitution of Co for Fe in $R_2Fe_{14}B$ compounds has been studied by several workers and reviewed by Buschow [89]. Replacing Fe with Co in $(Nd_2Fe_{14-x}Co_xB)$ leads to a continuous increase in T_c with increasing substitution [37,93]. With increase in x , magnetization first increases slightly and then decreases after $x \sim 2$ [37]. The anisotropy field decreases monotonously with increasing replacement of Fe by Co from 70.7 kOe at $x = 0$ to 55.3 kOe at $x = 10$ [1]. For the system $Nd_2Fe_{14}B$, the effect of various metal substitutions has been compiled by Buschow [72] and reproduced in Fig.II.7. Substitution of Si, Ni and Co for Fe raises T_c , whereas substitution of Al, Cr, Mn and Ru lowers T_c .

Substitution of C for B in $R_2Fe_{14}B$ has also been studied [94,95]. $Nd_2Fe_{14}C$ phase shows intrinsic properties which are comparable to those of $Nd_2Fe_{14}B$ [88].

Mischmetal Substitution

Magnetic properties of $MMCo_5$, MM_2Co_{17} and $MM_2Fe_{14}B$ type compounds are compiled in Table II.2. The values of magnetic properties for the corresponding Ce compounds (Ce is a major constituent element in Mischmetal), Sm and Nd compounds are also included in Table II.2 for comparison. The properties of $MM_2Fe_{14}B$

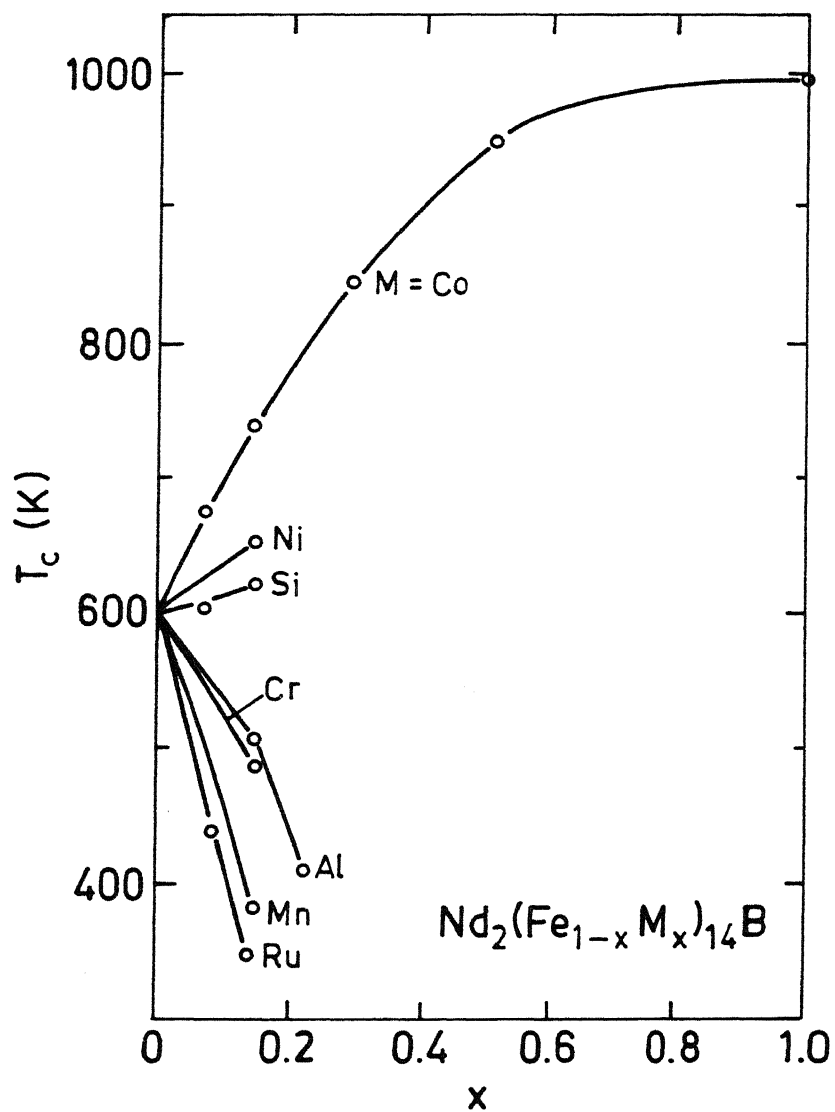


Fig.II.7 Composition dependence of Curie temperature in various $\text{Nd}_2(\text{Fe}_{1-x}\text{M}_x)_{14}\text{B}$ compounds (after Buschow [72])

Table II.2: Intrinsic Properties of MM Bearing Compounds as Compared to the Corresponding Ce, Sm, or Nd Compounds.

Compounds	T_c ($^{\circ}\text{C}$)	$4\pi M_s$ (kG)	H_A (kOe)	D.O.M.*
SmCo_5	747 [96]	9.6 [61] 11.0 [97]	210-290 [61,62]	c-axis
CeCo_5	464 [96]	8.7 [60] 7.5 [62]	170-210 [61,62]	c-axis
MMCo_5	500 [51]	8.2 [61]	185-195	c-axis
<hr/>				
$\text{Sm}_2\text{Co}_{17}$	917 [1]	12.6 [3]	65 [1]	c-axis
$\text{Ce}_2\text{Co}_{17}$	807 [1]	11.6 [3]	14 [1]	basal/cone
$\text{Ce}_2(\text{Co}_{0.7}\text{Fe}_{0.3})_{17}$	725 [75]	-	15-16 [75]	c-axis
$\text{MM}_2(\text{Co}_{0.7}\text{Fe}_{0.3})_{17}$	750 [98]	14.8 [98]	6.7 [98]	close to c-axis
<hr/>				
$\text{Nd}_2\text{Fe}_{14}\text{B}$	315 [2]	15.9 [2]	71 [1]	c-axis
$\text{Ce}_2\text{Fe}_{14}\text{B}$	164 [66]	11.6 [2]	29 [2]	c-axis
$\text{MM}_2\text{Fe}_{14}\text{B}$	210 [91]	-	50 [91]	c-axis

* D.O.M. - direction of easy magnetization

compound, although inferior to $\text{Nd}_2\text{Fe}_{14}\text{B}$, are considerably superior to $\text{Ce}_2\text{Fe}_{14}\text{B}$. Not much information seems to be available for the $\text{MM}_2\text{Co}_{17}$ phase. Ray and Strnat [83] reported that substitution of cobalt by Fe in $\text{MM}_2(\text{Co}_{1-x}\text{Fe}_x)_{17}$ (for $x = 0.1-0.45$) induces a change in the direction of magnetization vector from planar to uniaxial. Mittal [99] on the other hand found that uniaxial anisotropy in $\text{MM}_2(\text{Co}_{1-x}\text{Fe}_x)_{17}$ alloys, between $x = 0.1$ to 0.45 , is due to the presence of another phase (designated as S [100]) and not due to the real 2:17 stoichiometry phase. The S phase forms around RE:T ratio of 1:7 and is possibly structurally related with the 2:17 phase [101]. The real 2:17 stoichiometry phase do not show uniaxial anisotropy irrespective of the amount of Fe

substituted for cobalt [99]. The Curie temperature of $\text{MM}_2(\text{Co}_{1-x}\text{Fe}_x)_{17}$ phase decreases from 879 to 368 when x increases from 0.2 to 0.8 [99]. The Curie temperature of S phase was also found to decrease in $\text{MM}(\text{Co}_{1-y}\text{Fe}_y)_7$ alloys with increase in Fe content; typically the value decreased from 800 °C to 700 °C with increase in y from 0.4 to 0.6 [100]. H_A value (~ 7 kOe) reported for $\text{MM}_2(\text{Co}_{0.7}\text{Fe}_{0.3})_{17}$ composition (Table II.2) is considerably lower than the corresponding Ce composition (~ 15 kOe) it is possibly due to measurements made on a multiphase $\text{MM}_2(\text{Co}_{0.7}\text{Fe}_{0.3})_{17}$ alloy.

2.1.2 Microstructure and Coercivity

None of the 4f-3d compounds, in single phase form, is per se a permanent magnet [1-4]. Real magnets are multiphase systems with complex microstructures [33,34] that provide mechanisms for pinning of domain walls [52,102]. The coercive field strength of a permanent magnet is a results of several contributions from the microstructure [103], such as:

- (i) intrinsic properties of the hard magnetic phase;
- (ii) grain size of the hard magnetic phase;
- (iii) size, distribution and properties of the intermediate phase (coherent or non-coherent, chemical composition, soft hard or nonmagnetic etc.) isolating the hard magnetic phase grain;
- (iv) pinning of domain walls by small inclusion at grain boundaries or within the grain; etc.

In SmCo_5 and Nd-Fe-B magnets domain walls are predominantly pinned at grain boundaries by secondary phases or surface irregularities and inhomogeneities (nucleation controlled coercivity [52,102-104]), while in most "2-17" magnets they are pinned inside the main-phase grain mainly by precipitates and also by point defects, atomic disorder, dislocations, stacking faults etc. (referred to as "domain wall pinning controlled coercivity" [52,102-107]). These "2-17" magnets are also known as precipitation hardened magnets [106]. Magnets hardened by these two different mechanisms exhibit characteristic dependence of

hysteresis loop and coercivity on applied field [46,52] as illustrated for the $\text{Sm}(\text{Co,Fe,Cu,Zr})_{7.6}$ (2:17 type) and $\text{Nd}_{17}\text{Fe}_{76}\text{B}_7$ ($\text{Nd}_2\text{Fe}_{14}\text{B}$ based) magnets (Fig.II.8). In the case of precipitation hardened magnets a step-like dependence of H_c on applied field is observed.

Addition of copper plays an important role in enhancing coercivity of 2:17 magnets by precipitation hardening [108-110]. Small amounts of elements such as Zr, Hf or Ti etc. (in 2:17 magnets) and Al, Ga, Si or V etc. (in $\text{Nd}_2\text{Fe}_{14}\text{B}$ based magnets) are added to achieve the necessary subtle changes in phase composition and optimize metallurgical microstructures [3,4,111,112]. Complicated heat treatments are often required to bring about submicroscopic features that help to optimize structure-sensitive magnetic properties e.g. coercivity, shape of hysteresis loop, temperature stability [40,113,114] etc.

2.2 Phase Equilibria and Crystal Structure

Heat treatment, phase constituents and microstructural characteristics, etc., have considerable influence on the development of optimum magnetic properties in REPM [4,11]. In order to understand the behaviour of REPM alloys, to optimize their magnetic properties as well to exploit them more fully, it is necessary to have complete phase equilibria data. The scope of this section is limited to the phase diagrams of a few binary and multicomponent R-Co and R-Fe based systems which will serve as a prelude to next section and/or are expected to help in the interpretation of phase equilibria data of MM-Co-Fe-Cu-Zr, MM-Fe and MM-Fe-B systems. Structural features of some important intermediate phase are also covered briefly.

2.2.1 R-Co Systems

Phase equilibria in R-Co systems have been reviewed by Gupta [101]. RCo_5 and R_2Co_{17} phase are important from the point of view of developments in permanent magnets. RT_5 compounds (which

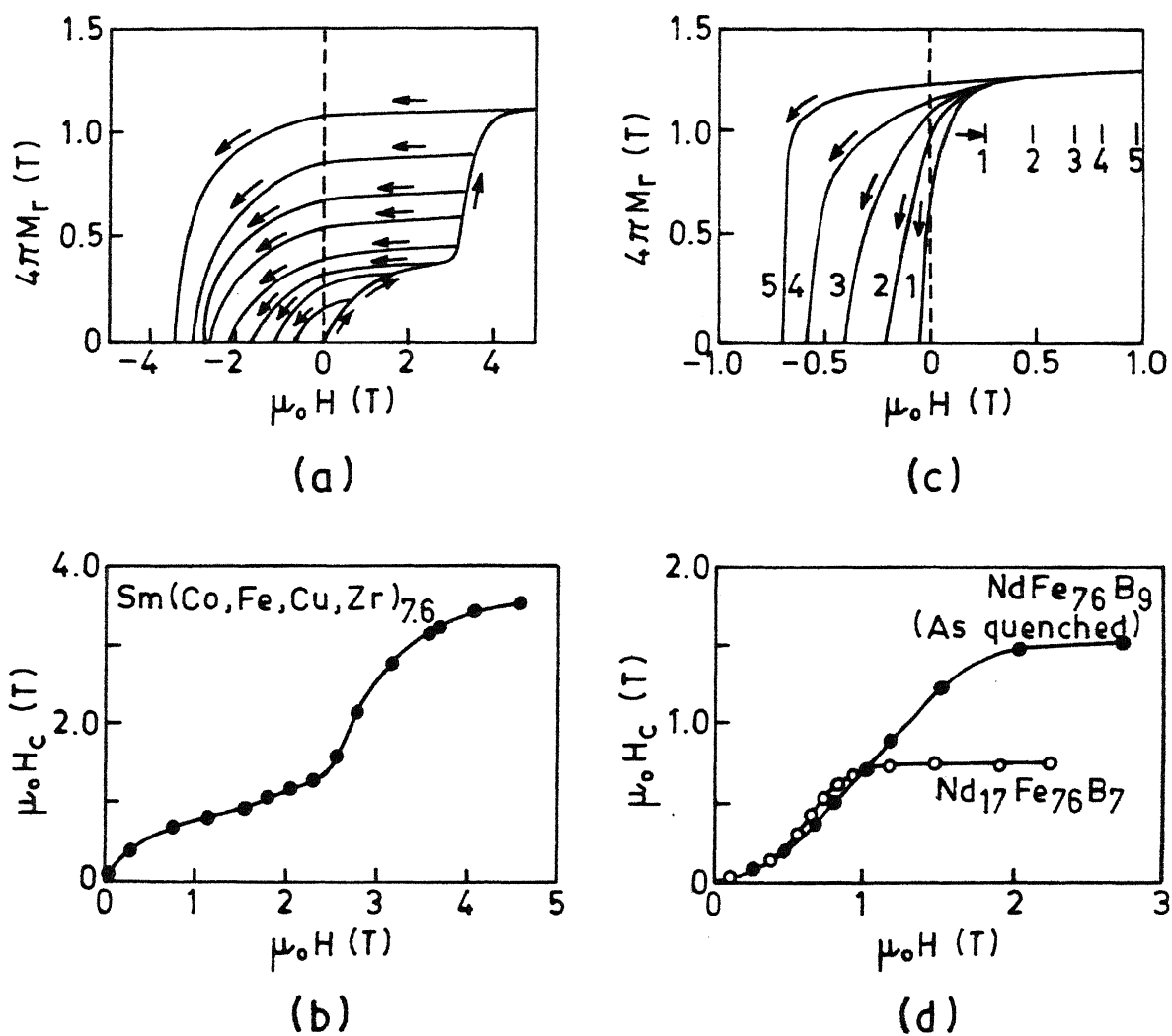


Fig.II.8 Hysteresis loops and H_c as a function of maximum applied field : (a),(b) $\text{Sm}(\text{Co}, \text{Fe}, \text{Cu}, \text{Zr})_{7.6}$; and (c),(d) $\text{Nd}_2\text{Fe}_{14}\text{B}$ based magnets (after Durst and Kronmüller [52])

includes RCo_5 have the CaCu_5 type hexagonal structure; R_2T_{17} occurs in three structure types, namely hexagonal $\text{Th}_2\text{Ni}_{17}$ type $[\text{R}_2\text{T}_{17}(\text{H})]$, rhombohedral $\text{Th}_2\text{Zn}_{17}$ type $[\text{R}_2\text{T}_{17}(\text{R})]$ and hexagonal disordered TbCu_7 type $[\text{R}_2\text{T}_{17}(\text{DH})]$ (vide Section 2.2.3 for more detail). The review here deals mainly with the cobalt rich end of selected binary and multicomponent systems.

2.2.1.1 Binary Systems

The binary R-Co phase diagrams show similar features [101, 115, 116]. The phase diagrams are characterized by a series of intermetallic compounds which show little or no solid solubility at low temperature. Summary of different intermediate phases found in various R-Co binary systems is presented in Fig.II.9.

As an illustration, Fig.II.10(a) shows the Sm-Co equilibrium phase diagram originally published by Buschow and Van der Goot [117]. Subsequent work by Williams et.al.[118] provided more definition to the phase boundaries. Cobalt rich portion of the phase diagram, which has been the subject matter of controversy [4], is given in Fig.II.10(b). SmCo_5 forms by a peritectic reaction located in the temperature range of $1293\text{--}1320^\circ\text{C}$. It is generally accepted that $\text{Sm}_2\text{Co}_{17}$ melts congruently in the temperature range of $1335\text{--}1375^\circ\text{C}$ [120]. From metallography data, however, Ray [121] has argued that even $\text{Sm}_2\text{Co}_{17}$ may be forming through a peritectic reaction at 1310°C .

2.2.1.2 Multicomponent Systems

Very little systematic phase equilibria data are available for the ternary or multicomponent systems involving R, Co and other transition metals [101]. The discussion on available phase equilibria data, relevant to this investigation, is covered in two parts: (A) $(\text{R}_1\text{--}\text{R}_2\text{...--}\text{R}_n)\text{--Co}$ systems, and (B) $(\text{R}_1\text{--}\text{R}_2\text{...--}\text{R}_n)\text{--Co--T}$ systems, where T = Fe, Cu, Zr or combination of these elements.

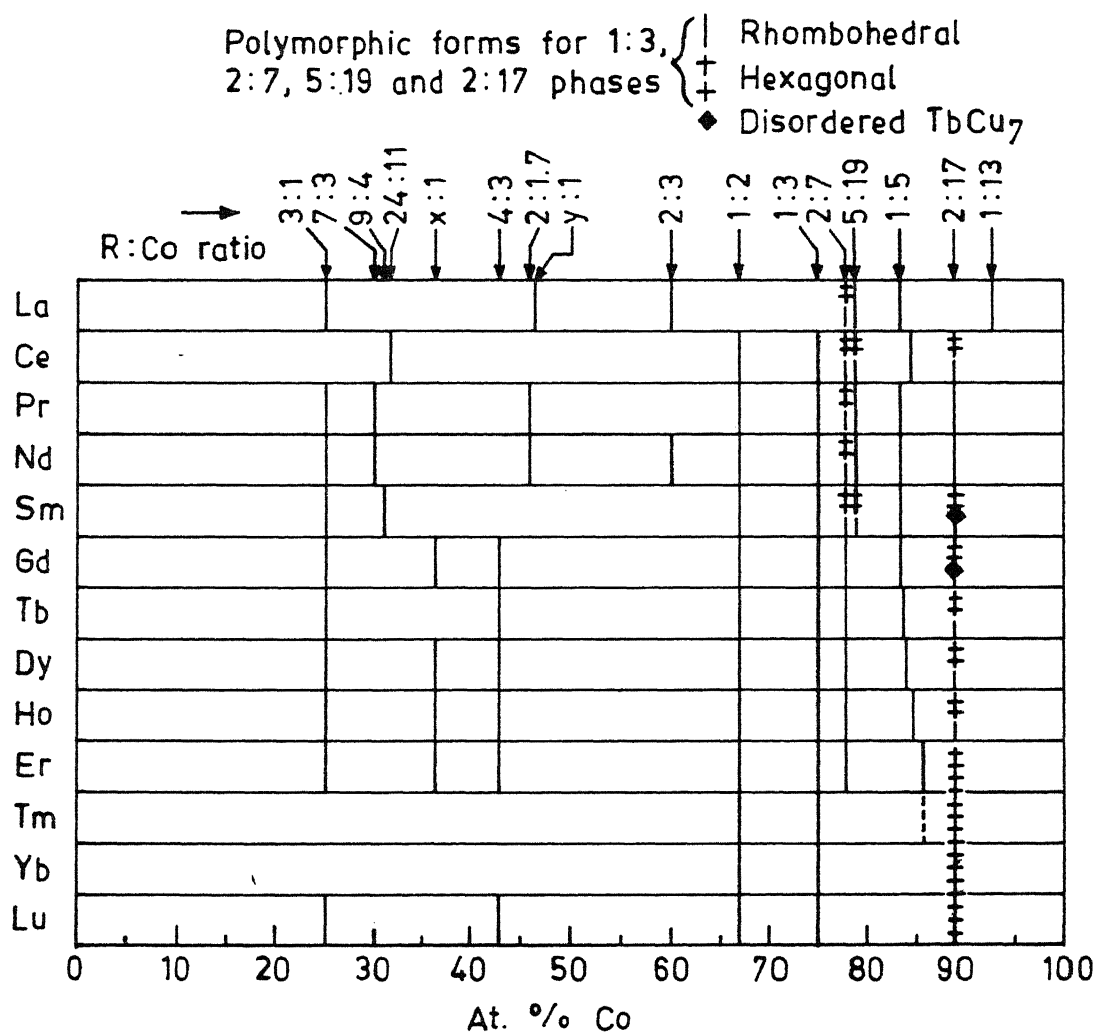


Fig.II.9 Intermediate phases found in the various R-Co binary systems (after Gupta [101])

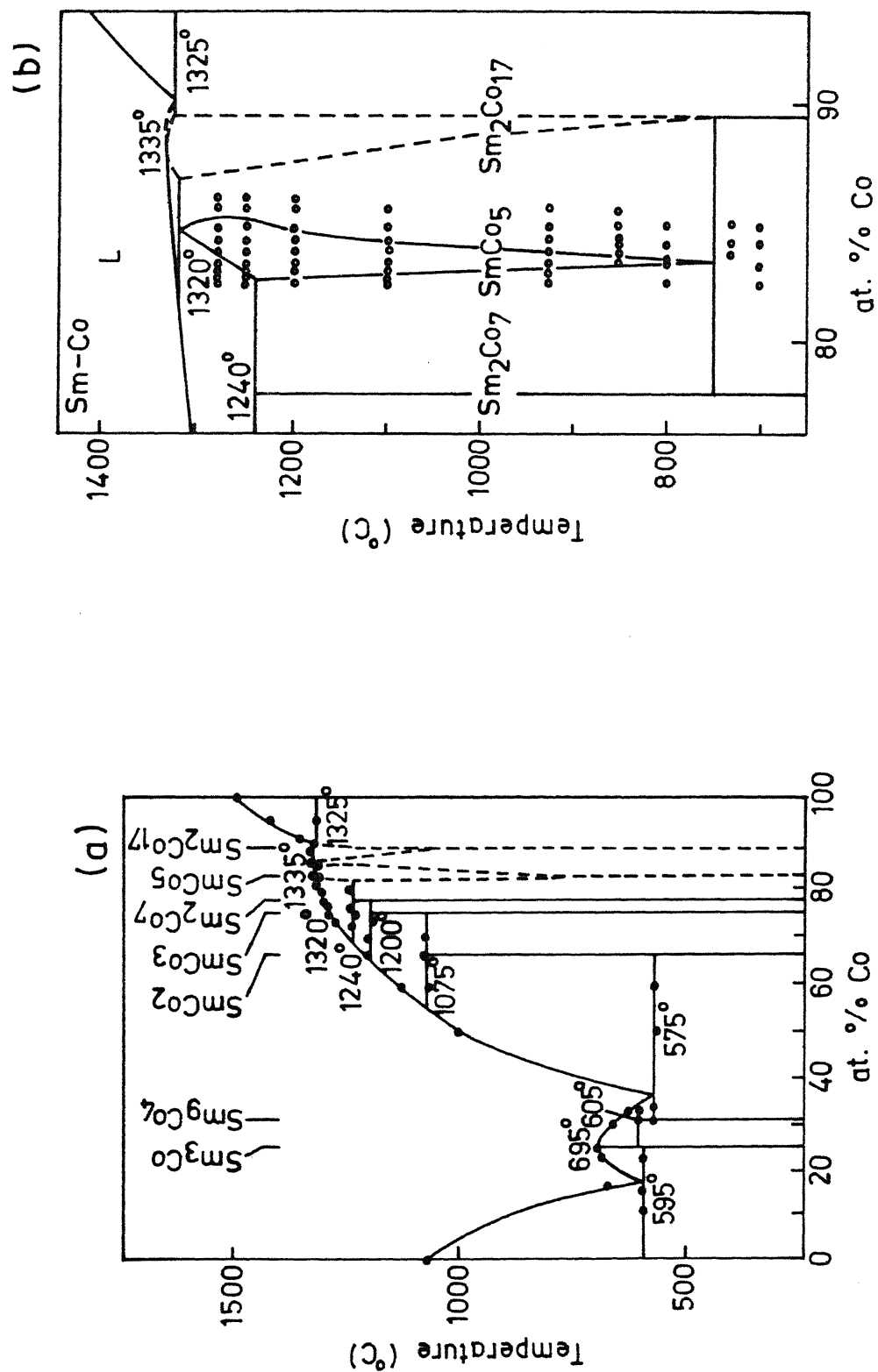


Fig.II.10 (a) Initial phase diagram of the Sm-Co system (after Buschow and Van der Goot [117])
 (b) Co-rich portion of the Sm-Co phase diagram (after den Broeder and Zijlstra [119])

(A) $(R_1-R_2\ldots-R_n)$ -Co Systems

Ce-La-Co System

This ternary system was studied at the high Co end by Khan and Feldman [122] and Khan [123] in two isothermal sections. Fig.II.11 shows the composite ternary isothermal diagram for 1000°C and 850°C. The interesting feature of the isothermal sections is that the RCo_5 phase, which exist in both R-Co binaries (vide Fig.II.9), forms a complete series of solid solutions. Large extension of the R_2Co_7 , R_5Co_{19} and R_2Co_{17} phases also occur. The R_2Co_7 phase exists in the two R-Co binaries in two different forms, and hence does not extend from one binary to the other. Similarly the R_2Co_{17} phase also does not extend upto the La-Co binary as the La_2Co_{17} phase does not exist. The La_5Co_{19} phase is not stable at 850°C.

Since the R elements show considerable solubility in each other [124, 125] behaviour similar to the above is to be expected with other elements.

MM-Co System

Because of its practical importance in the production of low cost magnets, a multicomponent system involving Mischmetal (MM: contains Ce, La, Nd and Pr in certain natural proportions) and Co has been studied by Schafer and Spyra [126,127] and Velu et.al.[128]. The phase equilibria, represented as MM-Co binary (Fig.II.12) show the same set of high Co intermediate phases as is found in the Ce-Co binary (Fig.II.9). In fact the phase equilibria is very similar to the Ce-Co system except for the opening up of the three phase peritectic equilibrium lines into areas.

(B) $(R_1, R_2\ldots-R_n)$ -Co-T Systems

Limited amount of information on ternary Sm-Co-Cu [120,129], R-Co-Fe (R = Sm, Ce) [130] were reported in the review by Gupta [101]. The MM-Fe-Co system has been studied in detail [131,132]. Partial phase diagrams in multicomponent Sm-Co-Fe-Cu and

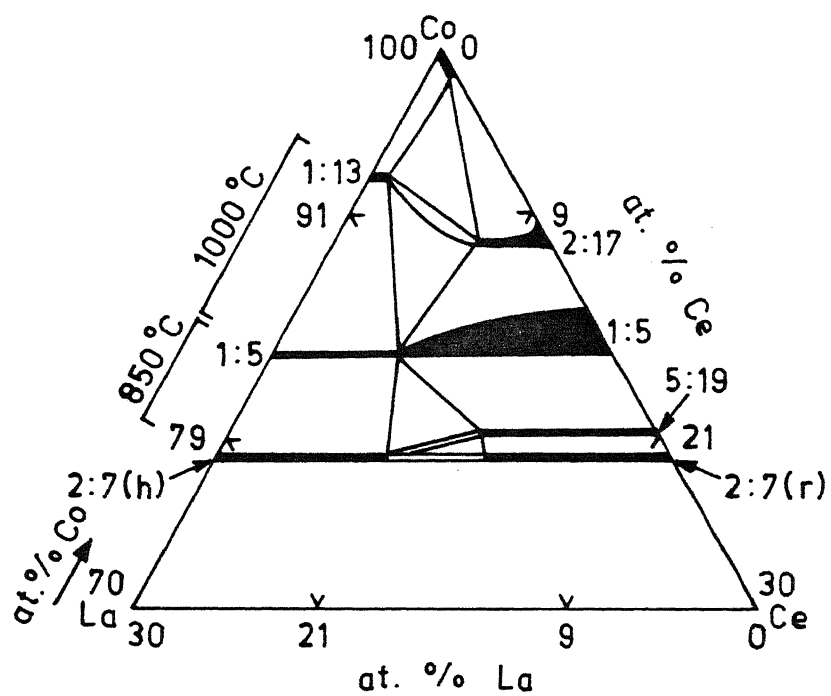


Fig.II.11 Ce-La-Co ternary system (after Khan and Feldman [122] and Khan [123])

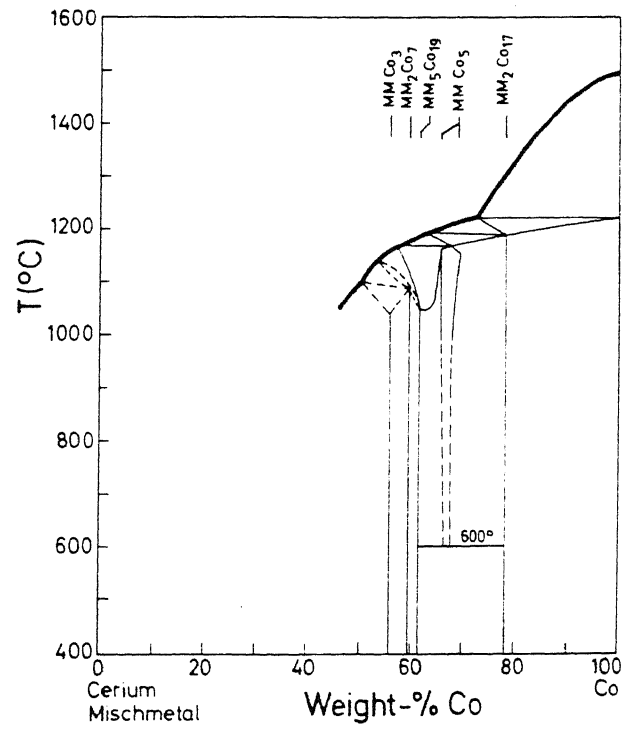


Fig.II.12 MM-Co phase diagram (after Schäfer and Spyra [126,127])

Sm-Co-Fe-Cu and Sm-Co-Fe-Cu-Zr have been reported very recently [133,134]. Phase equilibria in MM-Co-Fe, Sm-Co-Fe-Cu and Sm-Co-Fe-Cu-Zr are briefly described.

MM-Co-Fe System

RE-Co-Fe phase equilibria (where RE is the total rare-earths content of Mischmetal) at 900°C has been investigated by Mittal et.al.[131] and Laha et.al.[132]. The phase equilibria (Fig.II.13) at 900°C show that the 2:7, 1:5 and 2:17 phases extend from the RE-Co binary into the ternary but the latter two phases deviate from the stoichiometric lines towards higher transition element side. The 2:17 phase extends far into the ternary and possibly extends to the RE_2Fe_{17} phase in the RE-Fe binary. Four new ternary phases namely the S, T, A [131] and L [132], were found. Relevant structural data of these new phases are given in Table II.3 together with the data for the 2:7, 1:5 and 2:17 phases. The S phase, which has 'a' parameter quite similar to the 2:17 phase and 'c' parameter approximately three times that of the 2:17 phase,

Table II.3: Lattice Parameters of RE Containing Phases Observed in the RE-Co-Fe System at 900°C [131,132]

Phase	Lattice Parameters*, Å		c/a Ratio
	a	c	
$RE_2(Co,Fe)_7$	5.049	24.52	4.86
$RE_5(Co,Fe)_{19}$	—**	—	—
$RE(Co,Fe)_5$	4.993	4.005	0.802
$RE_2(Co,Fe)_{17}$	8.406	12.356	1.47
S	8.481	37.29	4.398
T	8.486	22.80	2.68
A	8.495	22.66	2.67
L	8.459	41.94	4.96

* Hexagonal unit cell; ** means not indexed

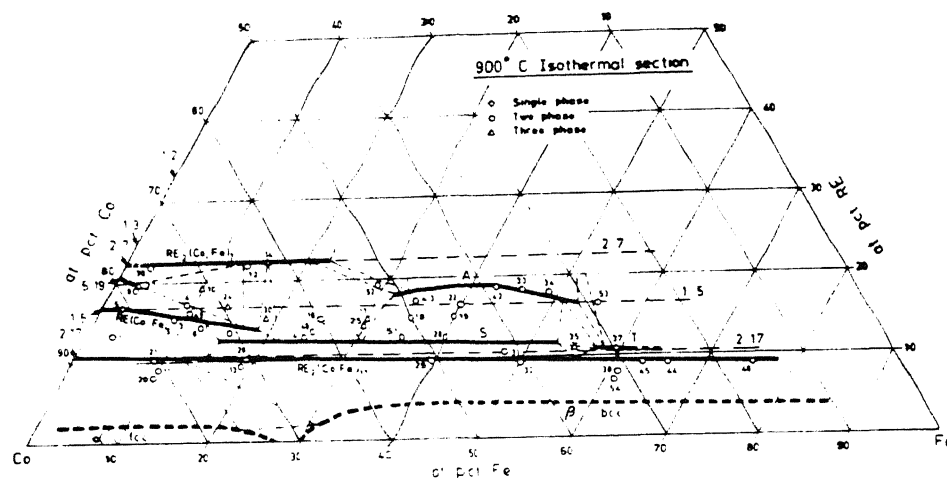


Fig.II.13 RE-Co-Fe phase diagram (after Mittal et.al. [131])

occurs quite close to the 2:17 stoichiometric line and extending almost parallel to it. According to Gupta [101], S phase and all other new phases are possibly structurally related to the 2:17 phase.

Sm-Co-Fe-Cu System

Phase equilibria in the Sm-Co-Fe-Cu system has been investigated by Morita et.al.[133] in the magnetically important composition region. Two isopleths with fixed Cu and Fe contents are shown in Fig.II.14(a),(b). The two sections correspond to 13 at.pct. Cu, 10 at.pct. Fe [Cu > Fe; Fig.II.14(a)] and 7 at.pct. Cu, 22 at.pct. Fe [Cu < Fe; Fig.II.14(b)], and Sm content varies from 6 to 16 at. pct. The same set of phases, which include liquid, Co-Fe solid solution, 2:17 [equivalent to $\text{Sm}_2\text{Co}_{17}$ structure in 2:17(H), 2:17(R) and 2:17(DH) modifications] and 1:5 phases, are observed in both Cu > Fe and Cu < Fe sections. With Cu > Fe, the 2:17 phase has the maximum solubility range of 10.5 to 13.0 at.pct. Sm at 1210 °C. The 2:17 phase crystallizes in any of the three crystal structures depending upon the Sm content and temperature. When Cu < Fe [Fig.II.14(b)] the 2:17 phase has the maximum solubility of 10.5 to 12.0 at.pct Sm at 1187 °C. However, it crystallizes in the 2:17(R) modification and its homogeneity region extends over a wide range of temperature. The relationship between crystal structures of 2:17 phases and Cu and Fe content are further investigated by these workers in order to correlate coercivity with the type of 2:17 phase produced (Fig.II.15).

Sm-Co-Fe-Cu-Zr System

Fig.II.16 shows the Sm-Co-7.0 at. pct. Cu-22 Fe-2.0 Zr (Cu < Fe, Zr) section (after Morita et.al.[133]). In addition to the phases observed in Fig.II.14(a),(b), the 2:7 phase enriched in Zr exists in this case. The 2:17 phase has the solubility range of 9.5 to 13.0 at.pct. Sm at 1170 °C, and furthermore, crystallizes in 2:17(H), [2:17(DH)+2:17(H)] or 2:17(DH) structure above 1000 °C. Zr addition expands the Sm solubility in the 2:17 phase towards both Sm rich and Sm poor directions and changes the crystal structure of 2:17 phase to 2:17(DH) and/or 2:17(H) at high temperature.

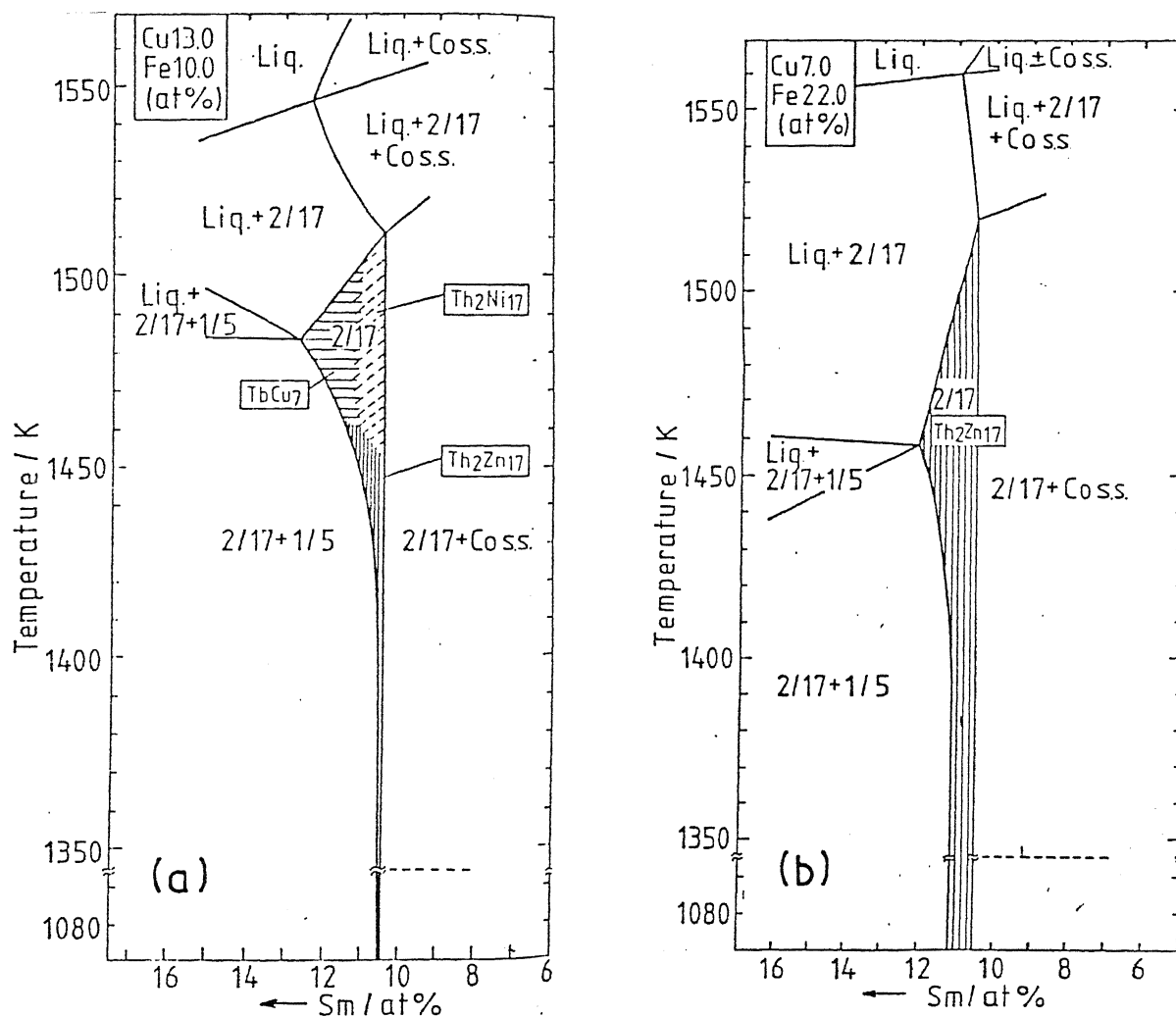


Fig.II.14 Sm-Co-Fe-Cu phase equilibria

- (a) Sm-Co-13.0 at.pct. Cu-10.0 at.pct. Fe (Cu > Fe) section of phase diagram; and
 (b) Sm-Co-7.0 at.pct. Cu-22.0 at.pct. Fe (Cu < Fe) section of phase diagram (after Morita et.al.[133])

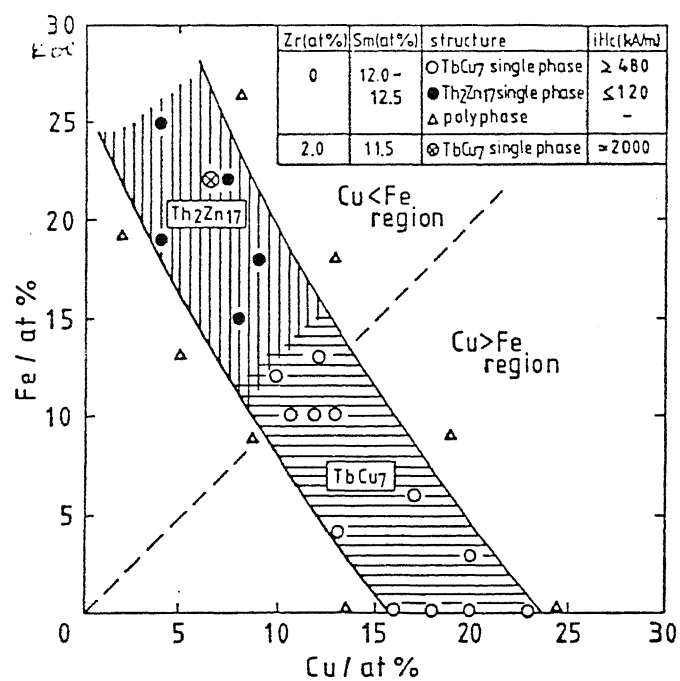


Fig.II.15 Relationship between crystal structure of 2:17 phase obtained after homogenizing and Cu and Fe contents for various alloys (after Morita et.al.[133])

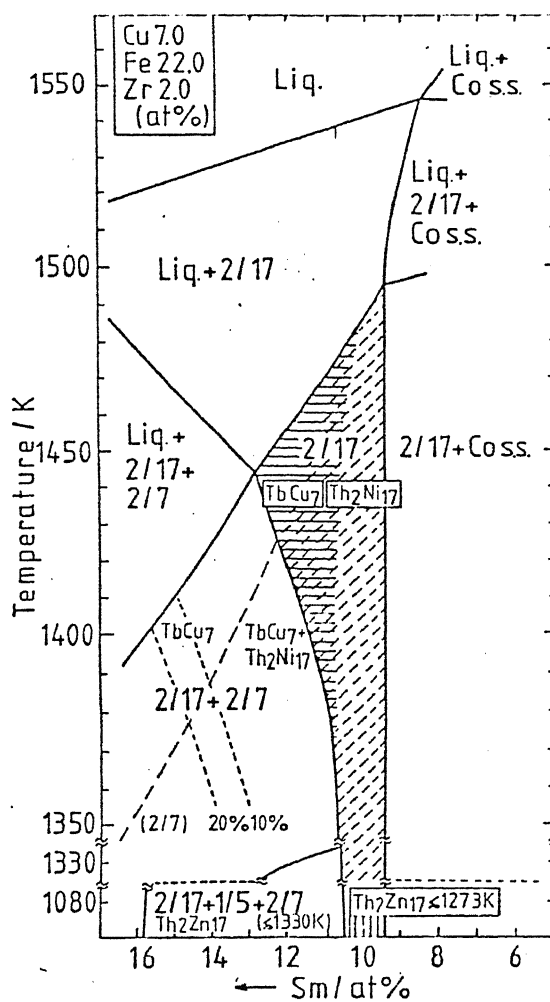


Fig.II.16 Sm-Co-7.0 at.pct. Cu-22.0 at.pct. Fe-2.0 at.pct. Zr section of Sm-Co-Fe-Cu-Zr phase diagram (after Morita et.al.[133])

Chin et.al.[134] further extended the work of Morita et.al. and reported three isopleths, namely, (Cu,Zr)-(Sm,Co,Fe), Sm-(Co,Fe,Cu,Zr) and (Co,Fe)-(Sm,Cu,Zr). The diagrams for the first two cases are reproduced in Fig.11.17(a),(b). The major phase in all the alloys investigated is either 2:17(H) or 2:17(R) phase. However, additional phases appear as a result of variation of alloy composition:

- (i) For the alloy system (Cu,Zr)-(11.9 at.pct. Sm-60.0 Co-18.9 Fe), keeping a fixed (Cu + Zr) content of 9.2 at.pct., the higher Zr content facilitates the precipitation of a 2:17 phase, which is richer in both Sm and Zr. Zr also extends the homogeneity range of the 2:17 phase. Towards the Zr lean end of this system 1:5 phase appears.
- (ii) For the alloy system Sm_X (68.1 Co-21.5 Fe-8.5 Cu-1.9 Zr) $_{1-X}$ ($X = 0.077-0.15$), higher Sm stabilizes the 2:17 phase, while to the Sm-lean end a Co-Fe phase with α -Co structure (hcp) precipitates.
- (iii) For the system (Co,Fe)-(11.9 Sm-7.5 Cu-1.7 Zr), fixing (Co + Fe) at 78.9 at.pct., the 2:17 phase remains unchanged for any variation in Co/Fe ratio.

2.2.2 R-Fe and R-Fe-B System

Phase equilibria in binary R-Fe and ternary R-Fe-B systems have been reviewed in this section with main emphasis on Ce-Fe (Ce is major constituent of MM) and Nd-Fe-B systems. Brief descriptions of Nd-Fe, Pr-Fe, Sm-Fe and La-Fe have also been included because of the presence of Nd, Pr, Sm and La in MM.

2.2.2.1 Binary R-Fe System

In the monograph entitled, 'Iron Binary Phase Diagrams' O. Kubaschewski [135] has summarized and evaluated the literature on R-Fe systems which appeared till 1981. In a later (1986) compilation of binary phase diagrams, Massalski et.al.[116] have adopted the R-Fe phase equilibria given by Kubaschewski without

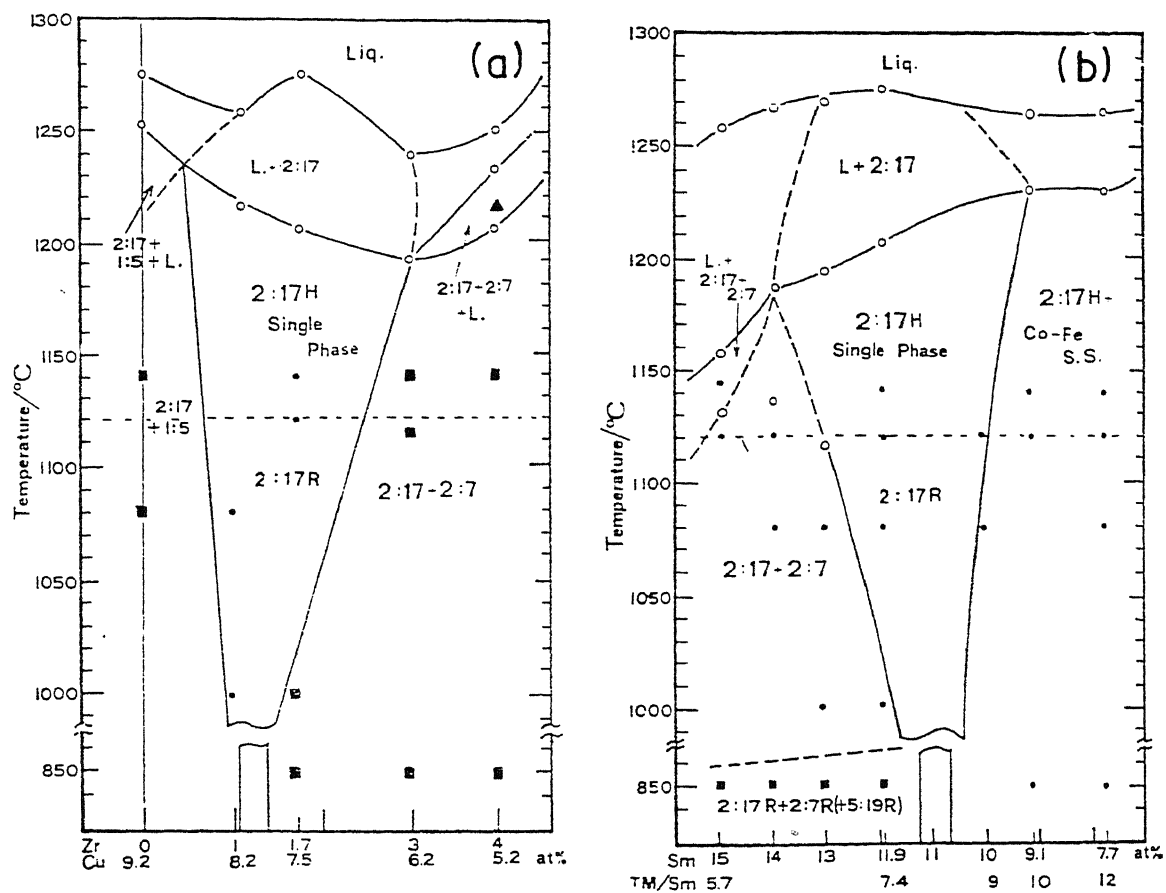


Fig.11.17 (a) Phase diagram section (Cu,Zr)-(Sm,Co,Fe) with fixed 11.9 at.pct. Sm, 60.0 at.pct. Co, 18.9 at.pct. Fe and Cu+Zr = 9.2 at.pct.

(b) phase diagram section Sm-(Co,Fe,Cu,Zr) (after Chin et.al.[134])

making any modification. More recently, the revised phase diagram of Nd-Fe system [136] and Ce-Fe system [137] have been published. The rare-earth metals in R-Fe systems exhibit many common features owing to the similarity of their electronic structures. The melting points and eutectic temperatures of binary systems with iron increase with the atomic weight of R. All these systems have a eutectic on the R-rich side, with R in equilibrium with RFe_2 (for all the R element except Nd and La) or R_5Fe_{17} (for R = Nd [136]). The heavier rare-earths [Eu (63) to Lu (71)] form four stable compounds with Fe, namely R_2Fe_{17} with either the Th_2Zn_{17} (R) or the Th_2Ni_{17} (H) structures, R_6Fe_{23} with Th_6Mn_{23} structure, RFe_3 with $PuNi_3$ structure and RFe_2 with $MgCu_2$ (Laves) structure. The number of compounds per system decreases with decreasing atomic number of R. Sm forms only three compounds. All other phases, except the R_6Fe_{23} , are stable in Sm-Fe system [135]. The lighter metals (Ce, Pr, and possibly Pm) form only two compounds with Fe, R_2Fe_{17} and RFe_2 [135]. Nd also form two phases, however, stable phases in the Nd-Fe system are R_2Fe_{17} and R_5Fe_{17} [136]. La-Fe system is an exception and no stable intermediate phase is observed in this system [135].

Ce-Fe System

This system has been studied by several workers [135] and the most recent investigation is by Chaung et.al.[137]. The Ce-Fe phase diagram, shown in Fig.II.18, is taken from the investigation of Chaung et.al.[137]. The iron rich section of phase diagram (also shown in Fig.II.18) has been worked out by these workers in more detail.

Two intermediate compounds $CeFe_2$ and Ce_2Fe_{17} exist in this system. The phase reported as $CeFe_7$ by some workers [138-140] actually corresponds to the Ce_2Fe_{17} [141]. Early workers [142,143] reported the occurrence of $CeFe_5$ phase. Later studies by Ray [138], Buschow [139] and Gebhart et.al.[140], however, have indicated its absence. Ce_2Fe_{17} occurs in two modifications, hexagonal as well as rhombohedral. The solubility of Ce in Fe at 850-900°C is less than 0.04 at.pct.[137]. The relevant structural

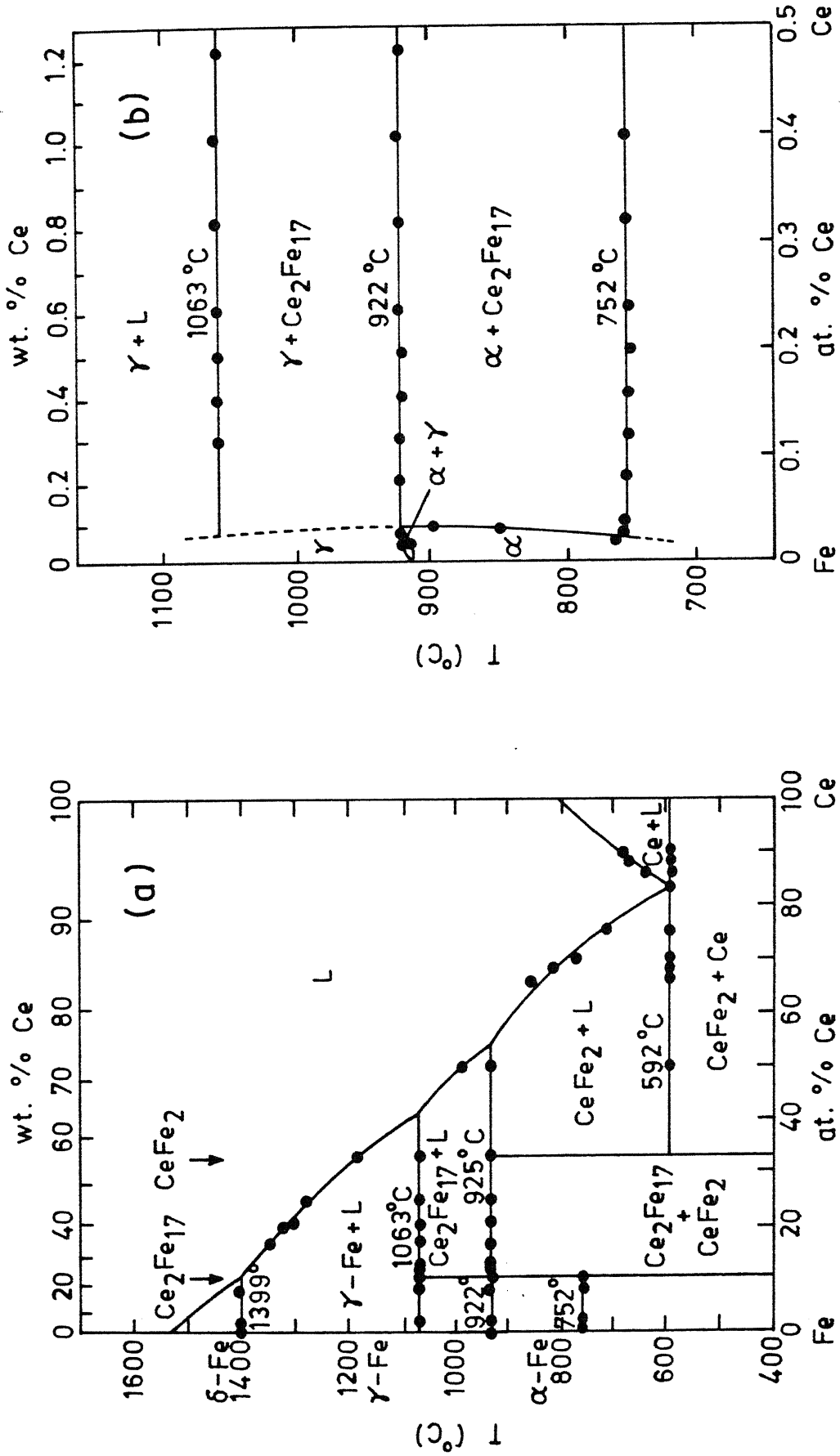


Fig.II.18 (a) Ce-Fe binary phase diagram, (b) iron-rich portion of the Ce-Fe phase diagram (after Chaung et.al.[137])

Table II.4: Structural Data of Phases in the Ce-Fe System [135]

Phase	Structure Type [#]	Lattice Parameters, Å
CeFe ₂	MgCu ₂ (C)	a = 7.302
Ce ₂ Fe ₁₇	Th ₂ Ni ₁₇ (H)	a = 8.490, c = 8.281
Ce ₂ Fe ₁₇	Th ₂ Zn ₁₇ (R)	a = 8.493 [*] , c = 12.41

[#] (C)-Cubic, (H)- Hexagonal, (R)- Rhombohedral

^{*} Lattice parameter for hexagonal unit cell.

data are given in Table II.4. CeFe₂ phase is ferromagnetic with $T_c \sim 230$ K. Ce₂Fe₁₇(R) phase shows an antiferromagnetic to ferromagnetic transition near 70 K and a ferromagnetic to paramagnetic transition at about 270 K [135].

The phase diagrams reported by Chaung et.al.[137] and Buschow and van Wieringen [144] are quite similar. The Ce₂Fe₁₇ and CeFe₂ phases form by the peritectic reactions of the liquid alloy with γ -Fe and Ce₂Fe₁₇ phases respectively. The former occurs at 1063°C whereas the latter occurs at 925°C. A eutectic reaction, $L \longrightarrow \text{CeFe}_2 + \text{Ce}$, occurs at 592°C; the eutectic composition being at 83.3 at.pct. Ce. The $\alpha \longrightarrow \gamma$ transformation temperature of Fe is increased from 911°C to 922°C owing to the dissolution of Ce in Fe [137]. This reaction is probably of peritectoid type [137]. The Curie temperature of α -Fe decreases with increase in Ce content in the solid solution. Buschow and van Wieringen [144] reported that after prolonged heating at 900°C followed by one week of annealing at 600°C, the structure of Ce₂Fe₁₇ compound was still duplex [Ce₂Fe₁₇(H) + Ce₂Fe₁₇(R)]. Attempts to establish the transition temperature, for Ce₂Fe₁₇(R) \longrightarrow Ce₂Fe₁₇(H), have not been successful [135,137]. According to Chaung et.al.[137] if allotropic transformation does occur in Ce₂Fe₁₇, this must occur below 690°C and is expected to be very sluggish.

R-Fe (R = Nd, Pr and Sm) Systems

Recent developments in Nd-Fe phase equilibria has been reviewed by Stadelmaier and Henig [55]. Landgraf et.al.[136] have investigated the Nd-Fe phase equilibria and published the revised phase diagram [Fig.II.19(a)]. The existence of $\text{Nd}_5\text{Fe}_{17}$ phase has been established by these workers [136]. Moreau et.al.[145] have carried out detailed structural characterization studied on $\text{Nd}_5\text{Fe}_{17}$ phase and reported that this phase has a hexagonal unit cell ($a = 20.214 \text{ \AA}$ and $c = 12.329 \text{ \AA}$) of considerable complexity consisting of 12 formula units or 264 atoms. The Curie temperature of $\text{Nd}_5\text{Fe}_{17}$ phase is 232°C [145]. The $\text{Nd}_2\text{Fe}_{17}$ phase occur in rhombohedral modification ($a = 8.590 \text{ \AA}$, $c = 12.470 \text{ \AA}$ [135]) and has a Curie temperature of $\sim 54^\circ\text{C}$ [150]. Schneider et.al.[146] found that the NdFe_2 phase reported in literature [135,147] is not a binary phase but a ternary phase stabilized by oxygen, and its Fe:Nd ratio is not 2:1 but higher.

Phase equilibria of Pr-Fe and Sm-Fe systems in Fig.II.19(b) and 19(c) are compiled from the monograph of Kubaschewski [132]. The phase equilibria shown in Fig.II.19(b),(c) are quite similar to the Ce-Fe system (Fig.II.18) except for the change in reaction temperatures and occurrence of a SmFe_3 phase in the Sm-Fe system.

La-Fe System

Brief description of La-Fe system is included here separately because no intermediate phase forms in this system. La-Fe system exhibits a eutectic at 91.5 at.pct. La, the eutectic temperature being 780°C , and a flattening of the liquidus between 8-19 at.pct. La Fig.II.19(d) [135]. The relative size of the component atoms and electron concentrations are involved in the stability of compounds. La is without 4f electrons and largest in size of the lanthanons. These two factors might be the reason for the lack of a compound forming ability [135].

2.2.2.2 R-Fe-B Systems

Ku'zma et.al.[148] have presented a broad overview of R-T-B

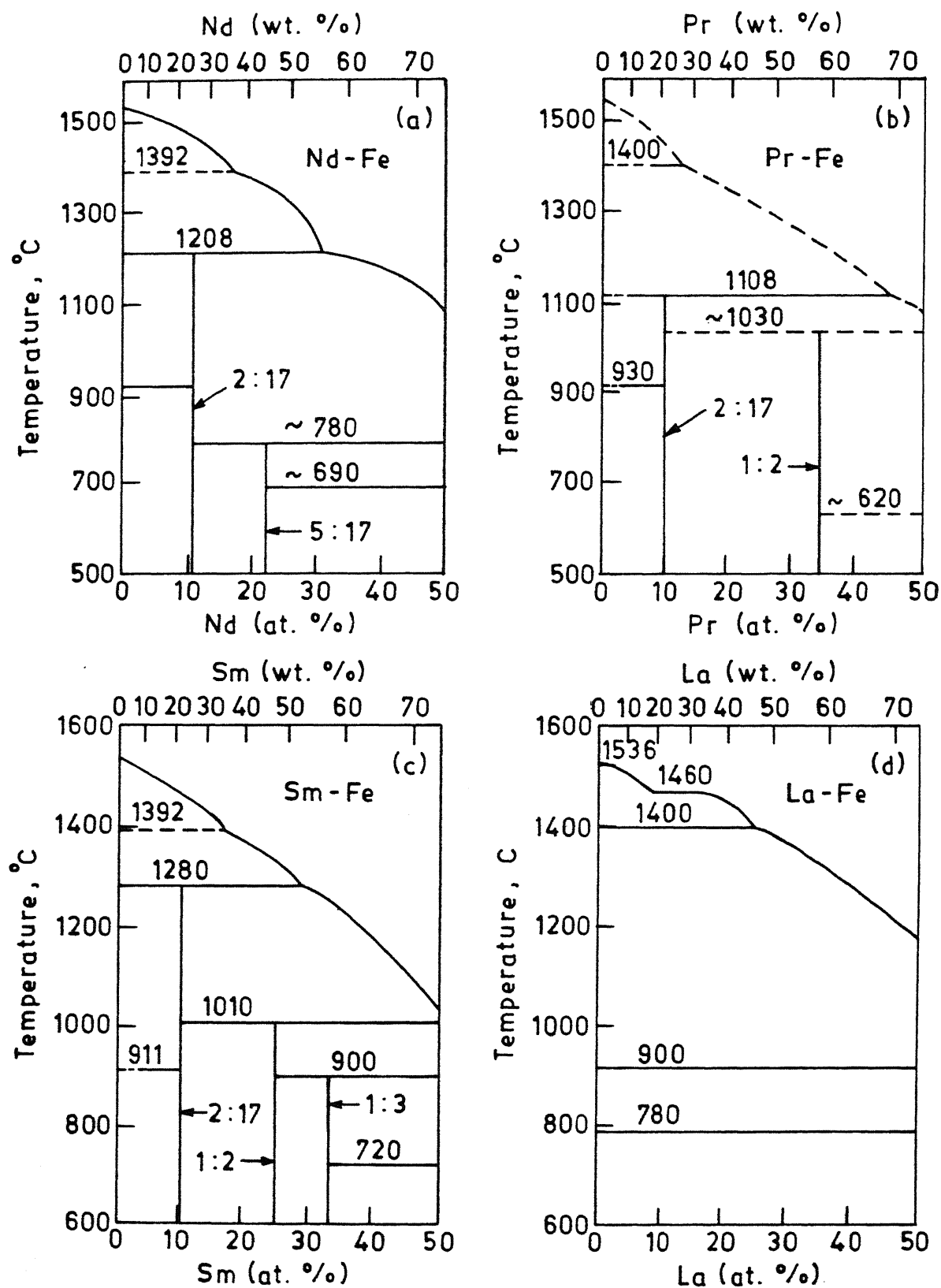


Fig.II.19 Selected R-Fe binary phase diagrams : (a) Nd-Fe (after Landgraf et.al.[136]); (b) Pr-Fe, (c) Sm-Fe, and (d) La-Fe (compiled from Kubaschewski [135])

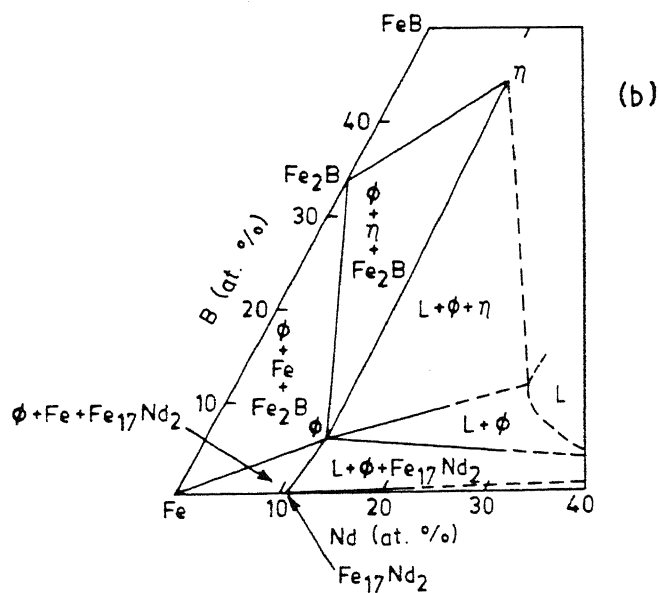
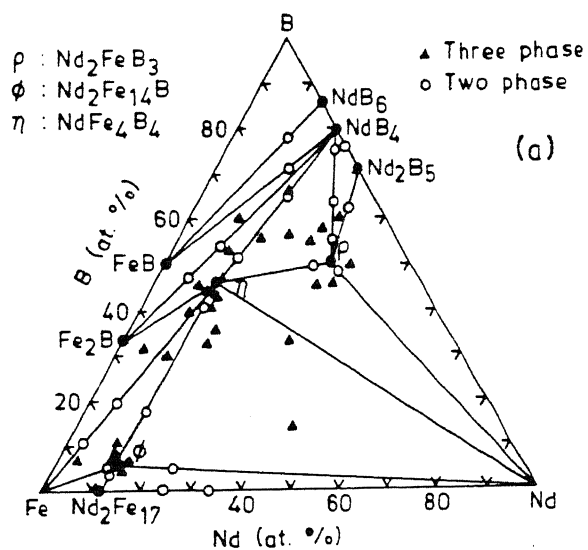


Fig.II.20 Ternary section of Nd-Fe-B : (a) data pertain to 900 °C for the Nd poor alloys and 700 °C for Nd rich alloys (after Buschow et.al.[153]); (b) data pertain to 1000 °C (after Schneider et.al.[150])

as ferromagnetic material at room temperature (Lorentz electron microscopy observation). The third ternary phase Nd_2FeB_3 (ρ) was indexed by Buschow et.al.[153]. Mossbauer spectra of this phase confirmed that this is not magnetically ordered at room temperature ($T_c = 64\text{K}$) [153]. Besides the ternary borides, the other phases encountered in the Nd-Fe-B system at 900 and 1000 $^{\circ}\text{C}$ are Fe_2B , FeB , $\text{Nd}_2\text{Fe}_{17}$, pure iron and liquid. Relevant structural data for the different intermediate phases are compiled in Table II.5.

Table II.5: Structural and Magnetic Characteristics of Binary and Ternary Phases in Nd-Fe-B System

Phase	Structure Type*	Lattice Parameter, Å	T_c K	Ref.
FeB	BCT	$a = 5.109, c = 4.249$	-	[135]
Fe_2B	O	$a = 5.51, b = 2.95, c = 4.06$	740	[135]
$\text{Nd}_2\text{Fe}_{17}$	H	$a = 8.59, c = 12.47$	327	[1]
$\text{Nd}_2\text{Fe}_{14}\text{B}$	T	$a = 8.804, c = 12.199$	581	[153]
$\text{Nd}_{1+\epsilon}\text{Fe}_4\text{B}_4$	T	$a = 7.117, c = 35.07$ ($\epsilon \sim 0.1$)	10	[153, 154]
Nd_2FeB_3	R	$a = 5.463, c = 24.281$	64	[153]

* BCT-body centered tetragonal, O-orthorhombic, H-hexagonal
T-tetragonal, R-rhombohedral

The phase relations at 900 $^{\circ}\text{C}$ [Fig.II.20(a)] do not differ from those reported at 600 $^{\circ}\text{C}$ [151], except for a Nd-rich liquid phase at 900 $^{\circ}\text{C}$, which takes the place of Nd at 600 $^{\circ}\text{C}$, and the existence of $\text{Nd}_5\text{Fe}_{17}$ phase at 600 $^{\circ}\text{C}$ [55, 136]. The 1000 $^{\circ}\text{C}$ isothermal section [Fig.II.20(b)] is also quite similar to the isothermal section at 900 $^{\circ}\text{C}$, except that in the quadrangle Fe- Fe_2B - η - ϕ the tie line $(\text{Fe}+\eta)$ shown at 900 $^{\circ}\text{C}$ and below is replaced by $(\text{Fe}_2\text{B} + \phi)$ at 1000 $^{\circ}\text{C}$. Tsai et.al.[158] on the other hand reported that instead of Fe- ϕ - Fe_2B a composition triangle of Fe- ϕ - η exists from room temperature to 1100 $^{\circ}\text{C}$.

Some workers [150,152,158,162] have also attempted to describe the solidification of the ternary alloys with the help of a liquidus projection, and this has been reviewed by Buschow [2]. The phase $\text{Nd}_2\text{Fe}_{14}\text{B}$ does not melt congruently [2]. This phase forms peritectically by the reaction, $\text{L} + \text{Fe} \rightarrow \phi$, on a critical tie line which corresponds to 1155°C [162] or 1180°C [150,158]. It has been noted that the peritectic region for the appearance of ϕ phase is 3 to 40 at.pct. Nd [158] and not 3 to 21 at.pct. [162].

Other Related Systems

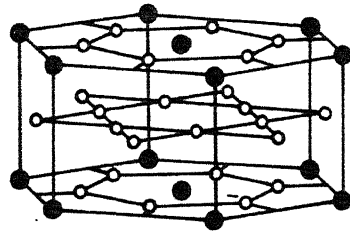
Nd-Fe-C and Nd-Fe-Al phase diagrams are reported by Grieb et.al. [163]. Partial phase diagrams of ternary Tb-Fe-B, Dy-Fe-B [164] and Pr-Co-B [165] systems and quaternary Nd-Dy-Fe-B and Nd-Tb-Fe-B systems [166] have also been published in recent literature.

2.2.3 Crystal Structure

2.2.3.1 RT_5 and R_2T_{17} Compounds

The 1:5 compounds have hexagonal crystal structure according to the prototype CaCu_5 shown in Fig.II.21(a). The lattice consist of an alternating sequence of differently composed atom layers, where one layer contains both (R and T) atoms but the other only transition metal atoms in hexagonal arrangement. The R_2T_{17} compounds generally occurs in two uniaxial variations [16], one hexagonal(H) of the type $\text{Th}_2\text{Ni}_{17}$ [Fig.II.21(b)] and the rhombohedral(R) of the type $\text{Th}_2\text{Zn}_{17}$ [Fig.II.21(c)]. The disordered TbCu_7 type (hexagonal) structure is observed for $\text{Sm}_2\text{Co}_{17}$ and $\text{Gd}_2\text{Co}_{17}$ [101]. The 1:5 and 2:17 are structurally quite similar. The structure formula for 2:17 stoichiometry compound can be derived from the 1:5 composition by replacing every third R atom with two transition metal atoms T according to the formula: $3(\text{RT}_5) - \text{R} + 2\text{T} = \text{R}_2\text{T}_{17}$. This T atom pair is arranged in the form of a dumb-bell which is oriented in the direction of c-axis and positioned symmetrically in relations to the planes in which R

(a)

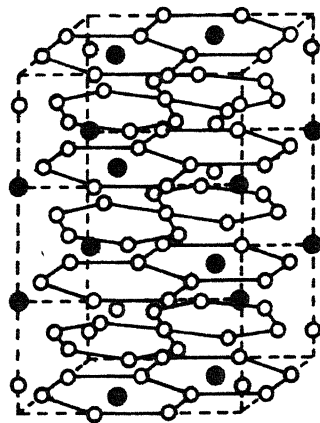
Hexagonal SmCo₅

$$a = 5.004 \text{ \AA}$$

$$c = 3.971 \text{ \AA}$$

● Sm ○ Co

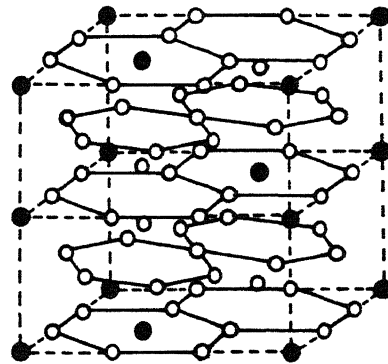
(b)

Rhombohedral Sm₂Co₁₇

$$a = 8.402 \text{ \AA}$$

$$c = 12.172 \text{ \AA}$$

(c)

Hexagonal Sm₂Co₁₇

$$a = 8.360 \text{ \AA}$$

$$c = 8.515 \text{ \AA}$$

Fig.II.21 Crystal structure of (a) RT_5 and (b), (c) R_2T_{17} (rhombohedral and hexagonal) compounds (after Hadjipanayis [167])

atoms are contained [16]. Whether rhombohedral or hexagonal modification of 2:17 is obtained depends on whether this replacement occurs such that the resulting stacking sequence is ABCABC... or ABAB... type (Fig.II.21) [167].

2.2.3.2 $R_2Fe_{14}B$ and RFe_4B_4 Compounds

The crystal structure of $Nd_2Fe_{14}B$ have been worked out by several workers [154-157]. A schematic representation of the crystal structure, as reported by Herbst et.al.[156], is shown in Fig.II.22(a). The tetragonal structure of the $Nd_2Fe_{14}B$ phase comprises of six crystallographically nonequivalent iron sites and two nonequivalent Nd sites. The crystal structure isomorphous with $Nd_2Fe_{14}B$ forms with all the rare-earth elements except Eu [2].

The compounds of composition $R_{1+\epsilon}Fe_4B_4$, where $\epsilon = 0.11-0.15$, ($R = Ce, Pr, Nd, Sm, Gd, Tb$) are built of incommensurate structures of rare-earth atoms (linear strings $\parallel \vec{c}$), iron atoms (chain of edge sharing tetrahedra $\parallel \vec{c}$) and B atom pairs [Fig.II.22(b)] [159,161]. The most interesting aspect of this structure is that the periodicities of the Fe, B subcell and R subcell differ along the c-direction [161].

2.3 $Sm_2(Co, Fe, Cu, Zr)_{17}$ and Nd-Fe-B Magnets

Having presented a general overview on REPM and phase equilibria in R-Co, R-Fe and R-Fe-B systems, various specific aspects of precipitation hardenable $Sm_2(Co, Fe, Cu, Zr)_{17}$ magnets and Nd-Fe-B magnets are briefly reviewed in this subsection.

2.3.1 $Sm_2(Co, Fe, Cu, Zr)_{17}$ Magnets

Because of the inability to achieve high coercivity in single phase Sm_2Co_{17} and $Sm_2(Co, Fe)_{17}$ compositions [4,11] the development of 2:17 magnets has concentrated mostly on the investigation of two phase precipitation hardenable alloy systems. This has entailed the gradual shifting of the R/T ratio from 1:5 towards

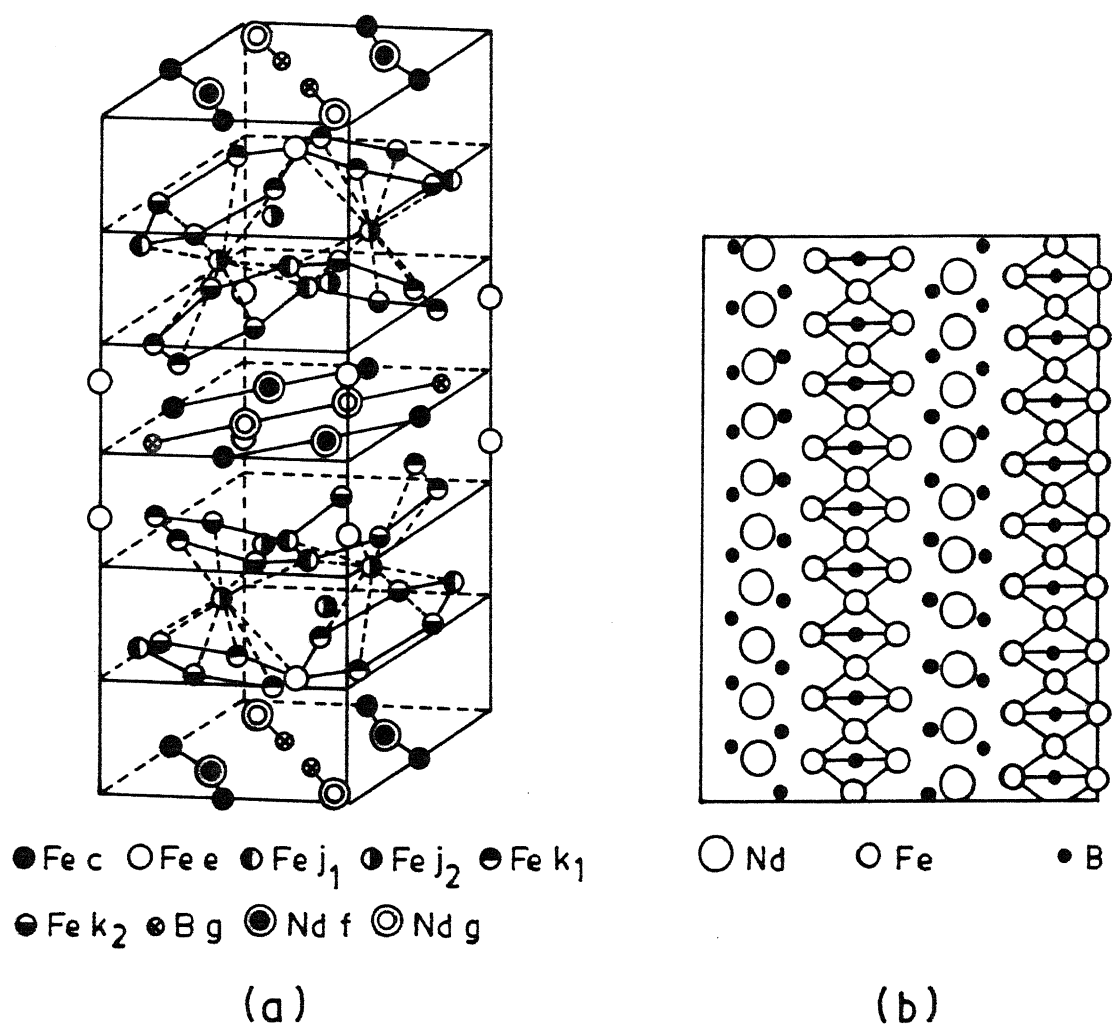


Fig.II.22 (a) Schematic representation of $\text{Nd}_2\text{Fe}_{14}\text{B}$ ($P4_2/\text{mm}$ space group) (after Herbst et.al.[156])
 (b) Projection of crystallographic structure of NdFe_4B_4 onto the (110) plane (after Givord et.al.[161])

that of 2:17. The approach has included the achievement of a single phase microstructure by solutionizing the alloy within the high temperature homogeneity range indicated on phase diagram and subsequently precipitating the second domain wall pinning 1:5 phase by aging at lower ($\sim 800^{\circ}\text{C}$) temperature. These magnets have evolved from the initial work of Nesbitt et.al.[168] with Cu serving as the principal element facilitating second phase precipitation. A further increase in coercivity was obtained in these alloys by the introduction of small amount of elements e.g. Zr, Ti, Hf, Nb, Mn, Cr etc. [4,11]. Besides chemical composition, magnetic properties (e.g. coercivity) of these magnets are very sensitive to microstructure and heat treatment. Magnetic properties of various $\text{Sm}(\text{Co},\text{Fe},\text{Cu},\text{X})_Z$ magnets ($\text{X} = \text{Zr, Ti, Cr}$ etc., and $Z = 6.8-8.5$) are compiled in Table 11.6. The Zr containing magnets show the best combination of magnetic properties [4,11].

2.3.1.1 Chemical Composition and Magnetic Features

The early efforts [4] to make $\text{Sm}_2(\text{Co},\text{Fe},\text{Cu},\text{Zr})_{17}$ magnets resulted in magnets with high energy product (upto 30 MGOe) but low coercivity (3-8 kOe). Ojima et.al.[15] reported a $(\text{BH})_{\text{max}}$ value of 30 MGOe and $H_c \approx 6.5$ kOe for $\text{Sm}(\text{Co}_{0.70}\text{Cu}_{0.09}\text{Fe}_{0.19}\text{Zr}_{0.01})_{8.5}$. The fabrication procedure consisted of high temperature sintering and solution treatment followed by intermediate ($\sim 800^{\circ}\text{C}$) to low temperature ($\sim 400^{\circ}\text{C}$) step aging for developing high coercivity (6.5 kOe) which was less than 3.5 kOe after isothermal aging at 800°C . Mishra et.al.[17] extended the previous work of Ojima et.al.[15]. The best magnet produced through this effort had an energy product of 33 MGOe with $4\pi M_r = 12$ kG and $H_c = 13$ kOe corresponding to the $\text{Sm}(\text{Co}_{0.65}\text{Cu}_{0.05}\text{Fe}_{0.28}\text{Zr}_{0.02})_{7.7}$ stoichiometry, somewhat richer in Sm than the previous compositions. Using composition more close to Sm_2T_{17} , Shimoda et.al.[170] were able to generate H_c value in the range of 10-20 kOe by isothermal aging of powdered alloys. The composition that showed the highest H_c corresponded to the $\text{Sm}(\text{Co}_{0.66}\text{Fe}_{0.24}\text{Cu}_{0.08}\text{Zr}_{0.02})_{8.35}$ stoichiometry; resin bonded

Table II.6: Some Typical $\text{Sm}(\text{Co}_{\text{bal.}}\text{Fe}_u\text{Cu}_v\text{Ti}_w)_2$ (Precipitation Hardenable) Magnet Alloys and their Magnetic Properties.

S.No.	Chemical composition					Properties			Reference
	Z	Co bal.	Fe u	Cu v	T w	$4\pi M_r$ kG	H_c kOe	$(BH)_{\text{max}}$ MGOe	
1.	8.0	0.85	0.05	0.10	-	10.2	10.6	22.0	[16]
2.	7.0	0.73	0.13	0.14	-	9.7	7.0	23.5	[16]
3.	6.8	0.76	0.10	0.14	-	10.4	6.3	26.4	[16]
4.	8.5	+	+	+	Cr/+	11.2	6.5	30.0	[16]
5.	7.0	0.73	0.12	0.14	Ti/0.01	9.3	9.5	21.5	[16]
6.	6.9	0.74	0.12	0.14	Ti/0.01	8.2	7.8	16.5	[16]
7.	7.7	0.65	0.28	0.05	Zr/0.02	12.0	13.0	33.0	[17]
8.	7.2	0.69	0.22	0.08	Zr/0.02	10.3	12.0	28.0	[17]
9.	8.2	0.67	0.22	0.08	Zr/0.03	10.1	33.0	27.0	[169]

+ means present in unspecified amount; - means not present

LIBRARY
116573
Doc. No. A.

magnets with $(BH)_{\max}$ over 18 MGOe were prepared from this composition. A disturbing observation reported by these workers was a concurrent decrease in saturation magnetization with increase in H_c . Tian-duo [169] made similar observation for resin bonded magnets with $Z = 8.0, 8.3$ and 8.6 . For sintered magnets, however, no such negative correlation between $4\pi M_s$ and H_c was observed. Using liquid phase sintering for Shimoda type of composition $\text{Sm}(\text{Co}_{0.67}\text{Cu}_{0.08}\text{Fe}_{0.22}\text{Zr}_{0.03})_{8.0-8.3}$, the highest value of coercive force (33 kOe) and energy product (27 MGOe) were obtained [169]. More recent work by Ray, Mildrum and Krupar [171] on similar alloys, represented as $\text{Sm}(\text{Co}_{0.90-v}\text{Fe}_v\text{Cu}_{0.08}\text{Zr}_{0.02})_{8.35}$ (where $v = 0.23-0.30$), have indicated that both high H_c and $(BH)_{\max}$ could be obtained concurrently over a range of compositions. Hyperstoichiometric $\text{Sm}(\text{Co,Fe,Cu,Zr})_Z$ magnets with $Z > 8.5$ to 10 have also attracted attention for their high coercivity [172].

$(BH)_{\max}$ values as a function of Fe and Cu content were reported by Tawara and Kaneko [173] for Zr containing 2:17 magnets with $4\pi M_r = 3-10$ KG and $H_c = 6.8$ kOe (Fig.II.23). The difficulty in reaching a maximum energy product greater than 30 MGOe for these magnets has been that any attempt to raise $4\pi M_r$ and $(BH)_{\max}$ by increasing the Fe content and/or decreasing Cu, Zr or Sm contents resulted in unacceptable loss in coercivity [18]. It was also reported that the Zr content must be increased linearly with increasing Fe content in order to maintain high coercivity [174]. Liu and Ray [18] has recently reported that, in $\text{Sm}(\text{Co}_{\text{bal}}\text{Fe}_v\text{Cu}_{0.056}\text{Zr}_{0.02})_{7.55}$ alloys, with increasing Fe content the remanence rises monotonically while intrinsic coercive force drops sharply for $0.27 < v < 0.29$ and then increases for $0.30 < v < 0.33$. For the nominal composition $\text{Sm}(\text{Co}_{0.612}\text{Fe}_{0.316}\text{Cu}_{0.052}\text{Zr}_{0.02})_{7.73}$ most magnets developed $(BH)_{\max}$ in the range 31-33 MGOe while some reached 33-34 MGOe with $H_c \sim 16.5$ kOe and $4\pi M_r \sim 12$ KG [18]. Morita et.al.[133] studied the relationship between H_c and Sm or Co content for alloys containing fixed Cu (7.0 at.pct.) and Fe (22.0 at.pct.) and Zr 0.0-3.4 at.pct. (Fig.II.24). It has been reported by these workers that H_c may range from 10 to 25 kOe

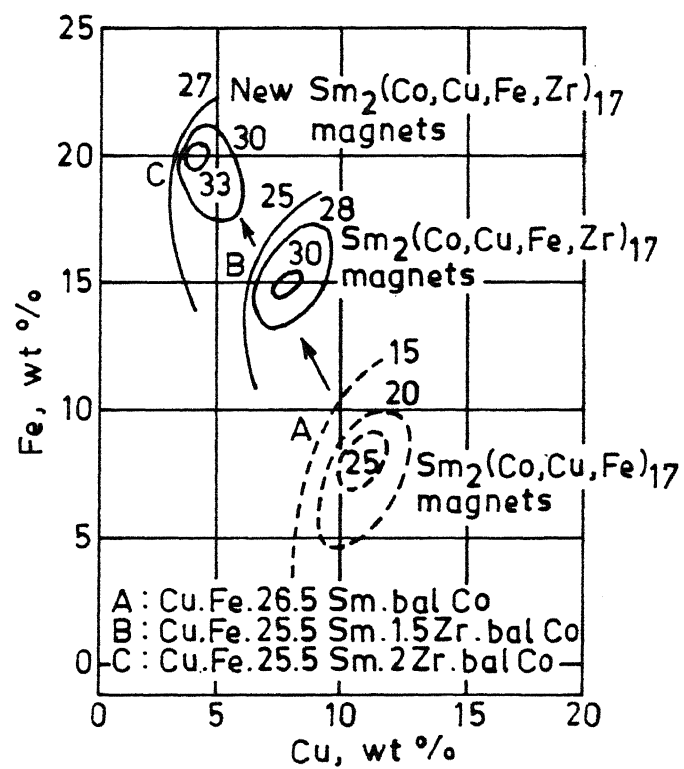


Fig.II.23 $(BH)_{\max}$ values for 2:17 type magnets as a function of Cu and Fe contents (after Tawara and Kaneko [173])

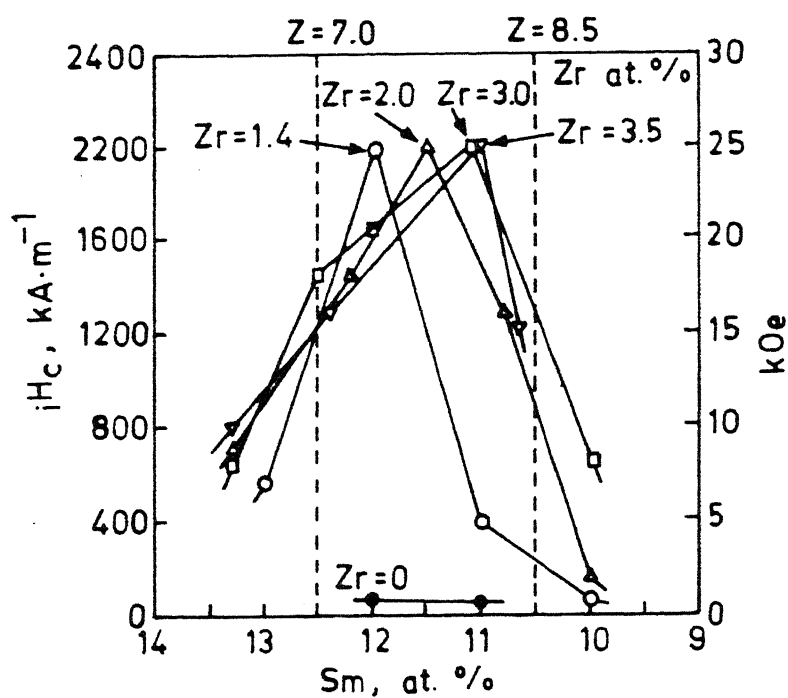


Fig.II.24 Relationship between intrinsic coercive force, iH_c , and Sm content for Sm-Co-7.0 at.pct. Cu-22.0 at.pct. Fe-0 to 3.5 at.pct Zr alloys (after Morita et.al.[133])

depending upon the Sm:T ratio of 7-8.5 and the Zr content.

Limited attempts have also been made to partially replace Sm with more abundant other light rare-earth elements e.g. Ce, Pr and Nd. Willman and Narasimhan [77] reported that partial substitution of Pr, Nd (or in combination), for Sm in $\text{Sm}_2(\text{Co,Fe,Cu,Zr})_{17}$ alloy increases the saturation magnetization without significantly decreasing the anisotropy field. Based on the contention that substitution of Sm by light rare-earths Pr, Nd and even Ce (all having higher magnetic moment than Sm) should result in an increase of saturation magnetization, Liu et.al.[81] studied the effect of Sm substitution in $(\text{Sm}_{1-X}\text{R}_X)_2(\text{Co,Fe,Cu,Zr})_{17}$ (where R = Ce, Pr, Nd, $\text{Pr}_{0.5}\text{Nd}_{0.5}$, $\text{Ce}_{0.2}\text{Pr}_{0.4}\text{Nd}_{0.4}$; and $X = 0-0.51$). It has been shown that both remanence and energy products are improved for $X = 0-0.2$ depending upon composition and heat treatment. For a composition $(\text{Sm}_{0.8}\text{R}_{0.2})(\text{Co}_{0.63}\text{Fe}_{0.286}\text{Cu}_{0.061}\text{Zr}_{0.02})_{7.59}$ (R = $\text{Ce}_{0.2}\text{Pr}_{0.4}\text{Nd}_{0.4}$) the values reported are $4\pi M_r = 11.57$ kG, $iH_c = 15.5$ kOe, $H_c = 10.3$ kOe and $(BH)_{\max} = 30$ MGOe. Akioka et.al.[80] successfully made resin bonded magnets of $\text{Sm}_{0.5}\text{Nd}_{0.4}\text{Ce}_{0.1}(\text{Co}_{0.67}\text{Cu}_{0.08}\text{Fe}_{0.22}\text{Zr}_{0.02})_{8.35}$ and $\text{Sm}_{0.5}\text{Pr}_{0.5}(\text{Co}_{0.67}\text{Cu}_{0.08}\text{Fe}_{0.22}\text{Zr}_{0.02})_{8.35}$. The magnetic properties of these magnets ($4\pi M_r = 8.1$ kG; $iH_c = 10.6-11.2$ kOe and $(BH)_{\max} = 14.5$ MGOe) are comparable to the magnets containing only Sm [171,172]. No literature seems to be available on the complete or partial substitution of Sm by MM.

2.3.1.2 Heat Treatment and Microstructure

The hard magnetic properties of $\text{Sm}_2(\text{Co,Fe,Cu,Zr})_{17}$ materials, such as coercivity, are strongly structure dependent and changes drastically with heat treatment which normally consist of homogenization of sintered or cast alloys between $1100-1200^\circ\text{C}$ followed by an isothermal aging around 800°C [4,11]. At times, isothermal aging is followed by step aging down to 400°C [4,11].

Some workers [4,133] have noted that the $\text{Sm}(\text{Co,Fe,Cu,Zr})_Z$ ($Z = 7-9$) alloys seem to be single phase $2:17(\text{H})$ at high temperature and all the Sm may be present in solution. Morita et.al.[133]

noted that $\text{Sm}(\text{Co,Cu,Fe,Zr})_2$ alloys, which consist of 2:17(OH) or [2:17(OH)+2:17(H)] structure, after quenching from high temperature, show high coercivity (Fig.II.15). Aging treatment results in general a cellular microstructure, which is revealed more clearly by transmission electron microscopy [17,32,33,167,175-178]. The cellular microstructure consists of 2:17(R) cells surrounded by 1:5 hexagonal boundaries [Fig.II.25(a),(b)]. The cell often exhibits a highly faulted structure and platelets of 2:17(H) phase running across many cells [4]. The 1:5 boundary phase forms coherently with the matrix of 2:17(R) phase [$(0001)_{1:5} // (0001)_{2:17}$, $(11\bar{2}0)_{1:5} // (01\bar{1}0)_{2:17}$] [167]. The platelets of 2:17(H) phase lies normal to c-axis of 2:17(R). 2:17(R) phase forms two twin related variants, ...ABCABC... and ACBACB, and stacking disorder converts one structure to another [167,176]. Since the substitutional solid solubility of Fe and Cu is low in the 1:5 and 2:17 type phases respectively, more so in the 2:17(R) than in the 2:17(H) structure, Cu tends to concentrate in the boundary phase and Fe, Cu, Zr segregates preferentially in the platelets phase [4]. Increase of H_c during aging treatment results from the attractive pinning interactions of domain walls with Cu-rich 1:5 type cell boundary phase as indicated by Lorentz electron microscopy [4]. H_c increase is also attributed to magnetoelastic coupling between magnetostrictive strain (associated with the domain wall) and coherency strains that develop during precipitation from the 1:5 and 2:17 lattice mismatch [178,179].

Tsai et.al.[180] observed a strong correlation between precipitation of zonal and grain boundary phases and large increase in H_c from aging. Hadjipanayis [167] reported that increase in H_c is associated with an increase in cell size. The size and shape of the cellular morphology of precipitation during aging has been suggested to develop through either a spinodal-type process during the isothermal aging of rapidly cooled disordered 2:17(R) phase [113] or through an allotropic diffusionless transformation of a high temperature 2:17(H) phase into a 2:17(R) phase and diffusion supported growth of 1:5 phase [176]. Increase

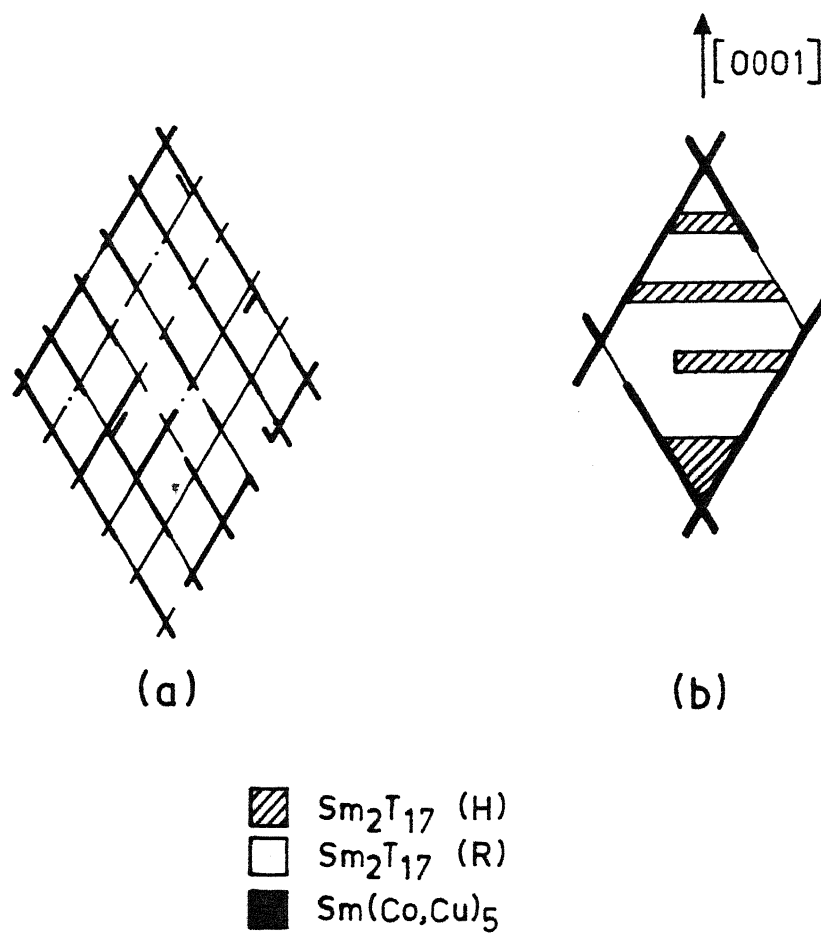


Fig.II.25 Schematic diagram showing (a) the typical ragged arrangement of the cellular microstructure, and (b) the different phases within the rhombic cells (after Fidler and Skalicky [177])

in the time of isothermal aging leads to an increase in cell size and formation of 2:17(H) platelets [17,180]. At too high an aging temperature, the structure coarsens leading to a decrease in H_C due to loss in coherency and subsequent breakdown [4]. Ivanova et.al.[181] attributed these latter changes to the development of a microstructure characterized by an equilibrium 1:5 phase and a soft magnetic $(Co,Fe,Cu)_3Zr$ phase with fcc structure. No significant changes in the cell morphology results from the step aging which may follow isothermal aging [182]. However, increase in H_C during step aging results due to additional chemical partitioning of solute Cu atoms in the respective phases, consistent with phase diagram considerations [176,182].

2.3.1.3 Role of Zirconium

Zirconium addition have been found to be most beneficial in developing best combination of properties in precipitation hardenable 2:17 type magnets [4]. Zr could affect magnetic properties, especially H_C , as described below :

- (i) Zr addition results in the increase of anisotropy field (Section 2.1.1) from dumb-bell cobalt substitution [75].
- (ii) Zr addition suppresses the precipitation of a low H_C fcc CoFe phase [113].
- (iii) Zr plays an important role in determining the cellular structure. In Zr-free alloys, isolated $< 60 \text{ \AA}$ size precipitates of Sm-Co-Cu were present and no cellular structure was seen [183].
- (iv) Zr facilitates platelets formation, which leads to rapid Cu enrichment of boundary phase resulting in the increase of H_C from increased pinning associated with higher chemical gradients [113,176].
- (v) Increase in Zr content initially leads to an increase in cell size and increase in the density of hexagonal platelets. At higher than optimum zirconium levels, H_C decreases due to reduction in cell size and precipitation of low H_C CoFeZr phase [183].
- (vi) Zr addition possibly also increases the misfit on habit

planes, thereby increasing coherency strains leading to increased pinning [176-179].

2.3.2 Nd-Fe-B Magnets

The Nd-Fe-B magnets derive their hard magnetic properties from the $\text{Nd}_2\text{Fe}_{14}\text{B}$ intermetallic phase, which has a theoretical energy product ($M_s^2/4$) of 60 MGOe. Magnets with energy product of 40 MGOe are already commercially available and magnets with still higher energy product are expected to be available in future [42]. Despite their excellent room temperature properties, two of their deficiencies have been of concern. These are : (A) lower Curie temperature, ($\sim 315^\circ\text{C}$) and poor corrosion resistance ; and (B) higher cost compared to ferrites and Alnico magnets (vide Table II.1). Substitution of Nd by other rare-earths and Fe by other elements have been attempted to overcome these problems. Parallel investigations have focused on the relationship between microstructure and coercivity. Various features of Nd-Fe-B magnets are presented in the light of these developments. Some of the recent reviews on these magnets are by Croat [42] (rapidly solidified Nd-Fe-B magnets), Higuchi and Hirosawa [43] (sintered magnets) and Buschow [2] (general review).

2.3.2.1 Chemical Composition and Magnetic Features

The best combination of properties in sintered magnets based on $\text{Nd}_2\text{Fe}_{14}\text{B}$ compound have been obtained using a composition close to $\text{Nd}_{15}\text{Fe}_{77}\text{B}_8$. Sagawa et.al.[19] reported the following properties for sintered magnets produced from this alloy composition : $4\pi M_r = 12.3 \text{ kG}$, $H_c = 11 \text{ kOe}$, $iH_c = 12 \text{ kOe}$ and $(BH)_{\text{max}} = 36 \text{ MGOe}$. The highest energy product ever achieved at room temperature on the ternary Nd-Fe-B is 50.5 MGOe [184]. The composition of the alloy ($\text{Nd}_{15}\text{Fe}_{77}\text{B}_8$) is hyperstoichiometric relative to the compound $\text{Nd}_2\text{Fe}_{14}\text{B}$ (with respect to Nd and B) so as to compensate for losses due to oxidation during processing [11]. Excess Nd prevents precipitation of free iron which is detrimental to the coercivity development [11]. Pan et.al.[185] studied the effect of B content

on the magnetic properties of sintered magnets prepared from $\text{Nd}_{16}\text{Fe}_{84-X}\text{B}_X$ ($X = 0-11$ at.pct.). A gradual increase in iH_c was observed with increasing boron content, and the values obtained for $X = 7$ are $4\pi M_r = 13.5$ kG, $iH_c = 9.5$ kOe and $(BH)_{\max} = 41.3$ MGOe; further increase in boron content resulted in a decrease for both $4\pi M_r$ and $(BH)_{\max}$.

2.3.2.2 Effect of Substitution

Various substitutions (for Nd and Fe) and additions in Nd-Fe-B magnets are made: (A) to improve thermal stability and corrosion resistance (especially the former); and (B) to produce low cost magnets.

(A) Thermal Stability and Corrosion Resistance

In contrast to $\text{Sm}_2(\text{Co,Fe,Cu,Zr})_{17}$ magnets ($T_c \sim 820^\circ\text{C}$, average temperature coefficients of $-0.02\%/^\circ\text{C}$ in $4\pi M_r$ and $-0.12\%/^\circ\text{C}$ in iH_c in the temperature range of $25-100^\circ\text{C}$ [180]) the thermal stability of ternary Nd-Fe-B magnet ($T_c \sim 310^\circ\text{C}$, average temperature coefficient of $-0.13\%/^\circ\text{C}$ in $4\pi M_r$ and $-0.6\%/^\circ\text{C}$ in iH_c in the temperature range of $25-100^\circ\text{C}$ [2]) is very inferior. The alloy substitution which are made to improve stability (Table II.7) can be subdivided in two categories: (i) substitutions which increase the Curie temperature of the hard phase and (ii) substitutions which introduces stability by increasing iH_c and loop squareness. Substitution of Fe by Co has been found to be most effective in raising Curie temperature (Fig.II.7) [111,190,192,193]. Unfortunately this substitution lowers coercivity which is a consequence of changed microstructure (vide next subsection 2.3.2.3) [190,194]. Substitution of Nd by Dy or Tb increases anisotropy field and consequently iH_c (Table II.7) [186]. Heavy rare-earths, such as Dy, are costly and hence other additions have also been tried. Addition of small amounts (1-5 at.pct. ; Table-II.7) of elements such as Al [195], Ga [111,190,195], Si [111], V [112], Nb, Ti, Zr [197], Mo [198-200] etc. (especially Al, Ga, and V), have been found to be effective in improving coercivity and thermal stability. These elements alter T_c and H_A

Table II.7: Magnetic Properties of $(\text{Nd}_{1-x}\text{R}_x)(\text{Fe}_{1-x}\text{X}_x\text{Y}_x\text{Z}_x)_2\text{B}$ Sintered Magnets

S. No.	Chemical composition						Properties *							
	P	q	r	R/x	X/u	Y/v	Z/w	$4\pi M_r$	H_c	H_c	(BH) max	T_c	α_1	α_2
1.	16	78	6	Dy/0.0	-	-	-	12.4	8.8	8.2	35	307	0.13	0.57
2.	16	78	6	Dy/0.2	-	-	-	10.7	25.0	10.2	27	315	0.09	0.42
3.	16	77	7.5	-	Al/0.00	-	-	12.5	8.5	-	-	-	-	-
4.	16	77	7.5	-	Al/0.03	-	-	12.0	12.6	-	-	-	-	-
5.	17	75	8	-	Co/0.0	-	-	12.6	10.2	-	37	318	-	-
6.	17	75	8	-	Co/0.3	-	-	10.8	3.6	-	27	553	-	-
7.	16	76	8	-	V/0.05	-	-	11.5	17.0	-	31	-	-	-
8.	16	78	6	Dy/0.3	Co/0.3	-	-	10.3	12.8	9.4	24	535	0.03	0.49
9.	16	78	6	-	Co/0.3	Al/0.02	-	12.5	10.9	9.4	35	520	0.07	0.88
10.	16	76	8	Dy/0.1	V/0.05	-	-	10.7	26.0	-	27	-	-	-
11.	15	78	7	-	Co/0.22	Ga/0.00	-	12.4	7.3	-	34	-	-	-
12.	15	78	7	-	Co/0.22	Ga/0.05	-	11.2	18.2	-	41	-	-	-
13.	15	77	8	-	Co/0.3	Ni/0.1	Ti/0.00	11.0	5.0	-	23	550	-	-
14.	15	77	8	-	Co/0.3	Ni/0.1	Ti/0.015	11.9	10.4	-	34	550	-	-

* Units: $4\pi M_r$ (kG), H_c or H_c (kOe), (BH)_{max} (MGOe), α (pct/ $^\circ\text{C}$); $\alpha_1 = \alpha_M$ & $\alpha_2 = \alpha_{H_c}$

Ref. S.No. (1,2,7,8 [187]) (3,4 [188]) (5,6 [189]) (7,10 [112]) (11,12 [190]) (13,14 [191])

only slightly, however, they influence the microstructure in such a way that coercivity increases [111]. Refractory oxides such as Dy_2O_3 , Tb_4O_7 and Al_2O_3 have also been used to enhance coercivity of Nd-Fe-B magnets [201-204], however, these addition results in lowering of remanence (due to magnetic dilution) and loss in the high temperature coercivity (possibly due to high oxygen content) [204,205]. Very recently it has been reported that small addition (0.1-0.2 wt.pct.) of nitrides e.g. BN, AlN, VN, TiN, CrN, HfN, TaN, ZrN or Si_3N_4 , can result in 6-20 pct. enhancement in coercivity with simultaneous improvement in $4\pi M_r$, $(BH)_{\max}$ and temperature coefficients. BN, AlN, TiN and Si_3N_4 have been found to have maximum beneficial effect [206,207].

The main cause of the lack of oxidation resistance and corrosion resistance of Nd-Fe-B magnets, leading to the so-called pulverization, is fast corrosion of Nd- and B-rich phases (i.e. $\text{Nd}_{1+\epsilon}\text{Fe}_4\text{B}_4$) (vide next subsection on microstructure) [208-211]. Various additions, such as Al, Co, V, Dy_2O_3 , Al_2O_3 , etc. have been found to enhance corrosion resistance by suppressing the formation of B-rich phase and/or blocking selective oxidation of the Nd-rich phases [212,213].

(B) Low Cost Magnets

Partial or complete replacement of Nd by other more abundant rare earth (such as La, Ce) or mixture of rare earths (Didimium, Mischmetal) have been studied by only a few workers [22,24,92,214-218]. Gong and Hadjipanayis [22] have pointed out that magnetic properties of $\text{MM}_2\text{Fe}_{14}\text{B}$ alloys may allow the production of permanent magnets with $(BH)_{\max}$ in the range of 10-20 MGOe. Permanent magnets containing Mischmetal with extra percentage of Nd and Pr have been reported to have good magnetic properties. Typically, Wan et.al.[24] reported best magnetic properties ($4\pi M_r = 11.5 \text{ kG}$, $H_c = 8.0 \text{ kOe}$, $(BH)_{\max} = 30 \text{ MGOe}$) for a $(\text{Nd}_{0.9}\text{Pr}_{0.1})_{9.5}\text{MM}_{6.5}\text{Fe}_{77}\text{B}_7$ magnet. Maocai et.al.[92] reported that when 50% Nd is replaced by Mischmetal, the magnets still exhibit moderate good magnetic properties with energy product ranging from 20-25 MGOe. Complete substitution of Nd by MM has

been attempted in meltspun ribbon [22,217]. Heat treatment of ribbons at about 700°C is required to develop coercivity [22]; heat treated ribbons of composition $\text{MM}_{17}\text{Fe}_{75}\text{B}_8$ showed M_s value of 80 emu/g, $H_c \approx 3.3$ kOe and $T_c \approx 240^{\circ}\text{C}$. Yamasaki et.al.[217,218] controlled the magnetic properties of the $\text{MM}_{16}\text{Fe}_{84-X}\text{B}_X$ ($X = 5-13$) ribbons by changing cooling rate (wheel velocity) and produced resin bonded magnets from optimum quenched $\text{MM}_{16}\text{Fe}_{75}\text{B}_9$ ribbons with the following properties: $4\pi M_r = 6.2$ kG, $H_c = 9.4$ kOe and $(BH)_{\text{max}} = 8.1$ MGOe. No serious effort appears to have been made to completely replace Nd by MM in sintered magnets. It has been reported, however, that MM containing alloys are more readily oxidized compared to the alloys containing only Nd [22].

2.3.2.3 Heat Treatment, Microstructure and Coercivity

The microstructure of sintered Nd-Fe-B magnets, with composition around $\text{Nd}_{15}\text{Fe}_{77}\text{B}_8$, consists of three major phases [34,219], namely, the hard magnetic phase $\text{Nd}_2\text{Fe}_{14}\text{B}$ (ϕ), the $\text{Nd}_{1+x}\text{Fe}_4\text{B}_4$ (B-rich phase or η) and a Nd-rich phase. The volume fractions of ϕ , η and Nd-rich phases in an ideal magnet may fall in the range of 80-85 pct., 0-5 pct. and 10-15 pct., respectively. Fig.II.26 schematically shows the distribution of different phases in a typical microstructure. Fidler [34] and Ramesh et.al.[220] reported the presence of oxygen containing phases (e.g. Nd_2O_3 , NdO) at the grain junctions and grain boundary of sintered magnets. In some of the magnets high amount of Fe-rich (e.g. Fe_2B) phase and α -Fe precipitates are also observed [11,34].

In the multiphase microstructure the hard magnetic phase ϕ is responsible for good magnetic properties. B-rich phase η which occurs in different metastable modifications is usually paramagnetic and undesirable [34,220]. Nd-rich phase which is liquid above 655°C [220] is responsible for good densification during sintering. The most Nd-rich phase distribute at the grain boundaries of the basic phase or the triangle region of the grain border (vide Fig.II.26). This phase is paramagnetic and is responsible for the decoupling of exchange energy between ϕ grains

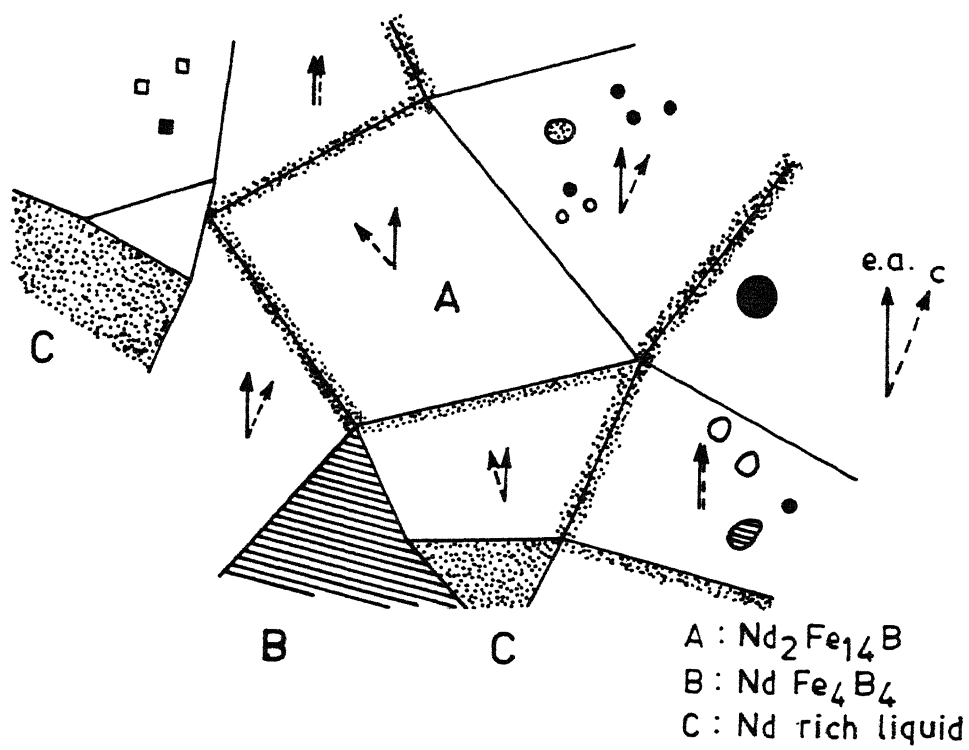


Fig.II.26 Schematic drawing of the multiphase microstructure found in the sintered Nd-Fe-B magnets (after Fidler [34])

[221] and hence important in the development of coercivity [195,219]. Nd-rich phase has variable composition [34] and its Nd content may vary from 60 upto 90% when the B content increases from 1 pct. upto 7% [222]. Recently, Lomerchand et.al. [223] have explained the formation of Nd-rich phase in terms of a miscibility gap in the Nd-Fe-B-O quaternary system. According to these workers the Nd-rich phase can be classed as NdO compound supersaturated with oxygen and stabilized with iron.

According to Sagawa et.al.[112], the following three points are important in Nd-Fe-B magnets to obtain high coercivity : (i) small grain size; (ii) good magnetic insulation among the grains of hard magnetic phase; and (iii) absence of soft magnetic impurity phases, or no direct contact of these phases with the grains of the hard magnetic phase. The surplus Nd over $\text{Nd}_2\text{Fe}_{14}\text{B}$ composition, which is contained in sintered Nd-Fe-B magnets, plays the following positive role in the development of microstructure and coercivity: (i) during sintering, liquid Nd may react with the soft magnetic impurity phases like $\text{Nd}_2\text{Fe}_{17}$, $\alpha\text{-Fe}$ and Fe_2B , formed on the surface of $\text{Nd}_2\text{Fe}_{14}\text{B}$ particles due to preferential oxidation of Nd, to change them into the hard magnetic phase $\text{Nd}_2\text{Fe}_{14}\text{B}$; and (ii) after sintering, the surplus of Nd remains at the grain boundaries insulating the grains magnetically from each other [112]. Oxygen level during processing has a profound effect on microstructure and coercivity. Ormerod [11] reported that in sintered Nd-Fe-B magnets, in which oxygen content had exceeded a critical level (dependent on Nd content of alloy), a large amount of soft $\alpha\text{-Fe}$ phase appeared, and the coercivity reduced to less than 200 Oe.

Rare-earth and other element substitution for Nd and Fe respectively may affect the microstructure in a number of ways. Ma and Krause [224] have reported that Dy addition not only increases the anisotropy field of the $\text{Nd}_2\text{Fe}_{14}\text{B}$ phase but it also results in fine grain structure, and a much larger increase in H_C is observed than predicted due to increase in H_A of the hard magnetic phase. La addition decreases H_A as well as worsens the function of

the Nd-rich grain boundary phase by segregating at the grain boundary and grain junctions [216]. The addition of cobalt leads to the formation of soft ferromagnetic cobalt rich phases, e.g. NdCo_2 (Laves phase), $\text{Nd}(\text{Co},\text{Fe})_3$ and $\text{Nd}(\text{Co},\text{Fe})_4\text{B}$, which leads to a decrease in H_c [190,194]. The precise role of Ga and Al substitution is not fully understood. It has been suggested that Ga and Al addition possibly increases the wettability of the Nd-rich phase which leads to better separation of the hard magnetic phase and ensuring increased exchange decoupling [195,221] and consequently increase in coercivity. Ga addition in Nd-(Fe,Co)-B magnets also suppresses the formation of soft Co-rich phase and results in the formation of new phases [$\text{Nd}(\text{Ga},\text{Fe},\text{Co})$ and $\text{Nd}(\text{Ga},\text{Fe},\text{Co})_2$] which are not harmful for coercivity development [190]. V addition suppresses the formation of undesirable $\text{Nd}_{1+x}\text{Fe}_4\text{B}_4$ phase and results in the formation of finely dispersed $\text{V}_{3-x}\text{Fe}_x\text{B}$ ($x \approx 1$) refractory phase which lead to a fine grain structure and enhancement of coercivity [112]. The other additions e.g. Ti, Mo, Zr etc. may also affect microstructure and consequently coercivity by affecting one or more of the three microstructural factors (Sagawa et.al. [112]) which influence coercivity of Nd-Fe-B magnets.

Post-sintering heat treatment (at $\sim 650^\circ\text{C}$) enhances coercivity of sintered Nd-Fe-B magnets. Sagawa et.al.[19] proposed that the enhancement of coercivity is due to the removal of damaged particle surfaces by the action of grain boundary liquid phase. In contrast to this, Stadelmaier et.al.[152] observed that the liquid phase inhibits grain growth and maintains or even reduces milled particle size in the sintered magnets. Some workers have attributed the increase in coercivity due to composition readjustment in the Nd-rich grain boundary phase [34,202]. Using small angle neutron scattering Fujii et.al.[225] found that the grains of hard magnetic phase in Nd-Fe-B and Nd-(Fe,Al)-B magnets were covered by a film of oxygen stabilized phase of $\sim 50 \text{ \AA}$ thickness; the thickness of film varied with heat treatment and correlated with coercivity. More recently Elbicki et.al.[226] have studied the microstructure of sintered and post-sintered heat

treated magnets using SEM and Auger spectroscopy and proposed a model for coercivity development during post-sintering heat treatment which is illustrated in Fig.II.27 and described below.

A typical $\text{Nd}_2\text{Fe}_{14}\text{B}$ large grain prior to post-sintering heat treatment is surrounded by Nd-rich (dead layer) and Fe-rich regions together with non-magnetic impurities (e.g. Nd_2O_3) [Fig.II.27(a)]. During post-sintering heat treatment, coercivity enhancement results from the following changes: (i) the bigger grains are broken into several smaller grains; (ii) surplus Nd in the sample diffuses into Fe-rich regions and converts them into $\text{Nd}_2\text{Fe}_{14}\text{B}$ or non-magnetic inclusions; and (iii) breaking the large grain disrupts the material such that some of the internal pores are cracked releasing some trapped gases which attack the surface, generating a protective film around the individual grains which is more uniform [Fig.II.27(b)].

2.4 Magnet Fabrication Methods

Kumar [4], Ormerod [11], Bohlmann [40], Adler et.al.[41] and Croat [42] have published comprehensive technical reviews on various aspects of different fabrication methods used for making Sm-Co and Nd-Fe-B magnets. Sankar [227] has summarized the recent advances in the area of REPM fabrication. Powder metallurgy technique, also referred to as the 'Powder-Orient-Press-Sinter-Process', is most commonly used for fabrication of rare-earth permanent magnets. There are other manufacturing techniques, significant among these are resin-bonding and rapid solidification techniques. Techniques such as die-up-set and hot isostatic pressing are gaining ground in recent times [4,42].

2.4.1 Powder-Orient-Press-Sinter-Process

The main process steps involved in the production of REPM by powder metallurgy route are shown in the flow diagram (Fig.II.28). Abbreviated summary for the functions of different operations is given in Table II.8. More details with respect to the fabrication

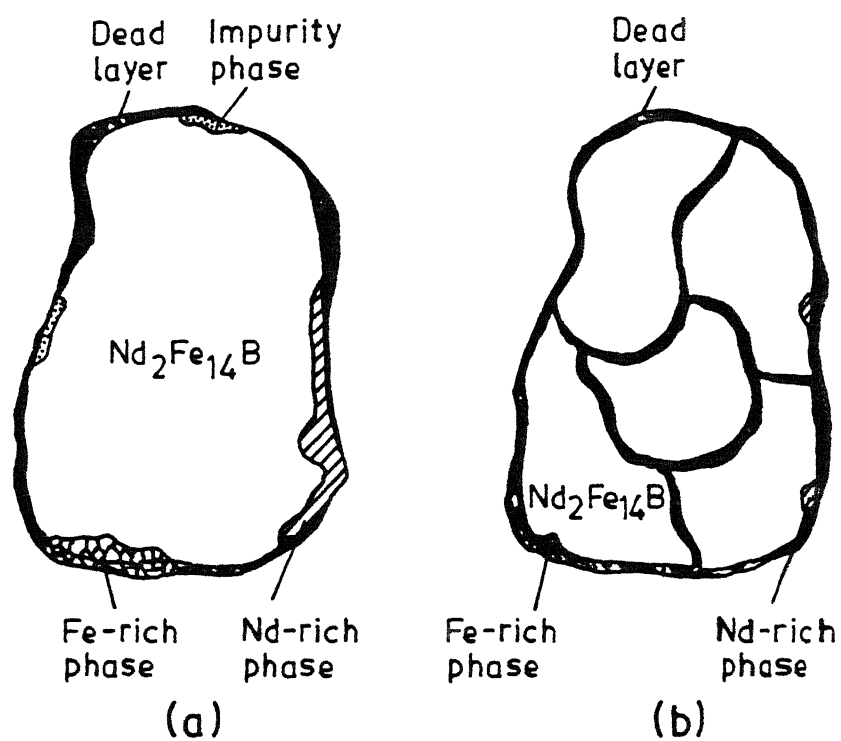


Fig.II.27 Schematic diagram illustrating possible micro structural and compositional changes during post sintering heat treatment of Nd-Fe-B magnets : (a) $\text{Nd}_2\text{Fe}_{14}\text{B}$ grain before heat treatment; and (b) after heat treatment (after Elbicki et.al.[226])

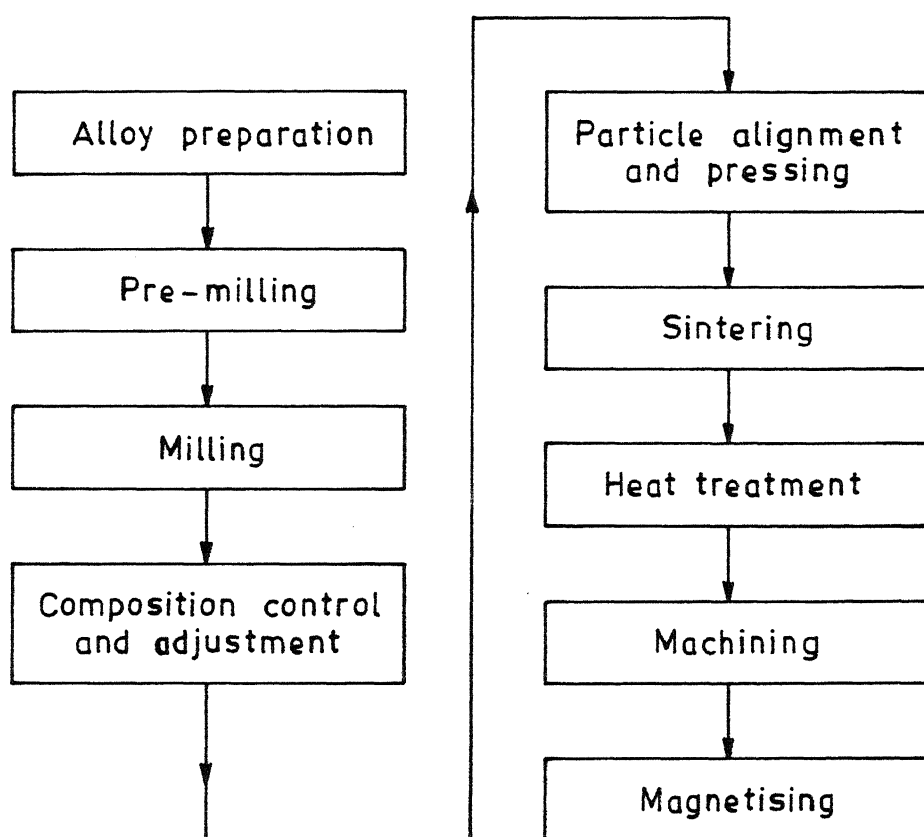


Fig.II.28 Schematic representation of the various process steps for the manufacturing of sintered rare-earth permanent magnets (after Ormerod [11])

of $\text{Sm}_2(\text{Co,Fe,Cu,Zr})_{17}$ and Nd-Fe-B magnets are presented in the subsections which follow.

Table II.8: Powder-Orient-Press-Sinter Process [40]

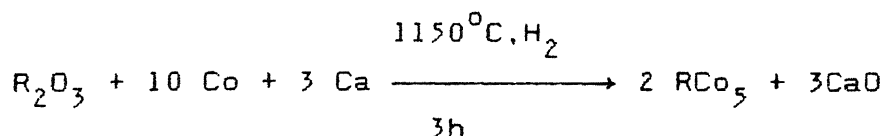
Operation	Function
WEIGH metals or oxides	To get stoichiometry in composition
VACUUM CAST or OXIDE REDUCTION	To form alloy/compounds
CRUSH / PULVERIZE or DEAGGLOMERATE (PRE-MILLING)	To make coarse powder
MECHANICAL ATTRITION (MILLING)	To get uniaxial, near single domain particles (fine powders)
BLEND (before, during or after)	To increase uniformity; add alloy for compensating oxidation losses and / or to aid sintering
ORIENT	To align particles with preferred direction of magnetization
PRESS	To fix alignment and to compact for green strength
SINTER	To densify for maximum flux, to improve orientation, to close pores
HEAT / COOL TREATMENTS	To increase or decrease phases affecting magnetics, e.g. coercivity
At this point, magnet material has its permanent properties; the major hysteresis loop characterizing each material is fixed.	
FINISH	To meet user specifications for dimensions, surface finishes, and magnetic state

2.4.1.1 Alloy Preparation

On an industrial scale, REPM alloys are usually produced by two methods. These are (i) vacuum induction melting, and (ii) calciothermic reduction (R-D process or co-reduction). Arc melting in argon atmosphere is extensively used for the laboratory preparation of alloys.

The calciothermic production of rare-earth alloys was developed independently by two groups working at General Electric, U.S.A. [228] and Th.Goldschmidt, F.R.G. [229]. In the General

Electric process cobalt powder, calcium granules and rare-earth oxide powder are blended together and then reacted under hydrogen at 1150°C. The reaction can be represented by the equation:



After cooling, the excess calcium and calcium oxide are removed from the reacted product by reacting with moist N_2 , then washing with water and dilute acid. This process is known as the reduction diffusion (R-D) process. The Goldschmidt process, known as co-reduction, is a variation of R-D process. In this process the reaction is carried out under vacuum at 1000°C and both cobalt powder and cobalt oxide are used as raw materials.

The applicability of R-D process, originally developed for the SmCo_5 magnets, for the manufacture of $\text{Sm}_2(\text{Co}, \text{Fe}, \text{Cu}, \text{Zr})_{17}$ magnets have been investigated by Chinese workers [230]. More recently, its applicability in the manufacture of Nd-Fe-B magnets has also been reported [2,231]. The advantage of vacuum induction process over the calciothermic reduction process is that it can provide a wide range of composition with very low oxygen contents (<200 ppm) [11]. The main advantage of calciothermic reduction process is that it has rare-earth oxide as the raw material, and direct production of alloy powders suitable for milling.

2.4.1.2 Pre-Milling

Depending on the method used for preparing the alloy, the material may require a size reduction stage prior to final milling. The alloy melted by vacuum induction is crushed in a high energy hammer mill, under nitrogen or argon atmosphere, to a particle size below 500 μm . Alloys prepared by calciothermic reduction are generally of particle size which is suitable for direct milling. Hydrogen decrepitation techniques are becoming increasingly important in the preparation of powder precursors

needed for the successful fabrication of Nd-Fe-B magnets [227,232].

2.4.1.3 Milling

The critical parameters to be controlled during milling are particle size, particle size distribution, damage to crystal structure and oxidation. Milling can be carried out by ball milling (vibration ball milling / attritor milling) or jet milling in an organic liquid, e.g. cyclohexane, toluene, freon under an inert atmosphere. After milling, the powder is either dried under vacuum or by heating under argon. Milling conditions are to be chosen to get both the required size distribution and minimum oxygen level. Milling for too short a time produces multi-grain particles, which will not align properly or fully sinter. Over milling produces excess oxygen pick-up and causes damage to surface of the particles. Fig.II.29 show the effect of milling time on the oxygen pick-up and particle size of the milled Nd-Fe-B and Sm-Co based alloy during vibration ball milling in Freon as reported by Ormerod [11]. The much higher rate of oxygen pick-up indicates the higher reactivity of the Nd-Fe-B alloys compared to the Sm containing alloys. The size reduction of Nd-Fe-B alloy takes place at a faster rate compared to the Sm-Co based alloy [2,11].

2.4.1.4 Composition Control and Adjustment

The magnetic properties of REPM magnets are critically dependent on the chemical composition (vide Sections 2.3.1.1 and 2.3.2.1). Any contamination, particularly oxidation of the alloy occurring during processing, depletes the alloy of the rare-earth component, resulting in a shift in composition to the transition metal rich side of the phase diagram. Shift in composition may cause a magnetically unfavorable phase distribution. Sm_2O_3 formation due to the pick up of oxygen during milling or sintering stage is compensated for by introducing a corresponding excess of Sm. This is often accomplished by blending the alloy powder with

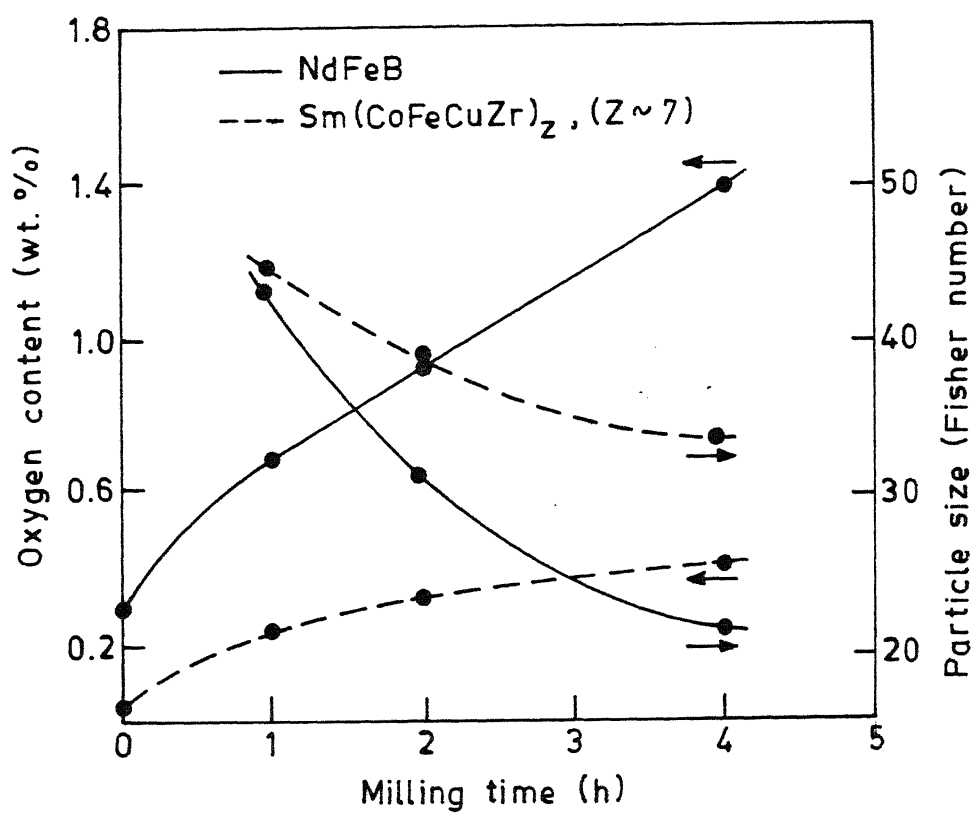


Fig.II.29 Effect of milling time on particle size (right scale) and on oxygen pick up (left scale) during ball milling in freon of Nd-Fe-B (full lines) and $\text{Sm}(\text{Co,Fe,Cu,Zr})_2$ (broken lines) alloys [2,11]

Sm-rich milled alloy powder or by adding excess Sm during the preparation of an alloy. For Nd-Fe-B magnets, the composition range for optimum magnetic properties is less critical than that for the Sm-Co magnets. The critical composition range of rare-earth component for Nd-Fe-B magnets is about a factor of ten greater than the critical range for Sm-Co magnets [2,11].

2.4.1.5 Particle Alignment and Pressing

To obtain a powder compact with maximum magnetization, the powder particles are magnetically aligned and pressed, such that the easy axis of magnetization of the particles are parallel. The powder compaction is performed by die-pressing or by iso-static pressing. In the first method, the aligning magnetic field is set up in the cavity of a non-magnetic die with its axis lying either in the direction of pressing or at right angles. High homogeneous field levels are required to produce a high level of uniformly aligned particles. The applied field can be continuous or a combination of continuous and pulsed. The degree of alignment is influenced by the particle shape, size and size distribution, the magnitude of the aligning field, and the pressing pressure. The pressing pressure should be sufficient to give the green powder compact enough mechanical strength to withstand handling but not high enough to cause particle misorientation.

Iso-static pressing is normally carried out on powders pre-aligned in a pulsed magnetic field of a level 3-4 times that used in uniaxial die pressing. This improves the degree of particle alignment, which is then maintained during iso-static pressing and results in higher remanence and energy product than it is possible to achieve in die pressed magnets.

2.4.1.6 Sintering and Heat Treatment

The sintering of REPM is carried out in inert gas atmosphere, reducing atmosphere or under vacuum. The sintering treatment should result in a magnet with a high density, and for magnets

with a nucleation and grain boundary pinning coercivity mechanism, no appreciable grain growth. A constant and well defined sintering temperature is necessary in order to ensure that the magnet has no open porosity which could lead to oxidation and aging during use. This requires density to be greater than 95 pct. of theoretical density. In the case of H_2 decrepitation method, the desorption of high purity H_2 during vacuum sintering and annealing produces a non-oxidizing atmosphere. The optimum temperature range for sintering 2:17 magnets (based on Sm) is between 1150-1200°C depending upon the composition. The as sintered coercivity of these magnets is very low and usually a complex post-sintering treatment, which may include both isothermal and step aging, is required to develop coercivity [Fig.II.30(a)] (vide Section 2.3.1.2 on the effect of heat treatment). The optimum sintering temperature range (1050-1150°C) for Nd-Fe-B magnets is much wider than the 2:17 magnets [Fig.II.30(b) [2,11]. The properties obtained in these magnets (directly after sintering) are such that they form useful magnets in the as sintered form [11,40]. A post-sintering heat treatment (around) 630°C further enhances coercivity and loop squareness [11,40] (vide Section 2.3.2.3 on the role of heat treatment).

2.4.1.7 Finishing and Magnetizing

Machined surfaces are required either to give the required magnetic contact with associated component in the final assembly or for size reasons. Slicing or surface grinding of REPM often use diamond or carbide grit embedded in discs or wheel. Finish grinding of Nd-Fe-B magnets (especially the one which contain Dy and Al) seems to retard atmospheric corrosion by developing a thin oxide layer. Magnetization may be carried out in the assembly where the magnet is used or before putting in the assembly. Magnetization fields are usually very high and may range from 15 kOe to 40 kOe [40].

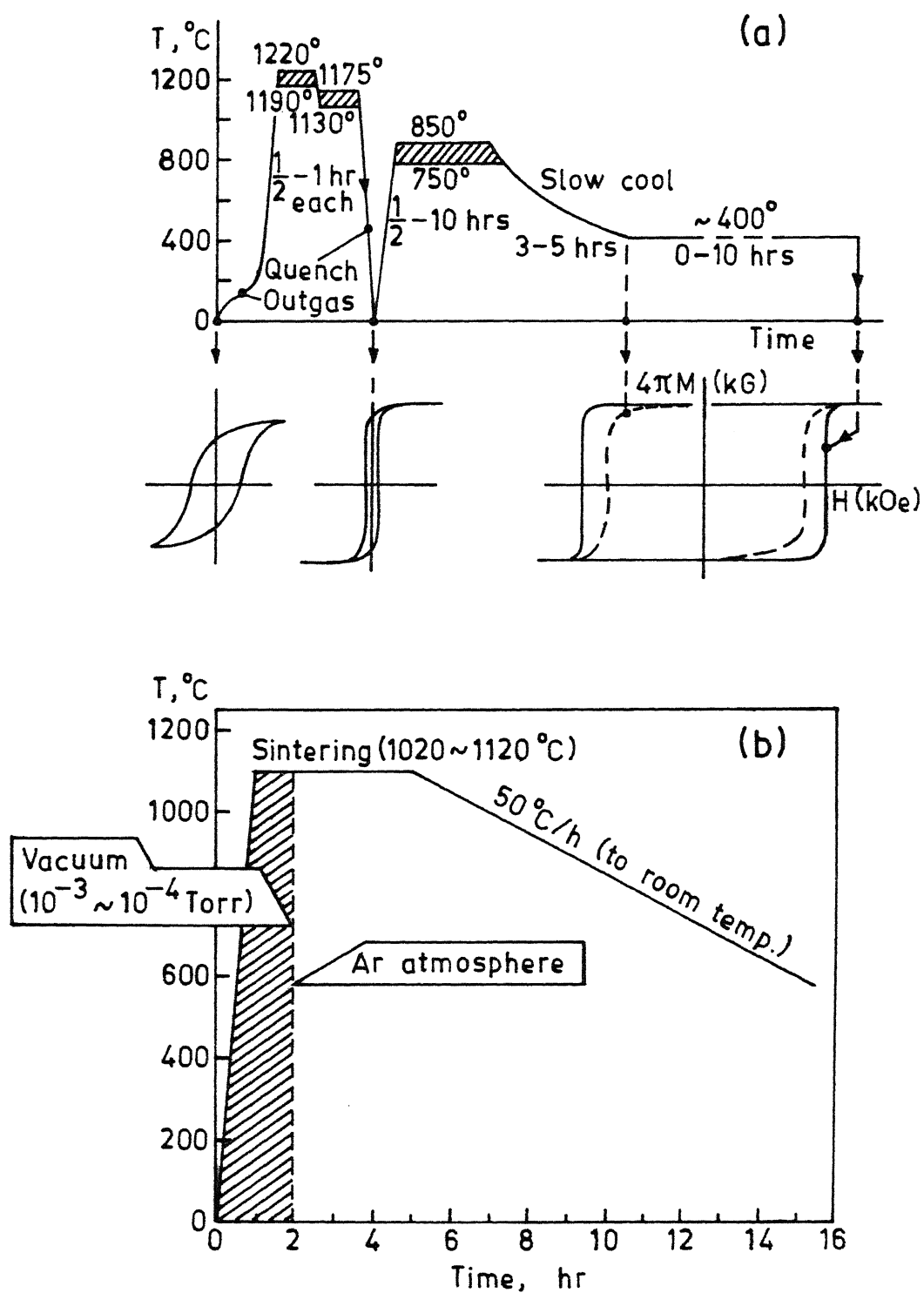


Fig.II.30 Typical sintering and heat treatment cycle for
 (a) $\text{Sm}(\text{Co,Fe,Cu,Zr})_{7.4}$ and similar "2-17" magnets,
 (after Kumar [4])
 (b) $\text{Nd}_2\text{Fe}_{14}\text{B}$ based magnets (after Okada and Homa [233])

2.4.2 Other Processes

More significant among other manufacturing technologies used for producing rare-earth permanent magnets are resin bonding and rapid solidification techniques. These techniques are described in detail by Japanese and other workers [4,40,42,233-239]. An abbreviated summary of different process steps and their functions is presented in Table II.9(a) and (b).

By melt quenching techniques (e.g. plasma-spraying and splat cooling) with cooling rate of 10^4 - 10^6 K s^{-1} , polycrystalline SmCo_5 films and foils with grain size smaller than $1 \mu\text{m}$ and very high coercivities have been produced [4,40]. Plasma spraying has been suggested as a process for fabricating magnets in various shapes and sizes [40]. Vapor deposition, chemical deposition or polishing/etching have also been proposed or are being used [40].

Table II.9(a): Bonded Particle Magnet Technology [40]

Operation	Function
VACUUM MELT / CAST	To form alloy
PULVERIZE / MILL	To get proper particle size for magnetics or mixing
HEAT TREAT	To have complete magnetics within each particle
MIX WITH BINDER	To coat / distribute without destroying magnetics
COMPACT, EXTRUDE or INJECT	To form the complete magnet, generate particle alignment
CURE	To set binder
SLICE / DEBURR	To cut to length, remove flash
At this stage magnets are complete to size, other finishing is optional	

Table II.9(b): Rapid Solidification Techniques [40]

VACUUM MELT AND QUENCH RAPIDLY	To produce ribbon or particles having ultrafine crystals
SHEAR / MIX	To cut ribbon or add binder
COMPACT / MECHANICALLY WORK	To densify, to form, to generate anisotropy
CURE / HEAT TREAT	To set binder / complete the metallurgy

2.5 Concluding Remarks : Samarium versus Neodymium Magnets

The alloys of Sm-Co and the Nd-Fe-B materials commercially show marked superiority in performance over the earlier permanent magnet materials (Table II.1) and afford viability to new device designs [2,6]. However, many experts struggle with the question whether Sm alloys have to be preferred over Nd alloys or vice versa. A literature study on REPM by Andriessen and Terpstra [48], and an article by Stablin and Bran [237] critically discusses this issue and the material which is presented here is taken from these sources.

The energy density of Nd-Fe-B alloys is higher than that of Sm-Co alloys (Table II.1) but the stability versus demagnetization of the latter is slightly higher than that of the first. Curie point of Nd-Fe-B magnets is very low compared to that of Sm-Co, and their application to devices operating at high temperature requires cooling. Furthermore, the mechanical strength of Nd-Fe-B alloys is far higher than that of the Sm-Co alloys, while the overall economy of Nd-Fe-B magnets production is moderate, it is higher for the Sm-Co magnets.

For environments where temperature is stable or where small variations in temperature rarely occur, Nd-Fe-B is the better choice upto slightly over 300 K. For high load line operation, Nd-Fe-B maintains this superiority to approximately 350 K. For temperature above 350 K, in applications that requires smaller temperature coefficients of the magnetic parameters, and for some low load line applications between 300-400 K, the SmCo generally gives superior performance.

CHAPTER III

STATEMENT OF THE PROBLEM

An overview of rare-earth permanent magnets in the previous chapters has highlighted the importance of the $\text{Sm}(\text{Co,Fe,Cu,Zr})_Z$ ($Z \sim 7$) and Nd-Fe-B magnets. The widespread application of these magnets is restricted due to their high cost attributed to Sm and Nd. The replacement of Sm by less costly light rare-earths (e.g. Ce, Pr etc.) have been successfully tried by some research workers [77,79-81] but these replacements also do not reduce the cost of the magnets significantly. No literature seems to be available regarding substitution of Sm by more plentiful MM (mixture of light rare-earths). Efforts to replace Nd by MM in Nd-Fe-B sintered magnets have also been quite limited [22,24,92]. The broad objective of this investigation has been to explore the prospects of totally replacing Sm and Nd by MM in $\text{Sm}(\text{Co,Fe,Cu,Zr})_Z$ ($Z \sim 7$) and Nd-Fe-B magnets, respectively.

It is quite apparent from the literature review that besides intrinsic properties of the basic magnetic phases, heat treatment and microstructure play a decisive role in the development of magnetic properties such as coercivity (H_C) and remanence ($4\pi M_r$). Thus, in order to select appropriate chemical composition for magnet fabrication in a particular system, the knowledge of phase equilibria is quite essential. No readily available literature was found regarding the phase equilibria in MM-Co-Fe-Cu-Zr and MM-Fe-B systems. Urgency of such information was felt immensely, and hence it was contemplated to study phase-equilibria in the MM-Co-Fe-Cu-Zr and the MM-Fe-B systems as a major part of this investigation. As a follow up of phase equilibria studies, it was envisaged to undertake some preliminary magnetic characterization studies on bulk alloys and resin bonded and sintered magnets. The objective of magnetic characterization studies was to foster awareness regarding the potential of some magnetically important phases and to identify problem areas for future investigations.

3.1 Phase Equilibria

MM-Co-Fe-Cu-Zr and the MM-Fe-B are multi-component systems and complete phase equilibria study is not possible. Hence, only limited composition range, in the vicinity of magnetically important region, had to be chosen. Since representation of phase equilibria in systems involving large number of elements is practically impossible, the total rare-earth content (RE) of Mischmetal (MM) has been treated as a single component. Also, in each case the phase equilibria studies are restricted to a single isothermal section around the possible sintering and/or solid solution treatment temperature.

3.1.1 RE-Co-Fe-Cu-Zr System

1100°C isothermal section in the RE-Co-Fe-Cu-Zr system (where RE represents total rare-earth content of Indian Mischmetal) was selected for investigation, around RE : Transition metal ratio of ~ 1:7, in a narrow composition region bounded by Co content of 55 to 75 at.pct., Fe content of 7 to 20 at.pct. and fixed Cu (8 at.pct.) and Zr (2 at.pct.) contents. The amounts of Cu and Zr were kept fixed to represent more conveniently the five component (RE-Co-Fe-Cu-Zr) system in a ternary diagram. The fixing of Cu and Zr contents at 8 at.pct. and 2 at.pct. respectively was done in the light of compositions used by several workers [17,133,170] for successfully fabricating $\text{Sm}(\text{Co,Fe,Cu,Zr})_Z$ ($Z = 7-9$) magnets with excellent combination of magnetic properties.

3.1.2 RE-Fe-B System

The phase equilibria studies were planned in the magnetically important composition region upto about 40 at.pct. RE and about 45 at.pct. B, at 1000°C. The range of chemical composition selected is similar to the one used by Schneider et.al.[150] in their studies on the 1000°C isothermal section of Nd-Fe-B system.

During the course of investigation on the 1000°C isothermal

3.2 Magnetic Characterization and Fabrication

The objective of these studies was to explore the possibility of fabricating hard permanent magnets in the RE-Co-Fe-Cu-Zr and RE-Fe-B systems. Magnetic characterization studies were contemplated on bulk alloys as well as on resin bonded and sintered magnets. The broad outline of the adopted research plan is as follows : (i) selection of suitable alloy composition for magnet fabrication; (ii) characterization of alloys used in magnet fabrication in terms of intrinsic magnetic properties; (iii) fabrication of resin bonded and sintered magnets under different experimental conditions; and (iv) magnetic and metallurgical characterization of magnets.

3.2.1 Bulk Alloys

Alloys in several rare-earth transition metal systems respond to magnetic hardening treatment by low temperature ($400-900^{\circ}\text{C}$) aging. In order to know whether the alloys in RE-Co-Fe-Cu-Zr and RE-Fe-B system respond to low temperature aging, aging studies on bulk alloys were contemplated. Since several new phases were observed in the RE-Co-Fe-Cu-Zr system at 1100°C , effect of aging on magnetic hardening was planned for several alloys consisting of different combination of phases. The alloy, which showed best aging response, was used for detailed aging studies at different temperatures. Since phase equilibria in the RE-Fe-B system at 1000°C was found to be quite similar to the Nd-Fe-B system, the alloy composition was selected on the basis of phase equilibria and available literature on Nd-Fe-B system.

3.2.2 Resin Bonded Magnets

Resin bonded magnets were prepared not only to find the possibility of fabricating such magnets, but also to obtain basic useful information on optimum milling time, saturation magnetization, anisotropy field (H_A) and axis of easy magnetization. Such information is desired both from the point of

view of resin bonded as well as sintered magnets. The laboratory fabrication of resin bonded magnets involves preparation of alloy powder (by hammering and milling), mixing the alloy powder with epoxy resin and hardener, aligning in the magnetic field and curing. There are several variables which can influence the magnetic properties, for example milling method (e.g. ball milling, rod milling, attritor milling etc.) particle size and size distribution, proportions of alloy powder and resin and hardener, magnetic field used for aligning the powder etc. Besides, the sequencing of aging and milling operation, for age hardenable alloy, can very significantly affect magnetic properties. The variables selected for study in this investigation include effect of size reduction by hammering (coarse powders), effect of milling time and effect of sequencing of aging and milling operations. The other parameters were fixed according to the experience of previous workers [238,239]. Since the alloys in RE-Fe-B system did not respond to aging treatment, studies on the effect of sequencing of milling and aging operation were limited to only RE-Co-Fe-Cu-Zr alloys. Particle size of milled powder is an important parameter which influences coercivity and remanence significantly. Augustin [240] has reviewed the various particle size measurement techniques and highlighted the general difficulty in the particle size measurement for the powder of magnetic materials due to magnetic coherence and agglomeration of spontaneously magnetized fine particles. Hence, only limited studies to measure particle size and size distribution were performed using SEM and an Image analyzer fitted with an optical microscope. The characterization of resin bonded pellets was done in terms of intrinsic coercivity (H_c), saturation magnetization ($4\pi M_s$) and remanence ($4\pi M_r$) using vibrating sample magnetometer (VSM).

3.2.3 Sintered Magnets

In sintered magnet fabrication, the parameters to be studied are : (i) composition of the alloy; (ii) size and size distribution of the powder; (iii) compacting method; (iv)

CHAPTER IV

MATERIALS AND EXPERIMENTAL PROCEDURES

The contents of this Chapter are covered under three major subsections. The first two subsections give details regarding alloy preparation and phase analysis techniques. The last subsection focuses on experimental details regarding magnet fabrication and characterization techniques.

4.1 Alloy Preparation

Large number of alloys were prepared in multi-component RE-Fe-Co-Cu-Zr, RE-Fe-B and RE-Fe systems. These alloys are labelled with symbols C_i , E_i and D_i ; subscript i indicates the alloy number. Further details of compositions of these alloys are given in Chapters V to VII.

4.1.1 Materials

Indian mischmetal (MM) was supplied by Raw Flints Pvt. Ltd., Rajkot. The MM contained 87 wt.pct. total rare-earths (RE). The rest included 12 wt.pct. Fe and 1 wt.pct. impurities. The wt.pct. of individual rare earths, from X-ray fluorescence analysis, was as follows : Ce ~ 47, Nd ~ 23, La ~ 23 and Pr ~ 7. The average atomic weight for the mixture of rare earths in the mischmetal was computed to be 140.09 on the basis of X-ray fluorescence analysis data. The mischmetal was stored in heavy oil to prevent air oxidation.

Cobalt, iron, copper and zirconium supplied by Semi Elements Inc., New York (USA) were of 99.9 pct. purity. Boron, supplied by Alpha Products, Danvers, MA (USA), was also of 99.9 pct. purity.

4.1.2 Melting of Alloys

The pieces of MM (after grinding off the oxide surface and

cleaning with acetone) and other metals were weighed according to the chosen composition and total weight of alloy (10-40 g) to be made.

Alloys were melted in a non-consumable tungsten electrode d.c. arc furnace on a water cooled copper crucible for 15-20 seconds. In order to have small and uniform losses during melting, metals with high melting point were stacked above the low melting ones. The furnace chamber was evacuated to 10-30 millitorr pressure and flushed with ultra-pure argon gas (supplied by Indian Oxygen Ltd., India; Grade IOLAR-2). The flushing was repeated twice to remove any traces of oxygen present in the melting chamber. Finally, melting was carried out under argon atmosphere. Arc current was set between 300-500 Amps at 40 Volts. For proper homogenization each alloy was remelted at least three times by keeping the alloy button upside down on the crucible. The melting losses were always below 0.5 wt.pct. Since the melting losses were small the alloys were not chemically analyzed. After melting, alloys were labelled and stored in a desiccator.

4.1.3 Annealing of Alloys

Before homogenizing an alloy, its surface was ground and cleaned. The as cast alloy buttons were sealed in evacuated (~ 20 millitorr pressure) quartz capsules and annealed at different temperatures between 700-1100 $^{\circ}\text{C}$ for 2 to 30 days depending upon the annealing temperature. The samples were water quenched to retain the equilibrium state corresponding to the annealing temperature.

4.2 Phase Analysis

Several techniques were employed to avoid ambiguity in phase analysis. These include optical microscopy, X-ray diffraction (XRD), thermomagnetic analysis (TMA), differential scanning calorimetry (DSC) and to a limited extent X-ray microanalysis in a scanning electron microscope (SEM-EDS). Some of these techniques

were also applied for the characterization of sintered and resin bonded magnets (Section 4.3).

4.2.1 Metallography

Annealed pieces of the alloys were broken into small parts using a chisel and the freshly fractured surface of the alloy piece was selected for metallographic investigation. The chosen surface of the broken alloy piece was ground flat using a belt surfacer or 1/0 emery paper. Some alloys were very brittle and hence careful specimen handling was necessary to prevent loss of particles during polishing operation. The ground piece of an alloy was mounted using a 'Simplimet' (Buehler) mounting press in hot pressing mode with trans-optic powder. The mounted specimen was polished successively on 1/0 through 4/0 emery paper taking care that no deep scratches are produced during polishing. The specimen was thoroughly washed in flowing water and subjected to fine polishing on a rotating wheel covered with selvyt cloth or Buehler micro cloth. 1 μ m size alumina powder suspended in distilled water was used as a polishing abrasive. After polishing, the specimen was washed in running tap water and dried under a high speed air blower. To reveal microstructure, polished specimens were etched with dilute HNO₃ of various strengths, varying between 0.25 pct. to 6 pct. (by volume). To control over etching of a specimen, a piece of cotton soaked in the etchant was rubbed lightly against the polished surface of the mounted metallographic specimen. The time of etching varied from 2 swabs to 10 swabs depending upon the composition of an alloy. Microstructures of the specimens were observed and photographed using the Zeiss Universal Metallograph and Leitz Metallux3 microscopes.

4.2.2 X-ray Diffraction

Powder X-ray diffraction technique was used for phase analysis, phase identification and determination of lattice parameters of different phases. Since majority of the alloys in all the alloy systems, except the high cobalt containing alloys in

the RE-Fe-Co-Cu-Zr system and high iron containing alloys in the RE-Fe and RE-Fe-B systems, are brittle, < $63\mu\text{m}$ (~ 250 mesh) powder specimens of homogenized alloys were used to obtain their XRD patterns. In the case of high cobalt containing alloys, the coarse ($\sim 60+100$ mesh) flaky powder of the ductile phase was separated from the fine powder (~ 250 mesh) of brittle phase during sieving. The coarse powder of the ductile phase was stress relieved at 1100°C for 5 minutes and water quenched before recording the XRD pattern. For the high iron containing alloys, a plain surface was made on the annealed alloy piece by grinding and polishing, and XRD pattern was recorded from the polished plain surface. A Seifert Iso-Debyeflex 2002 diffractometer was used for taking XRD patterns. Cr-radiation and slow scanning speeds were used for better resolution. A curved graphite crystal monochromator was used in the diffracted beam path to eliminate scattered radiations and Cr-K_{β} diffraction lines. Thus practically background free and β -reflection free high resolution diffraction patterns could be taken for phase analysis. Conditions used for obtaining diffraction traces are given in Table IV.1.

For indexing the diffraction patterns and to obtain precise lattice parameters values, a specific calibration procedure was adopted. A diffraction pattern of standard Si specimen was taken after proper alignment of the diffractometer. The 2θ position of each reflection from Si was calculated using its known lattice parameter ($a = 5.4301 \text{ \AA}$). The calculated and observed 2θ values were compared to find error $\Delta 2\theta$ in the measured angles. The $\Delta 2\theta_{\text{corr}}$ needed for different $2\theta_{\text{obs}}$ was plotted. For the same diffractometer conditions, a diffraction pattern of an alloy specimen was recorded, the diffraction line positions were determined and the correction to 2θ was applied using the plot of $\Delta 2\theta_{\text{corr}}$ vs. $2\theta_{\text{obs}}$ for standard Si sample. Corrected values of 2θ were used for indexing the diffraction pattern [241,242].

The XRD technique was also used for the determination of easy axis of magnetization. XRD patterns were recorded from the flat surface of a magnetically aligned resin bonded sample (i.e. from

TABLE IV.1: Operating Conditions for Tracing XRD Patterns using Seifert Iso-Debyeflex 2002D Diffractometer

Radiation	:	Cr unfiltered
Tube Voltage	:	40 kV
Tube Current	:	30 mA
Receiving slit width	:	0.2 mm
X-ray slit width	:	2 or 3 mm
Scanning speed	:	1.2°/min (or 0.6°/min in some cases)
Chart speed	:	15 mm/min (or 12 mm/min in some cases)
Time constant	:	3 sec or 10 sec.
Intensity range	:	200 counts/sec (or 10 K counts/min. in some cases)
Angular range of scan	:	$35^{\circ} \leq 2\theta \leq 155^{\circ}$
Monochromator	:	Graphite in the diffracted beam between the receiving slit and counter

the surface perpendicular to the magnetic alignment direction) and a randomly oriented sample. The diffraction pattern of the two samples were compared and from the changes in intensity of some diffraction lines the direction of easy magnetization was arrived at.

4.2.3 Thermomagnetic Analysis

Magnetic transition of ferromagnetic phases in a multi-phase alloy can be used for phase identification when X-ray diffraction method fails due to insufficient resolution of diffraction lines. Two different methods of thermomagnetic analysis (TMA), based on variation of magnetic moment or permeability with temperature, were used in this investigation.

A vibrating sample magnetometer (VSM) [PAR, Model 150A] fitted with a high temperature (600°C maximum) oven assembly was used to measure magnetic moment as a function of temperature. From the magnetic moment versus temperature graph the Curie temperature T_c of a phase was determined. Approximately 0.2 g of solid alloy sample was loaded in the boron nitride sample holder of the heater assembly. The heating system for the sample was evacuated to the required vacuum level of about 1 millitorr. The saddle point of the sample was adjusted in the residual field of electromagnet (~ 40 Oe). A temperature recorder-cum-controller (INDOTHERM-401) was used for the measurement of sample temperature. The furnace assembly was heated at a rate of $\sim 5^{\circ}\text{C}/\text{min}$ with the help of a IC regulated 0-30 V dc power supply (Networks, Model : NPS 30/50). The variation of magnetic moment with temperature was noted down at close intervals (2 to 10°C) of temperature during the heating cycle. Near the magnetic transition zone the magnetic moment data was taken at 1 or 2°C interval. The data points were plotted on a graph paper with magnetic moment as ordinate and sample temperature as abscissa. The ferromagnetic to paramagnetic transition for the sample is indicated by a sharp drop in magnetic moment in the TMA plot. The temperature at which maximum slope is produced in the magnetic moment versus temperature plot has been chosen as the Curie temperature of material. Fig.IV.1 shows the magnetic moment versus temperature plot for a standard Ni sample. The Curie temperature of standard Ni sample (360°C) was found to be quite close to the value reported in literature (358°C). The Curie temperatures of phases in the unknown samples were determined in a similar way.

The above mentioned method, found suitable only for phases having magnetic transition temperature below 600°C , was used for few alloys only. Most of the thermomagnetic analysis work was carried out using a high temperature (upto 1100°C) magnetic permeability testing apparatus fabricated locally. The details of this apparatus are available in published literature [243]. The apparatus (schematic diagram given in Fig.IV.2) essentially consists of a vacuum furnace and a chamber in which the sample can

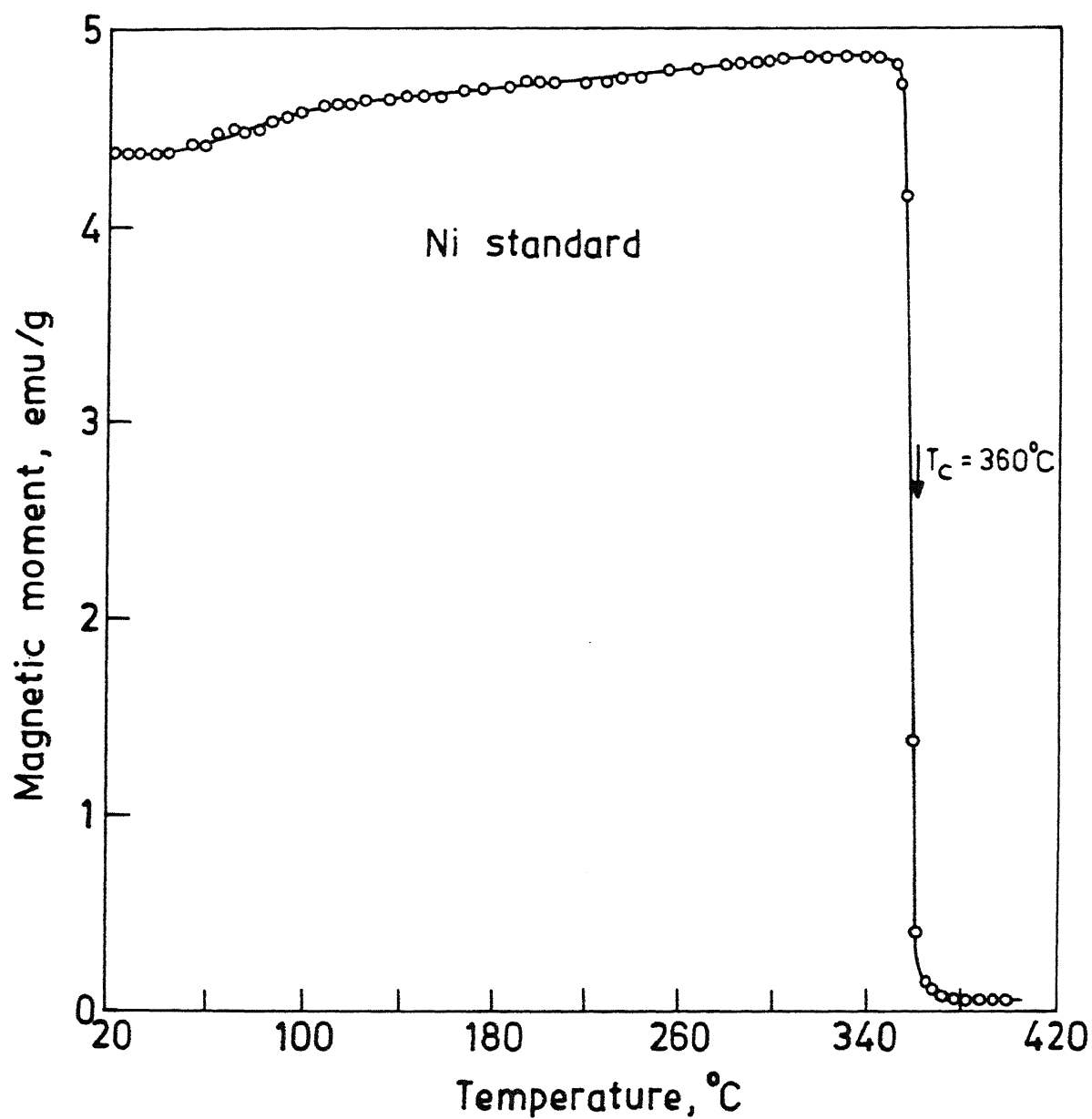


Fig. IV.1 Magnetic moment vs. temperature curve for Ni using a vibrating sample magnetometer in the residual field (about 40 Oe) of an electromagnet

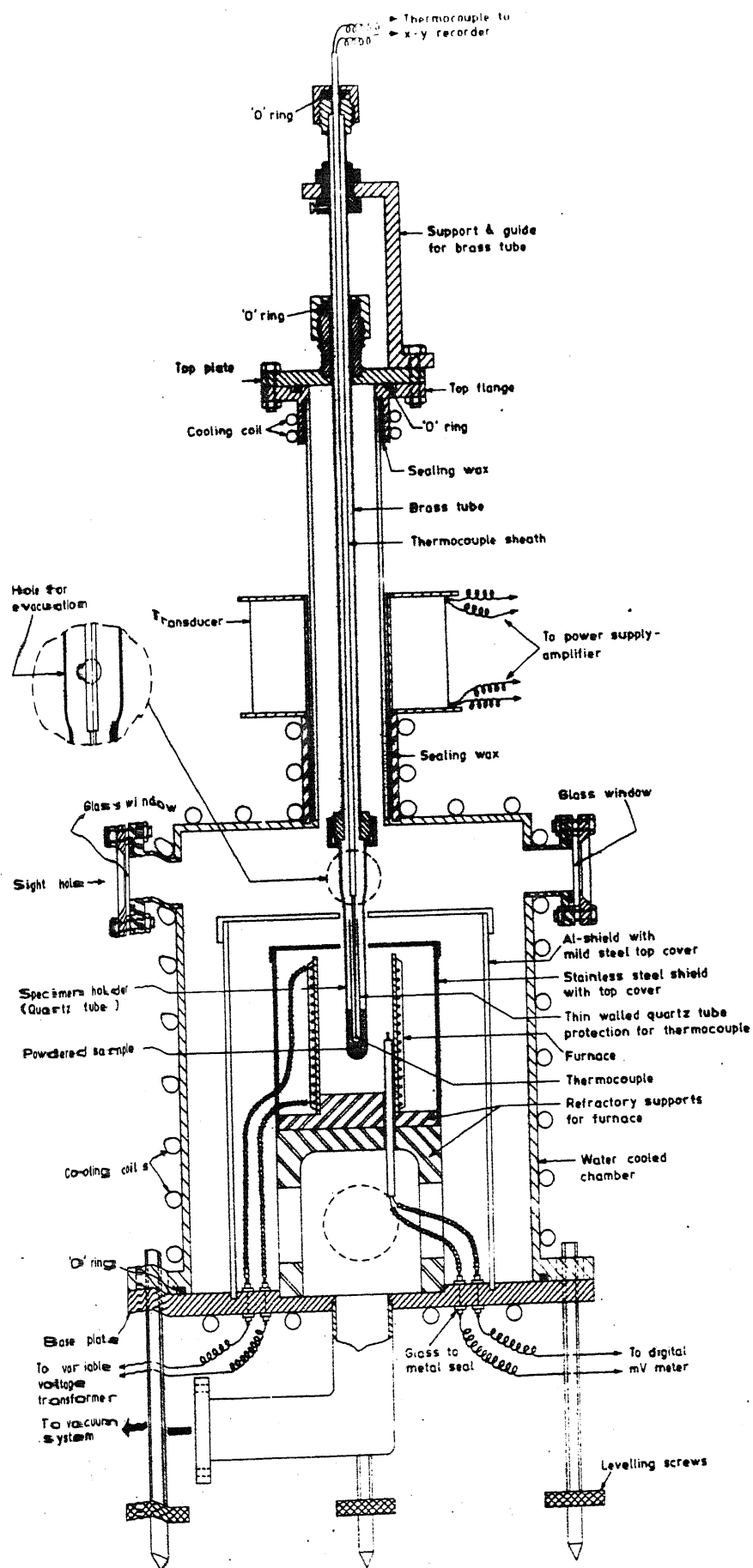


Fig. IV.2 Magnetic permeability testing apparatus used for thermomagnetic analysis

be cooled relatively slowly in a differential transformer coil (Fig.IV.3(a)) which is used as a transducer to detect para- to ferro- magnetic transition through a change in the permeability of the magnetic phase. The detection system consists of an assembly of transducer, amplifier, signal processor and an X-Y recorder as shown in Fig.IV.3(b). To detect magnetic transition of a given specimen the furnace chamber was first evacuated to better than 1 millitorr and the furnace was heated up slowly to the required temperature. During this period the specimen was kept far away from the furnace. On achieving appropriate furnace temperature, the specimen holder was lowered to put the specimen tube in the hot zone of the furnace. The specimen took only 6 to 7 minutes to heat up to the furnace temperature. On reaching a stable specimen temperature, the specimen tube was quickly withdrawn into the transducer coil section and allowed to cool. The specimen temperature and the output of the detection system were recorded on a X-Y recorder [Hewlett Packard, Model 7034A]. Unlike the magnetic moment versus temperature plot obtained using a VSM, the permeability versus temperature plot is a cooling curve. In the paramagnetic state the permeability versus temperature trace is parallel to the temperature axis. As the temperature crosses the Curie point, magnetic permeability of the material rises very rapidly. The point at which permeability begins to rise in the permeability versus temperature plot indicates the Curie temperature of a material. Estimation of Curie temperature using permeability testing apparatus was not as precise as using VSM due to the relatively rapid cooling rate, the difficulty of exactly locating the point at which permeability begins to rise, and the possibility of having short range magnetic order before the long range magnetic order sets in the material. In order to know the characteristic features of the permeability versus temperature trace, pure Ni and Fe sample were used as standard and the TMA plots for these are given in Fig.IV.4. When pure Ni is used as a standard (Fig.IV.4) the temperature at which the permeability begins to rise matched well with the standard value of T_c for Ni, i.e. 358°C . But when pure Fe was used it gave higher value of T_c ($\sim 845^\circ\text{C}$) than that reported in the literature ($\sim 770^\circ\text{C}$) [135].

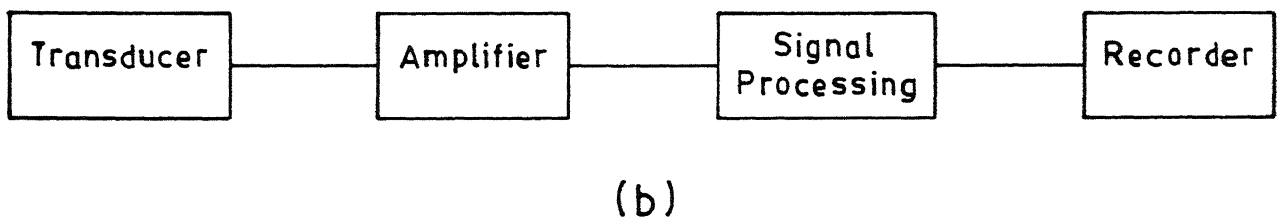
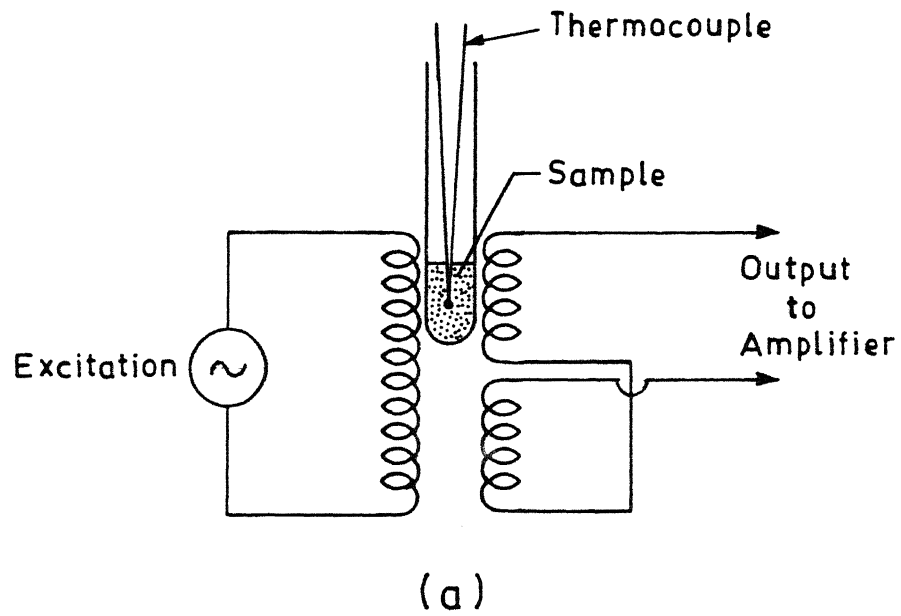


Fig.IV.3 (a) Transducer (schematic) and (b) detection system (block diagram) used in the permeability testing apparatus

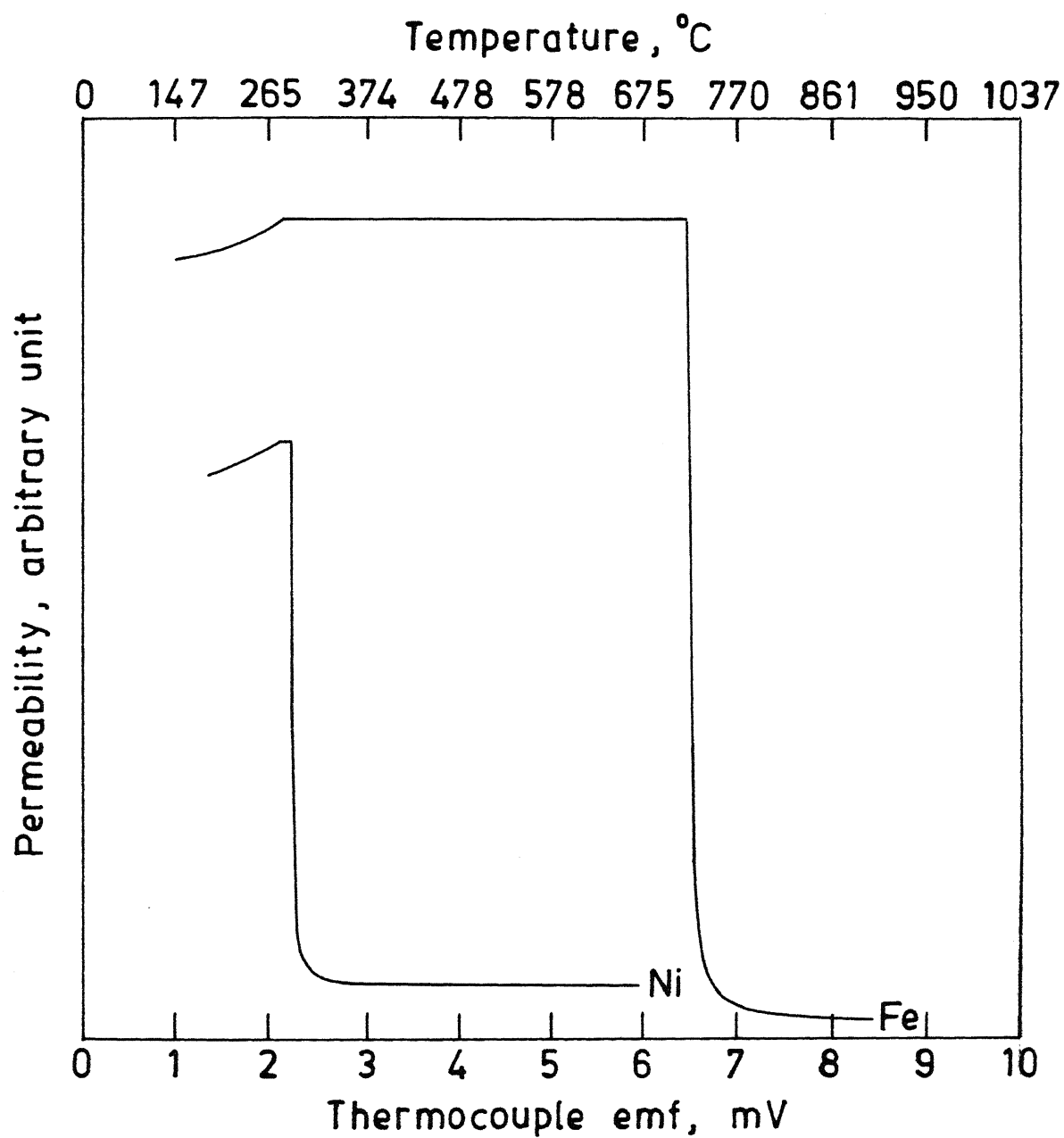


Fig.IV.4 Permeability vs. temperature traces for Ni and Fe samples

Even though T_c could not be determined accurately by this method, it was possible to detect the phases present upto 1100 °C if the phases had different T_c values. In multi-phase alloys the presence of ferromagnetic phases could be inferred by the appearance of a change in slope in the permeability vs. temperature curve.

4.2.4 Differential Scanning Calorimetry (DSC)

DSC was performed to know the transformation temperatures and to locate the approximate phase boundaries in the binary RE-Fe system. A Stanton Redcroft DSC 1500 with a maximum operating temperature of 1500 °C was used in this study. Since the samples are reactive, quartz sample holders were used. The sample was heated at a rate of 10 °C/min. Protective argon atmosphere was maintained in the chamber containing the sample to avoid oxidation. The temperature corresponding to the starting point of the peak in the DSC plot was taken as the transformation temperature. Due to the high reactivity of rare-earth alloys, no attempt was made to take DSC traces above 1000 °C.

4.2.5 SEM-EDS Microanalysis

Scanning electron microscopy studies were carried out on JEOL (JSM-840A) microscope fitted with an energy dispersive KEVEX X-ray microanalyser. SEM was operated in secondary electron (SE) mode under the following conditions :accelerating voltage 20 kV, tilt angle 10°-15°, working distance 39 mm. Samples used for metallographic observation were carefully removed with chisel and hammer from their plastic mounts and the polished slightly over etched alloy piece was mounted on a graphite stud with graphite paint (for good conductivity). Each phase was analyzed for four rare-earths (La, Ce, Nd and Pr) and four transition elements (Co, Fe, Cu and Zr). Boron could not be analyzed because of the limitation of the detection system i.e. the X-rays generated by this element are absorbed by the beryllium window separating the viewing chamber from the detection system.

4.3 Magnet Fabrication and Characterization

4.3.1 Aging Studies on Bulk Alloys

The objective of these studies on RE-Co-Fe-Cu-Zr and RE-Fe-B alloy systems was two fold :

- i) to select suitable alloy composition for the fabrication of resin bonded and sintered magnets and
- ii) to find out the response of alloys in these systems to low temperature aging treatment.

The 1100°C isothermal section of RE-Co-Fe-Cu-Zr system show different set of intermediate phases [244] as compared to the RE-Co and RE-Co-Fe systems [128,131]. To understand how magnetic characteristics of alloys of different chemical composition respond to low temperatures aging treatment, alloys of several compositions were studied. Devi [245] carried out low temperature (675°C) aging studies on 1100°C annealed sample of different alloys in RE-Co-Fe-Cu-Zr system and found that compared to all other alloy composition an alloy of composition $\text{RE}(\text{Co}_{0.76}\text{Fe}_{0.13}\text{Cu}_{0.09}\text{Zr}_{0.02})_6$ show superior response to magnetic hardening. Compared to 675°C, a very pronounced magnetic hardening behavior was observed at 620°C. In the present investigation, different batch of this alloy composition, i.e. $\text{RE}(\text{Co}_{0.76}\text{Fe}_{0.13}\text{Cu}_{0.09}\text{Zr}_{0.022})_6$, were annealed at 620°C upto about 200 hours and reproducibility of earlier results was checked. Prior to aging treatment, the samples were sealed in evacuated fused silica tube. As in the previous investigation, the magnetic measurement performed on the aged sample include saturation magnetization ($4\pi M_s$) and intrinsic coercivity H_c (vide section 4.3.3.2 for measurement technique).

In Nd-Fe-B system, several investigations focused on the selection of suitable chemical composition for magnet fabrication (section 2.3.2.1). An alloy of composition $\text{Nd}_{15}\text{Fe}_{77}\text{B}_8$ has been reported to yield very good magnetic properties. Since phase diagram of the RE-Fe-B system is very similar to the Nd-Fe-B

system [246], analogous composition (i.e. $\text{RE}_{15}\text{Fe}_{77}\text{B}_8$) was chosen in this investigation and response of this alloy to low temperature aging was studied. 1000°C annealed alloy of composition $\text{RE}_{15}\text{Fe}_{77}\text{B}_8$ was sealed under vacuum in fused silica tubes and tested for low temperature magnetic hardening at 600°C and 650°C upto 40 hours and at 700, 800 and 900°C for two hour.

4.3.2 Magnet Fabrication

The alloys which gave best properties in the bulk state were used for the fabrication of magnets. The alloys were first powdered and then used for making either resin bonded or sintered magnet samples. The response of several processing variables on the magnetic and other properties such as microstructure, density etc., was studied.

4.3.2.1 Communion

The communion of alloys (5-10g) involved preparation of coarse alloy powder using steel and agate mortars, and milling of coarse powder in a rod mill. Non-magnetic stainless steel rods (13.5 cm long and 0.31 cm dia; 100 to 200 in number) and stainless steel milling jar (8.1 cm dia and 13.6 cm deep) with a lid were thoroughly cleaned with 4/0 emery paper and acetone and dried. The lid of the jar had provision for evacuation and filling up with inert gas. The coarse alloy powder ($< 150 \mu\text{m}$) and the rods were put in the jar and it was filled with sufficient amount ($\sim 250 \text{ ml}$) of moisture free toluene (toluene treated with sodium) to dip the powder and rods completely during milling. The jar was closed with the lid having an 'O' ring seal and a valve. The jar was twice evacuated and flushed with high purity argon gas (IDLAR-II) and finally filled with argon. The jar was kept horizontally on rolls and milled at a speed of 80 r.p.m.. 100-200 mg of milled powder was taken out from the jar into small glass boats at predetermined intervals of time. The powders were dried in a vacuum desiccator.

Particle size estimation for the coarse powders was carried

out using conventional sieve analysis technique. Average particle size and size distribution of milled powder was measured by optical microscope fitted with an image analyzer (Bausch and Lomb, Model: Omnicon Alpha 500). Milled powder was used for preparing sample for optical microscopy. Magnetic particles have a tendency to attract each other and form agglomerate of particles. This leads to the over estimation of particle size. In order to minimize this problem and prepare reasonably well dispersed powder sample, few drops of the suspension of particles in acetone were dropped from a height of around one meter on a glass slide. Two to three slides were made for each sample. The number of particles falling in different size range were counted and used for plotting the size distribution and estimating average particle size.

Scanning electron microscope (JEOL-840A) was used for the morphological characterization of milled powder as well as oriented particles in the resin bonded pellets. SEM data on particle size were also used for cross checking the image analyzer result.

4.3.2.2 Resin Bonded Magnet

The alloy composition for the fabrication of resin bonded magnet samples was fixed on the basis of magnetic measurements on the bulk alloys. The powders which were used for making resin bonded magnets fall in three categories: (a) powders prepared from the homogenized alloys, (b) powders prepared from homogenized and aged alloys, and (c) powders prepared from homogenized alloys and subsequently aged. Aging of bulk alloys or powders was tried only in the case of RE-Co-Fe-Cu-Zr system because Nd-Fe-B alloys did not respond to the aging treatment. The powders were vacuum sealed before aging treatment. Interconnected fused silica ampules, containing an alloy powder and Ti chips, were evacuated (5-10 millitorr pressure) and sealed under vacuum. Ti chips were used as a getter to remove traces of oxygen and prevent oxidation of the powder. To remove traces of oxygen from the ampule containing alloy powder, ampule containing Ti chips was selectively heated to

red heat for 8-10 minutes. Lastly, the ampule containing Ti chips was separated leaving behind sealed alloy powder ready for aging treatment.

Some of the variables in magnet making (e.g. resin to hardener ratio, resin to metal powder ratio etc.) were fixed on the basis of experience of previous workers [238,239]. The details of adopted procedure are described below :

Epoxy resin and hardener in a definite proportion (resin : ^{en}harder = 3:1) were weighed separately on a glass slide and mixed thoroughly for making a homogeneous mixture. This resin to hardener ratio was important to ensure quick setting of the mixture. 7 parts of alloy powder and three parts of homogeneous mixture of resin and hardener (by weight) were mixed thoroughly, using a piece of stiff metal wire, to form a uniform paste. This homogeneous paste was filled into a small glass ampule of ~3 mm dia and ~7.5 mm long. About 5 min. time was required to fill the ampule and transfer it into the magnetic field. The closed end of the ampule was kept in contact with one of the pole pieces of the electromagnet and the field of the electromagnet was slowly increased to 9 kG. After 1 hour in the magnetic field (sufficient for preliminary setting), the ampule was removed from the magnet and allowed to cure for 24 hours in a desiccator. The cured ampules were used for different magnetic measurements, e.g. coercivity, magnetization, anisotropy field etc., and X-ray studies for the determination of easy axis of magnetization. Before the magnetic measurements were made on the cured samples, their weights were determined. This was required to compute the weight of the sample in any ampule. This sample weight was required to express the saturation magnetization and remanence in emu/g.

4.3.2.3 Sintered Magnets

Sintered magnet fabrication work was undertaken in both the systems. Fabrication of sintered magnets from alloy powders

involved four major steps : (i) compaction under magnetic field to prepare green pellets; (ii) sintering of green pellets; (iii) magnetization of sintered pellets; and (iv) post sintering heat treatment. Sintering of green pellets often results in composition shift. In order to tackle the problem of composition shift, large number of alloys, in the vicinity of alloy composition used in preliminary studies, were prepared and used for magnet fabrication. The experimental conditions in steps (i) and (iii) were kept constant and the effect of time and temperature parameters during sintering and post sintering heat treatments were studied in more details. The exact details of experimental procedures used in different stages are given below :

(i) Green Pellet Preparation

A locally fabricated non-magnetic stainless steel die barrel and hardened tool steel plungers were used for making green pellets. The powders were field-pressed in a pulse magnetic field of ~ 10 kG and under a total load of about 2 tons. A manually operated 20 ton hydraulic press and a magnet charger [RFL, Model: 747-6], fitted with a charging fixture of 8.8 cm dia and 7.0 cm height, was used for making pellets. The applied field direction and the pressing direction were parallel. Green pellets of 3 to 5 mm diameter and 4 to 7 mm in height were made. The weight and size (height and diameter) of pellets were measured for determining the green density.

(ii) Sintering

Interconnected fused silica ampules, containing green pellets and Ti chips, were evacuated and the pellets were vacuum degassed at 200°C for 10 minutes. Vacuum degassing was required to prevent breaking of green pellets during sintering. Ti chips were used as a getter to remove traces of oxygen from evacuated (10-20 millitorr pressure) and sealed ampules. The procedure used for removing oxygen from the ampule containing green pellets was the same as used during sealing of alloy powders for aging treatment (section 4.3.2.2). After removing oxygen by selectively heating the Ti chips, the ampule containing Ti chips was separated leaving

behind sealed green pellets ready for sintering. The vacuum sealed pellets were slowly inserted into the hot zone of the furnace kept at the pre-determined sintering temperature ($900-1100^{\circ}\text{C}$). It normally took around 10 min. for the pellets to reach the sintering temperature. Sintering time was counted from the time when the pellets reached the sintering temperature. At the end of sintering period (15-120 min.), the ampule with sintered pellets was taken out slowly and cooled in air. The sintered pellets were characterized for sintered density, microstructure and phases present.

(iii) Magnetizing

The sintered pellets were magnetized, prior to post sintering heat treatment, in the magnet charger fitted with a charging fixture of 2.75 cm inner dia and 7.0 cm depth. The charger can give a pulse field of 60 kG with a pulse width of 100-200 milliseconds. The field applied was in the direction parallel to the pressing direction used during green pellet making stage. Magnetic measurements were performed on the sintered and magnetized pellets.

(iv) Post Sintering Heat Treatment

Post sintering heat treatment studies were carried out on sintered pellets prepared in RE-Co-Fe-Cu-Zr system. The magnetized sintered pellets were subjected to aging treatment at different temperature ($580-620^{\circ}\text{C}$) for different lengths of time. Heat treated pellets were characterized in terms of magnetic properties, e.g. $4\pi M_s$, $4\pi M_r$, H_c etc.

4.3.3 Physical and Magnetic Characterization Techniques

4.3.3.1 Physical Characterization Techniques

This included determination of phase constituents, microstructure and sintered density. X-ray diffraction and metallography techniques were used respectively to study the phase constituents and microstructures of sintered pellets. The details

of these techniques are described before (section 4.2.1 and 4.2.2). Sintered density was measured by Archimedes liquid displacement method with toluene as liquid. The details are given below :

The weight of sintered pellet in air (W_1) was determined. Pores in the sample were impregnated with toluene by placing a beaker containing toluene and sample in a vacuum desiccator and creating vacuum using a rotary pump. When the air bubbles coming out from the sintered pellet subsided the pump was stopped. The excess toluene from the surface of the pellet was wiped off, and its weight in air (W_2) was taken. Next the weight of the pellet (W_3) was taken by suspending the pellet from the beam of the chemical balance with the help of a thread and immersing it in toluene. From the above data and the density of toluene ($\rho = 0.863 \text{ g/cm}^3$), sintered density of the pellet was calculated using the following formula

$$\text{sintered density} = \frac{W_1}{(W_2 - W_3) \rho}$$

4.3.3.2 Magnetic Characterization Using VSM

A vibrating sample Magnetometer (VSM) [PAR, Model 150A] was used for measurement of $4\pi M_s$, M_r/M_s and H_c . The principle of the VSM is described below in brief.

A small sample of the material whose magnetic moment is to be measured is placed in a sample holder. The sample holder is mounted on the end of a rod and suspended and vibrated in the field of an electromagnet. The sample is vibrated in a uniform magnetic field at a fixed frequency and amplitude. The induced field in the sample induces an emf in a pair of stationary pick up coils. The induced emf is amplified by a suitable electronic circuit and converted into magnetic moment in electromagnetic units (emu).

The system is calibrated using a 0.088 g sample of high purity Ni for which the saturation moment is 55 emu/g. The sample is mounted between the electromagnet pole pieces in a perspex sample holder and is aligned and adjusted thereby locating it symmetrically with respect to the detection coils. The main benefit of making this adjustment is that the different samples were adjusted to the same position relative to the pick up coils, thus minimizing the effect of geometry on the results of measurement. The sample is first taken to saturation by increasing the field strength (H) of the electromagnet to its maximum value (10-11 kOe) where the magnetometer panel meter reads the value of saturation magnetization in emu. The field strength is then decreased to a residual field of 20-30 Oe and the value of remanence is noted from the panel meter. Field direction is then reversed and the field strength is increased slowly till the panel meter reads negative moment. The magnetic (field) corresponding to zero moment corresponds to intrinsic coercivity (H_c). In some cases first and second quadrant hysteresis loop data points were also collected and plotted.

In order to determine magnetocrystalline anisotropy field (H_A) magnetization curves are recorded for resin bonded pellets both along and perpendicular to the magnetic alignment direction used during magnet fabrication. The anisotropy field is then defined as the field where the two magnetization curves meet.

CHAPTER V

PHASE EQUILIBRIA IN THE RE-CO-Fe-CU-Zr SYSTEM AT 1100°C

The result and discussion on 1100°C isothermal section of RE-Co-Fe-Cu-Zr system, where RE represents the total rare-earth content of Mischmetal (MM), are presented in this section. The investigated composition region of phase equilibria, which lies around RE/T ratio of $\sim 1:7$, is bounded by 5 to 19 at.pct. RE, 55 to 75 at.pct. Co, 7 to 20 at.pct. Fe, and Cu and Zr contents fixed at 8 and 2 at.pct., respectively.

5.1 Results

Chemical composition of the alloys used in the investigation of RE-Co-Fe-Cu-Zr phase equilibria are given in Table V.1. The different alloys of this system are designated by the symbol C_i , where subscript i indicates the alloy number. The alloys in Table V.1 are arranged in order of their decreasing iron content. Phase analysis of alloys and characterization of phases have been carried out using metallography, microhardness measurements, XRD, X-ray microanalysis (in SEM) and TMA. The details of alloy preparation and characterization techniques are given in Chapter IV.

Some of the data reported in this chapter are reproduced / compiled from a previous study [245] conducted by this investigator. The inclusion of the previous data was found essential for the sake of continuity and presenting the phase diagram which is completed as a part of this study.

In this system, the presence of two new intermediate phases (designated as U and N), a fcc solid solution phase γ and a Zr-rich Δ phase are established. Summary of phase analysis is presented in Table V.1, and details are given in the following subsections.

Table V.1: Chemical Composition and Phase Analysis of the RE-Co-Fe-Cu-Zr Alloys [All the alloys contained fixed amounts of Cu (8 at.pct.) and Zr (2 at.pct.)]

Alloy [#] Number (i)	Intended Alloy Composition (at.pct.)			Phase Analysis		
				Metallography	X-ray	TMA
	Fe	RE	Co	Number of Phases [*]		
7	18.8	15.2	56.0	2	U, L'	U, L'
8	18.8	13.0	58.2	2	U, L'	U
9	18.8	11.0	60.2	3	U, γ , L'	U, γ
20	18.8	9.0	62.2	3	U, γ	U, γ
1	16.0	17.2	56.8	2	U, L'	U, L'
2	16.0	16.2	57.8	2	U, L'	U, L'
3	16.0	15.2	58.8	2	U, L'	U, L'
13	16.0	14.0	60.0	2	U, L'	U, L'
4	16.0	12.0	62.0	3	U, γ	U, γ
5	16.0	11.0	63.0	3	U, γ	U, γ
6	16.0	10.0	64.0	3	U, γ	U, γ
21	16.0	7.5	66.5	3	U, γ	U, γ
22	16.0	5.2	68.8	3	γ , U	γ , U
31	13.0	20.0	57.0	2	N, L'	-
29	13.0	18.2	58.8	2	N, L'	-
28	13.0	17.2	59.8	2	N, L'	-
10	13.0	16.2	60.8	2	N, L'	-
11	13.0	14.2	62.8	2	N, L'	N, U, L'
12	13.0	12.0	65.0	3	U, γ	U, γ
14	13.0	10.0	67.0	3	U, γ	U, γ
32	12.0	18.5	59.5	2	N, L'	-
33	12.0	16.8	61.2	2	N, L'	-
30	12.0	16.0	62.0	2	N, L'	-
15	10.8	16.0	63.2	2	N, L'	-
16	10.8	14.2	65.0	2	N	N, U
17	10.8	12.2	67.0	3	N, U, γ	N, U, γ
18	10.8	10.2	69.0	2	U, γ	U, γ
19	10.8	8.2	71.0	2	U, γ	U, γ
23	10.8	5.2	74.0	2	U, γ	U, γ
24	7.8	12.2	70.0	3	N, U, γ	N, U, γ
25	7.8	10.2	72.0	3	N, U, γ	N, U, γ
26	7.8	8.2	74.0	2	U, γ	U, γ

Alloy designation C_i

* The number does not include the Δ phase detected in most of the alloys (vide text, section 5.2.2)

5.1.1 Metallography and Microhardness Measurements

5.1.1.1 Metallographic Analysis

Since most of the alloys of this system are brittle, especially the high RE containing alloys, extreme care was taken to avoid chipping off of the brittle phases during rough polishing. As the high RE side alloys are very reactive, they needed dilute etchant (< 2 pct. HNO_3 (v/v)). The strength of the etchant had to be increased upto 6 pct. HNO_3 with increase in Co content of the investigated alloys. All the alloys were found to consist of two or more phases. The results of metallographic analysis for different alloys are summarized in Table V.1. The microstructure of some representative alloys are shown in Fig.V.1(a)-(f).

The microstructure of alloy C_7 [Fig.V.1(a)] showed small white islands (Δ phase) and black regions (with some internal structure) surrounding the matrix grains of the U phase. The black regions are the liquid phase* (L) existing in equilibrium with the U phase at 1100°C . The microstructure of alloy C_{15} [Fig.V.1(b)] showed the liquid and Δ phases in the matrix of N phase. In all the high RE containing alloys the Δ phase particles were present but their amount did not vary in any systematic manner with the alloy composition. It was, however, noted that Δ phase particles were relatively more when the alloy contained more liquid phase at 1100°C . The morphology of liquid phase was found to change with decrease in RE content. It became more globular with decrease in RE content as shown in the microstructure of alloy C_{20} [Fig.V.1(c)]. The microstructure in Fig.V.1(c) besides showing the U and liquid phases also showed islands of γ phase. The alloys C_8 , C_1 , C_2 , C_3 and C_{13} showed essentially two phases (L+U) together with small amount of particles of the Δ phase, whereas the alloys

* In this and subsequent chapters, L signifies the liquid phase at the reaction temperature and L' refers to solid phase/s resulting from the non-equilibrium solidification of liquid during water quenching of alloys from the high temperature.

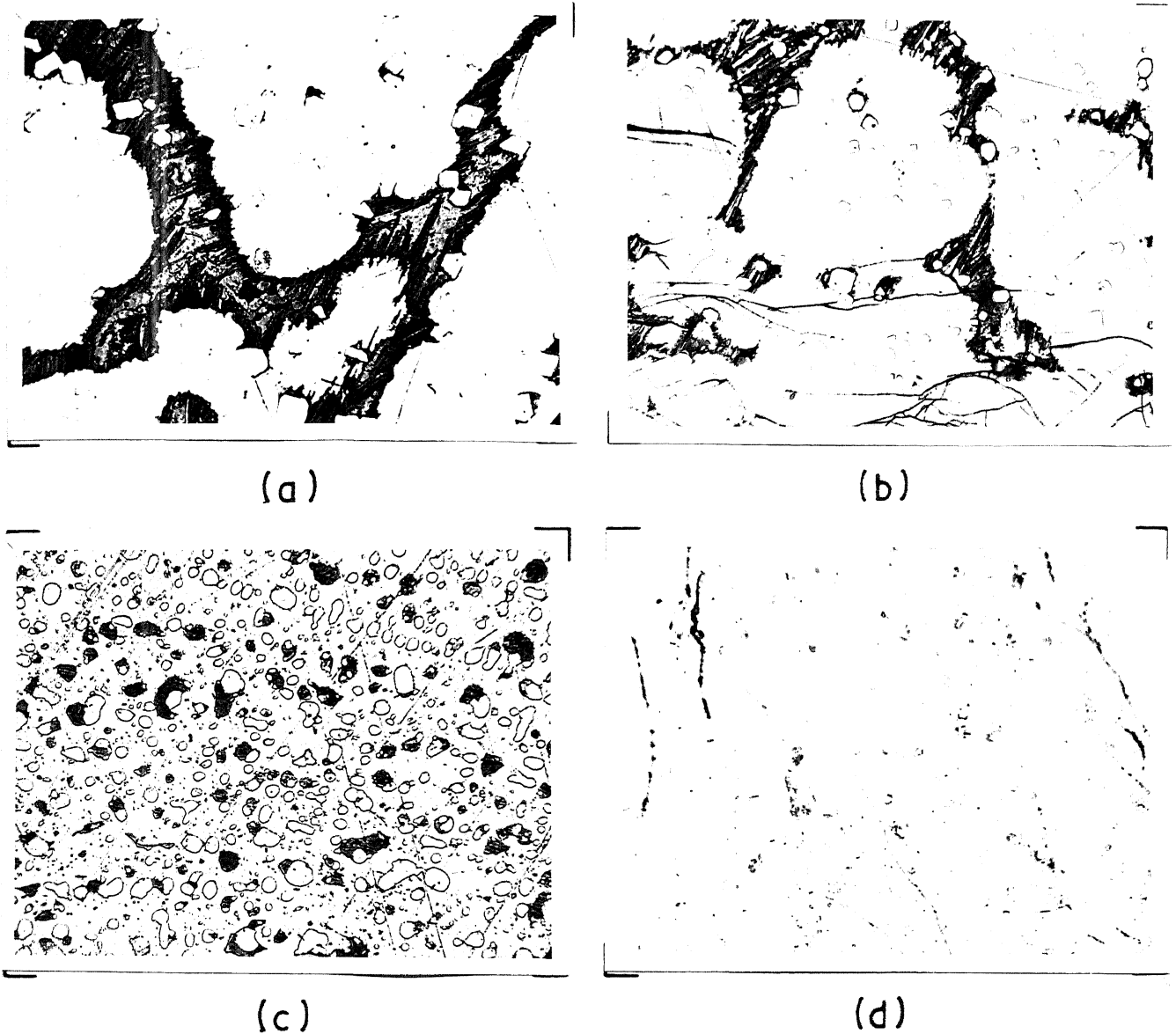
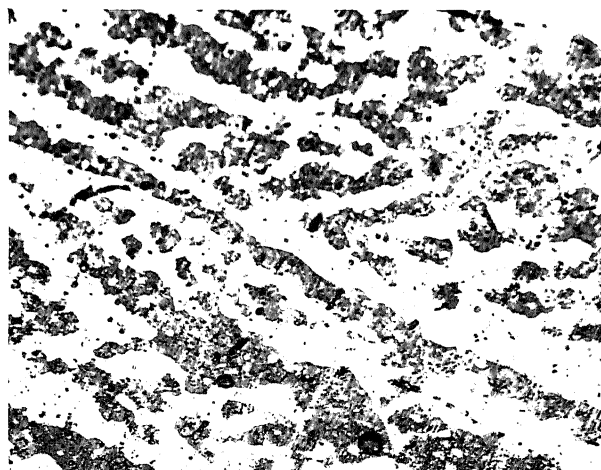


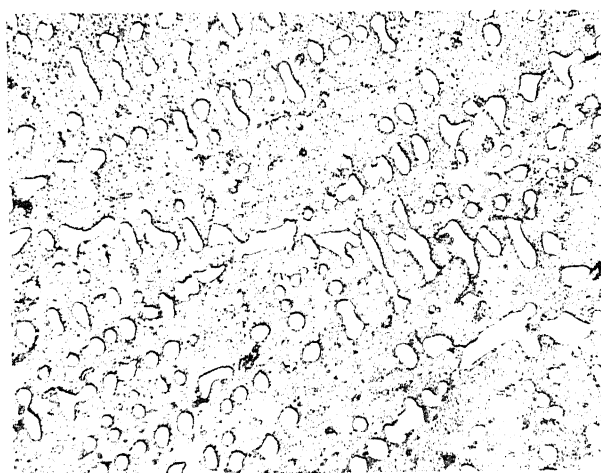
Fig.V.1 Representative optical micrographs of RE-Co-Fe- Cu-Zr alloys (homogenized at 1100 °C) (Magnification 400x):

- (a) alloy C₇ (3 phases), matrix - N, white islands - Δ, and grey or dark grey regions - L
- (b) alloy C₁₅ (3 phases), matrix - U, white islands - Δ, and grey or dark grey regions - L
- (c) alloy C₂₀ (3 phases), matrix - U, white regions - γ, and grey regions - L
- (d) alloy C₁₆ (2 phases), matrix - N, second phase - Δ/U/γ

(Contd.)



(e)



(f)

Fig.V.1 (Contd. ...) [Mag. 400x]

(e) alloy C_{17} (3 phases), white phase - U, light grey - N, small white crystals - Δ/γ

(f) alloy C_{19} (2 phases), matrix - U, white phase - γ

C₉, C₂₀, C₄, C₅, C₆, C₂₁ and C₂₂ showed L+U+ γ phase. The alloys containing 12 to 13 at.pct. Fe and greater than 14 at.pct. RE (C₃₁, C₂₉, C₂₈, C₁₀, C₁₁, C₃₂, C₃₃ and C₃₀) showed the presence of only the N and liquid phases together with small particles of Δ phase. The alloys with Fe content of 13 at.pct. and \leq 12 at.pct. RE (C₁₂ and C₁₄), however, showed the presence of three phases U+L+ γ . In these cases, the presence of the Δ phase particles could not be ascertained because the γ phase islands and the Δ phase particles were quite small and had similar appearance under the bright field illumination of the microscope. Out of the alloys containing 10.75 at.pct. Fe and $<$ 15 at.pct. RE, the alloys C₁₆ showed two phases N and white crystals of another phase which could not be identified (by XRD) [Fig.V.1(d)], the alloy C₁₇ showed the presence of three phases U+N+ γ [Fig.V.1(e)], whereas the alloy C₁₈, C₁₉ and C₂₃ showed only two phases U+ γ [Fig.V.1(f)]. At 7.75 at.pct. Fe level the alloys C₂₄ and C₂₅ were also found to have three phases U+N+ γ , whereas, the alloy C₂₆ contained two phases U+ γ .

5.1.1.2 Microhardness Measurements

Microhardness measurement was carried out on different phases in several alloys, in order to differentiate between them. Since the measured values of microhardness varied somewhat from alloy to alloy, an average value of microhardness for a given phase was computed using all the microhardness data. No clear difference in the microhardness between the matrix phases U or N in the various alloys could be established. The microhardness value for the U as well as the N phases was found to be in the range of 1200 to 1350 VPN [this wide variation in the microhardness may be due to the small load ($49.03 \text{ mN} \cong 5\text{g}$) applied for indentation to restrict the indentation within the small single phase region of interest]. The Δ and γ phases showed distinctly different microhardness values of approximately 2100 and 320 VPN, respectively.

5.1.2 X-Ray Diffraction Analysis

The analysis of X-ray diffraction pattern in this system was found to be quite complex due to the following reasons : (i) the

intermediate phases present in this system have their major diffraction lines lying in the same 2θ angular range; (ii) the presence of solidified liquid (L') in all the high RE containing alloys; and (iii) stress induced transformation (fcc \rightarrow bcc) in high cobalt containing alloys [244,245]. In order to avoid stress induced transformation in high Co containing alloys, the alloy powders were annealed at 1100°C and water quenched prior to recording the XRD patterns.

Three X-ray identifiable phases exist in the investigated alloys : (a) the U phase, (b) the N phase, and (c) the γ phase. Fig.V.2 shows the diffraction pattern of the U phase [alloy C_{18} ; Fig.V.2(a)], the N phase [alloy C_{16} ; Fig.V.2(c)] and of an alloy C_{17} [Fig.V.2(b)] in which both the U and N phases are present. The similarity between the major diffraction lines of the U and N phases is evident in the diffraction patterns presented. The difference between the strongest and other peaks of these two phases could be more clearly seen only at a slow scanning speed (1.2° or 0.6° $2\theta/\text{min}$) and with monochromatic CrK_{α} radiation. A comparison of the diffraction patterns of the U and N phases with the standard patterns of phases reported in the RE-Co-Fe system [131,132] indicated that the intermediate phases existing in the RE-Co-Fe-Cu-Zr system are different from those of the RE-Co-Fe system.

The XRD patterns of the U and N phases were indexed on the basis of XRD data for the alloy C_{18} [in which the U phase is the major phase; Fig.V.2(a)] and C_{16} [in which the N phase is the major phase; Fig.V.2(c)], respectively. For precise estimation of lattice parameter a standard calibration procedure, as described in Section 4.2.2, was used. The indexed XRD patterns of the U and N phase are given in Fig.V.2. The lattice parameter values and the calculated and observed d-spacings are compiled in Tables V.2 and V.3. The U phase could be indexed on the basis of a hexagonal unit cell of lattice parameters $a = 8.452 \text{ \AA}$ and $c = 24.57 \text{ \AA}$ and c/a ratio of 2.91 (Table V.2). In the case of the N phase the lattice parameters of the hexagonal unit cell were $a = 4.940 \text{ \AA}$ and $c = 20.420 \text{ \AA}$ with c/a ratio of 4.13 (Table V.3). The calculated and

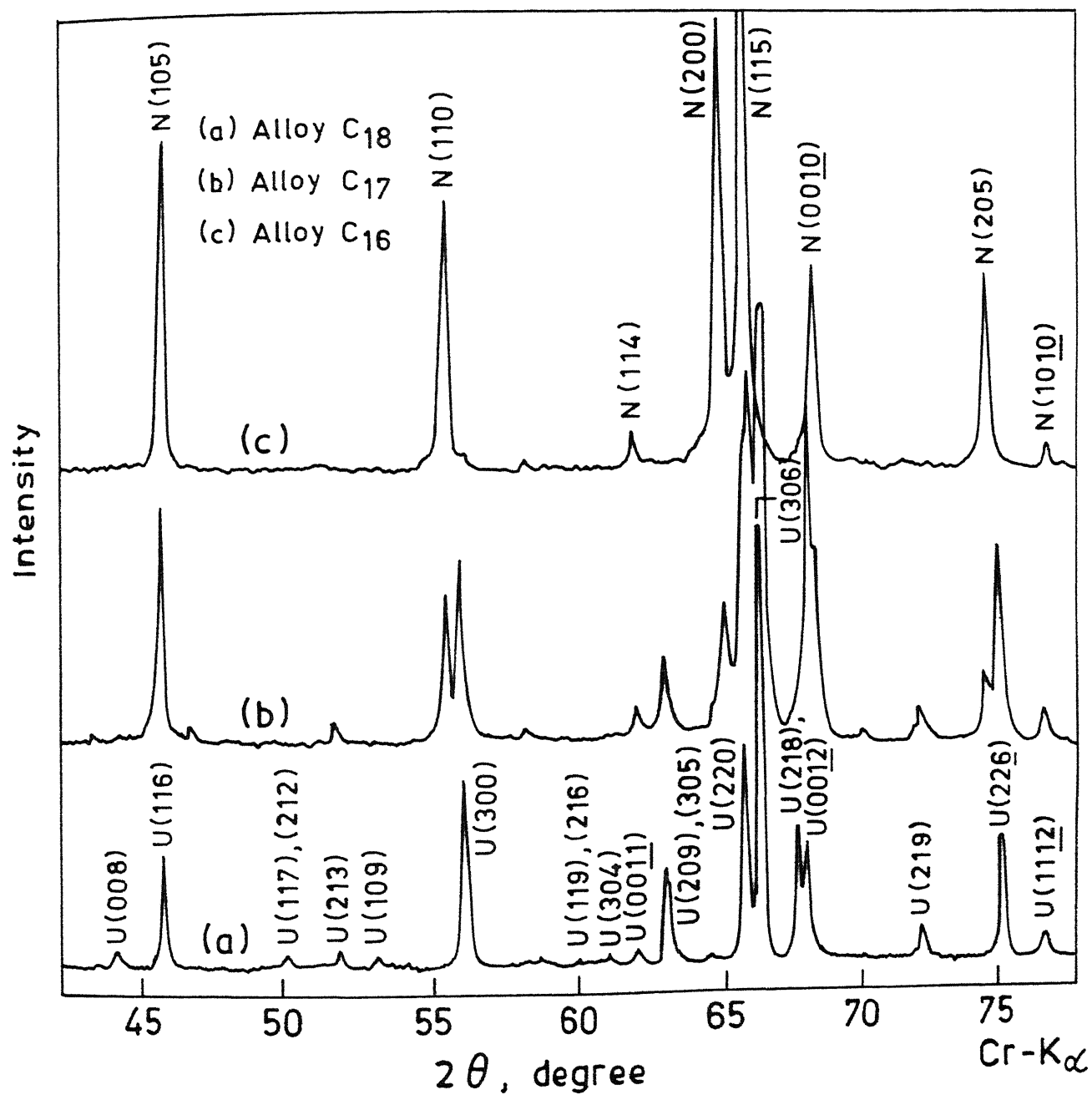


Fig.V.2 XRD patterns of typical RE-Co-Fe-Cu-Zr alloys (homogenized at 1100 °C) containing U, N or mixture of U and N phases : (a) alloy C₁₈ (U phase); (b) alloy C₁₇ (U+N phases); and (c) alloy C₁₆ (N phase)

Table V.2: Powder X-ray Diffraction Data of the U Phase in Alloy C₁₈

Unit cell		a		c		c/a	
Hexagonal		8.452 Å		24.571 Å		2.91	
Relative Intensity*	d _{obs} Å	hkl	d _{calc} Å	Relative Intensity	d _{obs} Å	hkl	d _{calc} Å
vw	3.340	203	3.341	w	1.571	408	1.572
vvw	3.056	008	3.071	w ⁺	1.488	416	1.488
m ⁻	2.942	116	2.941	w ⁺	1.472	328	1.473
vvw	2.702	117	2.700	vw	1.430	329	1.430
		212	2.699	vw	1.410	2115	1.409
vw	2.621	213	2.621			2213	1.409
vvw	2.559	109	2.558			330	1.409
m	2.439	300	2.440	w ⁺	1.330	336	1.332
vvw	2.293	119	2.293	w	1.300	3016	1.300
		216	2.292			4111	1.299
vvw	2.256	304	2.267			1118	1.299
vw ⁻	2.219	0011	2.233	vvw	1.292	0019	1.293
m ⁻	2.189	209	2.188	vyw	1.290	509	1.290
		305	2.185	w ⁺	1.262	428	1.261
m	2.113	220	2.113	w ⁺	1.261	4112	1.259
vvs	2.096	306	2.096	w ⁺	1.235	429	1.234
m ⁻	2.051	218	2.055	w ⁺	1.221	3310	1.222
		0012	2.048			→ 4015	1.221
w ⁻	1.944	219	1.943	w ⁺	1.220	4113	1.220
m ⁻	1.878	226	1.878			→ 600	1.220
vw ⁺	1.845	1112	1.843	m ⁻	1.194	2217	1.193
w ⁺	1.787	2012	1.787				
		403	1.786				
vvw	1.645	323	1.645				

* Relative intensity scale : vvs- very very strong, m- medium, w- weak, vw- very weak, vwv- very very weak

→ Reflections used for the lattice parameters calculation

Table V.3: Powder X-ray Diffraction Data of the N Phase in Alloy C₁₆

Unit cell	a	c	c/a
Hexagonal	4.940 Å	20.419 Å	4.13
Relative Intensity [#]	d _{obs.} Å	hkl	d _{cal.} Å
s	2.956	105	2.954
s	2.469	110	2.470
w	2.225	114	2.223
vs	2.139	200	2.139
vvs	2.112	115	2.114
s	2.042	0,0,10	2.042
		203	2.041
s	1.895	205	1.895
vw	1.843	1,0,10	1.843
vw	1.629	210	1.617
w ₋	1.574	1,1,10	1.574
m ₋	1.503	215	1.503
m	1.477	→ 2,0,10	1.477
w	1.426	→ 300	1.426
vvw	1.413	302	1.412
vvw	1.365	218	1.366
m	1.347	305	1.346
vw ₋	1.298	1,0,15	1.297
m ₋	1.234	220	1.235
		221	1.233
s	1.192	1,1,15	1.192

Relative intensity scale : vvs - very very strong, vs - very strong, s - strong, m - medium, w - weak, vw - very weak, vvw - very very weak

→ Reflections used for the lattice parameters calculation

observed d-spacings match well for both the U and N phases.

The ductile phase γ could be separated from the brittle phases after sieving the alloy powder through -250 mesh sieve. The ductile particles from alloy C₁₄, after annealing at 1100°C for 10 minutes (for stress relieving), were used for the recording the diffraction pattern of the γ phase for indexing. The γ phase showed only three reflections in the angular range scanned using CrK $_{\alpha}$ radiation. The indexed diffraction pattern of the γ phase for the alloy C₁₄ is given in Table V.4. The lattice parameter of γ phase (for alloy C₁₄) was found to be $a = 3.558 \text{ \AA}$.

Table V.4: Powder X-ray Diffraction Data of the γ Phase in Alloy C₁₄

Unit cell fcc	a 3.558 Å		
Relative Intensity [#]	d _{obs.} Å	hkl	d _{cal.} Å
vvs	2.055	111	2.054
m ₊	1.779	→ 200	1.779
m ⁺	1.259	220	1.258

Relative intensity scale : vvs - very very strong, m - medium
 → Reflection used for the lattice parameter calculation (since the (220) reflection is broad, (200) reflection is used for the lattice parameter calculation)

The alloys annealed at 1100°C were water quenched to room temperature in order to retain the equilibrium phases existing at that temperature. The solidification of liquid phase during quenching gave rise to non-equilibrium phases. With careful analysis of several diffraction patterns, it was found possible to identify a few lines arising out of these non-equilibrium phases as shown in Fig.V.3. The Δ phase (identified by metallography) could not be detected in XRD analysis because its amount in all the investigated alloys was very small.

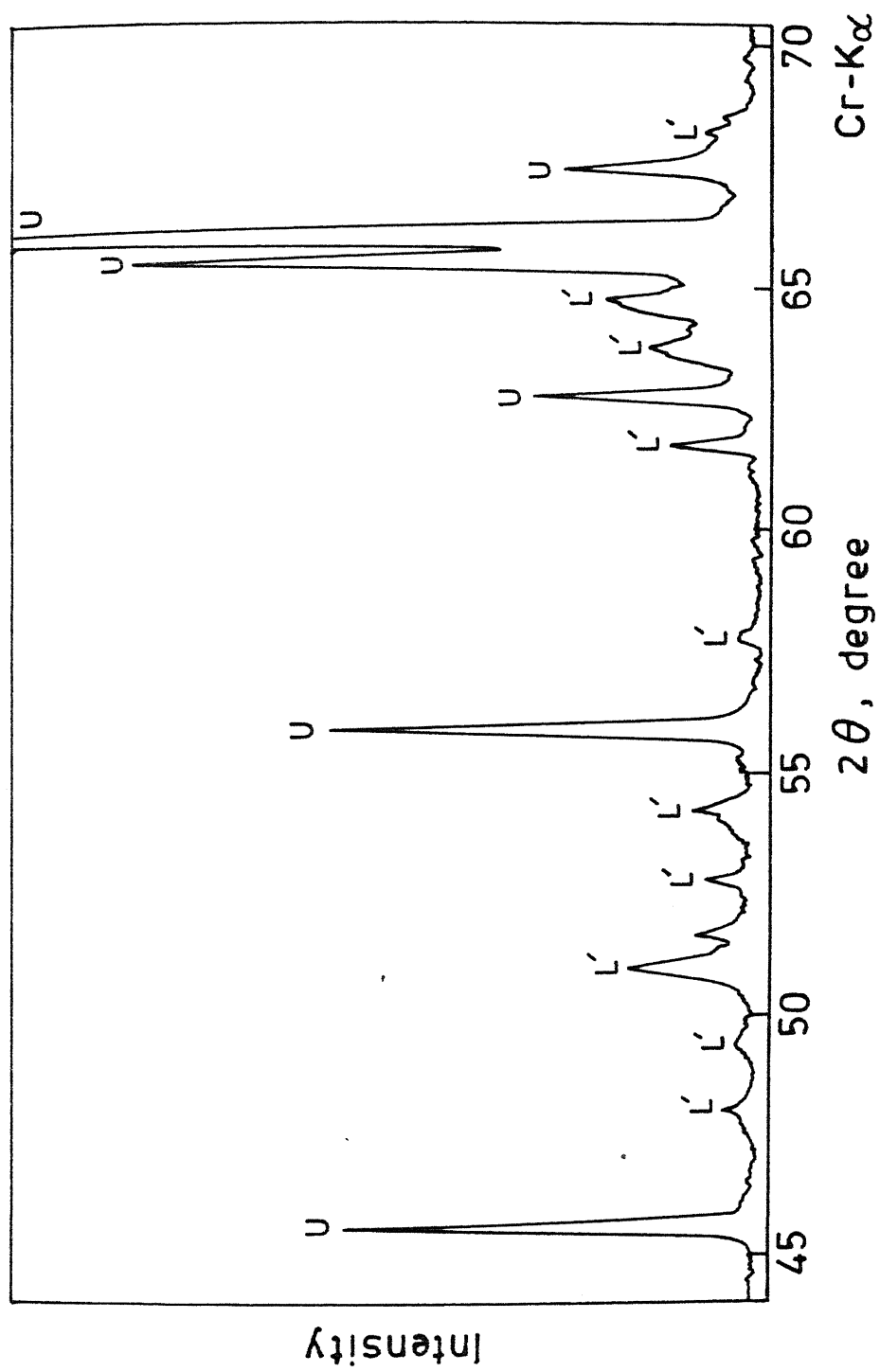


Fig.V.3 XRD pattern of an alloy (C₇) containing solidified liquid phase (L')

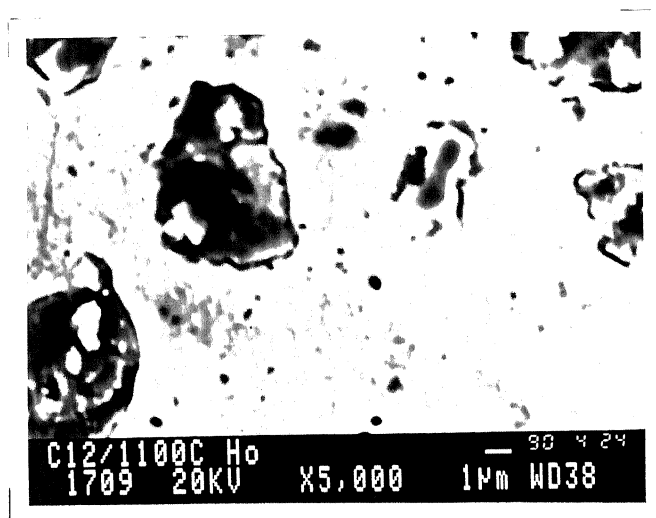
Identification of the phases present in different alloys was done by comparing diffraction patterns with the indexed pattern of each phase. The summary of phases identified by XRD in different alloys is presented in Table V.1. The XRD pattern of alloy C₁₆ showed the presence of only N phase. The tiny white particles of another phase observed in the microstructure of alloy C₁₆ [Fig.V.1(d)] could not be identified as it was present in a very small amount.

5.1.3 Scanning Electron Microscopy (SE-Mode) and X-Ray Microanalysis

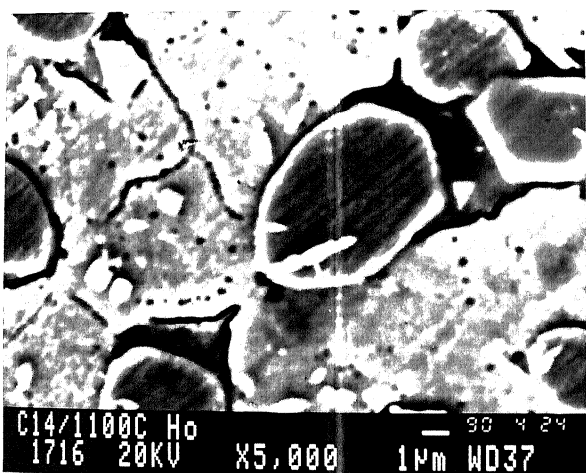
Qualitative X-ray microanalysis (SEM-EDS) studies on the RE-Co-Fe-Cu-Zr alloys were undertaken to characterize the different phases in terms of major and minor elements present, and rare-earth elements among various phases. The alloys chosen for SEM-EDS analysis are reasonably close to each other in their gross composition but having the different phases existing in the RE-Co-Fe-Cu-Zr system. The SEM micrographs shown in Fig.V.4(a)-(c) are for the alloy C₁₂, C₁₄ and C₁₆ used for the X-ray microanalysis studies.

X-ray microanalysis data for the U and N phases are given in Fig.V.5(a) and 5(b), respectively. The elemental distribution in the U and N phases are very similar. The only difference which appears in the SEM-EDS spectra of U and N phase is somewhat higher cobalt content of the U phase. The X-ray intensities due to the rare-earth elements from the two phases U and N also appear to be very similar. This suggests that no gross partitioning of the rare-earth elements take place between the two phases.

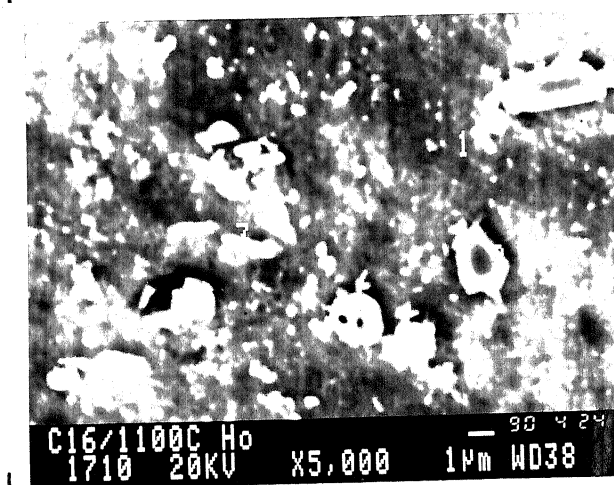
SEM-EDS spectra for the γ phase [alloy C₁₄; Fig.V.4(b)] show that this phase is rich in Co and Fe and contain some amount of Cu [Fig.V.6(a)]. The amounts of rare-earth elements and Zr in this phase are not sufficiently high for detection. The Δ phase [alloy C₁₆; Fig.V.4(a)-(c)] is found to contain reasonably high amounts of Zr, Co and Fe and only small amount of Cu [Fig.V.6(b)]. The



(a)



(b)



(c)

Fig.V.4 SEM (SE-mode) micrographs of RE-Co-Fe-Cu-Zr alloys used for the X-ray microanalysis of different phases

- (a) alloy C₁₂, matrix - U, tiny white particles - Δ, grey/black regions - L
- (b) alloy C₁₄, matrix - U, grey - γ, dark grey - L, white particles - Δ
- (c) alloy C₁₆, matrix - N, white phase - U/Δ/γ

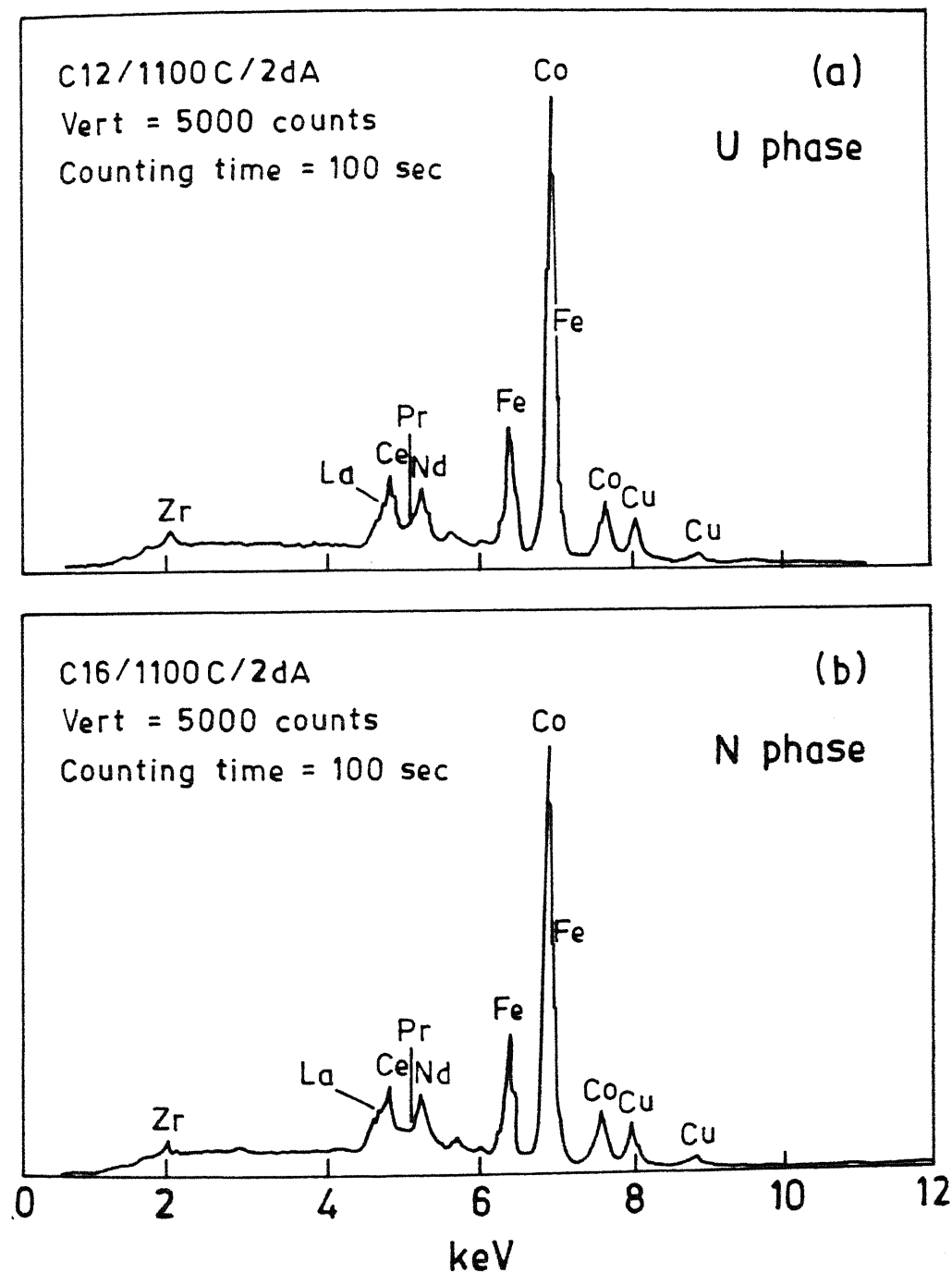


Fig.V.5 X-ray spectra (SEM-EDS) of (a) U phase, and (b) N phase grains

intensity ratio between Zr and (Fe,Co) present in Δ phase is about 1:3.

The SEM-EDS spectra from the liquid phase region of alloy C_{12} [Fig.V.4(a)] show that the liquid phase is rich in rare-earth elements and Cu and relatively (relative to other phases) smaller amounts of Co and Fe are present in it (Fig.V.7). Very small amount of Zr is also present in the liquid phase. In the liquid phase there does not seem to be any preferential segregation of any one of the rare-earth elements.

5.1.4 Thermomagnetic Analysis (TMA)

The TMA of the RE-Co-Fe-Cu-Zr alloys has been possible because the magnetic transformation of various phases were found to be reasonably different from each other [243-245]. TMA was done using a high temperature permeability testing apparatus (vide section 4.2.3). There were often overlap of two magnetic transitions in the permeability versus temperature curves due to the multi-phase nature of the alloys. Hence, great care was required in interpreting the results. TMA results of some of the investigated alloys are shown in Fig.V.8. Summary of phases identified by TMA is presented in Table V.1.

The results of TMA were analyzed in conjunction with the XRD and metallographic data. The TMA plots of the two alloys C_{13} and C_3 show the Curie temperature of U phase to be approximately 830°C . Compared to these alloys the TMA plot of alloy C_{15} shows that the magnetic transformation for the N phase is somewhat low, $T_c \sim 730^{\circ}\text{C}$. Using these characteristic features of the TMA plots of U and N phases the other TMA plots could be analyzed. For example, the broad peak in the TMA trace of alloy C_{16} clearly shows slope changes corresponding to the U and N phases. On this basis, using the TMA plot of alloy C_{11} it was concluded that this alloy has, besides the liquid and N phase, some small amount of U phase even though it could not be identified through metallography and XRD analysis. The presence of small amount of U phase in alloy C_{11} is also indicated by the temperature at which the initial rise

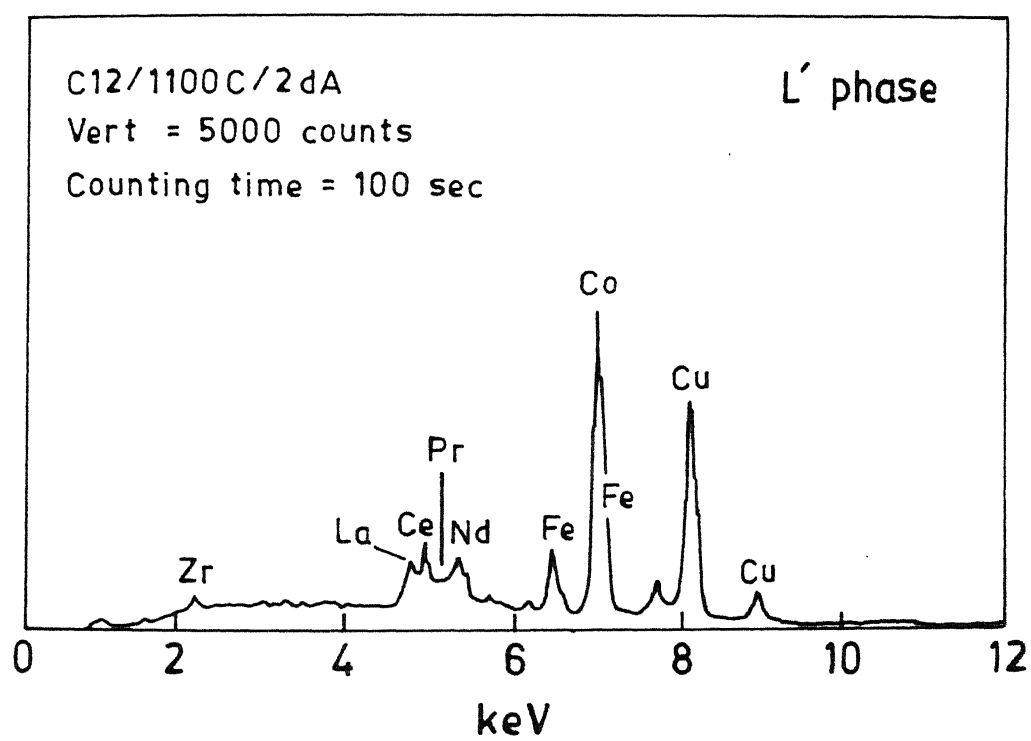


Fig.V.7 X-ray spectra (SEM-EDS) of solidified liquid (L') regions

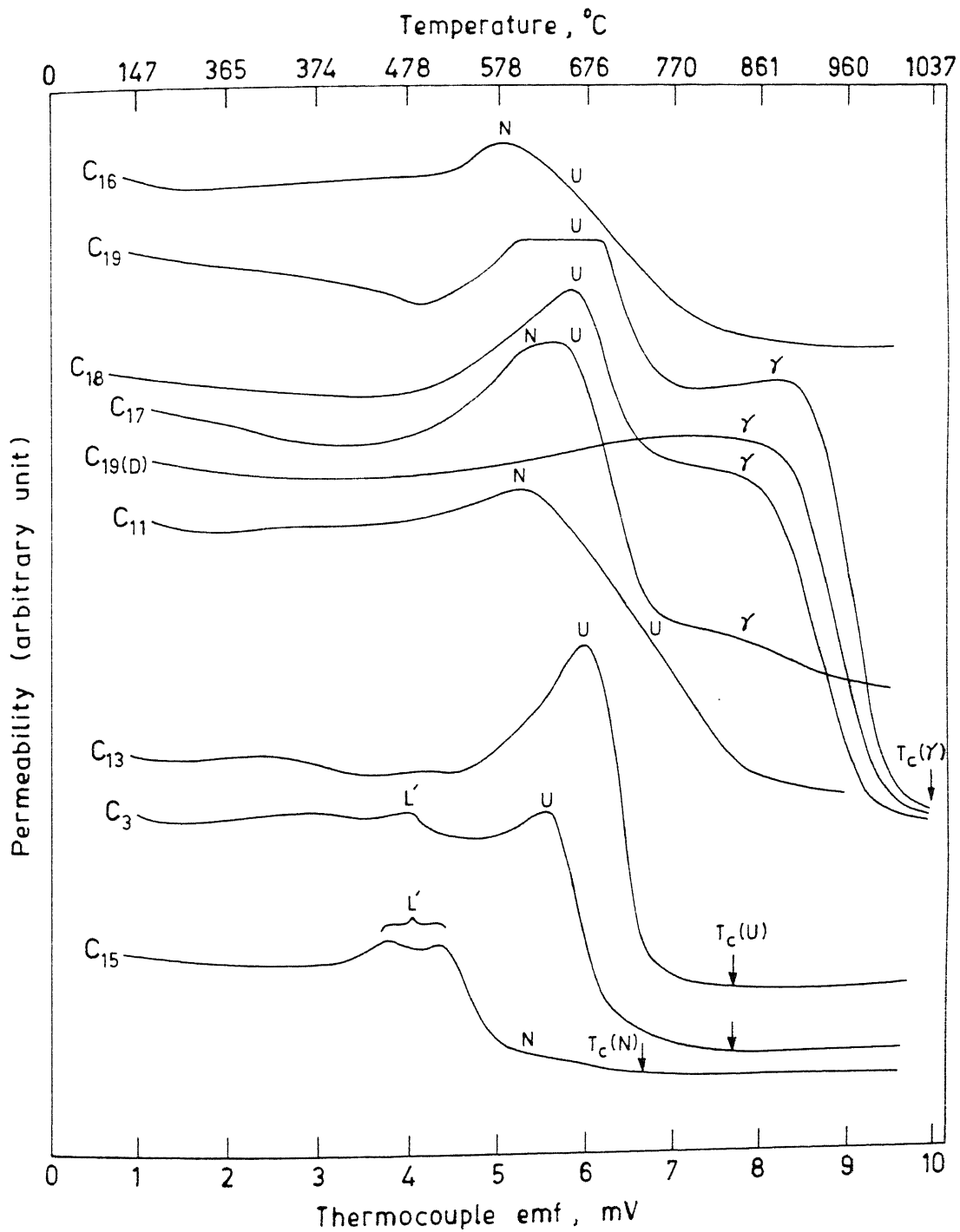


Fig.V.8 TMA plots of some typical RE-Co-Fe-Cu-Zr alloys obtained using high temperature permeability testing apparatus (C_{19(D)} is the ductile phase separated from the powders of alloy C₁₉) (compiled from Devi (1985) [245])

in permeability is observed; the temperature is quite close to the T_c of U phase. Magnetic transitions were observed corresponding to the solidified liquid and these are designated as L' in the TMA plots of alloy C_3 , C_{13} and C_{15} . The ductile γ phase in alloy C_{19} was separated from the brittle phase (U), after grinding a piece of alloy C_{19} and sieving, and the sample is labelled as $C_{19}(D)$. The TMA trace of this ductile phase is shown in Fig.V.8. Curie temperature of γ phase, as indicated by the TMA plot for $C_{19}(D)$, is about 1045°C . The alloy C_{19} shows two magnetic transitions, one due to the γ phase and the other due to the U phase. The amount of γ phase in the alloy C_{17} is very small [only very small particles can be seen in the micrograph of Fig.V.1(e)]. In the TMA trace of alloy C_{17} the sharpness of rise of permeability has decreased because the amount of γ phase has decreased (Fig.V.8). The presence of the second phase (U phase) in the alloy C_{17} gives rise to a second peak just after the magnetic transformation of the γ phase. Moreover, it may also be seen that the fall in the permeability of alloy C_{17} , after the permeability peak for U phase is reached, is not as sharp as in the case of alloy C_{13} containing U+L phases and C_{18} containing U+ γ +L phases. This is due to the presence of the N phase. The N phase peak becomes more clear in the TMA traces of alloy C_{16} and C_{11} containing N+U phases.

5.2 Discussion

The discussion which follows is subdivided into two parts. A detailed discussion on the phases observed is included in the first part. The second part focuses on the RE-Co-Fe-Cu-Zr phase equilibria at 1100°C with emphasis on the assumption made in the construction of the diagram and broad description of the phase diagram.

5.2.1 Phases Present in the System

Morita et. al.[133] and Chin et.al.[134] studied the phase equilibria in the Sm-Co-Fe-Cu-Zr system in the magnetically important region (Sm:T ~ 1:7) and observed the following phases : (a) 2:7, (b) 1:5, (c) 2:17, (d) cobalt solid solution, and (e)

liquid (Fig.II.16 and II.17). The 2:17 phase was the major phase present in all the alloys studied by these workers [133,134]. Addition of Zr (2 at.pct.) in the Sm-Co-7.0 at.pct.Cu-22 at.pct.Fe has been shown to increase the solubility of Sm in the 2:17 phase and stabilization of 2:7 phase on the higher Sm side [133]. The 2:17 phase was also found to be stable in the RE-Co-Fe-Cu system [245] and this led Devi et.al.[244] to conclude that the occurrence of the new phases U and N was the result of Zr addition in the RE-Co-Fe-Cu system. Besides the intermediate phases U and N the other phases observed in the RE-Co-Fe-Cu-Zr system at 1100 °C are the fcc solid solution phase γ , hard phase Δ and liquid. No attempt was made to characterize the phases resulting from the non-equilibrium solidification of liquid during quenching (Fig.V.3).

5.2.1.1 The U and N Phases

Several rare-earth bearing intermediate phases, with RE_2Co_7 , $\text{RE}_5\text{Co}_{19}$, RECo_5 and $\text{RE}_2\text{Co}_{17}$ compositions, have been reported in the RE-Co system [101,126-128]. In addition to these phases, Mittal et.al.[131] and Laha et.al.[132] reported several new phases (designated as S, T, A, L etc. by these workers; Table II.3) in the RE-Co-Fe system. The diffraction pattern of the S phase was found to be quite similar to the 2:17 phase, and the diffraction pattern of A, T and L phases also resembled the 2:17 phase or the S phase [101,131,132]. Gupta [101] contended that since the S, A and T phases showed diffraction patterns similar to the 2:17 phase, they are possibly structurally related. In order to know whether the new phases U and N have any similarity with the earlier reported phases, their lattice parameters and Curie temperatures are compared with those of the phases observed in the RE-T systems (Table V.5 and V.6). The following important points which will be helpful in further discussion may be noted for the earlier reported phases (Table V.5): (i) all the phases with stoichiometry between 2:7 to 1:5 have their 'a' parameter around 5 Å and only the 'c' parameter varies with change in the composition; (ii) the 2:17 phase or the new phases reported by earlier workers [131,132] have a common 'a' parameter around 8.45

Table V.5: Comparison of Lattice Parameters of the U and N Phase with the Phases Observed in RE-Co, RE-Co-Fe and RE-Co-Fe-Cu Systems

Phase	Lattice Parameters, Å							
	I* [128]		II [131,132]		III [244]		IV	
	a	c	a	c	a	c	a	c
2:7 (R)	5.02	36.71	5.05	24.52	-	-	-	-
2:7 (H)	4.99	24.69	-	-	-	-	-	-
5:19	5.01	48.65	-	-	-	-	-	-
1:5	4.98	4.00	4.99	4.01	-	-	-	-
2:17	8.47	12.14	8.41	12.36	8.43	12.29	-	-
S	-	-	8.48	37.29	-	-	-	-
T	-	-	8.49	22.80	-	-	-	-
A	-	-	8.50	22.66	-	-	-	-
L	-	-	8.46	41.94	-	-	-	-
U	-	-	-	-	-	-	8.45	24.57
N	-	-	-	-	-	-	4.94	20.42

* System : I - RE-Co, II - RE-Co-Fe, III - RE-Co-Fe-Cu,
IV - RE-Co-Fe-Cu-Zr

Table V.6: Comparison of Curie Temperatures of the U and N Phase with the Phases Observed in RE-Co, RE-Co-Fe and RE-Co-Fe-Cu Systems

Phase	Curie Temperature, °C			
	I *	II ^θ	III	IV
1:3	<20 [128]	-	-	-
2:7	67 [128] # ≤ 179 [132] 70 [248] #		-	-
5:19	270 [128] # ~ 280 [132] 230 [248] #		-	-
1:5	541 [128] # ~ 550 [132] 500 [248] #		-	-
N	-	-	-	730 [244]
U	-	-	-	830 [244]
S	-	~ 830 [132]	-	-
2:17	>735 [128] # ~ 900 [132] 830 [248] #		815 [244]	-

* System : I - RE-Co, II - RE-Co-Fe, III - RE-Co-Fe-Cu,
IV - RE-Co-Fe-Cu-Zr.

^θ Values for ternary compound containing about 15 at.pct. Fe.

Theoretically calculated values.

Å and only the 'c' parameters differ, e.g. the 'c' parameter of the S phase is approximately three times that of the 2:17 phase and for A and T phases it is slightly less than two times; and (iii) there is a gradual decrease in the Curie temperature as the stoichiometry of the intermediate phase shifts from 2:17 to 2:7.

In the earlier exploratory investigation of the isothermal section of the RE-Co-Fe-Cu-Zr system [245], the U phase was tentatively indexed on the basis of a hexagonal unit cell of dimension $a = 5.907 \text{ Å}$, $c = 33.324 \text{ Å}$ and c/a ratio 5.64 (details of indexing are given in Appendix-B). These parameters were reported by Devi et.al.[244] in a subsequent publication. Both 'a' (5.907 Å) and 'c' (33.324 Å) parameters do not have any resemblance with any of the phases of the RE-Co and RE-Co-Fe systems with stoichiometry between 2:7 and 2:17 or the ternary phases related with 2:17 phase, namely, S, T, A and L (Table V.5). This implied that either the U phase has no structural similarity with the other phases reported in the RE-Co and RE-Co-Fe systems or a proper representation of the unit cell parameters was not found. Hence, an attempt was made to re-index the U phase diffraction pattern. In this attempt the 'a' parameter was chosen close to the 2:17 phase and 'c' parameter was varied to get a best fit of the data. It resulted in an appropriate indexing of the U phase with a hexagonal unit cell of dimension $a = 8.452 \text{ Å}$ and $c = 24.57 \text{ Å}$ and c/a ratio of 2.91 (Table V.2). The 'a' parameter of the re-indexed U phase is approximately the same as that of the 2:17 phase observed in the Re-Co-Fe-Cu or any other RE-transition metal system [Table V.5]; and the 'c' parameter 24.57 Å ($\approx 12.289 \times 2$) is twice that of the 2:17 phase ($c = 12.289 \text{ Å}$). X-ray diffraction pattern of the U phase closely resembled the diffraction pattern of 2:17 phase observed in RE-Co-Fe-Cu system [245] except that for the U phase several extra lines of medium and low intensity were also present. This indicates that the U phase is possibly structurally similar to the 2:17 phase and belongs to the same class of S, T, A and L phases with $a \approx a_{2:17}$ and $c \approx n \times c_{2:17}$. The Curie temperature data in Table V 6 indicate that the Curie temperature of the U phase is somewhat lower than the typical T_c values observed for the 2:17 and the S phases.

The XRD pattern of randomly oriented samples of the N phase alloy C_{11} and C_{16} shows several reflections. Devi et.al.[244] indexed the N phase diffraction pattern on the basis of a hexagonal unit cell of dimension $a = 4.997 \text{ \AA}$, $c = 20.698 \text{ \AA}$ and c/a ratio of 4.14 (details of indexing given in Appendix-B). In a subsequent XRD study of a magnetically aligned resin bonded pellet of the N phase alloy C_{11} (the alignment direction is perpendicular to the surface on which X-ray were falling), it was found that the intensity of one reflection increased many folds and the intensity of all other reflections decreased considerably. Similar effects are produced when X-ray pattern is taken from a magnetically aligned uniaxially anisotropic material [249]. The high intensity X-ray diffraction peaks from magnetically aligned uniaxially anisotropic material are of the type (001). For the N phase diffraction pattern, the diffraction line showing an increase in intensity due to magnetic alignment of powder sample, however, has a (hkl) type of indices other than the (001) type [244]. This indicated that the tentative indexing of the N phase diffraction pattern done by Devi et.al.[244] is possibly not correct. Hence a further attempt was made to re-index the N phase diffraction pattern assuming the strong peak of the aligned sample as (001) type. It was found that the fit between the observed and calculated d-values improved provided somewhat lower values of 'a' and 'c' parameters ($a = 4.940 \text{ \AA}$, $c = 20.42 \text{ \AA}$, $c/a = 4.13$) were used for indexing (Table V.3). The XRD pattern of the magnetically aligned powder could also be interpreted easily on the basis of re-indexed N phase pattern (section 8.1.1.2). The 'a' parameter (4.940 \AA) of the N phase is similar to the phases with stoichiometry 2:7, 5:19 and 1:5, however its 'c' parameter (20.42 \AA) is quite distinct indicating that this is a new phase. Interestingly, the 'c' parameter of the N phase is five times that of the $\text{RE}(\text{Co,Fe})_5$ phase. The XRD pattern of the N phase resembles that of the 1:5 phase, except for the presence of a few extra weak lines, indicating that this phase may be structurally related to the 1:5 phase.

5.2.1.2 The γ Phase

The fcc γ phase observed in this investigation is a solid solution of Co predominantly with Fe and contain small amount of Cu; the solubility of RE in γ phase is very small [Fig.V.6(a)]. The γ phase undergoes stress induced transformation to α [244,245]. The lattice parameter of γ phase ($a = 3.558 \text{ \AA}$) in alloy C₁₄ of the RE-Co-Fe-Cu-Zr system (Table V.4) and that of an alloy of approximately the same composition in the RE-Co-Fe-Cu system ($a = 3.559 \text{ \AA}$) are quite similar. This indicates that Zr addition does not affect the lattice parameter significantly and Zr possibly has very low solubility in the γ phase. Low solubility of Zr is also indicated by the SEM-EDS results, and is not surprising because the atomic volume of Zr ($23.27 \text{ \AA}^3/\text{atom}$ [242]) is quite large as compared to cobalt ($11.13 \text{ \AA}^3/\text{atom}$). The Curie temperature of the γ phase, i.e. 1045°C (alloy C₁₉; Fig.V.8), is less than that of pure cobalt which has a T_c of 1115°C . Decrease in the T_c of Co with dissolution of Fe is well established [135].

5.2.1.3 The Δ Phase

The Δ phase is very hard (microhardness $\sim 2100 \text{ VPN}$) compared with all other phases, namely the U and N ($1200\text{--}1350 \text{ VPN}$) and the γ (330 VPN) phases. In terms of chemical composition, the Δ phase is rich in Co, Fe and Zr and contain small amount of Cu and RE [Fig.V.6(b)]. Since the amount of the Δ phase is very small in all the investigated alloys, no structural information could be derived for this phase by X-ray diffraction technique. SEM-EDS analysis of the Δ phase indicates that the Zr:(Co,Fe) ratio in this phase is about 1:3 [Fig.V.6(b)]. In the Zr-Fe binary system a fcc ZrFe_3 phase exists [135]. A ZrT_x ($x \sim 2\text{--}3$) type fcc Laves phase also exists in the Zr-Co system [115,116]. $\text{Zr}(\text{CoFeCu})_3$ is a stable phase and Ivanova et.al.[181] have reported its existence in the overaged $\text{Sm}(\text{Co,Fe,Cu,Zr})_2$ ($Z \sim 7$) magnets. Thus, it may be possible that the Δ phase is a $\text{Zr}(\text{CoFe})_3$ type phase having some solid solubility for Cu.

5.2.2 Phase Equilibria

5.2.2.1 Assumptions

In order to construct the phase equilibria for the multi-component RE-Co-Fe-Cu-Zr system, several assumptions and simplifications had to be made to represent phase equilibria and construct the phase diagram. These are discussed below.

The rare-earth elements Ce, Nd, Pr, La are soluble in each other to a large extent [101]. During phase equilibria studies on RE-Co and RE-Co-Fe systems [128,131], no gross partitioning of an individual rare-earth element was observed in any particular phase. SEM-EDS studies on phases present in the RE-Co-Fe-Cu-Zr system (section 5.1.3) also indicated that no individual rare-earth element segregates preferentially in the U, N or any other phase. Hence, total rare-earth content of the Mischmetal (RE) is treated as a single component.

Earlier investigators of the RE-Co-Fe phase equilibria [99,247] reported melting losses less than 1 pct. and observed a good match between the intended alloy composition and the composition of the arc-melted alloy determined by chemical analysis. Since the melting procedure employed in this study was the same as used by the previous workers, and through careful melting of the alloys the melting losses were made still smaller (< 0.5 wt.pct.), it has been assumed that the intended alloy compositions represent the actual composition of the alloys.

The Δ phase was present in all the alloys containing reasonably high RE contents. The amount of the Δ phase was however quite small in all the alloys. If this phase is an equilibrium phase, the amount of this phase should vary in a systematic manner with variation in alloy composition. This was not found to be the case in the alloys investigated. Hence, it was assumed that the Δ phase is possibly not an equilibrium phase, and it was not considered for the construction of the phase diagram.

Since the liquid phase present in various alloys at 1100°C went through non-equilibrium cooling during quenching of an alloy, no attempt was made to identify the phases in the solidified liquid. These phases were also not considered for the construction of the phase diagram.

Since the Cu and Zr contents of the alloys are fixed at 8 at.pct. and 2 at.pct., respectively, the phase diagram is drawn like a ternary diagram in terms of RE, Co and Fe.

5.2.2.2 The Phase Diagram

Phase diagram for the investigated region of the RE-Co-Fe-Cu-Zr system (around RE:T \sim 1:7) at 1100°C was drawn using the phase analysis results compiled in Table V.1 and taking into consideration the above mentioned assumptions and simplifications (Fig.V.9). The two and three phase alloys are shown in the diagram by circles and triangles, respectively. The exact locations of the phase boundaries for the single two and three phase regions were not determined and dashed lines indicate only the approximate locations of the phase regions.

The phase analysis data by XRD, metallography and TMA indicated the two intermediate phases U and N to be very close to each other. This is also born out by the SEM-EDS analysis of the U and N phases (Fig.V.5). The U phase region is located at somewhat higher Co side relative to the N phase region. The approximate region of occurrence of the N phase is about 14.3 at.pct. RE, 65 at.pct. Co and 10.8 at.pct. Fe (i.e. near the alloy C_{16}). On the other hand, the U phase occurs at around 12 at.pct. RE, 66 at.pct. Co and 12 at.pct. Fe (i.e. close to the alloy C_{12} and C_{17}). On the basis of these compositions, the RE:T ratio for the N and U phases turn out to be \sim 6 and 7, respectively. The Curie temperature of intermediate phases present in the RE-Co system decreases as the stoichiometry of the phase changes from 2:17 to 1:3 (Table V.6). Decrease in Curie temperature with change in stoichiometry from 2:17 to 2:7 is also observed for the the RE-Co-Fe intermediate phases containing about the same amount of Fe. The Curie

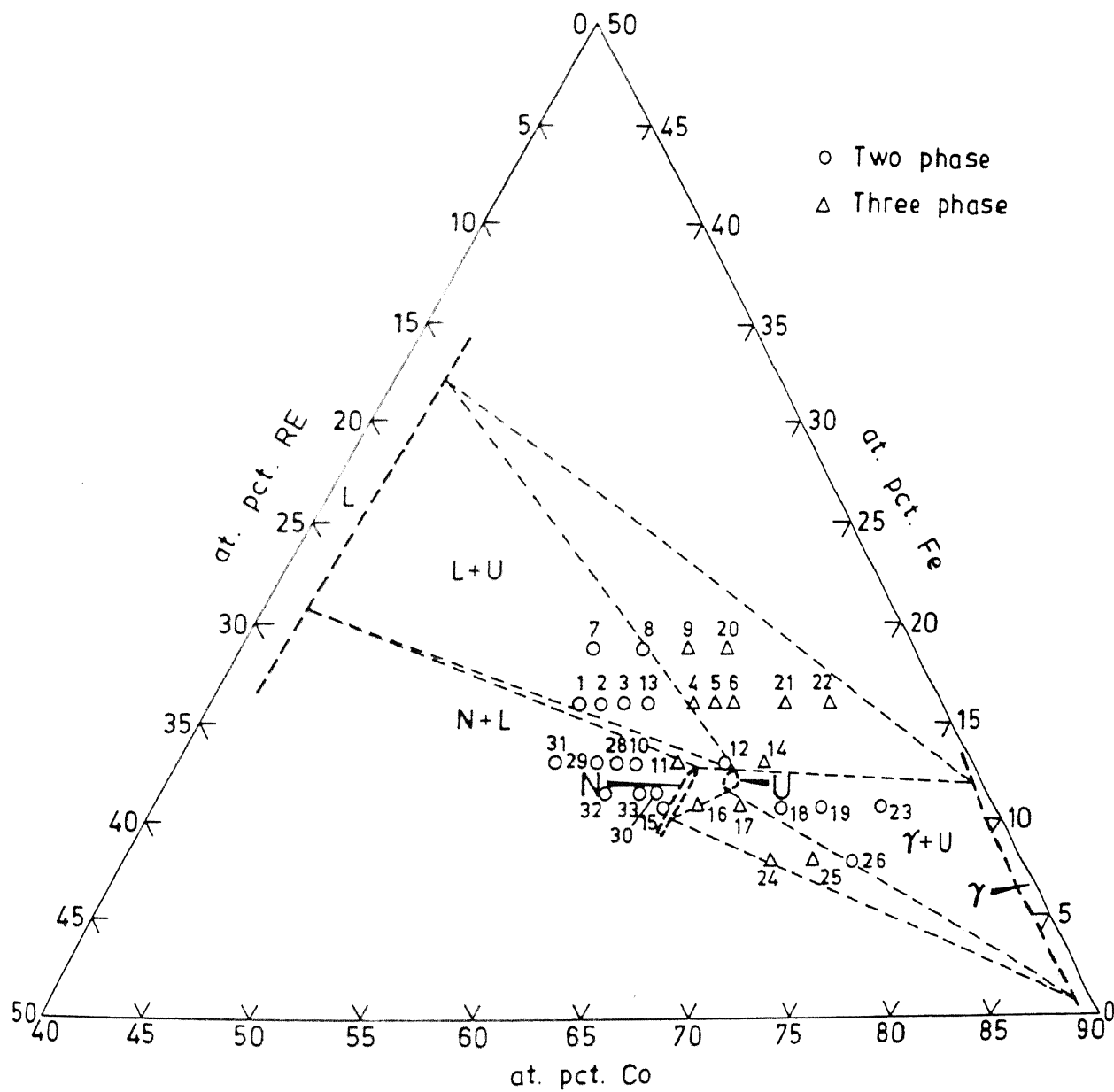


Fig.V.9 1100 °C isothermal section of RE-Co-Fe-Cu-Zr system at fixed Cu (8.0 at.pct.) and Zr (2.0 at.pct.) contents

temperatures given in Table V.6 for RE-Co-Fe intermediate phases are for the alloys containing 10-20 at.pct. Fe. In the RE-Co-Fe alloys, the 2:7 phase Curie temperature is $\leq 200^{\circ}\text{C}$, the value observed for the 1:5 is about 550°C and the highest value $\sim 900^{\circ}\text{C}$ is for the 2:17 phase. The S phase, characterized by a RE:T ratio of 1:6.9, has a Curie temperature ($\sim 830^{\circ}\text{C}$) which lies between the Curie temperature of 1:5 and 2:17 stoichiometry phases. These observations indicates that the Curie temperature and stoichiometry are interrelated and possibly one can be used to predict the another. The Curie temperatures of U phase for alloy C_{16} , containing 16.0 at.pct. Fe is found to be $\sim 830^{\circ}\text{C}$ and the Curie temperature of N phase in alloy (C_{15}), containing about 11 at.pct. Fe, is $\sim 740^{\circ}\text{C}$. The correlation between Curie temperature and stoichiometry, indicated by the data presented in Table V.6 for the RE-Co and the RE-Co-Fe intermediate phases, suggests for the U and N phase a RE:T ratio between 1:5 and 2:17, and higher RE:T ratio for the U phase than the N phase. Thus the RE:T ratio of ~ 6 and ~ 7 for the N and U phase, derived from their approximate location in the phase diagram (Fig.V.9), is also supported by their Curie temperatures. The phase analysis of alloys suggest that the U and N phases are very restricted in their composition limits. This means that not much variation in the lattice parameters of these phases is to be expected. Since single phase alloys were not available for confirming this, an attempt was made to study the variation of lattice parameters of the U and N phase utilizing the two and three phase alloys (Fig.V.10). The lattice parameters of the N phase alloys were calculated using $(0,0,10)$ and (205) reflections, whereas, the (220) and $(0,0,12)$ reflections were used for the U phase. Fig.V.10(a) shows that the lattice parameters of the N phase have practically the same values for all the alloys. This indicate that the N phase region is very narrow and the lattice parameters are not sensitive to any small variation in the chemical compositions of the N phase. On the other hand for the U phase the 'c' parameter remains the same for all the alloys but the 'a' parameter shows some variation when the two phase alloys containing γ phase are used for lattice parameter determination. Devi [245] reported that the Curie temperature of the U phase

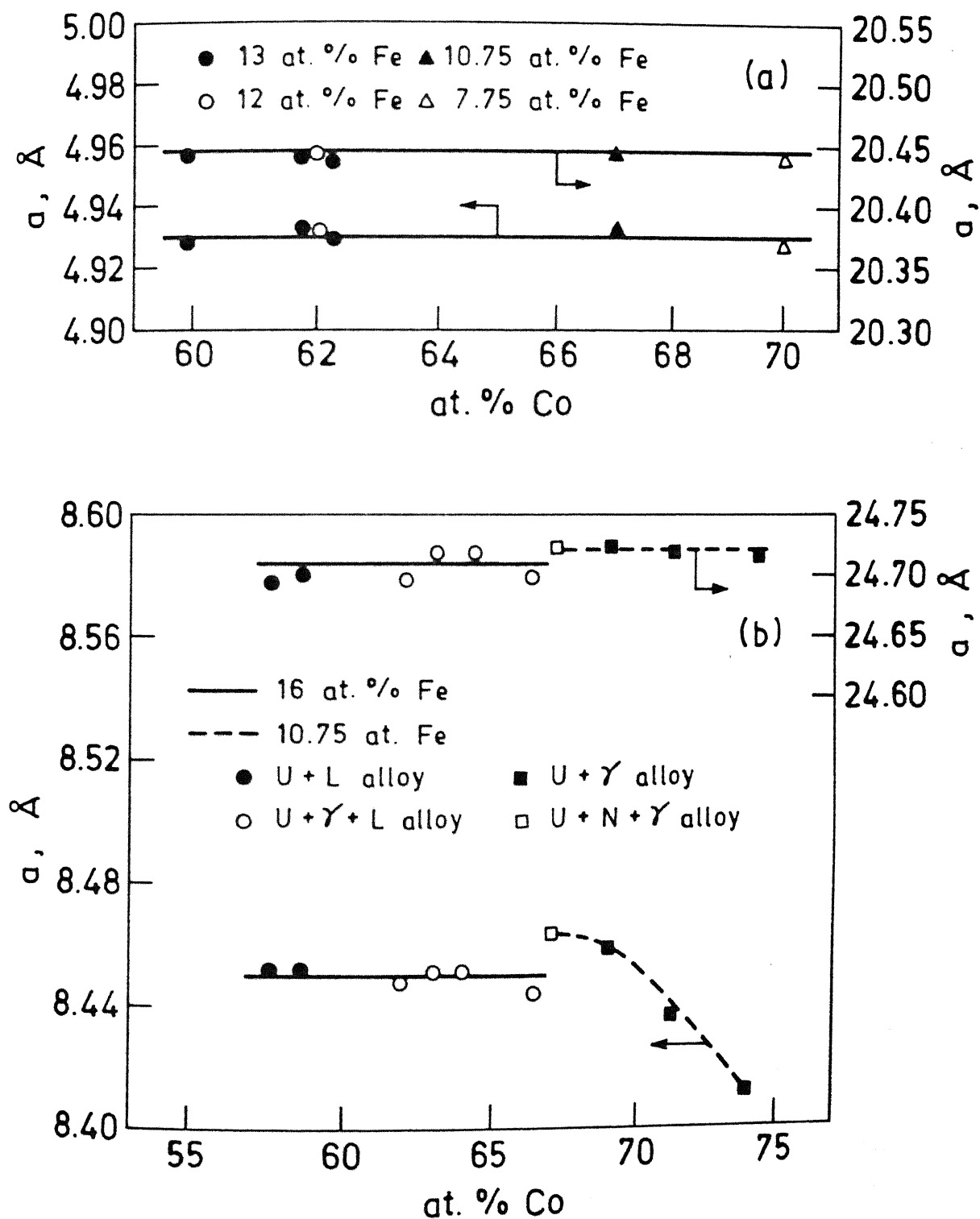


Fig.V.10 Variation of lattice parameters as a function of chemical composition : (a) N phase; and (b) U phase

varies with alloy composition. Thus, both lattice parameter variation and variation in the Curie temperature with alloy composition suggest a small solubility range for the U phase.

In this study the alloys with higher than 75 at.pct. Co were not prepared. The phase analysis of two and three phase alloys, containing different Fe contents between 9 and 17 at.pct. and Co contents between 70 and 75 at.pct., show the presence of the γ phase. Of these alloys, the alloy C_{25} and C_{22} are three phase alloys containing the $\gamma+U+N$ and $U+\gamma+L$ phases, respectively, whereas the alloy C_{26} and C_{23} are two phase alloys containing $U+\gamma$ phases. This suggests a possible extension of the γ phase region from the Co-end towards higher Fe side. The SEM-EDS analysis of the γ phase (Fig.V.6) shows that it has practically no solubility of the RE components. Thus the γ phase region is expected to be very narrow with an extension only along the Co-Fe line. The lattice parameter of the γ phase was measured for some of the two and three phase alloys using (200) reflection (Fig.V.11). Like a phase in a truly three phase region, the γ phase in the three phase alloys C_4 , C_6 , C_{21} and C_{22} (containing 16 at.pct. Fe) did not show any variation in the lattice parameter with alloy composition. Similarly for the three phase alloys C_{24} , C_{25} and two phase alloy C_{26} (all contain 7.8 at.pct. Fe) having the $U+N+\gamma$ and $U+\gamma$ phases, no variation in the lattice parameters of the γ phase with alloy composition occurs. This shows that the alloy C_{26} which is a two phase alloy containing $U+\gamma$ phases is an alloy located at the boundary of the $U+N+\gamma$ and $U+\gamma$ phase regions. For the lower Fe containing three phase and two phase alloys C_{24} , C_{25} and C_{26} , the lattice parameter of the γ phase is smaller than that observed for the higher Fe containing three phase alloys C_4 , C_6 , C_{21} and C_{22} . The two phase ($U+\gamma$) alloys C_{18} , C_{19} and C_{23} (all contain 10.8 at.pct. Fe) which lies between the two three phase regions $U+\gamma+L$ and $\gamma+U+N$, however, showed a small change in lattice parameter with change in alloy composition, the lattice parameter increased with increase in Co content of the alloys. This trend is consistent with the expected phase equilibria in two phase ($\gamma+U$) region. These results thus suggest that the γ phase lattice parameter increases with increase in Fe content. This observation

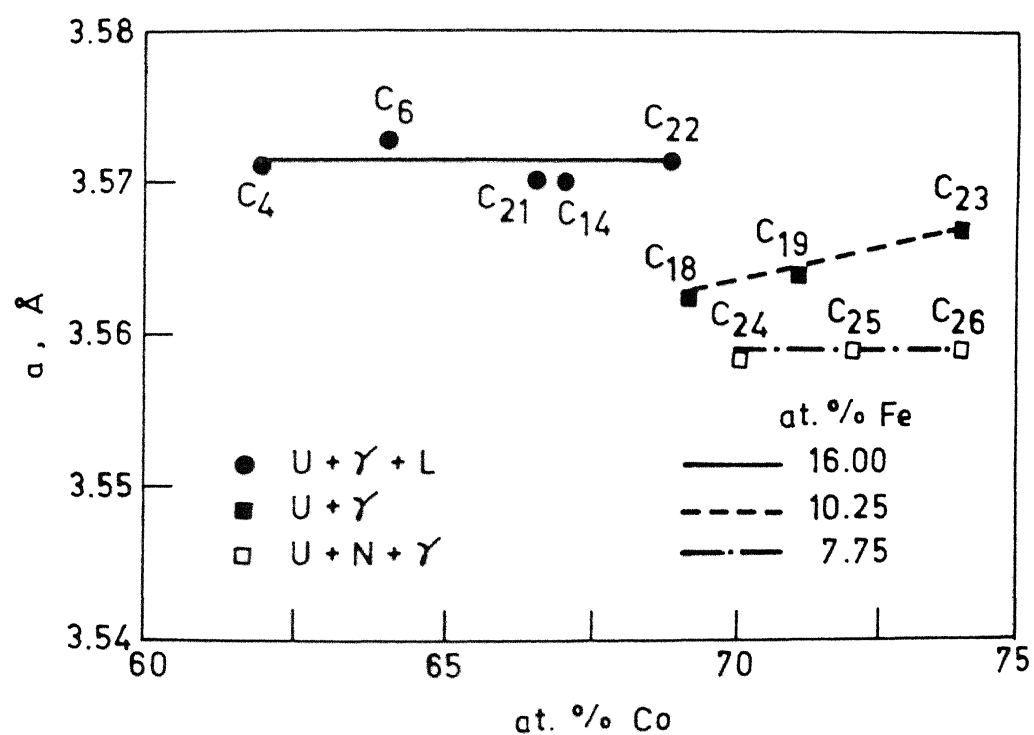


Fig.V.11 Variation of lattice parameter of the γ phase as a function of chemical composition

is also consistent with the lattice parameter variation in the Co-Fe alloys [135].

Besides the N, U and γ phase regions, there are a number of two and three phase regions in the investigated phase diagram. There are four two phase regions, namely : (i) the (U+L) region on the high Fe and high RE side (alloy C₇, C₈, C₁, C₂, C₃ and C₁₅); (ii) the (U+ γ) region on the high Co and low Fe (<12 at.pct.) side (alloy C₁₈, C₁₉, C₂₃ and C₂₆); (iii) the (N+L) region on the low Fe and high RE side (alloy C₂₇, C₂₈, C₂₉, C₃₁ and C₁₅); and (iv) the (N+U) very narrow region separating the U and N phases. The XRD pattern of alloy C₁₆ showed lines only due to the N phase indicating that the amount of any other phase in this alloy is quite small. The optical micrograph of alloy C₁₆ also showed it to be essentially single phase together with small amount of another phase [Fig.V.1(d)]. The presence of other phases the U and γ in micrograph of this alloy could not be ascertained because of the difficulty in distinguishing these phases from the Δ phase. TMA trace of this alloy (Fig.V.8) corroborated the presence of the N phase and further indicated that the U phase is also present. Very small amount of a phase present in a multiphase alloy is difficult to detect even by TMA. It is not unlikely that some of the white particles present in the microstructure of alloy C₁₆ [Fig.V.1(d)] may be due to the presence of γ phase as found in the case of alloy C₁₇ [Fig.V.1(e)] by TMA (Fig.V.8). In the published RE-Co-Fe-Cu-Zr phase equilibria at 1100 °C, Devi et.al.[244] represented alloy C₁₆ as a three phase alloy consisting of N phase and small amount of U and possibly γ phase. The presence of γ phase in alloy C₁₆ needs further confirmation by TEM with selected area electron diffraction analysis and EDS analysis. The three phase regions in the diagram are U+ γ +L (alloys C₈, C₉, C₂₀, C₄, C₅, C₂₁, C₂₂, C₁₂ and C₁₄), N+U+ γ (alloys C₁₇, C₂₄ and C₂₅) and very narrow N+U+L region (alloy C₁₁). XRD pattern of several alloys, e.g. C₂₀, C₄, C₅, C₆, C₂₁, C₂₂ etc., did not show any diffraction peaks due to the solidified liquid (Table V.1) and presence of liquid in these alloys was inferred from metallographic analysis only. Both metallography and XRD analysis indicated that the alloy C₁₁ contains (N+L) phases. The U phase

could not be detected in alloy C₁₁ through these characterization methods. TMA trace of this alloy indicated that in addition to N phase U phase is also possibly present in small amount (section 5.3.4). Thus, keeping in view the TMA results the alloy C₁₁ is located in the three phase N+U+L region.

5.3 Summary

A partial phase equilibria in the RE-Co-Fe-Cu-Zr system has been established at 1100 °C, around RE:T ratio of ~ 1:7, using metallography, XRD, SEM-EDS analysis and TMA. Existence of two new phases U and N, located around RE:T ratio of ~1:7 and 1:6 respectively have been established. U and N phases which appear to be structurally similar to the 2:17 and 1:5 phases, have lattice parameters (hexagonal cell) of $a = 8.452 \text{ \AA}$, $c = 24.57 \text{ \AA}$ and $a = 4.940 \text{ \AA}$, $c = 20.42 \text{ \AA}$, and $T_c \sim 830$ and $740 \text{ }^\circ\text{C}$, respectively. Both the U and N phases are restricted in their composition limits. The U phase appears to have a small solubility range. The other phases which are found at 1100 °C include a cobalt rich fcc solid solution phase (γ) ($a = 3.558 \text{ \AA}$, $T_c \sim 1045 \text{ }^\circ\text{C}$), a Zr rich hard phase Δ and a liquid phase.

CHAPTER VI

PHASE EQUILIBRIA IN THE RE-Fe-B SYSTEM AT 1000 °C

This chapter concerns with the results and discussion on the 1000°C isothermal section of the RE-Fe-B system. The phase equilibria has been investigated in the composition range which is of interest to the permanent magnet workers, i.e. at the iron rich side, upto about 40 at pct. RE and about 45 at.pct. B.

6.1 Results

Thirty alloys were arc melted in this system and annealed at 1000°C for 3 days. The intended chemical composition of the alloys is given in Table VI.1. The alloys are designated with symbol E_i , where the subscript i indicates the alloy number. Since the phase $RE_2Fe_{14}B$ (Γ) is magnetically the most important phase, large number of alloys were made in the close vicinity of the expected Γ phase region to delineate its phase region as well as to determine the phases in equilibrium with it.

The phase analysis of alloys was carried out mainly using metallography, XRD and TMA. The presence of two ternary intermediate phases, identified as $RE_2Fe_{14}B$ (Γ) and $REFe_4B_4$ (Δ), a bcc Fe solid solution phase (α) and a Fe_2B (β) phase have been established. The summary of phase analysis results is presented in Table VI.1 and details are given in the following subsections.

6.1.1 Metallographic Analysis

The high rare-earth containing alloys having liquid phase at 1000°C were highly brittle. Low grinding speeds were used to avoid chipping off of the brittle solidified liquid phase. 0.25 to 3.0 pct. (v/v) dilute HNO_3 was used as etchant. Dilute etchant was used for the high RE containing alloys. The alloys containing large amount of Δ phase were quite prone to oxidation in open atmosphere and polished surface of these alloys (e.g. E_{19}) tarnished very fast.

Table VI.1: Chemical Composition and Phase Analysis of the Investigated RE-Fe-B Alloys

Alloy # Number (i)	Intended Alloy Composition (at.pct.)			Phase Analysis*		
	RE	Fe	B	Metallography	X-ray	TMA
				Number of Phases		
1	5.0	90.0	5.0	3	α, Γ, β	α, Γ, β
2	10.0	85.0	5.0	2	α, Γ	α, Γ
3	15.0	80.0	5.0	3	Γ, L', α	Γ, α
4	20.0	75.0	5.0	2	Γ, L'	Γ, α
5	25.0	70.0	5.0	2	Γ, L'	Γ
8	5.0	80.0	15.0	3	α, Γ, β	α, β, Γ
9	15.0	70.0	15.0	3	Γ, Δ	Γ
10	25.0	60.0	15.0	3	Γ, L', Δ	Γ
11	35.0	50.0	15.0	3	Γ, L', Δ	-
12	5.0	70.0	25.0	3	β, Δ, Γ	β, Γ
13	15.0	60.0	25.0	3	Γ, Δ	Γ
14	25.0	50.0	25.0	3	Δ, Γ, L'	-
16	5.0	60.0	35.0	3	β, Δ, Γ	β, Γ
17	15.0	50.0	35.0	3	Γ, Δ	Γ
18	25.0	40.0	35.0	2	L', Δ	-
19	11.1	44.5	44.4	2	β, Δ	β
20	11.8	82.3	5.9	2	Γ, α	Γ, α
23	11.0	87.0	2.0	3	Γ, α, L'	Γ, α
24	11.8	80.3	7.9	3	Γ, Δ, β	Γ, β
25	2.0	64.7	33.3	3	Γ, Δ, β	Γ, β
26	15.0	77.0	8.0	3	Γ, Δ	Γ
27	11.0	82.0	7.0	3	Γ, α	Γ, α
28	13.0	82.0	5.0	3	Γ, α, L'	-
29	13.0	80.5	6.5	3	Γ	-
30	12.5	81.5	6.0	1	Γ	Γ
31	12.0	81.5	6.5	3	Γ, Δ	-
32	0.5	66.0	33.5	3	β, Δ	-
33	1.0	98.5	0.5	2	α	α
34	11.5	87.5	1.0	3	Γ, α, L'	-
35	1.0	97.5	1.5	3	α	-

Alloy designation E₁* Phase designation: α - bcc terminal solid solution; β - Fe₂B; Γ - RE₂Fe₁₄B; Δ - RE Fe₄B₄; L' - solidified liquid

The summary of the phases identified in different alloys is given in Table VI.1. Only one alloy has a single phase microstructure. Seven of the investigated alloys are found to have two phases in their microstructure and the rest consist of three phases. The microstructures of some of the representative alloys with complete description are shown in Fig.VI.1 and VI.2.

Microstructures in Fig.VI.1(a)-(h) correspond to a few typical alloys which have their compositions close to or around the expected Γ phase region. Alloy E_{30} turned out to be a single phase (identified as Γ by XRD; section 6.1.2) alloy [Fig.VI.1(a)]. In the microstructure of all other alloys [Fig.VI.1(b)-(h)], Γ phase occurred as the matrix phase together with other phase/s. Alloy E_{28} , which is close to E_{30} but having 1 at.pct. lower B content (Table VI.1), was found to be a three phase alloy [Fig.VI.1(b)] consisting of elongated grains of Γ phase, white rounded islands of the α phase and black solidified liquid. The microstructure of alloy E_4 and E_5 , having the same amount of B as in alloy E_{28} but RE content >20.0 at.pct., showed only two phases, Γ and liquid, and white islands of α phase were found missing [Fig.VI.1(c)]. Another alloy E_{34} , having still lower B content compared to E_{28} but higher amount of Fe, also showed a three phase microstructure similar to the alloy E_{28} ; the grains of Γ phase in the microstructure showed twins [Fig.VI.1(d)]. The alloy E_{20} , containing the same amount of B as in alloy E_{30} and to the higher Fe content side of alloy E_{30} (Table VI.1), showed the presence of two phases Γ and α [Fig.VI.1(e)]. The alloy E_{27} , close to alloy E_{20} but with higher B content, showed, besides the Γ and α phases, the presence of a third phase which was identified as the β phase [Fig.VI.1(f)]. The alloy E_{31} which is very close to alloy E_{30} but with slightly higher amount of B (0.5 at.pct.) turned out to be a three phase alloy containing Γ , β and Δ phases [Fig.VI.1(g)]. The alloy E_{29} containing the same amount of B as in alloy E_{31} but with more RE content (Table VI.1) showed again three phases [Fig.VI.1(h)] namely the Γ , Δ and liquid (L) phases.

Few more microstructures shown in Fig.VI.2(a)-(d) are for the

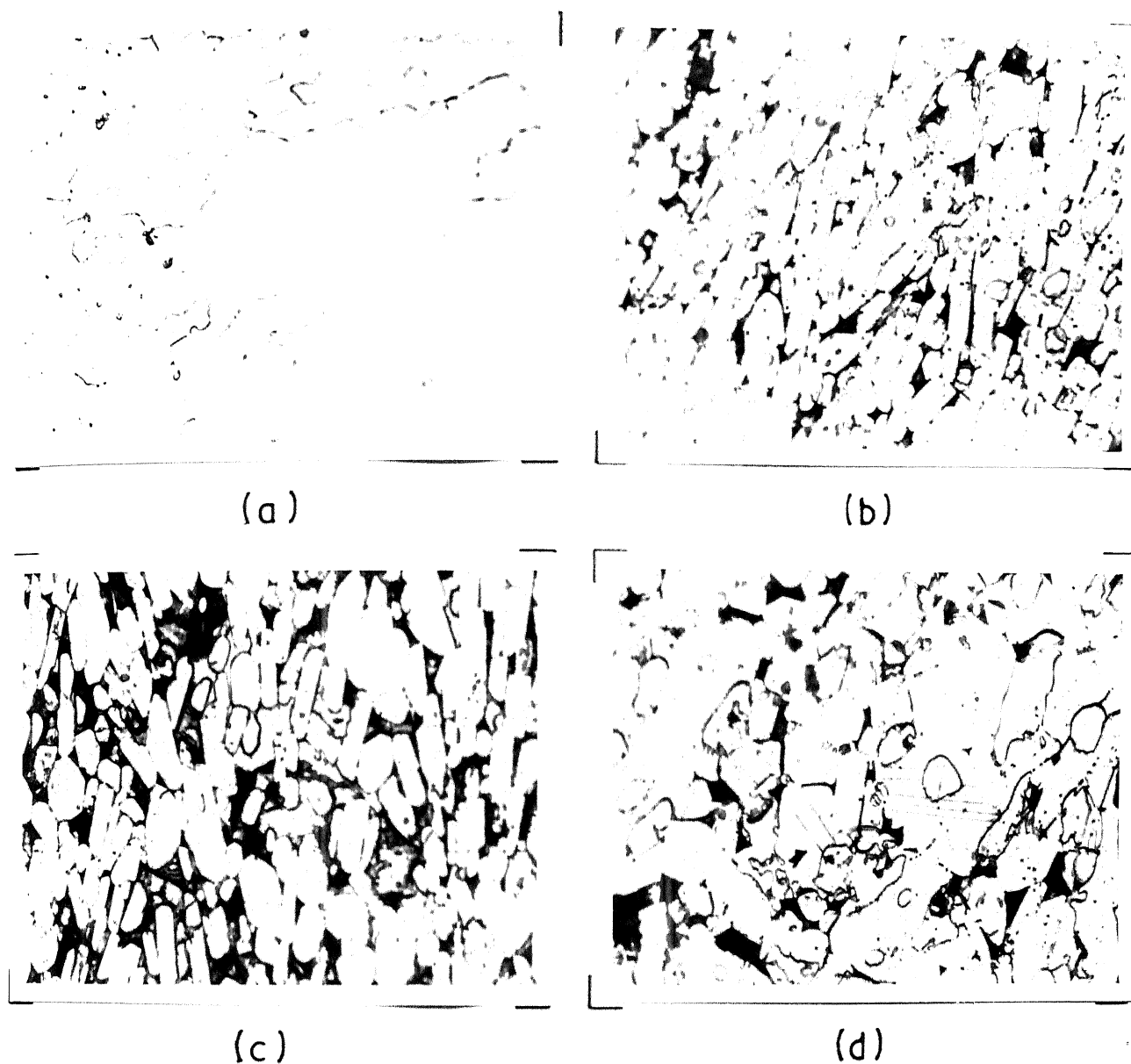


Fig. VI.1 Representative optical micrographs of RE-Fe-B alloys having composition close to the expected Γ phase region [Mag. 400 \times]

- (a) alloy E₃₀ (single phase), Γ
- (b) alloy E₂₈ (3 phases), matrix (elongated grains) - Γ , white islands - α , black region - L
- (c) alloy E₄ (2 phases), matrix - Γ , black region - L
- (d) alloy E₃₄ (3 phases), matrix (showing twins) - Γ , white islands - α , black region - L

(Contd. ...)

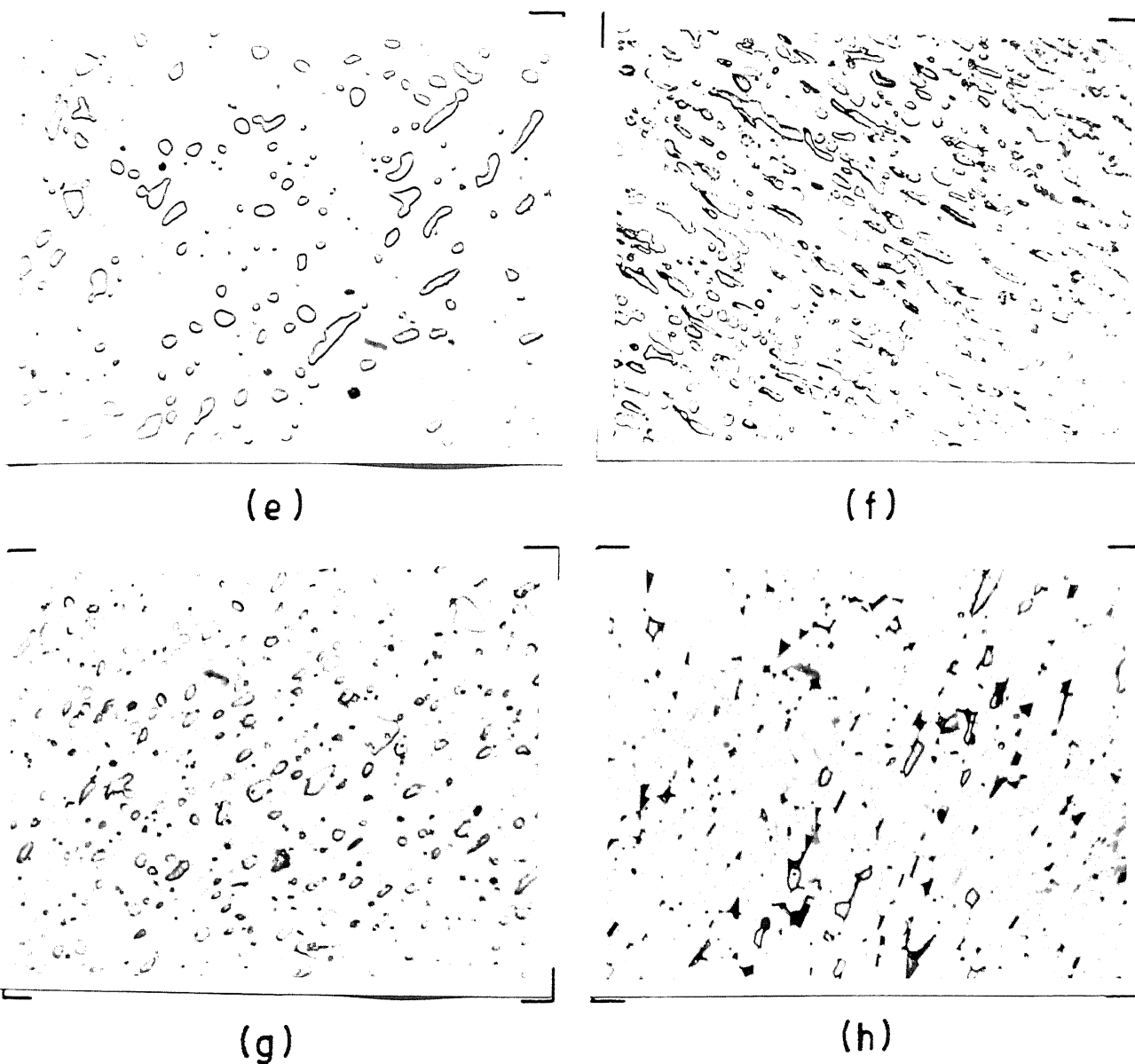


Fig.VI.1 (Contd. ...) [Mag. 400x]

- (e) alloy E_{20} (2 phases), matrix - Γ , second phase - α
- (f) alloy E_{27} (3 phases), matrix - Γ , islands (with sharp boundary) - β , islands (irregular boundary) - α
- (g) alloy E_{31} (3 phases), matrix - Γ , grey regions - Δ , white islands - β
- (h) alloy E_{29} (3 phases), matrix - Γ , grey regions - Δ , white triangles - L

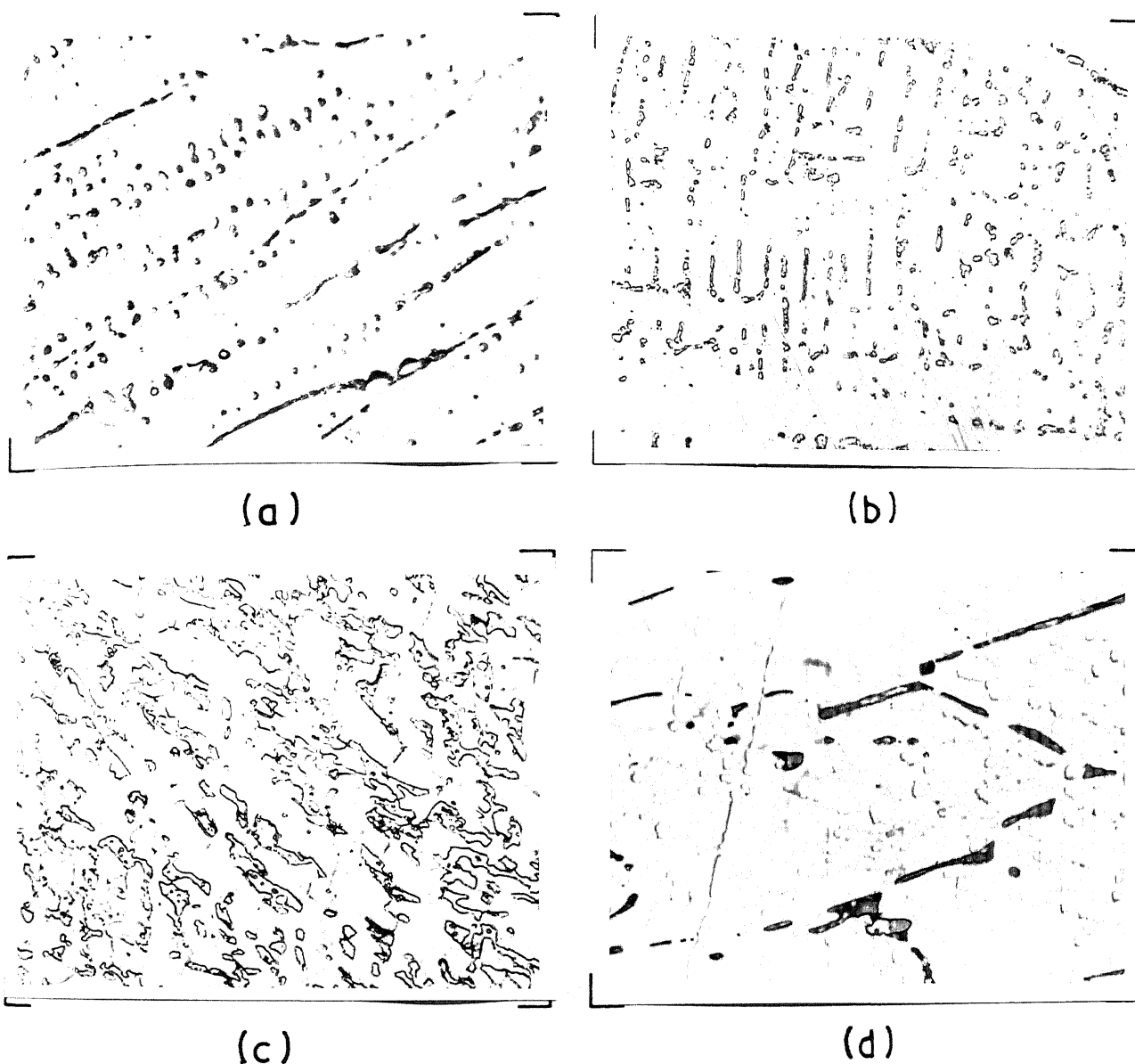


Fig.VI.2 Optical micrographs of typical RE-Fe-B alloys located away from the expected Γ phase region [Mag. 400x]:

- (a) E_{33} (2 phases) matrix - α , second phase - Γ
- (b) E_{35} (3 phases) matrix - α , elongated islands with sharp boundaries - Γ , circular regions with faint boundaries - β
- (c) E_8 (3 phases), soft phase with scratch lines - α , white islands with sharp boundaries, Γ , grains with faint boundaries - β
- (d) E_{32} (3 phases), matrix - β , dark grey regions - Δ , white islands - Γ

alloys which are located away from the Γ phase region and had the α or the β as the matrix phase. The microstructures of the alloys E_{33} , E_{35} and E_8 in Fig.VI.2(a)-(c) had α as the matrix phase. Alloy E_{33} , located very close to the Fe-end (0.5 at.pct. B and 1.0 at.pct RE), showed a two phase microstructure in which the Γ phase appeared in the matrix of the α phase as strings of small particles with sharp boundaries [Fig.VI.2(a)]. Alloy E_{35} and E_8 showed three phase microstructure consisting of α , Γ and β phases [Fig.VI.2(b)-(c)]. Alloy E_{35} , which had composition close to alloy E_{33} and contained 1 at.pct. higher B, showed only very small amount of the β phase, occurring as rounded particles but with less sharp boundary as compared to the Γ phase [Fig.VI.2(b)]. The distinction between β and Γ phases, in terms of sharpness of phase boundary, becomes more clear in the microstructure of alloy E_8 which contained higher amount of these phases [Fig.VI.2(c)]. Alloy E_{32} , having composition close to Fe_2B stoichiometry but with small amount of RE (0.5 at.pct.), also showed three phase microstructure [Fig.VI.2(d)] in which the β phase appeared as the matrix phase together with the Δ and Γ phases.

6.1.2 X-Ray Diffraction Analysis

Through X-ray diffraction analysis, two ternary intermediate phases, namely, $RE_2Fe_{14}B$ (Γ) and $REFe_4B_4$ (Δ), a bcc α phase and a Fe_2B (β) phase were identified. No indication of the presence of RE_2Fe_{17} phase could be found in any of the RE-Fe-B alloys.

The XRD patterns of the two ternary intermediate phases Γ and Δ are shown in Fig.VI.3(a) and 3(b). XRD pattern of the Γ phase [alloy E_{30} ; Fig.VI.3(a)] could be indexed completely on the basis of a tetragonal cell ($RE_2Fe_{14}B$ type phase) and is given in Table VI.2. The lattice parameters of the Γ phase were found to be $a = 8.784 \text{ \AA}$, $c = 12.177 \text{ \AA}$ and $c/a = 1.39$. The second ternary intermediate phase Δ was indexed using the XRD pattern of a two phase alloy, containing small amount of Fe_2B phase [alloy E_{19} ; Fig.VI.3(b)], on the basis of a tetragonal cell of lattice parameters $a = 7.106 \text{ \AA}$, $c = 17.011 \text{ \AA}$ and $c/a = 2.39$ (Table VI.3).

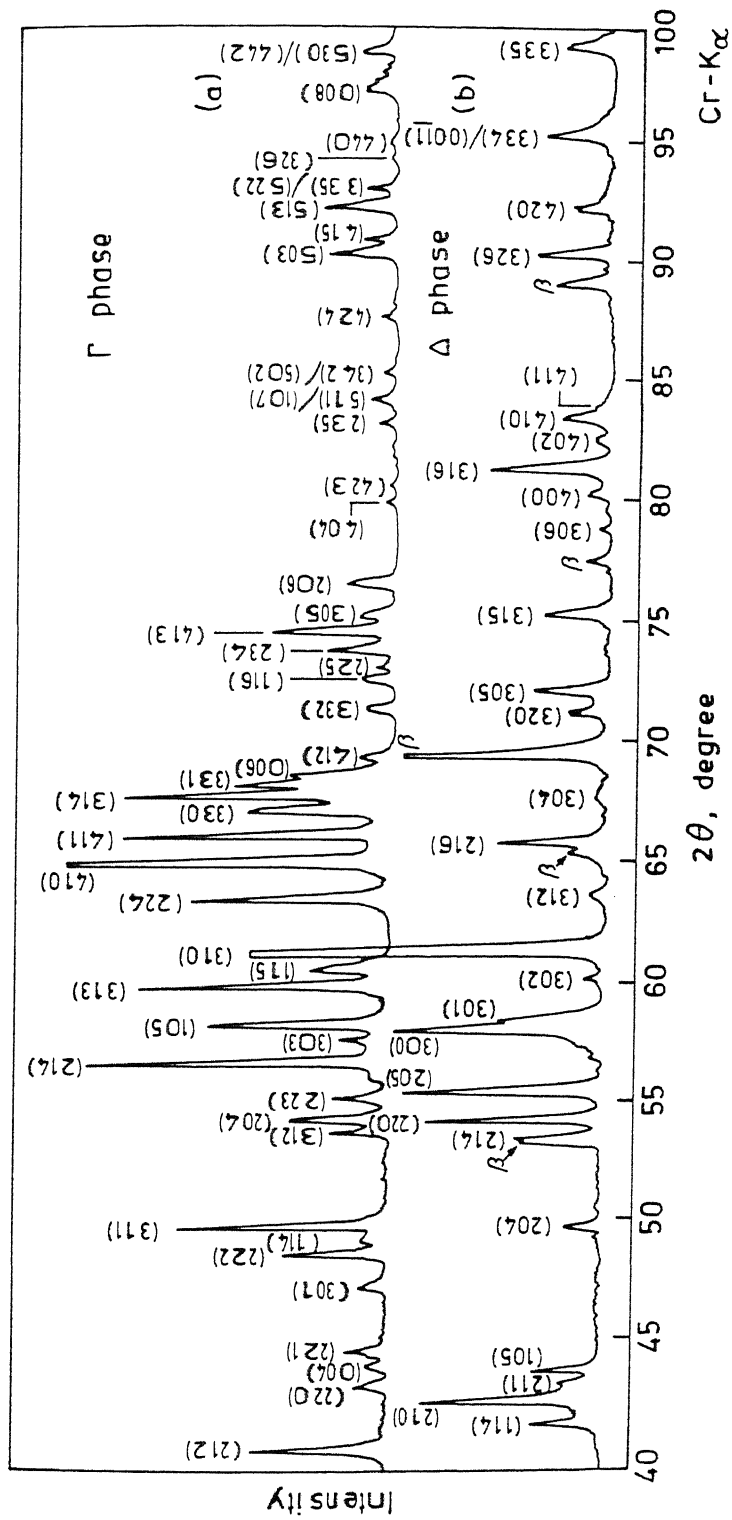


Fig. VI.3 XRD patterns of some RE-Fe-B alloys : (a) alloy E_{30} [single phase $RE_2Fe_{14}B$ (Γ)]; (b) alloy E_{19} [major phase $REFe_4B_4$ (Δ)]

Table VI.2: Powder X-ray Diffraction Data of the $\text{RE}_2\text{Fe}_{14}\text{B}$ (Γ) Phase (Alloy E_{30})

Unit cell tetragonal		a 8.784 Å		c 12.177 Å		c/a 1.39	
Relative Intensity*	d_{obs} Å	hkl	d_{calc} Å	Relative Intensity	d_{obs} Å	hkl	d_{calc} Å
w	3.923	210	3.928	m ⁻	1.613	503	1.612
w ₋	3.685	103	3.685	w ₋	1.604	415	1.603
m ₋	3.559	202	3.562	m ₋	1.586	513	1.586
m ₋	3.302	212	3.301	w	1.576	335	1.577
m ₋	3.101	220	3.106			522	1.576
w ₋	3.046	004	3.044	vw	1.560	326	1.559
m ₋	3.006	221	3.009	vw	1.552	440	1.553
m ₋	2.844	301	2.847	w	1.522	008	1.522
m	2.767	222	2.766	vw	1.514	523	1.513
w	2.734	114	2.734	w	1.505	530	1.506
s ₋	2.706	311	2.708			442	1.505
m ₋	2.527	312	2.527	m ₋	1.476	317	1.474
m ₋	2.504	204	2.502			118	1.478
m ₋	2.466	223	2.466	w	1.439	208	1.438
s	2.407	214	2.406			524	1.438
w	2.373	303	2.375	m ₋	1.424	305	1.425
s	2.348	105	2.347			505	1.425
s ₋	2.293	313	2.292	m ₋	1.407	515	1.406
m ₋	2.266	115	2.267	w	1.383	444	1.383
s	2.175	224	2.174	vw	1.368	228	1.367
vs	2.129	410	2.130	m ₋	1.354	262	1.354
s	2.098	411	2.099			525	1.355
m	2.069	330	2.070	w	1.349	534	1.350
s	2.053	314	2.052			417	1.347
m ₋	2.041	331	2.041	w	1.313	516	1.313
m ₋	2.030	006	2.029	w ₋	1.281	535	1.281
w	2.010	412	2.011	m ₋	1.252	408	1.251
w	1.959	332	1.960			544	1.251
w	1.930	116	1.929	w	1.247	701	1.248
vw	1.916	225	1.916			363	1.246
m ₋	1.902	234	1.902	m ₋	1.240	229	1.240
m	1.887	413	1.886	m ₋	1.230	702	1.229
w ₋	1.872	305	1.872	m ₋ **	1.218	0,0,10	1.218
m ₋	1.844	206	1.842	m ₋	1.207	720	1.207
vw	1.781	404	1.781	m ₋	1.204	428	1.203
vw	1.767	423	1.768			364	1.203
w	1.722	235	1.722	m	1.201	721	1.201
w	1.705	511	1.706	m	1.200	703	1.199
		107	1.706	w	1.189	553	1.188
w	1.687	342	1.688			527	1.190
		502	1.688	vw**	1.187	606	1.187
w	1.650	424	1.650	m ₋ **	1.184	722	1.184

* Relative intensity scale: vs- very strong; s- strong; m- medium; w- weak; vw- very weak

** Reflections used for the lattice parameters calculation

Table VI.3: Powder X-ray Diffraction Data of the REFe_4B_4 (Δ) Phase
(Alloy E_{19})

Unit cell tetragonal		a 7.106 Å		c 17.011 Å		c/a 2.39	
Relative Intensity *	d_{obs} Å	hkl	d_{calc} Å	Relative Intensity	d_{obs} Å	hkl	d_{calc} Å
m	3.238	114	3.246	m	1.758	316	1.761
m	3.161	210	3.178	vw	1.737	402	1.739
w	3.114	211	3.124	m	1.721	410	1.723
m	3.072	105	3.069	vw	1.713	411	1.715
w	2.717	204	2.727	m	1.616	326	1.618
m	2.546	214	2.546	w	1.589	420	1.589
m	2.511	220	2.512	m	1.550	334	1.558
m	2.461	205	2.457			0.0.11	1.546
s	2.361	300	2.369	w**	1.503	335	1.503
m	2.349	301	2.346	m**	1.394	510	1.394
vw	2.288	302	2.282	vw	1.336	418	1.339
vvs	2.247	310	2.247	m	1.319	520	1.319
vw	2.174	312	2.172	w	1.287	1.0.13	1.287
m	2.111	216	2.116			252	1.285
vw	2.057	304	2.069	vw	1.264	1.1.13	1.266
m	2.005	207	2.006			254	1.260
w	1.967	320	1.971	m	1.257	440	1.256
m	1.945	305	1.944	w**	1.251	516	1.251
m	1.876	315	1.875	w	1.237	2.2.12	1.235
vw	1.805	306	1.818			255	1.230
vw	1.777	400	1.776				

strong; m-

* Relative intensity scale: vs- very strong; s- medium; w- weak; vw- very strong

** Reflections used for the lattice parameters calculation

The calculated and observed d-spacings of the Γ and Δ phases matched well (Tables VI.2 and VI.3).

The indexed diffraction pattern of the β phase (alloy E_{32} , Fig.VI.4) is given in Table VI.4. The β phase has been indexed on the basis of a tetragonal cell of lattice parameters $a = 5.104 \text{ \AA}$, $c = 4.254 \text{ \AA}$ and $c/a = 0.833$. In the Fe-rich alloys, instead of finding a fcc Fe solid solution phase γ at 1000°C , a bcc α phase was observed. The α phase is found to have a lattice parameter $a = 2.868 \text{ \AA}$ (alloy E_{33}).

Table VI.4: Powder X-ray Diffraction Data of the β phase (Fe_2B) in Alloy E_{32} .

Unit cell		a	c	c/a
tetragonal		5.104 \AA	4.254 \AA	0.833
Line no	Relative Intensity [#]	$d_{\text{Obs.}}$ \AA	hkl	$d_{\text{cal.}}$ \AA
1	m	3.610	110	3.609
2	vs	2.553	200	2.553
3	m	2.123	002	2.127
4	vvs	2.011	121	2.012
5	m	1.831	112	1.832
6	m	1.633	202	1.634
7	vw	1.376	222	1.373
8*	s	1.286	132	1.286
9*	vvs	1.203	330	1.203
10	vs	1.190	141	1.189

[#] Relative intensity scale: vvs - very very strong, vs - very strong, s - strong, m - medium, w - weak, vw - very weak

* Reflections used for the lattice parameters calculation

A liquid (L) exists at 1000°C in the alloys containing more than 40 at.pct. RE. The liquid during quenching of alloys produced solid phases which also gave diffraction lines. The X-ray diffraction lines arising out of the solidified liquid are marked as L' in the XRD patterns of alloys E_{18} , E_{14} and E_{11} (Fig.VI.5). No attempt was made to identify the phases arising out of the

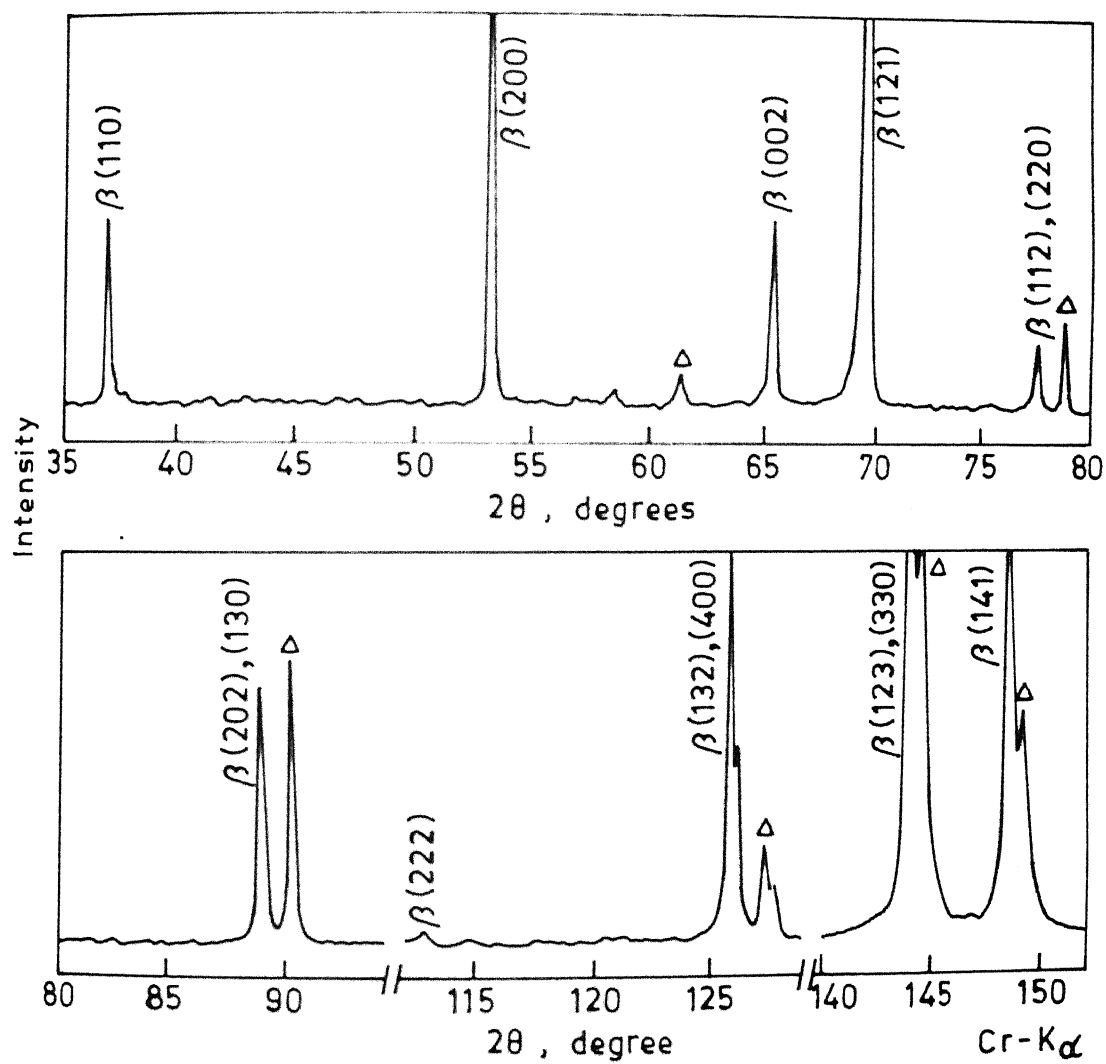


Fig.VI.4 XRD pattern of the Fe_2B (β) phase (alloy E_{32}) (the peaks marked as Δ corresponds to the REFe_4B_4 phase)

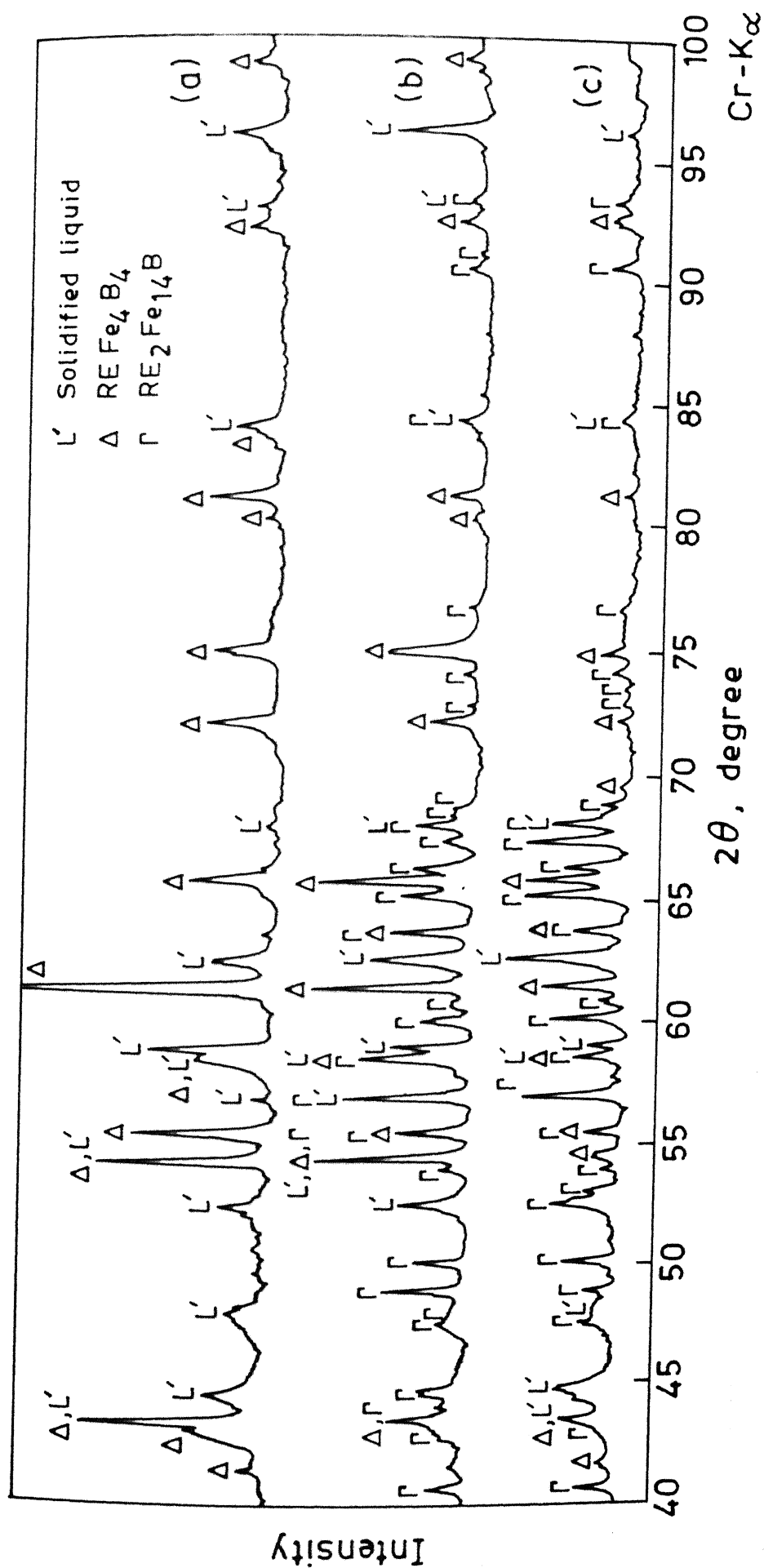


Fig.VI.5 XRD patterns of some RE-Fe-B alloys containing solidified liquid (L'): (a) alloy E_{18} , ($\Delta+L'$); (b) alloy E_{14} , ($\Gamma+\Delta+L'$); and (c) alloy E_{11} , ($\Gamma+\Delta+L'$)

quenched liquid as these phases are produced under non-equilibrium condition and not present at 1000°C .

Identification of phases present in different alloys was done by comparing their diffraction patterns with the indexed XRD patterns of each of the phases. Phase analysis results for all the investigated alloys are summarized in Table VI.1. In general the number of phases identified by X-ray matches with the metallography results (Table VI.1). Only in those cases where the amount of the second phase and / or the third phase were too small, e.g. alloy E_{35} , E_{27} etc., the identification of all the phases could not be done through X-ray diffraction data. The presence of the phases arising out of the solidified liquid in alloy E_9 , E_{13} , E_{17} , E_{26} and E_{29} also could not be inferred from their XRD patterns because the amount of liquid present in these alloys at 1000°C was small.

6.1.3 Thermomagnetic Analysis (TMA)

TMA of the RE-Fe-B alloys was done, mostly using the high temperature permeability testing apparatus, for the identification of phases. Since the TMA using permeability testing apparatus did not give accurate value of T_c (vide section 4.2.3) a few experiments were also carried out using a VSM to determine T_c for a few phases. For some typical alloys the results of TMA using permeability testing apparatus are compiled in Fig.VI.6(a) and 6(b). Fig.VI.7 gives the results obtained using a VSM. Two alloys close to the 2:14:1 and 1:4:4 stoichiometries were prepared in the Nd-Fe-B system for comparison of data obtained in the RE-Fe-B system. The TMA curves for the alloys X and A in Fig.VI.6 and VI.7 correspond to the intended compositions of $\text{Nd}_2\text{Fe}_{14}\text{B}$ and NdFe_4B_4 phases, respectively. The summary of phases identified by TMA in different alloys is presented in Table VI.1.

The most important magnetic phase in the RE-Fe-B system is the Γ phase. The TMA traces of 2:14:1 phase of RE-Fe-B (Γ phase, alloy E_{30}) and Nd-Fe-B system (ϕ phase, alloy X), obtained using

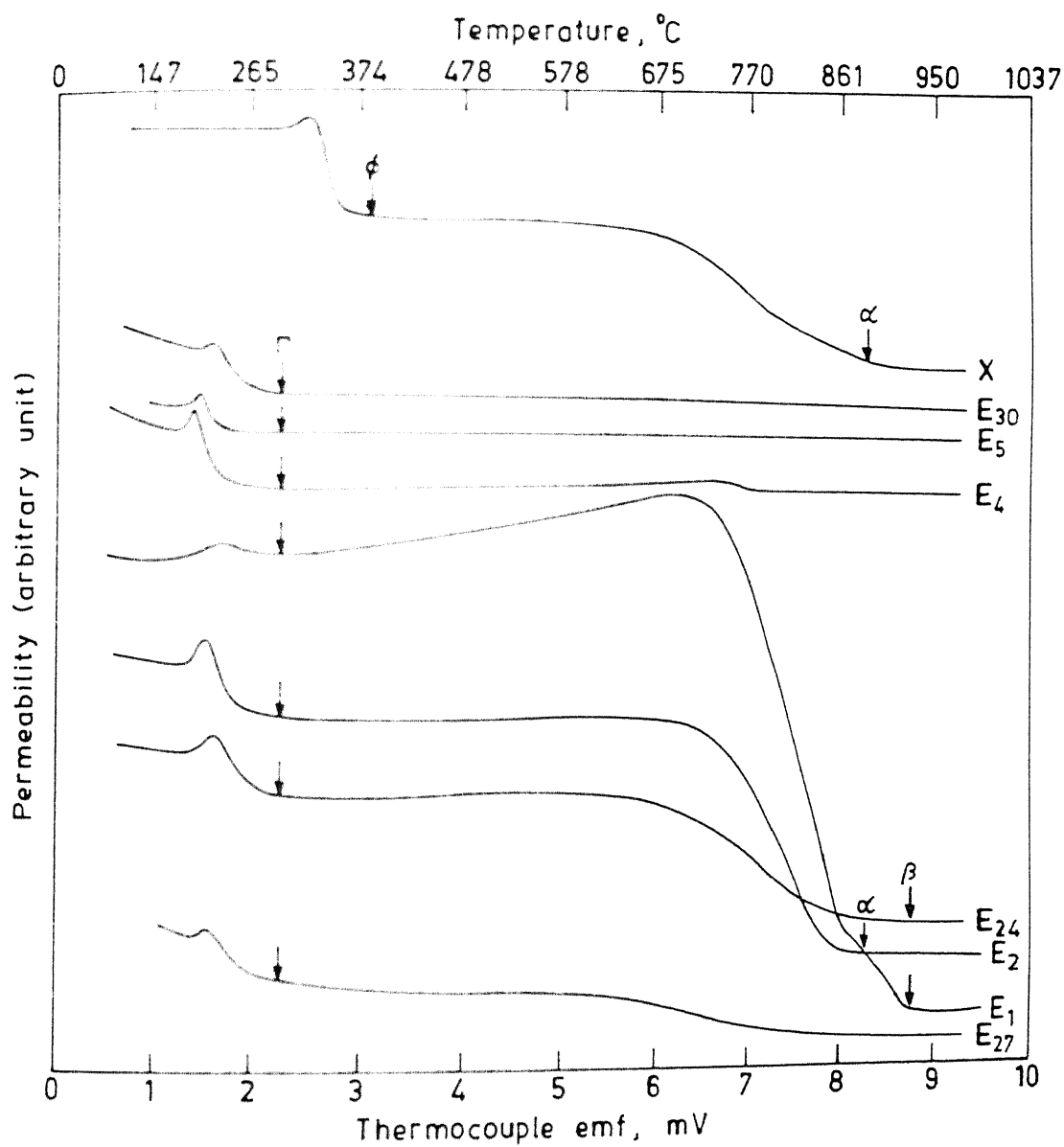


Fig.VI.6 TMA traces of some typical RE-Fe-B alloys

(a) alloy E_1 , E_2 , E_{24} , E_{27} , E_4 , E_5 , E_{30} and X (alloy X is a Nd-Fe-B alloy and corresponds to the 2:14:1 composition)

(Contd. ...)

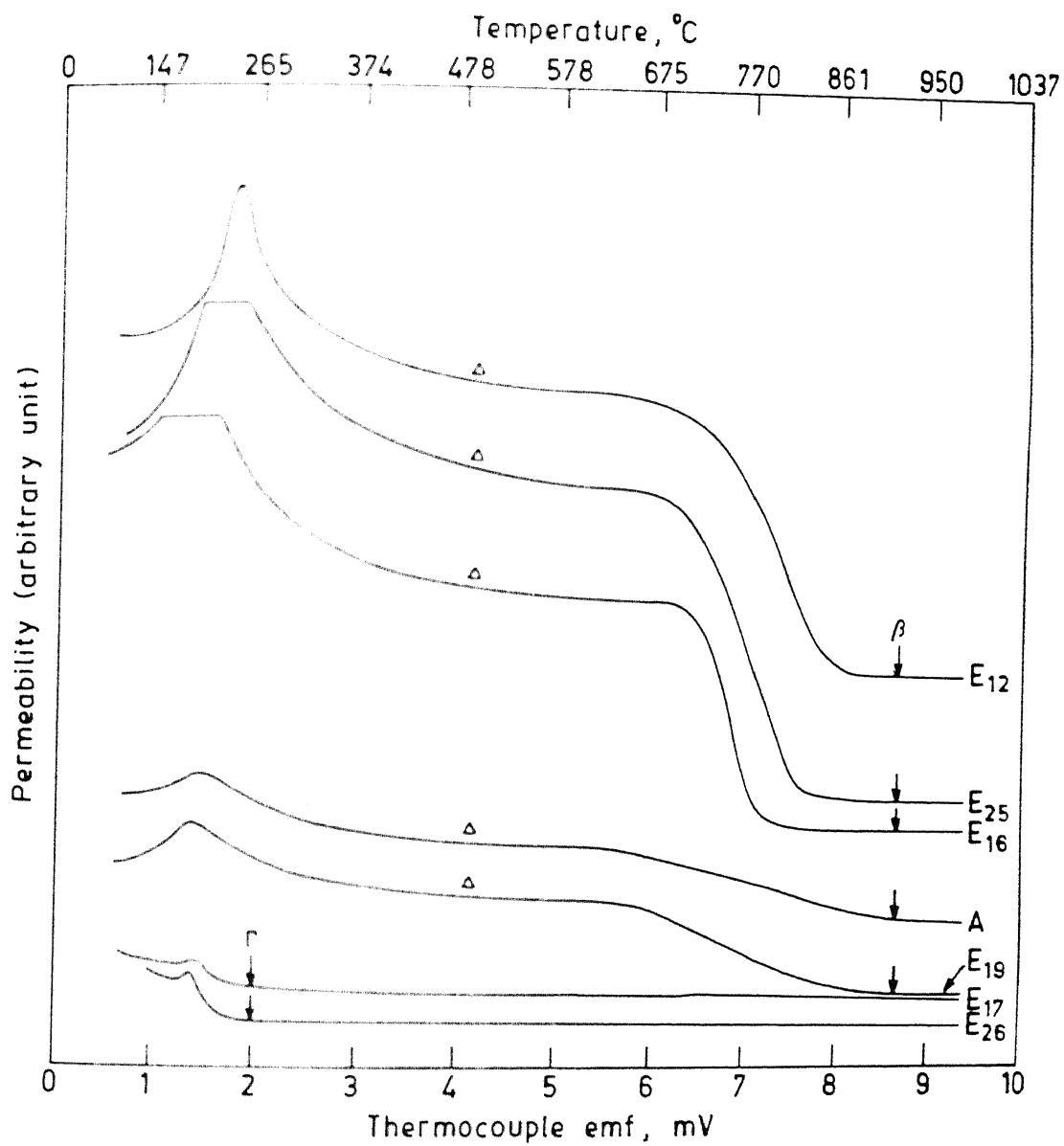


Fig.VI.6 (Contd. ...)

(b) alloy E_{26} , E_{17} , E_{19} , E_{16} , E_{25} , E_{12} and A (alloy A is a Nd-Fe-B alloy and corresponds to the 1:4:4 composition)

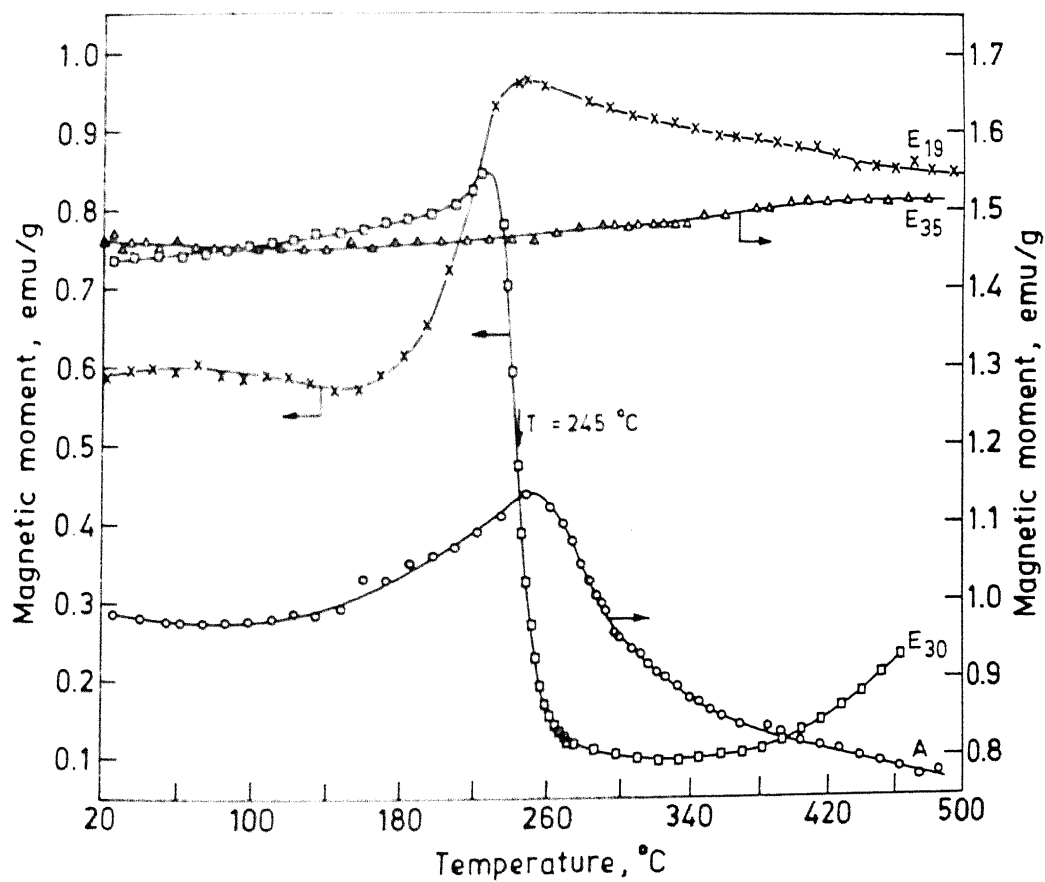


Fig.VI.7 Magnetic moment vs. temperature curves for alloy E₁₉, E₃₅, E₃₀, and A (alloy A is a Nd-Fe-B alloy and corresponds to the 1:4:4 composition)

permeability testing apparatus, are given in Fig.VI.6(a). The magnetic transition of the Γ phase occurs at a slightly lower temperature than the $\text{Nd}_2\text{Fe}_{14}\text{B}$ or ϕ phase. The sharp magnetic transition due to Γ phase could be observed in all the alloys containing reasonable amount of Γ phase. Alloys containing Γ and solidified liquid phase (e.g. E_5) also showed only one magnetic transition due to the Γ phase indicating the non-magnetic character of the phases resulting from the non-equilibrium solidification of liquid [Fig.VI.6(a)]. α and β phases showed distinctly different magnetic transitions at higher temperatures; the rise in permeability was observed at around $770\text{--}850^\circ\text{C}$ and $900\text{--}930^\circ\text{C}$, respectively. It was found possible to identify phases through TMA analysis because of the appreciable difference in the magnetic transition temperatures. For example, alloy E_2 and E_{24} showed magnetic transitions due to α & Γ and β & Γ phases respectively [Fig.VI.6(a)]. In alloy E_4 , which was found to consist of only two phases (Γ +L) by metallography, a small magnetic effect is observed close to the α phase magnetic transition [Fig.VI.6(a)]. This indicates that alloy E_4 contains small amount of α phase which was not identified by metallography and XRD. Alloy E_1 clearly showed all the three magnetic transitions due to the β , α and Γ phases [Fig.VI.6(a)]. Three phase alloy E_{27} also showed high temperature magnetic transition but since the amounts of α and β phases were small only a single small rise in permeability was possible to see. The permeability versus temperature traces of alloys E_{12} , E_{16} , E_{25} and E_{19} , containing Δ phase together with β and / or Γ phases, showed peculiar magnetic effect after the high temperature magnetic transition due to the β phase was over [Fig.VI.6(b)]. In these alloys, TMA curves showed a cusp like behaviour at lower temperature, i.e. a rise in permeability was observed at about 490°C and a peak appeared at $\sim 210^\circ\text{C}$. The cusp like behaviour was also observed in alloy A of composition similar to that of alloy E_{19} but Mischmetal completely replaced by Nd. However, alloy E_{17} (Δ phase is the matrix phase in this alloy) and E_{26} , containing (Δ + Γ +L) phases, according to metallography and XRD analysis (Table VI.1), showed only one magnetic transition due to the Γ phase and

all these rare-earth elements [1,2]. Hence a large mutual solid solubility of the $R_2Fe_{14}B$ compounds is to be expected. Since the relative intensity of the diffraction lines of the Γ phase matched well with those of the $Nd_2Fe_{14}B$ phase, the crystal structure of the Γ phase is expected to be the same as that of the $Nd_2Fe_{14}B$ phase [Fig.II.22(a)] with RE atoms randomly occupying the Nd positions.

The T_c value of $245^\circ C$ for the Γ phase is lower than the widely reported T_c value for the $Nd_2Fe_{14}B$ phase (i.e. $315^\circ C$) [1,2]. Maocai et.al.[92] have reported that upto 50 pct. substitution of Nd in $(Nd_{1-x}MM_x)_{17}B_8Fe_{77}$ alloys does not alter the T_c of $(Nd,MM)_2Fe_{14}B$ phase. In the present investigation the T_c of $RE_2Fe_{14}B$ phase is found to be $70^\circ C$ less than the T_c of $Nd_2Fe_{14}B$ phase. This may indicate that replacement of Nd by MM produced an effect on T_c beyond 50 pct. replacement of Nd by MM. It is interesting to note that T_c of the Γ phase is considerably higher than the corresponding Ce compound ($T_c \sim 172^\circ C$) [1]. During the course of phase equilibria studies on RE-Co system, Velu et.al.[250] observed that the T_c of RE_xCo_y compounds can be predicted from the simple weighted average [i.e. $T_c(RE_xCo_y) = \sum(wt.pct.R \text{ in RE}) \cdot T_c(R_xCo_y) \times 10^{-2}$] which can be calculated using the T_c of R_xCo_y compounds (R = rare-earth element present in MM) and the chemical composition of the Mischmetal. Using the T_c values of $Ce_2Fe_{14}B$ ($172^\circ C$), $La_2Fe_{14}B$ ($243^\circ C$), $Nd_2Fe_{14}B$ ($315^\circ C$) and $Pr_2Fe_{14}B$ ($292^\circ C$) [1,2], the calculated weighted average value of T_c for the Γ phase [i.e. $\sum(wt.pct.R) \cdot T_c(R_2Fe_{14}B) \times 10^{-2}$] turns out to be $227^\circ C$. The calculated value is about $18^\circ C$ less than the experimentally found value ($245^\circ C$) obtained using VSM. Since the Curie temperatures of different $R_2Fe_{14}B$ compounds, used in the above calculation, were measured by different workers by different techniques [1,2,37], this $18^\circ C$ difference between the calculated and observed T_c value can be justified.

6.2.1.2 The Δ Phase

The Δ phase belongs to the family of structures represented

as the $R_{1+\epsilon}Fe_4B_4$ phase; where $\epsilon \approx 0.1$. The XRD pattern of Δ phase could be indexed on the basis of a tetragonal unit cell of lattice parameters $a = 7.106 \text{ \AA}$, $c = 17.011 \text{ \AA}$ and $c/a = 2.39$. The value of 'a' parameter has been found to be quite close to the RFe_4B_4 phase [159] but the 'c' parameter is rather small. This may not be surprising because the value of 'c' parameter for RFe_4B_4 phases (with different rare-earth elements) shows wide variation from 58.67 to 144.57 \AA [159], owing to the variation of stacking sequence of atom planes in the c-direction [vide structure of $Nd_{1+\epsilon}Fe_4B_4$ in Fig.II.22(b) and its description].

The Δ phase containing alloys, e.g. E_{16} , E_{19} etc. showed a cusp like magnetic transition behaviour in both permeability vs. temperature curves [Fig.VI.6(b)] as well as in the magnetic moment vs. temperature curves (Fig.VI.7). Strikingly similar behaviour was also observed for the alloy A with composition same as that of alloy E_{19} but MM completely replaced by Nd (Fig.VI.6(b) and VI.7). Even though magnetic transition has been observed for the $NdFe_4B_4$ phase [159], Mössbauer studies [153,158] did not corroborate the ferromagnetic state of this phase at room temperature. Different explanations have been given for the magnetic transition observed in the $NdFe_4B_4$ alloys. Bezingue et.al.[159] and Givord et.al.[161] suggested that the magnetic transition observed in the $NdFe_4B_4$ alloys was due to the presence of small amount of $Nd_2Fe_{14}B$ phase. While the presence of small amount of $Nd_2Fe_{14}B$ may be a possible explanation for the cusp like behaviour of alloys close to the Δ phase region, a similar magnetic effect should then be expected in alloys containing very small amount of $RE_2Fe_{14}B$ phase. The TMA plot for alloy E_{35} which contains very small amount of $RE_2Fe_{14}B$ phase [Fig.VI.2(b)] does not show any such behaviour. Though the alloy E_{16} , containing the β phase as the matrix phase with reasonable amount of the Δ phase and small amount of the Γ phase in its microstructure, shows the cusp like behaviour in the temperature range of 200-500 $^{\circ}\text{C}$; the alloy E_{17} , which is having the Δ phase as its matrix phase with small amount of the Γ and solidified liquid phases in its microstructure, showed only the magnetic transition due to the Γ phase [Fig.VII.6(b)]. No cusp like behaviour could be found in the permeability vs. temperature

trace of alloy E_{17} [Fig.VI.6(b)]. Thus the presence of small amount of Γ phase in the Δ matrix does not appear to be the reason for the cusp like behaviour in the TMA traces.

More recently, Fidler [34] has studied the $NdFe_4B_4$ phase using Lorentz electron microscopy and electron microprobe. It has been revealed by these studies [34] that the $NdFe_4B_4$ phase occurs in several metastable modifications with Nd/Fe ratio between 3.6 to 3.9. Contrary to the Curie temperature measurements [159], which has shown a Curie temperature of ~ 13 K for the $NdFe_4B_4$ phase, certain metastable modifications at room temperature show magnetic domain structure similar to a ferromagnetic material [34]. Thus, it is possible that the observed cusp like behaviour in the TMA trace of the $NdFe_4B_4$ as well as the $REFe_4B_4$ phases (Fig.VI.6(b) and VI.7) is due to the presence of ferromagnetic metastable modifications of the 1:4:4 phase. At present no satisfactory explanation is available for the cusp like behaviour observed in the TMA traces of the $NdFe_4B_4$ and $REFe_4B_4$ phases. Further work, possibly with high temperature Lorentz electron microscopy, is required for a more definite explanation of the magnetic transition observed in some of the alloys containing the Δ or the $NdFe_4B_4$ phase.

6.2.1.3 The α Phase

X-ray diffraction as well as TMA studies confirmed the presence of the α phase in the RE-Fe-B alloys quenched from 1000 $^{\circ}C$. The α phase was found to have a lattice parameter, $a = 2.868$ Å (for alloy E_{33}), quite close to the lattice parameter of pure α -Fe (i.e. 2.864 Å [242]) indicating very low solid solubility of RE and B in α -Fe (this solid solution of α -Fe is referred to as the α phase). This observation is supported by the reported very low solubility of B (0.01 at.pct.) and rare-earth elements (< 0.5 at.pct.) in α -Fe [135].

In the Ce-Fe and Nd-Fe systems, the bcc α -Fe phase has been shown to be stable upto 925 $^{\circ}C$ and 935 $^{\circ}C$, respectively [135]. The

result of the present investigation may suggest that the α solid solution phase is either stabilized at 1000 °C by the addition of RE and B, or possibly it arises due to an instantaneous transformation of the fcc Fe solid phase γ to the bcc α phase during quenching of alloys. To investigate this, a Fe rich alloy E₃₃ (annealed at 1000 °C for 3 days and quenched to room temperature) was subjected to DSC study. The DSC trace, given in Fig.VI.8, showed two thermal effects. The first endothermic peak in the DSC plot corresponds to the ferromagnetic to paramagnetic transition of the α phase. The peak occurs at a temperature of ~ 764 °C which is very close to the T_c of pure α -Fe (770 °C). The second endothermic peak starting at ~ 917 °C is very sharp like a first order transformation. Since the second DSC peak in Fig.VII.8 is like a first order transformation and the transformation temperature is very close to the α -Fe to γ -Fe transition temperature and the fact that in most R-Fe systems a peritectoid reaction involving the α -Fe, γ -Fe and R_2Fe_{17} phase occurs near this temperature, it is possible that this thermal effect is related to the $\alpha \rightarrow \gamma$ transition. This is discussed in more detail in the next chapter.

6.2.1.4 The β Phase

The alloy E₃₂, which is very close to the Fe₂B composition (0.5 at.pct. RE, 66.0 at.pct. Fe and 33.5 at.pct. B), turned out to be a three phase alloy consisting of the β (matrix), Δ and Γ phases [Fig.VI.2(d)]. This alloy was used to determine the lattice parameters of the β phase. The lattice parameters of the tetragonal unit cell of β phase ($a = 5.104$ Å, $c = 4.254$ Å, $c/a = 0.833$, Table VI.4) were found to agree well with the lattice parameters of the Fe₂B phase observed in the Fe-B system ($a = 5.109$ Å, $c = 4.249$ Å, $c/a = 0.832$ [251]).

The TMA trace of alloy E₂₅ containing the β phase [Fig.VI.6(b)] indicates the magnetic transition temperature to be about ~ 900 °C. The magnetic transition temperature for the Fe₂B phase is reported to be 740 °C [135]. Since the solubility of RE in Fe₂B phase appears to be very small, this large change in T_c

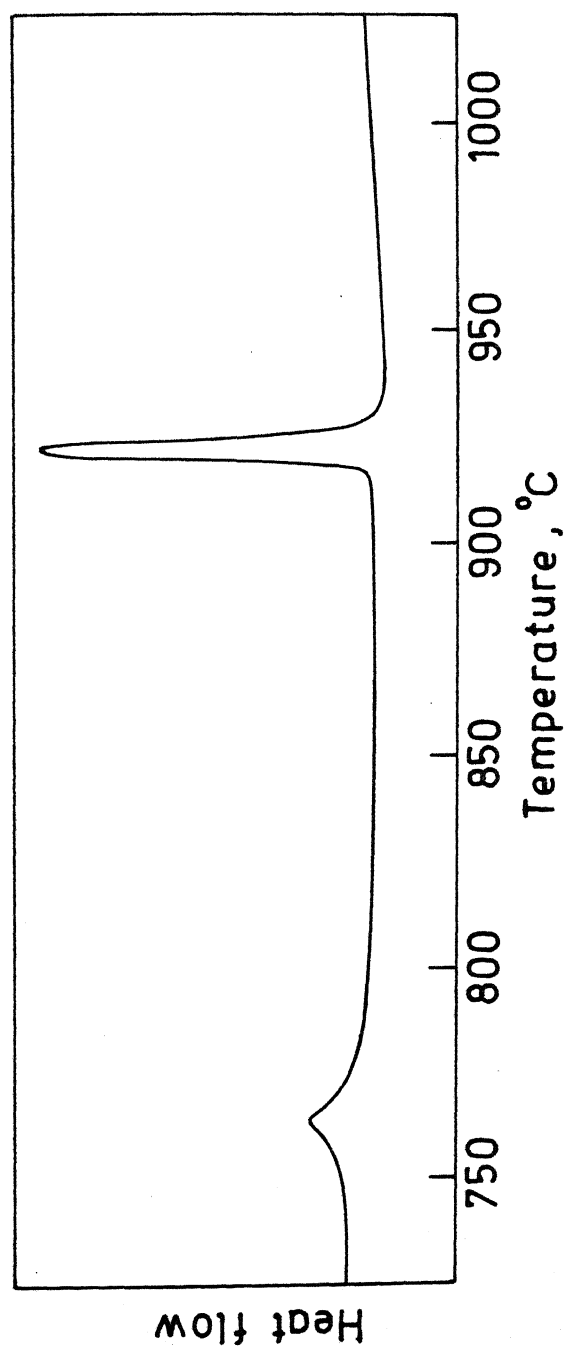


Fig.VI.8 DSC trace of alloy E₃₃ annealed at 1000 °C for 3 days

can not be attributed to the solubility of RE in Fe_2B . As discussed earlier (section 4.2.3) the magnetic transition temperature is not accurately determined by the permeability testing apparatus because of the fact that T_c in this case is being considered at the point where slope change in the γ TMA trace occurs as the specimens cools from high temperature. This is expected to give a higher T_c value, especially if the short range magnetic order is set up before the spontaneous magnetization. In the case of both pure Fe (Fig.IV.4) and alloy E₂₅, the change in the slope of TMA plot starts reasonably early and the T_c obtained from the TMA plots is rather high. The Curie temperature of the Fe_2B phase could not be determined by the use of VSM fitted with an oven assembly because the maximum temperature attainable in this system was about 500 °C.

6.2.2 Phase Equilibria

The RE-Fe-B is a multicomponent system, RE represents the total rare-earth content of the Mischmetal (MM). As assumed in the case of the RE-Co-Fe-Cu-Zr alloys, RE is being treated as a single component so that the phase equilibria can be represented as a ternary system. This description of the multicomponent system, involving MM, as a ternary system has been found successful in interpreting the phase equilibria data in the RE-Co-Fe system [131,132] as well as the RE-Co-Fe-Cu-Zr system [244], and is expected to be applicable to the result of RE-Fe-B system.

In the investigated composition region of the RE-Fe-B system, two ternary intermediate phases Γ and Δ were located near the $\text{RE}_2\text{Fe}_{14}\text{B}$ and REFe_4B_4 stoichiometries, respectively. The existence of only two binary phases, namely the α and the β , was observed. Unlike the Nd-Fe-B system, in which the $\text{Nd}_2\text{Fe}_{17}$ phase is observed in equilibrium with the $\text{Nd}_2\text{Fe}_{14}\text{B}$ phase, no $\text{RE}_2\text{Fe}_{17}$ phase could be detected in any of the RE-Fe-B alloys. A liquid (L) exists at the high RE content region (at RE > 40 at.pct.) of the RE-Fe-B system.

The phase analysis of the investigated alloys, through metallography, XRD and TMA indicates (Table VI.1) that, except for one alloy (alloy E_{30}), all other alloys contain either two or three phases. The presence of two or three phases in alloy E_{33} and E_{35} [Fig.VI.2(a) and 2(b)] and E_{32} [Fig.VI.2(d)] indicated that the Fe solid solution phase α (or possibly fcc γ at the temperature of investigation) and the intermediate phase Fe_2B do not extend far into the RE-Fe-B ternary. The three phase alloys E_{35} and E_{27} , which are very close to the α and Γ phase regions respectively, indicate the extent of the $\alpha+\Gamma+\beta$ three phase region.

The alloy E_{34} (11.5 at.pct. RE, 1.0 at.pct. B and 87.5 at.pct. Fe), located very close to the RE-Fe binary, was found to have three phases α , Γ and L. In most of the R-Fe systems, a R_2Fe_{17} phase exist near about 88 at.pct. Fe composition. Since none of the investigated alloys, including E_{34} , showed the presence of the RE_2Fe_{17} phase, it may be concluded that either the RE_2Fe_{17} phase does not exist in the RE-Fe system or it is not stable at the temperature of investigation i.e. 1000 °C. In the latter case, possibly it does not extend far into the RE-Fe-B ternary.

The alloy E_2 was found to have three phases, Γ , α and liquid. The X-ray and TMA also confirmed the presence of the α and Γ phases. The same was the case for alloys E_{28} and E_3 . Alloy E_4 showed essentially two phases which could be identified through metallography and X-ray as the Γ and liquid phase. TMA [Fig.VI.6(a)] however showed in alloy E_4 , besides the magnetic transition due to the Γ phase, another high temperature magnetic transition close to that of the α phase. This indicated the presence of small amount of α phase in alloy E_4 which was not possible to detect through X-ray diffraction and as well as metallography. On the other hand, alloy E_5 has shown only two phases, Γ and liquid, and TMA confirmed the presence of Γ phase. Thus, the three phase region ($\Gamma+\alpha+L$) extends from alloy E_2 to E_4 .

Metallographic analysis showed that alloy E_{29} , E_{26} , E_{17} , E_{14} , E_{13} , E_{11} , E_{10} and E_9 have similar three phase microstructure consisting of Γ , Δ and L . The Δ phase was not detected in the XRD pattern of alloy E_{29} because it was present in very small amount [Fig.VI.1(h)]. All these alloys thus established the presence of a wide $\Gamma+\Delta+L$ three phase field. The alloy E_{18} showed a two phase microstructure consisting of Δ and liquid, and thus established the equilibrium between the Δ and liquid phase at 1000 °C.

In the case of the alloy E_{31} only two phases ($\Gamma+\Delta$) were found by XRD analysis and the presence of a third phase β was inferred through comparison of its microstructure [Fig.VI.1(g)] with that of the alloy E_{24} which had a similar microstructure (Γ , Δ , β , Table VI.1) but with higher (X-ray detectable) amount of β phase. Through metallography, alloys E_{12} , E_{25} , E_{32} and E_{16} were also found to have three phases Γ , β and Δ and the presence of all these phases could be confirmed also by XRD in all the alloys except E_{32} . The presence of the Γ phase in alloy E_{32} [Fig.VI.2(d)] could not be detected through XRD because of its very small amount. All these results thus established the presence of a wide $\Gamma+\beta+\Delta$ phase field.

With the help of phase analysis of alloys (Table VI.1), a partial 1000 °C isothermal section of the RE-Fe-B system was constructed as shown in Fig.VI.9. Since the melting losses were very small (< 0.5 wt.pct.), it was assumed that the intended and actual composition of the alloys were the same. In the shown phase diagram (Fig.VI.9), single phase composition is represented by a closed circle, two phase compositions by open circles and three phase compositions by open triangles. Owing to the limited number of alloys investigated, the location of the phase boundaries for the two or three phase regions could not be determined very accurately. The composition of none of the investigated alloys fell in the two phase regions $\alpha+\beta$, $\Gamma+\beta$ and $\Gamma+\Delta$. Hence, only the approximate locations of the phase regions are shown in the phases diagram.

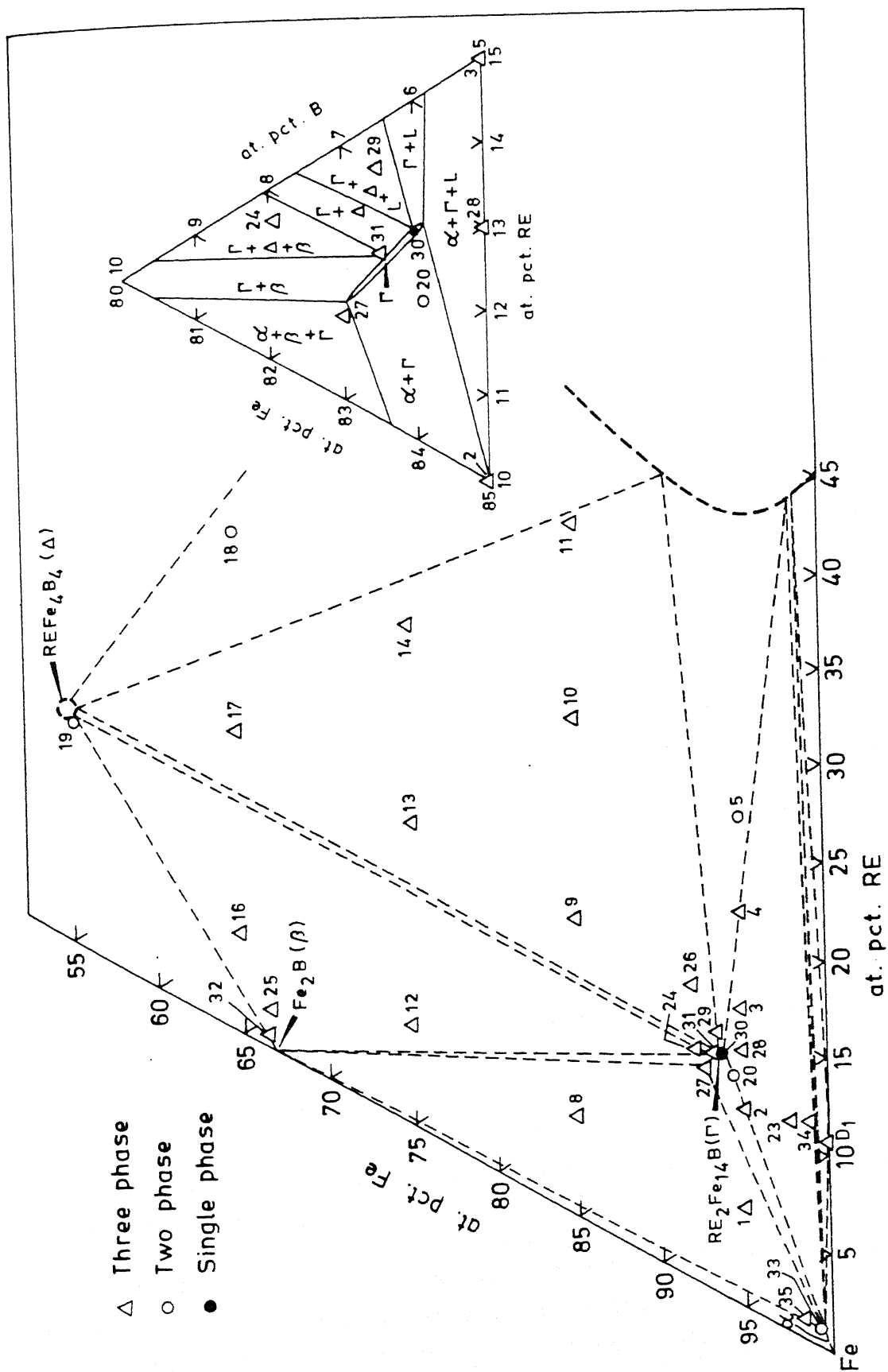


Fig.VI.9 RE-Fe-B isothermal section at 1000 °C

Since the 2:14:1 phase is the most important phase for the fabrication of Nd-Fe-B permanent magnets, the ternary phase region near the $\text{RE}_2\text{Fe}_{14}\text{B}$ stoichiometry has been located with greater precision than the other regions (see insert in Fig.VI.9). Alloy E_{30} containing 12.5 at.pct. RE, 81.5 at.pct. Fe and 6.0 at.pct. B, was found to be single Γ phase. The immediate environment of Γ phase comprises of four two phase regions ($\Gamma+\alpha$, $\Gamma+\beta$, $\Gamma+\Delta$ and $\Gamma+\text{L}$) and four three phase regions ($\Gamma+\alpha+\beta$, $\Gamma+\Delta+\beta$, $\Gamma+\Delta+\text{L}$, and $\Gamma+\alpha+\text{L}$).

The alloy E_{30} is a single phase (Γ) alloy. Alloy E_{31} , having the same amount of Fe as alloy E_{30} and 0.5 at.pct. higher B, shows the presence of three phases, the Γ , Δ and β , in its microstructure [Fig.VI.1(h)]; the amount of second (Δ) and third (β) phases are very small. Alloy E_{27} , which contains about the same amount of Fe as alloy E_{30} but with 1.0 at. pct. more B, shows three phases, Γ , α and β , in its microstructure [Fig.VI.1(f)] and the amount of second (α) and third (β) phase in this alloy are also very small. Alloy E_{20} , which is having the about the same amount of B as alloy E_{30} and 0.8 at.pct. more Fe, shows a two phase microstructure with small amount of the second phase α in the matrix of Γ phase [Fig.VI.1(e)]. These metallographic observations indicate that the Γ phase has a small extension (about 1 at.pct.) along approximately a constant Fe line and possibly the width of the phase region is not large (Fig.VI.9).

Lattice parameters of Γ phase were calculated from the diffraction pattern of multiphase alloys and compared with the lattice parameters of Γ phase in alloy E_{30} (Table VI.5). Practically no change in lattice parameters of the Γ phase is observed with the change of alloy composition. This suggest that the Γ phase region is very narrow and small change in the composition of Γ phase does not produce any appreciable effect on the lattice parameters.

Most of the TMA work was carried out using the permeability testing apparatus. As discussed earlier (section 4.2.3), accurate measurement of T_c is difficult from these TMA traces. For the single phase alloy E_{30} the T_c was determined more accurately by

Table VI.5: Lattice Parameters and Curie Temperature of Γ Phase in the Alloys of Different Chemical Compositions

Alloy	Composition, at.pct.			Lattice Parameters*, Å		T_c °C
	RE	Fe	B	a	c	
E ₂	10.0	85.0	5.0	-	-	246
E ₂₇	11.0	82.0	7.0	8.78 ₄	12.17 ₇	245
E ₂₀	11.8	82.3	5.9	8.78 ₈	12.17 ₆	-
E ₂₄	11.8	80.3	7.9	8.78 ₃	12.17 ₇	251
E ₃₁	12.0	81.5	6.5	8.78 ₃	12.17 ₅	-
E ₃₀	12.5	81.5	6.0	8.78 ₄	12.17 ₇	250
E ₂₉	13.0	80.5	6.5	8.78 ₃	12.18 ₀	-
E ₃	15.0	80.0	5.0	-	-	248
E ₂₆	15.0	77.7	8.0	8.78 ₇	12.17 ₉	248

E₃₀ is single phase (Γ) alloy

* Calculated using (0,0,10) and (722) reflections

making use of magnetic moment vs. temperature curve obtained through a VSM attached with a high temperature oven assembly. The permeability vs. temperature trace for the same alloy showed a sharp magnetic transition due to the Γ phase and the T_c determined using the VSM coincided with the temperature at which the permeability vs. temperature trace showed maximum slope during cooling of the specimen from high temperature. Thus T_c may be estimated for the Γ phase alloys from the permeability vs. temperature traces if the above criterion, i.e. the temperature corresponding to the maximum slope of the the TMA trace obtained using permeability testing apparatus, is used to estimate T_c . On this basis T_c was determined for the alloys surrounding the Γ phase region and is given in Table VI.5. The results indicate a small variation in T_c , the higher B end alloy E₂₇ having slightly lower T_c than the low B end alloy E₃₀. This also supports the observation that the Γ phase has a small extension more or less along a constant Fe line.

Even though the RE-Fe-B system is a multicomponent system, the determined RE-Fe-B phase equilibria at 1000 °C do not appear to be any different from what is expected for a ternary system. The 1000 °C isothermal section of the RE-Fe-B system, in general, agrees well with the 1000 °C section of the Nd-Fe-B system (Fig.II.20). Similar set of ternary intermediate phases, with 2:14:1 and 1:4:4 stoichiometry, α and Fe_2B phases and a liquid are observed in both the systems. In terms of the phases found, the only difference which occurs in the two systems is the absence of the 2:17 stoichiometry phase in the RE-Fe-B system. Very limited extension of the α and Fe_2B phases is observed in both the systems. Conflicting claims have been made in the literature [153,158] regarding the solid solubility region of the $\text{Nd}_2\text{Fe}_{14}\text{B}$ phase. Buschow et.al.[153] reported that the $\text{Nd}_2\text{Fe}_{14}\text{B}$ has a single composition stoichiometry. More recent investigation of Tsai et.al.[158] have indicated a homogeneity region for Nd in the $\text{Nd}_2\text{Fe}_{14}\text{B}$ phase (0.6 at.pct. at 1000 °C). The reported claim of Tsai et.al. seems to strengthen the finding of this investigation that the Γ phase has a small homogeneity region. The phase regions in the immediate surroundings of the single phase region of 2:14:1, 1:4:4 etc are also quite similar in the two phase equilibria (Fig.II.20 ,Fig.VI.9). Since no 2:17 phase is found in any of the investigated RE-Fe-B alloys, (2:17+2:14:1) tie line observed in the case of Nd-Fe-B was found missing in the RE-Fe-B system. This gave rise to a single three phase field ($\Gamma+\alpha+L$) instead of two three phase fields, namely 2:14:1+Fe+2:17 and 2:14:1+2:17+L observed in the Nd-Fe-B system.

The absence of the $\text{RE}_2\text{Fe}_{17}$ phase in the RE-Fe-B system was intriguing and this led to a detail study of the Fe-RE system at the Fe rich side which is given in the chapter VII. A binary RE-Fe alloy of 2:17 stoichiometry composition (marked as D_1 in Fig.VI.9) was found to have three phases ($\alpha+\text{RE}_2\text{Fe}_{17}$ +liquid) indicating the presence of a three phase region close to the RE-Fe end of RE-Fe-B triangle.

6.3 Summary

The 1000 °C isothermal section of the RE-Fe-B system has been established at the iron rich side, upto about 40 at.pct. RE and about 45 at.pct. B, using metallography, XRD and TMA techniques. Two ternary intermediate phases Γ and Δ , which are structurally similar to the $R_2Fe_{14}B$ and RFe_4B_4 phases, have been identified. The Γ and Δ phases are tetragonal with lattice parameters $a = 8.784 \text{ \AA}$, $c = 12.177 \text{ \AA}$ and $a = 7.106 \text{ \AA}$, $c = 17.011 \text{ \AA}$, respectively. The Curie temperature of the Γ phase is $\sim 245 \text{ }^\circ\text{C}$. The Δ phase also shows a peculiar magnetic transition between 240 and 440 °C and its magnetic behaviour is not well understood. Besides the ternary intermediate phases Γ and Δ , the other phases observed are a bcc Fe solid solution phase α , a Fe_2B (β) phase and a liquid. The bcc α phase possibly arises out of the transformation of the fcc Fe solid solution phase γ when the alloys are quenched to room temperature after equilibration at 1000 °C. The α and β phases have practically no solubility of RE. The Γ phase appears to have a small homogeneity region. The phase equilibria at 1000 °C is quite similar to the Nd-Fe-B system except that no RE_2Fe_{17} phase is observed in equilibrium with any of the ternary phases in the the RE-Fe-B system at 1000 °C.

CHAPTER VII

PHASE EQUILIBRIA IN THE RE-Fe SYSTEM

During the phase equilibria studies on RE-Fe-B system, no ternary alloy showed the presence of the $\text{RE}_2\text{Fe}_{17}$ phase even when the B content was as low as 1.0 at.pct. The presence of the bcc α phase at 1000°C was also somewhat unusual as it is not found stable at this temperature in any of the R-Fe binaries, where R = Ce, Nd, Pr, Sm etc (section 2.2.2). All these observations led to a detailed study of the phase equilibria in RE-Fe system at the Fe end in the composition range of 0.5 to 33.3 at.pct. RE.

7.1 Results

Thirteen alloys were prepared to investigate the Fe end of RE-Fe system. The chemical composition of the alloys are given in Table VII.1. The alloys labelled as D_{000} , D_{00} , D_0 and D_{12} had 0.5 to 5.0 at.pct. RE, D_{13} , D_1 to D_{10} had RE content between 9.5 to 13.5 at.pct. and D_2 to D_5 had RE content between 16.67 to 33.3 at.pct.. Of these alloys, the alloy D_1 has the composition corresponding to the 2:17 stoichiometry and D_5 that of the 1:2 stoichiometry. The composition of alloy D_4 is located close to the 5:17 stoichiometry. The alloys were annealed at 700, 900, 950, 1000, 1050, 1100 and 1150°C for various lengths of time as given in Table VII.1.

A summary of phase analysis results using metallography, XRD, TMA and DSC is presented in Table VII.1. Differential scanning calorimetry (DSC) technique was used to establish the various transformation temperatures. The phases that are encountered in RE-Fe system are the $\text{RE}_2\text{Fe}_{17}$ phase, the REFe_2 phase and a bcc Fe solid solution phase (here in referred to as α phase). A liquid phase was also encountered in various alloys when annealed at different temperatures. No $\text{RE}_5\text{Fe}_{17}$ phase was found in any of the investigated alloys. The details of results obtained are given in the subsections which follow.

Table VII.1: Chemical Composition and Phase Analysis of the RE-Fe Alloys

Alloy Code	Intended Composition (at.pct.)		Annealing		Phase Analysis			
	RE	Fe	Temp. °C	Time days	Metallo- graphy	XRD	TMA	DTA Transition Temps. °C
(i)	(ii)	(iii)	(iv)	(v)	(vi)	(vii)	(viii)	(ix)
D ₀₀₀	0.5	99.5	900	14	α, 2:17	α, 2:17	—	764, 915
			1000	10	α, 2:17	α, 2:17	—	—
			1100	2	α, L	α	—	—
D ₀₀	1.0	99.0	1000	10	α, 2:17	α, 2:17	—	765, 917
			1100	10	α, L	α	—	—
			1150	1	α, L	α	—	—
D ₀	2.0	98.0	900	14	α, 2:17	α, 2:17	—	764, 920
			1000	4	α, 2:17, L	α, 2:17	—	—
			1100	2	α, L	α	—	—
D ₁₂	5.0	95.0	900	7	α, 2:17	α, 2:17	—	764, 930
D ₁₃	9.5	90.5	900	7	2:17, α	2:17, α	—	764, 936
D ₁	10.5	89.5	700	30	2:17, α	2:17, α	2:17	—
			800	7	2:17, α	2:17, α	—	—
			900	16	2:17, α	2:17, α	α, 2:17	—
			930	7	2:17, α	2:17, α	—	—
			1000	3	2:17, α, L	2:17, α	α, 2:17	—
			1100	2	α, L	α, 2:17*	—	—

Contd.

... Contd.

(i)	(ii)	(iii)	(iv)	(v)	(vi)	(vii)	(viii)	(ix)
D _{1A}	11.5	88.5	800	7	2:17,α	2:17,α	-	-
			900	7	2:17,α	2:17,α	-	-
			1000	3	2:17,α,L	2:17,α	-	-
D _{1B}	12.5	87.5	800	7	2:17,α	2:17,α	-	-
			900	7	2:17,α	2:17,α	-	-
			1000	6	2:17,α,L	2:17,α	-	-
D _{1C}	13.5	86.5	800	7	2:17,α	2:17,α	-	-
			900	7	2:17,α	2:17,α	-	-
			1000	3	2:17,α,L	2:17,α, <u>1:2</u>	-	-
D ₂	16.7	83.3	700	30	2:17,1:2	2:17,1:2	-	770
			900	16	2:17,L	2:17, <u>1:2</u>	-	-
			1000	3	2:17,L	2:17, <u>1:2</u>	-	-
D ₃	20.8	79.2	700	30	2:17,1:2	2:17,1:2	-	-
			900	6	2:17,L	2:17, <u>1:2</u>	-	-
			1000	3	2:17,L	2:17, <u>1:2</u>	-	-
γ ₄	22.2	77.8	700	30	2:17,1:2	2:17,1:2	2:17	750
			900	16	2:17,L	2:17, <u>1:2</u>	-	-
			1000	3	2:17,L	2:17, <u>1:2</u>	2:17	-
D ₅	33.3	66.7	700	5	1:2,2:17,L	1:2,2:17	-	677
			900	7	2:17,L	2:17, <u>1:2</u>	-	-
			1000	3	2:17,L	2:17, <u>1:2</u>	-	-

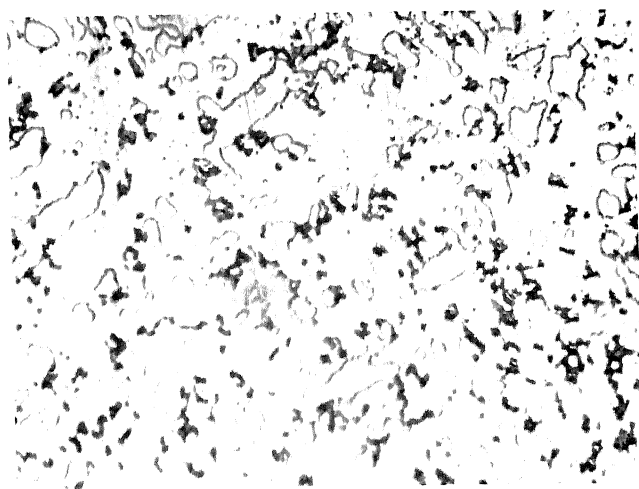
* Underline means that the phase has solidified from the liquid phase during quenching from the annealing temperature (vide text, section 7.1.2).

7.1.1 Metallographic Analysis

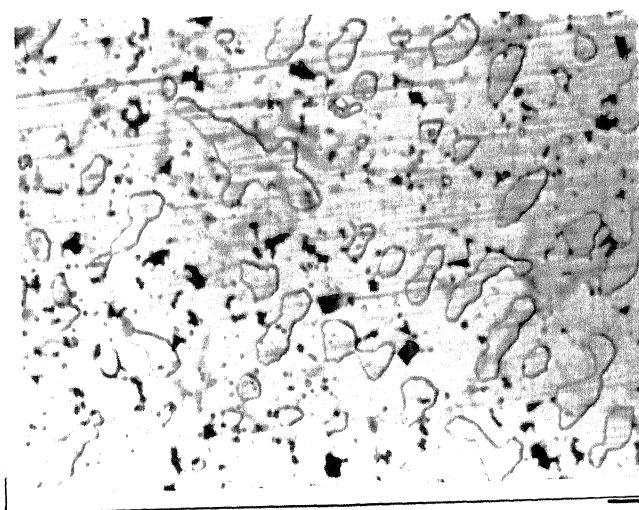
The microstructure of the RE-Fe alloys, especially those with higher RE contents, could be seen even in the as polished condition. However, 0.5-1 pct. HNO_3 was used as etching reagent for producing better contrast and easy identification of the phases present. The number of phases observed in each alloy and their possible identity, as inferred in conjunction with X-ray diffraction analysis (vide next subsection 7.1.2 on X-ray results), are listed in Table VII.1. All the investigated alloys contained two or three phases. Some typical micrographs of alloys at different temperatures are given in Fig.VII.1 to VII.3.

Micrograph in Fig.VII.1(a) corresponds to alloy D_1 annealed at 700°C . The microstructure of D_1 consists of the $\text{RE}_2\text{Fe}_{17}$ matrix phase and a second phase which is the α phase. The small dark grey regions which occur could not be identified. The dark grey regions also occurred in this alloy after annealing at 900°C with no appreciable change in the relative amount [Fig.VII.1(b)]. This suggests that the dark grey regions are possibly small etched out regions or an impurity phase. The alloys $D_1(800^\circ\text{C})$, D_{000} , D_{00} , D_0 , D_{12} , D_{13} , D_{1A} , D_{1B} , D_{1C} (900°C) and $D_1(930^\circ\text{C})$ also showed microstructures similar to the alloy D_1 annealed at 700°C but with the amount of the $\text{RE}_2\text{Fe}_{17}$ phase increasing with increase in the RE content of the alloy. The microstructure of alloy D_{1C} (900°C) consisted of essentially the $\text{RE}_2\text{Fe}_{17}$ phase with very small amount of the α phase.

The alloys D_2 to D_5 contain still higher amount of RE than D_{1C} . The alloys D_2 to D_4 show at 700°C similar two phase microstructure in which the α phase was not found. In the microstructure of alloy D_3 [Fig.VII.2(a)] the white matrix phase and the second grey phase correspond to the $\text{RE}_2\text{Fe}_{17}$ and the REFe_2 phases, respectively. While an initial increase in RE content upto 22.2 at.pct. (alloy D_4) increases only the relative amount of the REFe_2 phase, a further increase in RE content showed in alloy D_5 (700°C) [Fig.VII.2(b)] three phases in the microstructure; the

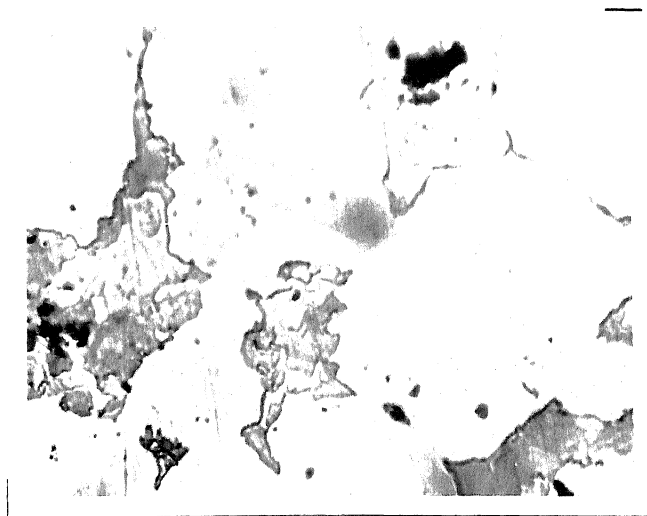


(a)

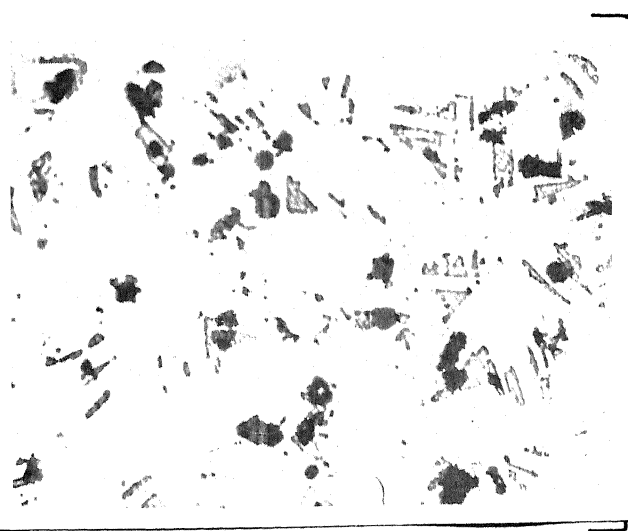


(b)

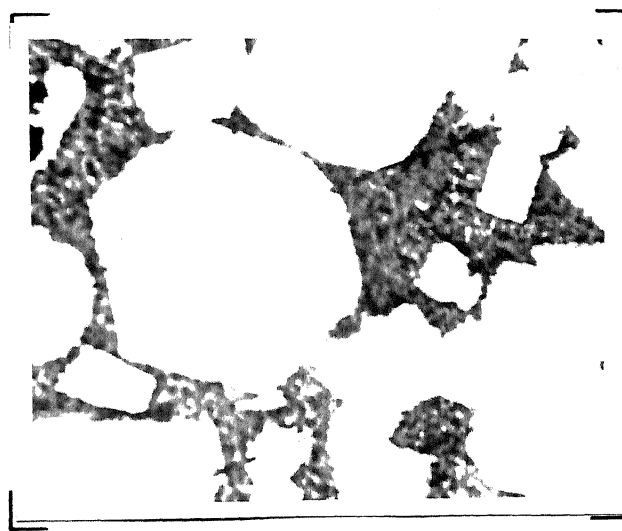
Fig.VII.1 Optical micrographs of alloy D₁ annealed at
(a) 700 °C (2 phases), matrix - 2:17, second phase - α
(b) 900 °C (2 phases), matrix - 2:17, second phase - α
(Mag. 400x)



(a)



(b)



(c)

Fig.VII.2 Typical optical micrographs of some high RE containing RE-Fe alloys annealed at 700 °C and 900 °C

(a) D_3 (700 °C), 2 phases : matrix - 2:17 phase, grey regions - 1:2 phase

(b) D_5 (700 °C), 3 phases : matrix - 1:2 phase, white islands - 2:17, grey triangles - L, black regions - pits

(c) D_4 (900 °C), 2 phases : matrix - 2:17, dark reg.- L
[Mag. (a),(b) 400x and (c) 100x]

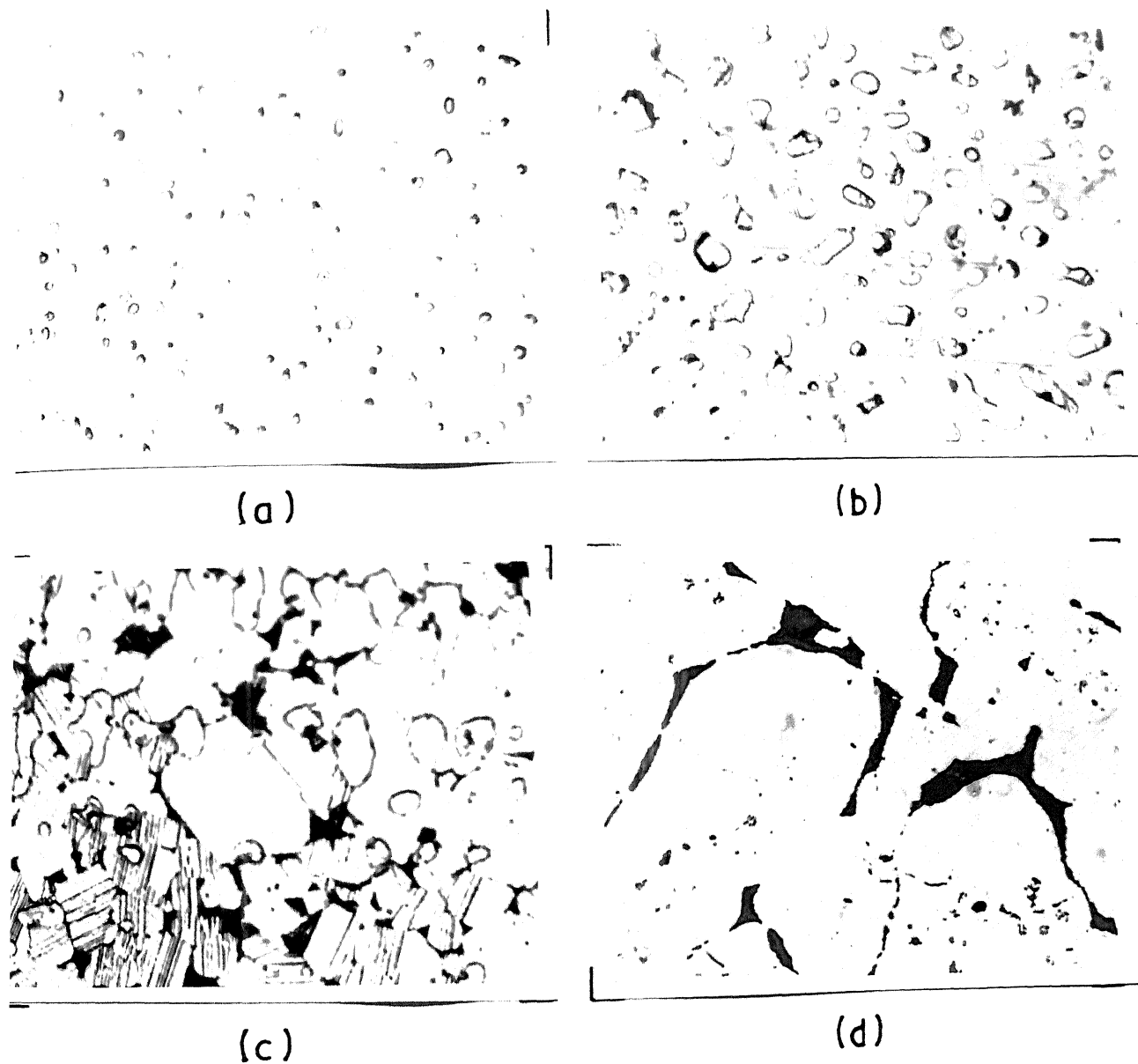


Fig.VII.3 Typical optical micrographs of some high Fe containing RE-Fe alloys annealed at 1000 °C and 1100 °C:

- (a) D_{000} (1000 °C), 2 phases : matrix α , 2nd phase 2:17
 - (b) D_0 (1000 °C), 3 phases : matrix α , white islands with twins 2:17, black regions L
 - (c) D_1 (1000 °C), 3 phases : matrix with twins 2:17, white islands α , black regions L
 - (d) D_0 (1100 °C), 2 phases : matrix α , black regions L
- [Mag. (a)-(c) 400x and (d) 200x]

grey matrix of REFe_2 phase, white islands of the $\text{RE}_2\text{Fe}_{17}$ phase and additional dark grey regions of solidified liquid. The solidified liquid phase has a tendency to chip off very easily during polishing and this led to the formation of pits which appear as very dark regions in Fig.VII.2(b). Unlike the alloys D_{000} to D_{1C} , which at 900°C show microstructural features similar to those at 700°C , the alloys D_2 to D_5 showed at 900°C (also at 1000°C) a two phase microstructure consisting of the $\text{RE}_2\text{Fe}_{17}$ phase and a liquid phase [Fig.VII.2(c)].

Figs.VII.3(a)-(b) show the microstructures of alloys D_{000} and D_0 annealed at 1000°C . The alloy D_{000} and D_{00} consist of two phases, namely, the Fe solid solution phase (white matrix) and small particles of the $\text{RE}_2\text{Fe}_{17}$ phase; the relative proportion of the $\text{RE}_2\text{Fe}_{17}$ phase was more in the alloy D_{00} . The alloy D_0 at 1000°C shows [Fig.VII.3(b)] larger amount of $\text{RE}_2\text{Fe}_{17}$ phase and also shows the presence of a liquid phase (small black region) besides the Fe solid solution matrix phase. At 1000°C , the alloys D_1 , D_{1A} , D_{1B} and D_{1C} also showed three phase microstructure similar to the alloy D_0 but with higher amounts of liquid and the $\text{RE}_2\text{Fe}_{17}$ phases [Fig.VII.3(c)]. The grains of the $\text{RE}_2\text{Fe}_{17}$ phase appear to be heavily twinned [Fig.VII.3(b), (c)]. The microstructures of D_{000} , D_{00} , D_0 , D_1 annealed at 1100°C and D_{00} annealed at 1150°C show the presence of two phases, namely, Fe solid solution phase α and solidified liquid [Fig.VII.3(d)].

7.1.2 X-Ray Diffraction Analysis

A terminal solid solution, bcc α phase, two intermediate phases, namely the $\text{RE}_2\text{Fe}_{17}$ and the REFe_2 phases, were identified on the basis of X-ray diffraction data. X-ray diffraction patterns for some selected alloys homogenized at 700, 900, 1000 and 1100°C , are compiled in Fig.VII.4 to 7.

The indexed diffraction patterns of the two intermediate phases $\text{RE}_2\text{Fe}_{17}$ and REFe_2 are given in Tables VII.2 and VII.3. The diffraction pattern of the alloy D_1 annealed at 700°C [Fig.VII.4(a)] could be indexed on the basis of a hexagonal unit

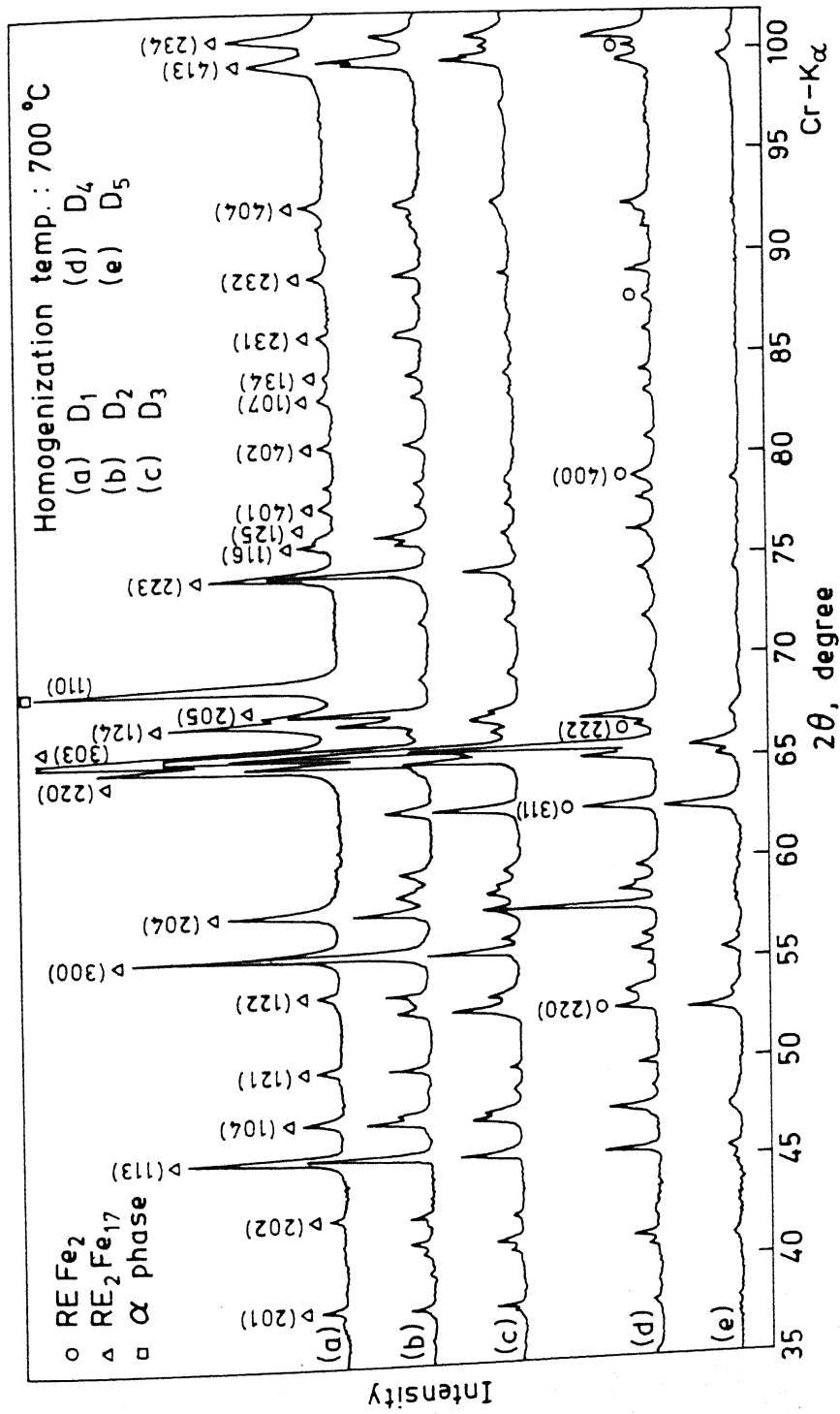


Fig.VII.4 XRD patterns of some RE-Fe alloys homogenized at 700 °C : (a) D₁; (b) D₂; (c) D₃; (d) D₄; and (e) D₅

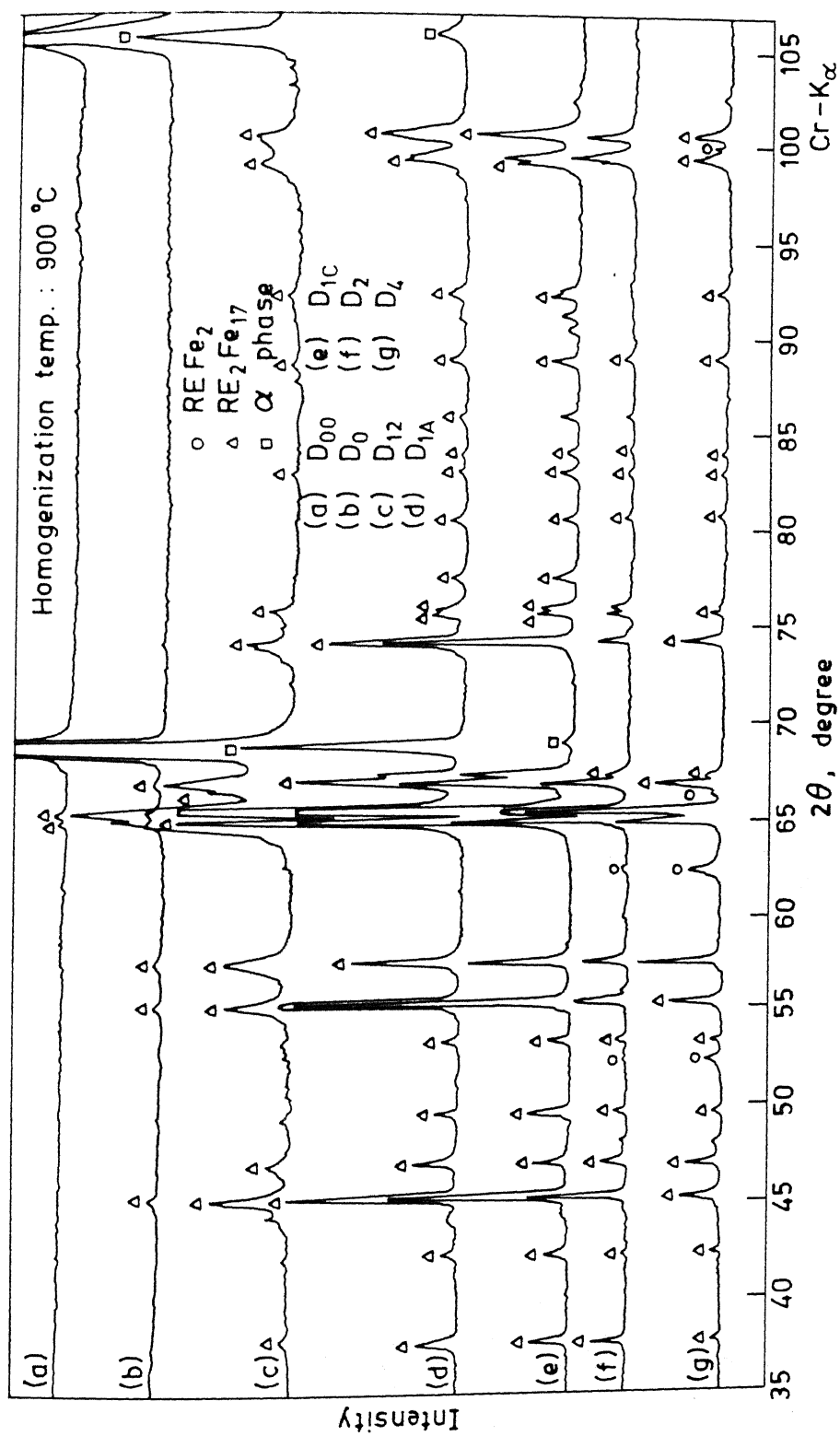


Fig.VII.5 XRD patterns of some RE-Fe alloys homogenized at 900 °C : (a) D₀₀; (b) D₀; (c) D₁₂; (d) D_{1A}; (e) D_{1C} (f) D₂; and (g) D₄

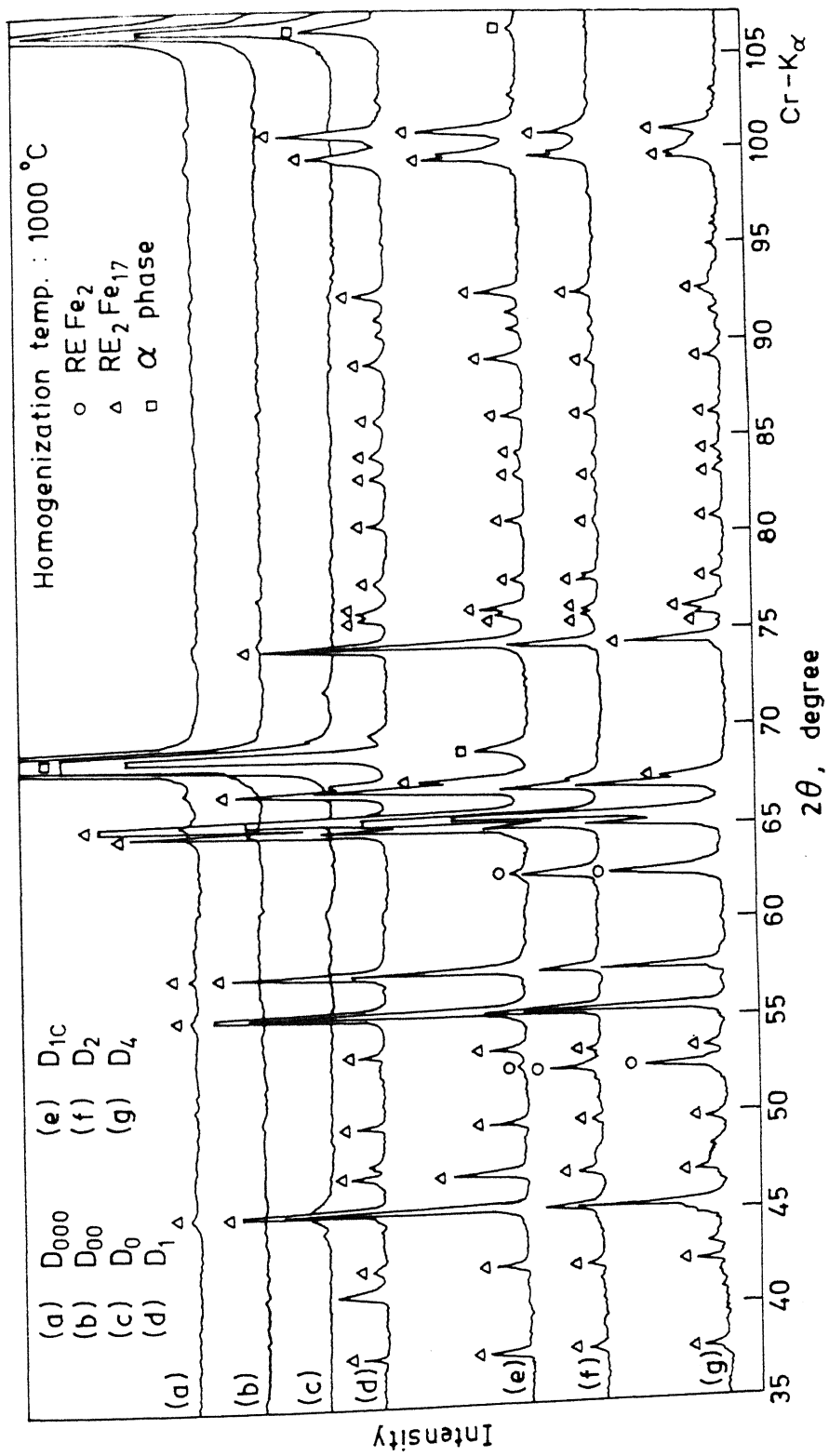


Fig.VII.6 XRD patterns of some RE-Fe alloys homogenized at 1000 °C : (a) D₀₀₀; (b) D₀₀; (c) D₀; (d) D₁; and (e) D_{1C} (f) D₂; and (g) D₄

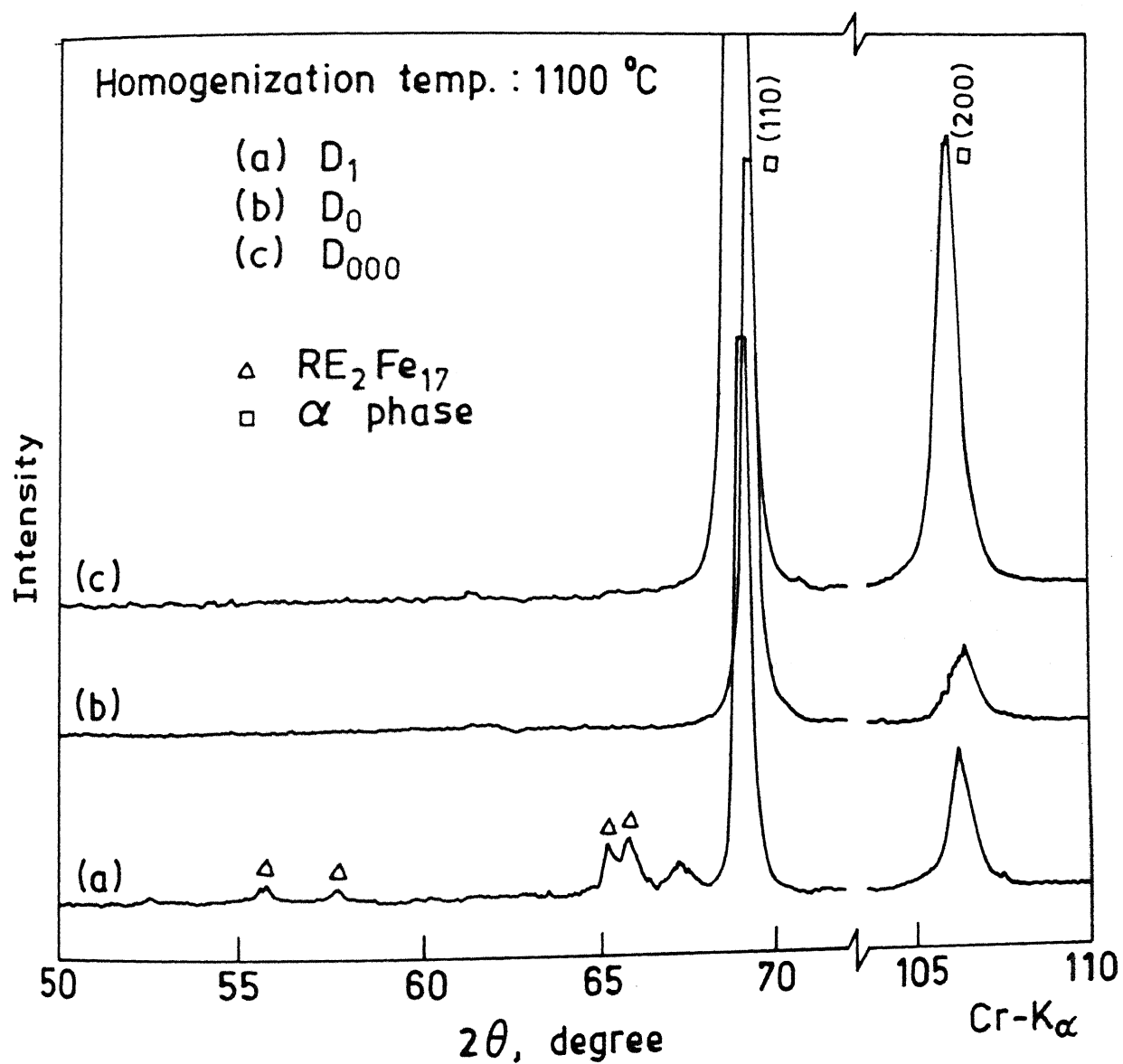


Fig.VII.7 XRD patterns of some RE-Fe alloys homogenized at 1100 °C :
(a) D_1 ; (b) D_0 ; and (c) D_{000}

Table VII.2: Powder X-ray Diffraction Data of $\text{RE}_2\text{Fe}_{17}$ Phase (Alloy D_1 , annealed at 700°C for 30 days)

Unit cell		a		c		c/a	
Hexagonal		8.525 Å		12.420 Å		1.46	
Relative Intensity [#]	d _{obs} Å	hkl	d _{calc} Å	Relative Intensity	d _{obs} Å	hkl	d _{calc} Å
w	3.538	201	3.538	vw	1.079	134*	1.709
w	3.173	202	3.173	vw	1.678	231	1.678
s	2.971	113	2.970	vw	1.634	232	1.634
w	2.864	104	2.862	vw	1.587	404	1.587
vw	2.722	121	2.723	m	1.501	413*	1.501
vw	2.545	122	2.545	m	1.487	234	1.487
s	2.460	300	2.461	vw	1.422	330	1.421
m	2.378	204	2.376	vw	1.400	235	1.399
vs	2.131	220	2.131	m	1.345	333	1.344
vvs	2.116	303	2.115	vw	1.335	504	1.333
s	2.074	124	2.075	vw	1.316	511	1.319
m	2.064	205	2.061			308	1.313
m	1.896	223	1.895	vw	1.274	424	1.273
w	1.864	116	1.862	m	1.230	600	1.230
vw	1.857	125	1.855	m	1.227	237	1.225
vw	1.826	401	1.826	w	1.219	514	1.219
vw	1.770	402	1.769	m	1.206	602	1.207
vw	1.728	107	1.725	vw	1.191	432	1.192

Relative intensity scale: vvs- very very strong, vs- very strong, s- strong, m- medium, w- weak, vw- very weak, vvw- very very weak

* Reflections used for the lattice parameters calculation

Table VII.3: Powder X-ray Diffraction Data of REFe_2 Phase (Alloy D_4 , annealed at 700°C for 30 days)

Unit cell	a		
fcc	7.299 Å		
Relative Intensity [#]	d _{obs.} Å	hkl	d _{cal.} Å
w	3.303	*	-
m	2.584	220	2.581
w	2.432	-	-
w	2.334	-	-
w	2.305	-	-
s	2.206	311	2.200
m	2.088	222	2.107
vw/b	1.949	-	-
m	1.803	400	1.824
vw	1.653	331	1.674
m	1.493	422**	1.493
m	1.407	333, 511	1.404
vw/b	1.385	-	-
w	1.294	440	1.290

Relative intensity scale : s - strong, m - medium, w - weak, vw/b - very weak and broad

* - Means not indexed

** Reflection used for the lattice parameter calculation

cell of $\text{RE}_2\text{Fe}_{17}$ (R) phase with lattice parameters of $a = 8.525 \text{ \AA}$, $c = 12.420 \text{ \AA}$ and c/a ratio of 1.46. The diffraction pattern of the REFe_2 phase could be indexed, using diffraction pattern of the alloy D_4 (700°C) [Fig.VII.4(d)], on the basis of the MgCu_2 type fcc Laves phase structure. The lattice parameter of the fcc unit cell has been found to be 7.299 \AA . The observed and calculated d-spacings match quite well for both the intermediate phases (Table VII.2 and VII.3). Due to the use of CrK_α radiation the α phase gave only two reflections (110) and (200) with d-spacings of 2.027 \AA and 1.434 \AA , respectively (Fig.VII.7). The lattice parameter of the α phase was calculated using the (200) reflection and found to be 2.868 \AA .

Identification of the phases present in various alloys at different temperatures was done by comparing their diffraction patterns with the indexed pattern of each phase. The labelled diffraction patterns of a few alloys are given in Fig.VII.4 to VII.7 and a complete summary of phase analysis by XRD is given in Table VII.1. As evident from the labelled diffraction patterns [Fig.VII 4 to 7], except for a few weak or very weak diffraction peaks, all the diffraction peaks in the XRD patterns could be identified on the basis of the phases found in the RE-Fe system.

The XRD results were in good agreement with the results of metallographic analysis. XRD pattern of alloy D_1 (1100°C), which had a two phase (α +Liquid) microstructure similar to the alloy D_0 [Fig.VII.3(d)] but with larger amount of liquid, showed, besides the major peaks due to the α phase, the presence of weak diffraction peaks due to the $\text{RE}_2\text{Fe}_{17}$ phase. This indicated that a non-equilibrium solidification of liquid phase present in the alloy D_1 at 1000°C resulted in the formation of the 2:17 stoichiometry phase. The microstructures of the alloys D_2 to D_5 , annealed at 900 and 1000°C , showed the presence of only two phases, a liquid phase and the $\text{RE}_2\text{Fe}_{17}$ phase (see section 7.1.1 on metallography and Table VII.1). In these cases also the XRD patterns (Fig.VII.5 and VII.6) showed the diffraction lines due to the REFe_2 phase indicating that the REFe_2 phase formed during solidification of the liquid phase.

7.1.3 Thermomagnetic Analysis

Thermomagnetic analysis of some of the alloys was carried out to corroborate the X-ray and metallography data, and establish the Curie temperature of different phases. A high temperature permeability testing apparatus and a vibrating sample magnetometer (VSM) fitted with a high temperature assembly were used for TMA studies.

The TMA traces for the alloys D_1 (annealed at 900 and 1000°C) and D_4 (annealed at 1000°C), obtained using permeability testing apparatus, are given in Fig.VII.8. Two magnetic transitions were observed for the alloy D_1 . The high temperature magnetic transition, observed around 860°C [Fig.VII.8(a), (b)], corresponds to the magnetic transition of the α phase. The second magnetic transition at $\sim 80^\circ\text{C}$ corresponds to the $\text{RE}_2\text{Fe}_{17}$ phase. Since the alloy D_4 does not contain the α phase, no high temperature magnetic transition is found in this case. It shows only one magnetic transition, that is due to the $\text{RE}_2\text{Fe}_{17}$ phase [Fig.VII.8(c)].

Figure VII.9 shows the magnetic moment versus temperature data, for a few RE-Fe alloys, obtained using a VSM. The $\text{RE}_2\text{Fe}_{17}$ phase in alloy D_1 showed magnetic transition temperature of about 40° and 46°C when it was annealed at 700°C and 900°C, respectively [Fig.VII.9(a), (b)]. The magnetic transition for the $\text{RE}_2\text{Fe}_{17}$ phase in alloy D_{12} was not sharp [Fig.VII.9(c)] because in this alloy the amount of the $\text{RE}_2\text{Fe}_{17}$ phase is relatively very small.

7.1.4 Differential Scanning Calorimetry (DSC)

DSC was done on some of the annealed alloys to determine transformation temperatures and locate phase boundaries. DSC curves for 9 alloys, having 0.5 to 33.3 at.pct. RE, are given in Fig.VII.10.

The first endothermic peak at 764-765°C for the alloys D_{000} .

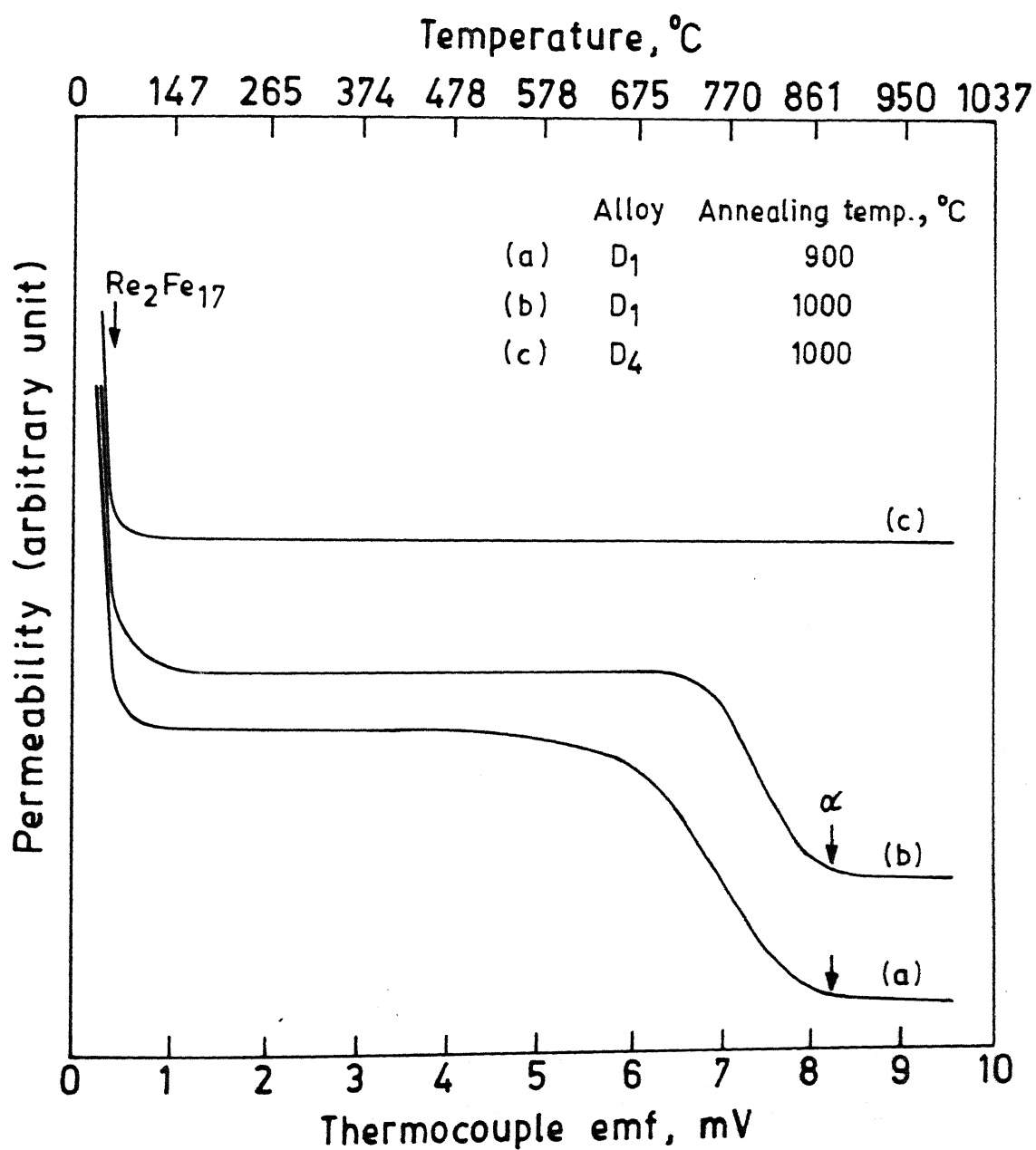


Fig.VII.8 TMA curves of a few RE-Fe alloys obtained using high temperature magnetic permeability testing apparatus :
 (a) D₁ (900 °C); (b) D₁ (1000 °C); and (c) D₄ (1000 °C)

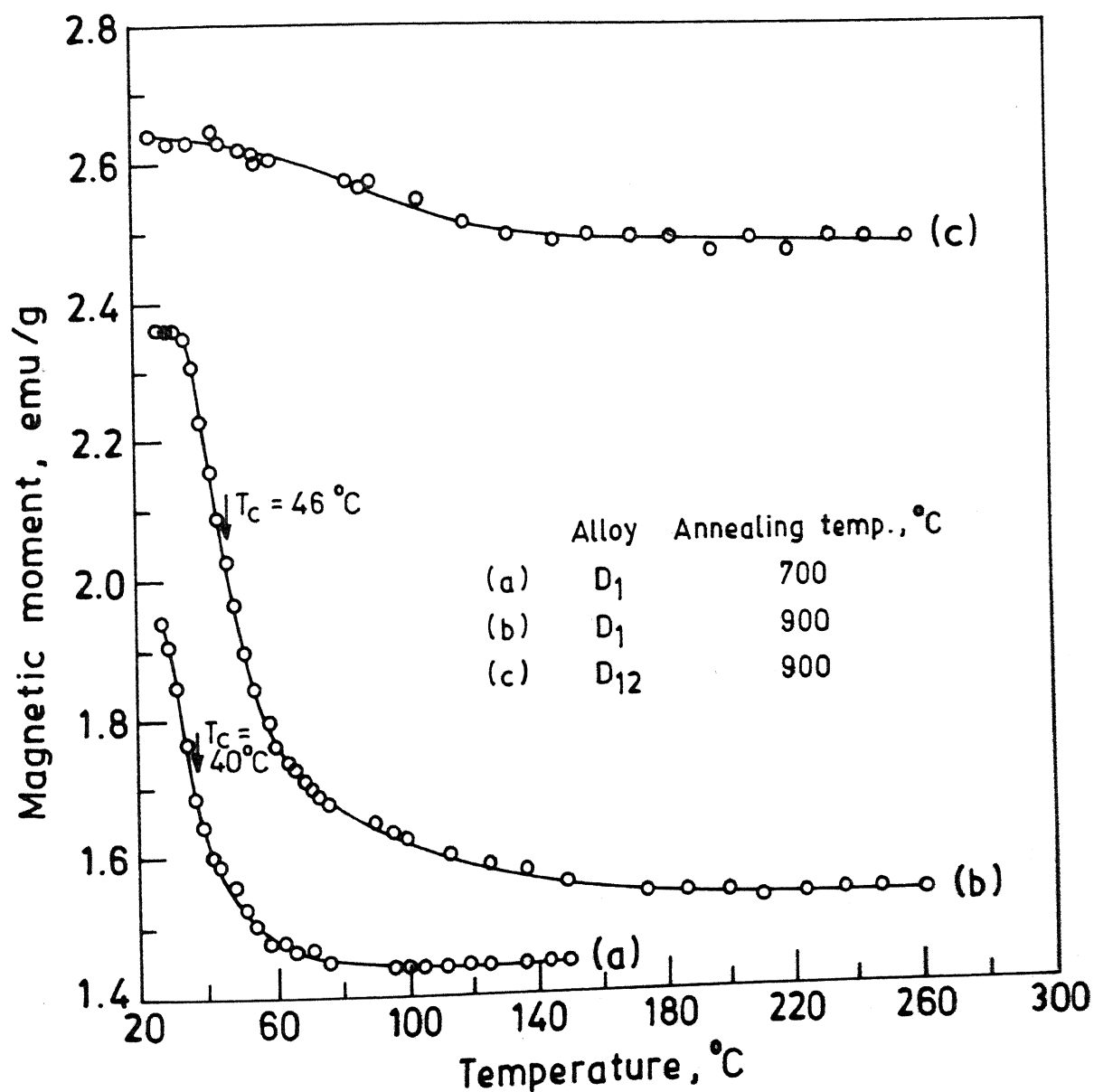


Fig.VII.9 TMA curves of a few RE-Fe alloys obtained using a vibrating sample magnetometer (measured in the residual field of 40 Oe) : (a) D₁ (700 °C); (b) D₁ (900 °C); and (c) D₁₂ (900 °C)

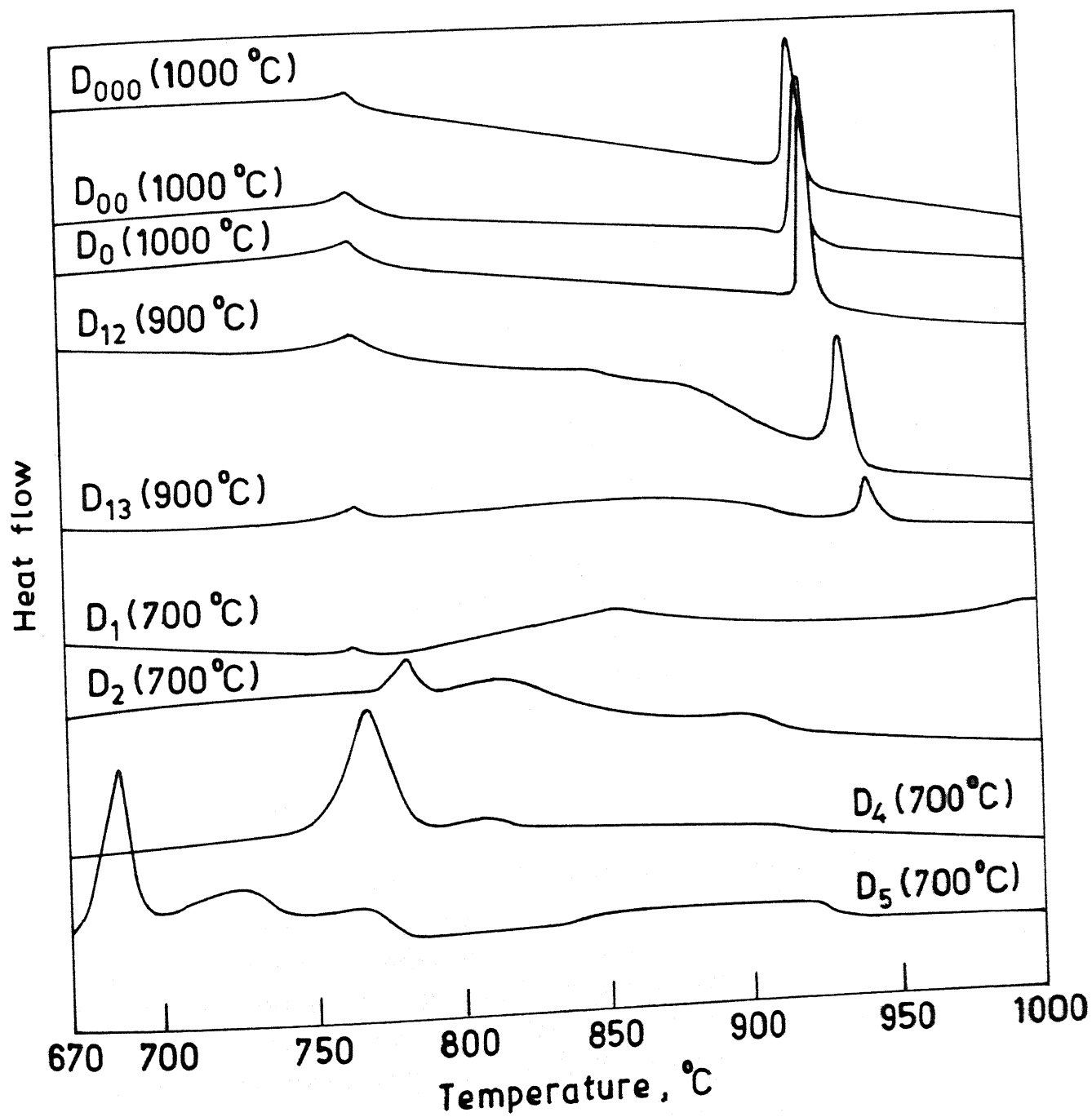


Fig.VII.10 DSC traces of a few RE-Fe alloys

D_{00} , D_0 , D_{12} , D_{13} and D_1 corresponds to the ferromagnetic to paramagnetic transformation temperature of the bcc α phase. In the alloys D_1 and D_{13} , this endothermic peak is observed at the same temperature but the height of the peak is considerably reduced due to the presence of a relatively small amount of α phase in these alloys. The beginning of the second endothermic peak (which is very sharp like a first order transformation) for the same set of alloys, except in the case of alloy D_1 for which it is absent, occurs at different temperatures (Table VII.1). The transformation start for alloy the D_{000} is $\sim 915^\circ\text{C}$ and it increases with increase in RE content of the alloy. The highest start of transition temperature is for the alloy D_{13} which is $\sim 936^\circ\text{C}$.

Alloys D_2 to D_5 show somewhat similar type of thermal effect occurring over a wide temperature region. the start of the transformation is again found to vary with increase in RE content. Unlike the low RE content alloys, in these cases, however, the transformation start temperature decreases and the peak height increases as the RE content increases. The complete transformation appears to occur over a range of temperature and show more than one peak, the first peak is always the highest and others are of lower peak height. Detailed study of the nature of these multiple peaks in the case of high rare-earth containing alloys have not been done.

7.2 Discussion

The discussion presented here on RE-Fe system focuses on the phases observed in this system and construction of the phase diagram based on the observations made. The phase diagram has been constructed using the results of metallography, XRD, TMA and DSC. Salient features of RE-Fe system are critically compared with other R-Fe systems, especially, Ce-Fe and Nd-Fe systems.

7.2.1 Phases

The stability of phases in the RE-Fe system is expected to be influenced by the elements present in the Mischmetal. The

Mischmetal used in this investigation is Ce based, the other elements being present in it are La, Nd and Pr. Of these rare-earth elements, La does not form any intermediate phase with Fe [135]. In the Ce-Fe and Pr-Fe systems, two intermediate phases, namely R_2Fe_{17} and RFe_2 , have been reported [116,135]. The Nd-Fe system on the other hand shows the presence of two intermediate phases, the Nd_2Fe_{17} and Nd_5Fe_{17} phase, the latter phase is stable below $777^\circ C$ [55,136]. In the present investigation several alloys were annealed at $700^\circ C$ for 30 days. Even after this long annealing the alloys with greater than 15 at.pct. RE showed the presence of the two intermediate phases, RE_2Fe_{17} and $REFe_2$, and the RE_5Fe_{17} phase was not observed. This indicates that in the presence of very large amount of Ce (and possibly due to Pr) the $REFe_2$ phase is stabilized in preference to the RE_5Fe_{17} phase.

The observed lattice parameters of the RE_2Fe_{17} and the $REFe_2$ phases are compared with the corresponding Ce compounds (Table VII.4). The lattice parameters of the RE_2Fe_{17} phase match well with the rhombohedral modification of the Ce_2Fe_{17} phase [Th_2Zn_{17} structure type, Fig.II.21(c)]. Unlike the Ce_2Fe_{17} phase, the RE_2Fe_{17} phase is magnetic at room temperature. The Curie temperature of the RE_2Fe_{17} phase ($\sim 45^\circ C$) is close to that of the Nd_2Fe_{17} phase ($\sim 54^\circ C$ [150]). The other intermediate phase $REFe_2$ is paramagnetic at room temperature and its lattice parameter is quite similar to the Laves phase $CeFe_2$.

The grains of RE_2Fe_{17} phase in the microstructure of alloy D_0 , D_1 etc. [Fig.VII.3(b),(c)] showed high concentration of twins. Presence of twinned structure in the 2:17 stoichiometry phase, e.g. $Nd_2Fe_{17}(R)$, $Sm_2Co_{17}(R)$ etc., have also been reported in the literature [150,167,176]. TEM studies [167,176] have established that small amount of 2:17(H) phase forms due to change in the stacking sequence in the narrow twin regions. Twinned structure observed in the RE_2Fe_{17} phase may probably also be related to the occurrence of very small amount of the $RE_2Fe_{17}(H)$ phase which is not detected in the X-ray diffraction patterns.

Table VII.4: Lattice Parameters and Curie Temperatures of RE-Fe Compounds Found in this Investigation and the R-Fe Compounds in the Ce-Fe and Nd-Fe Systems

Compounds	Lattice Parameter, Å		T_c °C	Reference
	a	c		
RE_2Fe_{17}	8.525	12.420	~ 45	*
Ce_2Fe_{17} (H)	8.490	8.281	-	[135]
Ce_2Fe_{17} (R)	8.493 [#]	12.410 [#]	-3	[135]
Nd_2Fe_{17} (R)	8.590 [#]	12.470 [#]	54	[135,150]
Nd_5Fe_{17} (H)	20.210	12.350	230	[136]
$REFe_2$	7.299 [#]	-	< RT	*
$CeFe_2$	7.302 [#]	-	-43	[135]

* - present investigation; # - lattice parameters for hexagonal unit cell; [#] - cubic, Laves phase.

The α phase has a lattice parameter ($a = 2.868 \text{ \AA}$) quite close to the lattice parameter of pure α -Fe ($a = 2.864 \text{ \AA}$ [242]) which implies very low solid solubility of RE in iron. Chuang et.al.[137] have reported that the Curie temperature of α -Fe phase decreases from 769 to 752°C when the amount of Ce dissolved increases from 0 to 0.08 at.pct., and beyond 0.08 at.pct. of Ce the Curie temperature remains constant at 752°C . The somewhat lower T_c (764°C) of α phase in the RE-Fe system, as indicated by the DSC traces (Fig.VII.10), also may be due to a small solubility of RE in α phase. The presence of the reasonably large amount of $\text{RE}_2\text{Fe}_{17}$ phase in alloy D_{000} containing 0.5 at.pct. RE [Fig.VII.3(a)], annealed at 1000°C , indicates that the solubility of RE in Fe is much less than 0.5 at.pct.

X-ray results indicated that the α phase exists even at 1000°C and higher temperatures (Fig.VII.4 to 7). This observation was somewhat surprising because in no R-Fe system the α -Fe phase is stable at a temperature higher than 935°C [132]. The DSC traces of alloy D_{000} to D_{13} showed a sharp peak at temperatures slightly above 912°C . This peak shifted to higher temperatures from 915°C for alloy D_{000} to 936°C for alloy D_{13} . This thermal effect however became less prominent as the RE content of the alloys increased and finally not seen in the alloy D_1 and other still higher RE containing alloys. X-ray and metallography results (section 7.1.1 and 7.1.2) have indicated that the amount of α phase continuously decreases from alloy D_{000} to D_{13} . There appears to be a direct correlation between the decrease in the intensity of the thermal effect observed at temperature slightly above 912°C and the continuous decrease in the amount of the α phase with the increase in the RE content of the alloys in the two phase region between Fe and $\text{RE}_2\text{Fe}_{17}$ compositions. The sharp DSC peak at $T > 912^\circ\text{C}$ appears to be due to α to γ transformation. The presence of the α phase in low RE alloys annealed and quenched from above 950°C is possibly due to insuppressibility of the γ to α transformation during quenching in water. Further high temperature X-ray studies are required for more positive identification of the presence of the γ phase at high temperature.

7.2.2 Phase Equilibria

During XRD analysis of the annealed RE-Fe alloys, most of the diffraction peaks could be assigned to the intermediate phases $\text{RE}_2\text{Fe}_{17}$ and REFe_2 or the solid solution phase α (Fig.VII.4-7). Some of the weak or very weak peaks, which could not be identified, may arise due to one or more of the following factors: (a) non-equilibrium phases resulting due to solidification of the liquid phase during quenching of an alloy from homogenization temperature to room temperature; (b) 30 days may be inadequate homogenization time at 700°C for complete transformation of the cast structure into equilibrium structure; (c) partial oxidation of alloy (especially high RE alloys D_2 to D_5 and alloys containing large amount of liquid phase) during various stages of alloy preparation and heat treatment, e.g. melting, homogenization, powdering etc.; and (d) impurities present in the mischmetal. Since unidentified weak or very weak diffraction peaks results due to non-equilibrium and/or impurity phases and there were only a few of these present, these peaks were not considered for the construction of the phase diagram.

All the alloys containing less than 13.5 at.pct. RE showed the presence of two phases ($\alpha + \text{RE}_2\text{Fe}_{17}$) at or below 900°C (Table VII.1). The alloy containing 13.5 at.pct. RE (D_{1C}) comprised of mainly $\text{RE}_2\text{Fe}_{17}$ phase with very small amount of α phase. On the other hand alloy D_2 (16.67 at.pct. RE) did not show the presence of the α phase, it contained two phases, $\text{RE}_2\text{Fe}_{17}$ and liquid or REFe_2 depending upon the temperature. These results suggest that the $\text{RE}_2\text{Fe}_{17}$ phase exists close to the composition of the alloy D_{1C} , at slightly higher RE content than predicted from the 2:17 stoichiometry. Ray [138] has also reported similar composition shift for the 2:17 phase in R-Fe systems ($\text{R} = \text{Ce}, \text{Nd}, \text{Pr}$ and Sm). A small difference in the T_c of the $\text{RE}_2\text{Fe}_{17}$ phase in alloy D_1 annealed at 900°C and 700°C (Fig.VII.9) possibly indicates that the $\text{RE}_2\text{Fe}_{17}$ phase is not a single composition phase but has a small solubility limit.

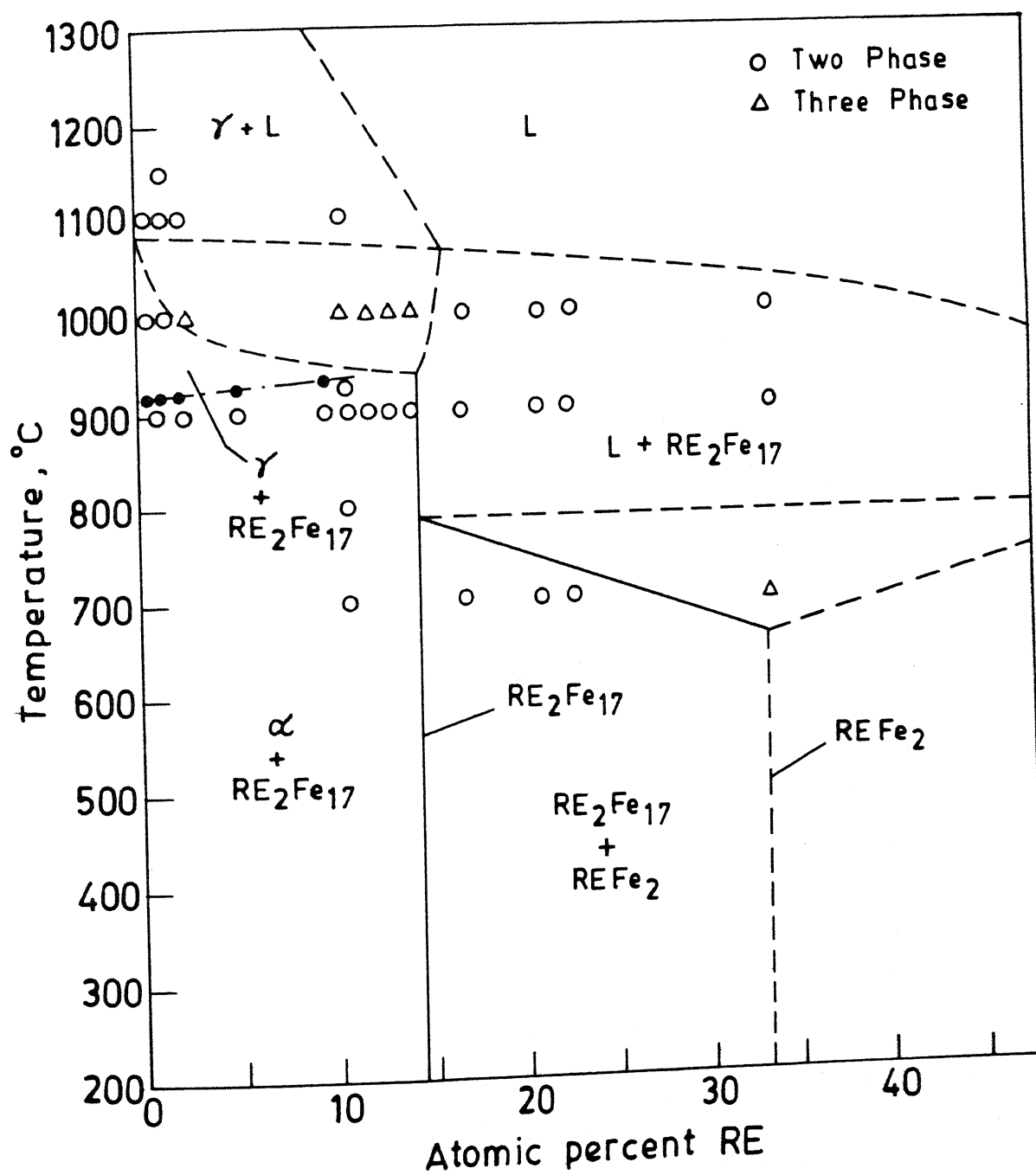


Fig.VII.11 (a) Phase equilibria in the RE-Fe system

(contd. ...)

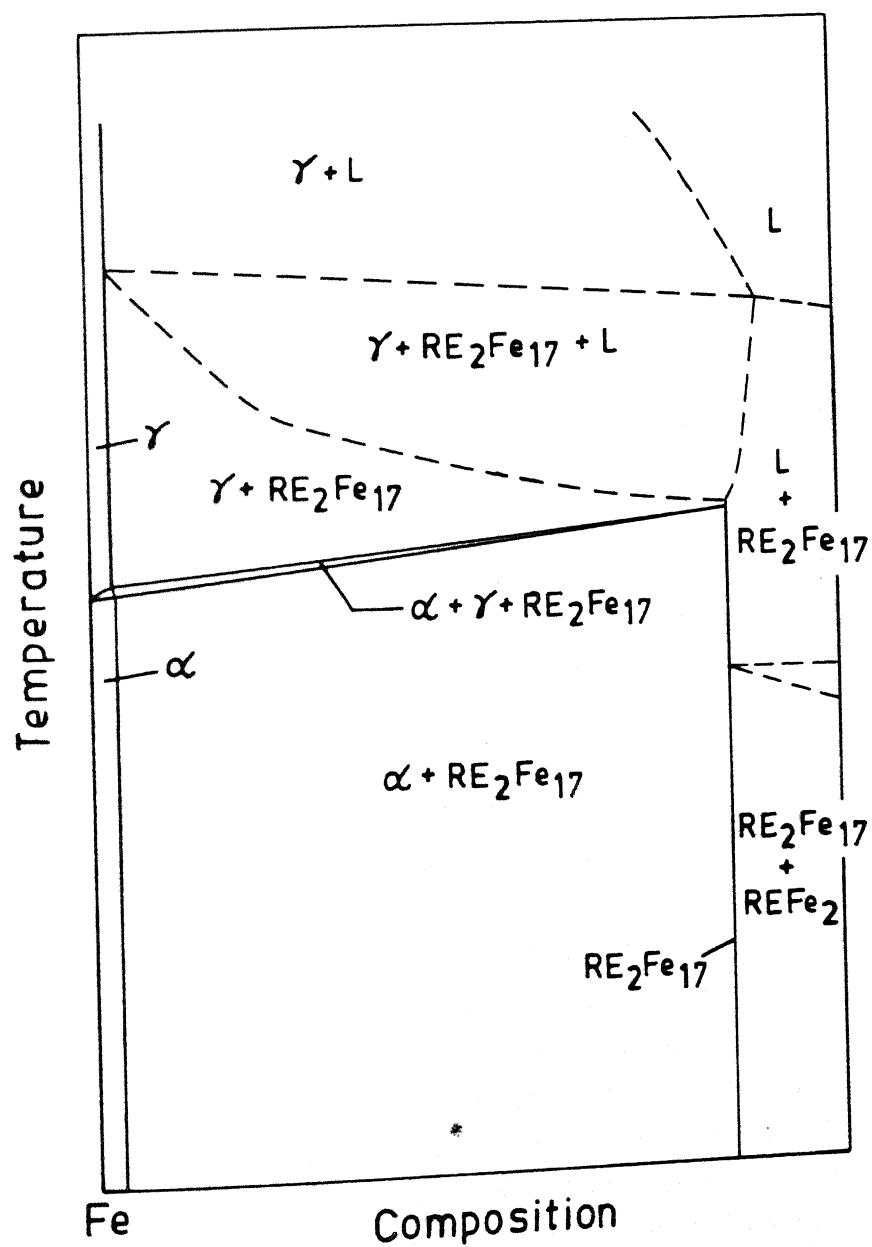


Fig.VII.11 (Contd.)

(b) Schematic phase diagram of the RE-Fe system showing a possible peritectoid type reaction at the Fe-end

the DSC data suggest $\alpha \rightarrow \gamma$ transformation of Fe at temperature slightly higher than 912°C [shown by dash dot line in Fig.VII.11(a)]. In R-Fe systems an invariant reaction occurs at 912°C or at a slightly higher temperature. This invariant reaction has been identified as peritectoid reaction: $\gamma\text{-Fe} + \text{R}_2\text{Fe}_{17} \rightarrow \alpha\text{-Fe}$; the reaction temperature being 922 and 930°C for $\text{R} = \text{Ce}$ and Pr , respectively [135,137]. DSC study of the alloy D_{000} (0.5 at.pct. RE) indicates the α to γ transformation at $\sim 915^{\circ}\text{C}$, and for alloys with higher RE contents this reaction temperature increases. It may be possible to interpret the phase equilibria at the low RE content region of the RE-Fe system if it is assumed that the α phase forms through a peritectoid reaction as reported in the R-Fe systems. Unlike the binary R-Fe systems, the peritectoid reaction is expected to give rise to a narrow three phase region ($\alpha + \gamma + \text{RE}_2\text{Fe}_{17}$) in the RE-Fe system [Fig.VII.11(b)]. Since the temperature corresponding to the thermal effect observed in the DSC traces increases from 915 to 936°C , the three phase region ($\alpha + \gamma + \text{RE}_2\text{Fe}_{17}$) must be tilted upwards to give rise to the reaction at higher temperature as the RE content of the alloy increases.

Comparison of the RE-Fe phase equilibria with R-Fe systems ($\text{R} = \text{Ce}, \text{Pr}, \text{Nd}$; Fig.II.18 and Fig.II.19) indicates that the determined phase diagram is quite similar to the Ce-Fe and the Pr-Fe binary systems except for the opening up of three phase peritectic (and possibly peritectoid) equilibrium reaction lines into areas. The RE-Fe phase equilibria is somewhat similar to the Nd-Fe system if we consider the composition region upto $\text{Nd}_2\text{Fe}_{17}$. Beyond this composition the notable difference being the presence of $\text{Nd}_5\text{Fe}_{17}$ phase instead of the REFe_2 phase (see section 7.2.1 for discussion on phases). The opening up of three phase peritectic lines into areas is not a surprising observation because the RE-Fe system, which is represented as a binary, is not a true binary system. Similar opening up of the peritectic reaction lines into areas has also been observed in the RE-Co system [101,126,127].

7.3 Summary

Phase equilibria in the RE-Fe system has been determined in the temperature range of 700 and 1150°C at the Fe end upto 33.3 at.pct. RE. Two intermediate phases $\text{RE}_2\text{Fe}_{17}$ and REFe_2 , and a Fe solid solution phase are observed. No $\text{RE}_5\text{Fe}_{17}$ phase was observed down to 700 °C. The lattice parameters of hexagonal unit cell of $\text{RE}_2\text{Fe}_{17}$ (R) phase, which has a Curie temperature between 40-45°C, are $a = 8.525 \text{ \AA}$, $c = 12.420 \text{ \AA}$ and c/a ratio 1.46. The REFe_2 phase is a cubic Laves phase with $a = 7.299 \text{ \AA}$. The γ phase can not be retained by quenching alloys from high temperature. The solubility of RE in Fe is less than 0.5 at.pct. The RE-Fe system is quite similar to the R-Fe systems (R = Ce, Pr) except for the opening up of peritectic reactions into two broad three phase regions consisting of ($\gamma + \text{RE}_2\text{Fe}_{17} + \text{Liquid}$) and ($\text{RE}_2\text{Fe}_{17} + \text{REFe}_2 + \text{Liquid}$). The results also indicate a possible peritectoid formation of the α phase and suggest the presence of a narrow three phase region ($\alpha + \gamma + \text{RE}_2\text{Fe}_{17}$).

CHAPTER VIII

MAGNETIC CHARACTERIZATION IN THE RE-CO-Fe-CU-Zr AND THE RE-Fe-B SYSTEMS

The contents of this Chapter focus on the results and discussion of some preliminary magnetic characterization experiments which were performed to explore the possibility of fabricating hard permanent magnets using the RE-Co-Fe-Cu-Zr and the RE-Fe-B alloys. The work strategy involved systematic characterization (e.g. magnetic, metallurgical etc.) studies on bulk alloys, and resin bonded and sintered magnets.

The discussion which follows the results in each major section, dealing with the RE-Co-Fe-Cu-Zr and the RE-Fe-B systems, concentrates on the intrinsic magnetic properties of the important phases, magnetic properties of resin bonded magnets, possible explanation of magnetic properties of sintered magnets in terms of intrinsic and extrinsic factors involved, and likely direction of future research to tackle some of the problems encountered in magnet fabrication.

8.1 Magnetic Characterization of RE-Co-Fe-Cu-Zr Alloys

The phase equilibria study of the RE-Co-Fe-Cu-Zr system indicated the presence of two new intermediate phases U and N. Since both U and N phases were magnetic (Curie temperature 830°C and 740°C respectively; see section 5.3.4) a large number of alloys had to be investigated to find a suitable alloy composition for the best magnetic characteristics. Unaged bulk U phase alloys had higher σ_s and iH_c (typical values $\sim 110 \text{ emu/g}$, 40 Oe for alloy C_8) compared to N phase alloys (typical values $\sim 75 \text{ emu/g}$, 20 Oe for alloy C_{11}). However, the N phase alloys showed a remarkably superior magnetic hardening behaviour due to aging and hence preferred for further processing. The N phase showed a moderate H_A value of $\geq 25 \text{ kOe}$ and the desired uniaxial anisotropy.

8.1.1 Results

The results of magnetic characterization studies on some of the RE-Co-Fe-Cu-Zr alloys are presented in five subsections. The first subsection, on the selection of alloy composition for further processing, concerns the studies on the effect of aging treatment on the magnetic hardenability of bulk alloys of different chemical composition. The second and third subsections deals with the aging behaviour and intrinsic magnetic properties, e.g. saturation magnetization (σ_s), anisotropy field (H_A), direction of easy magnetization etc., of the N phase alloys of composition $[\text{RE}(\text{Co}_{0.76}\text{Fe}_{0.13}\text{Cu}_{0.09}\text{Zr}_{0.02})_6]$; designated as alloy C_{11}] found suitable during the course of preliminary exploratory aging studies on the bulk alloys [245]. The results of the physical and magnetic characterization of resin bonded and sintered magnets are included in the fourth and fifth subsection, respectively. Some of the results presented in the first two subsections are adopted/compiled from a previous study by this investigator [245]. These results are included here mainly for the sake of continuity and presenting the overall results in coherent manner.

8.1.1.1 Selection of Alloy Composition for Processing

In an exploratory study [245] for finding the suitability of RE-Co-Fe-Cu-Zr alloy composition for magnet fabrication, solid specimens of a few alloys (C_4 , C_8 , C_9 , C_{11} , C_{12} , C_{13} and C_{17}) were chosen for low temperature heat treatment. The σ_s and H_c values of these alloys (before the low temperature heat treatment), together with the chemical composition and phase constituents present, are given in Table VIII.1. A 1100°C annealed piece of each chosen alloy was aged at 675°C for different lengths of time and H_c was measured after each duration of heat treatment. The results in Fig.VIII.1 show that the alloys containing N phase are more susceptible to magnetic hardening by aging treatment as compared to the U phase alloys. Among all the alloys studied, alloy C_{11} , which is essentially an N phase alloy, was found to be most promising and selected for further investigation.

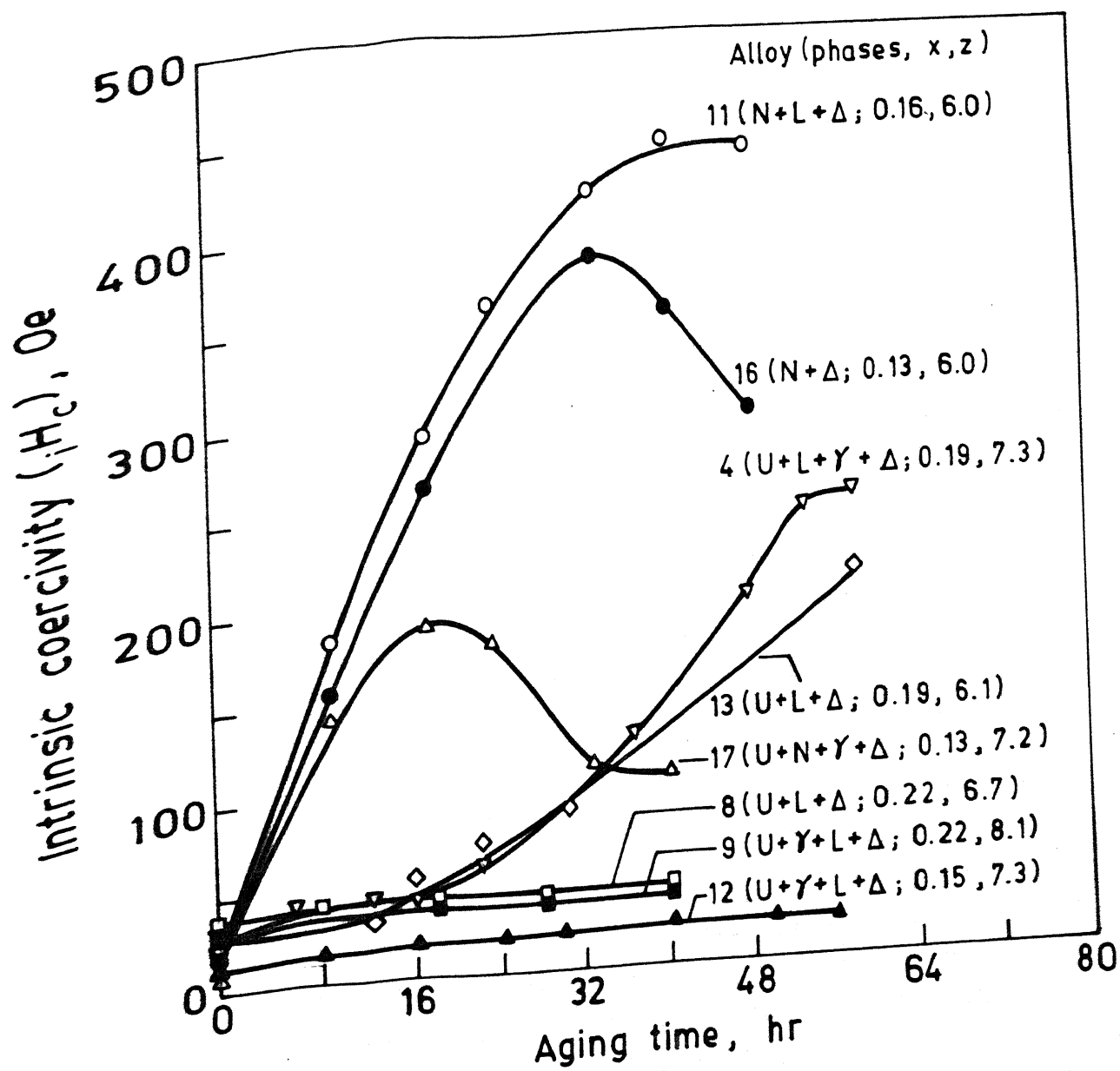


Fig. VIII.1 Effect of aging time on the intrinsic coercivity (H_c) for $RE(Co_{0.89-x}Fe_xCu_{0.09}Zr_{0.02})_2$ alloys at $675^\circ C$ (data from Devi (1985) [245])

Table VIII.1: Chemical Composition, Phases and Initial Magnetic Properties of the $[\text{RE}(\text{Co}_{0.89-x}\text{Fe}_x\text{Cu}_{0.09}\text{Zr}_{0.02})\text{Z}]$ Used for Low Temperature Aging Treatment Studies

Alloy (C_1) i	Composition		Phases	Magnetic Properties	
	x	z		σ_s (emu/g)	iH_c (Oe)
4	0.19	7.3	U,L, γ , Δ	99	23
8	0.22	6.7	U,L, Δ	108	38
9	0.22	8.1	U, γ ,L, Δ	118	30
11	0.16	6.0	N,L, Δ	75	20
12	0.15	7.3	U, γ ,L, Δ	101	11
13	0.19	6.1	U,L, Δ	100	32
16	0.13	6.0	N, Δ	72	20
17	0.13	7.2	U,N, γ , Δ	85	10

8.1.1.2 Aging Behaviour of N Phase Alloys

The effect of aging temperature (650 and 620°C) on the magnetic hardenability of the alloy C_{11} [batch code : $C_{11}(A)$] was studied in detail. As compared to 675°C, there was not much improvement in the iH_c values at 650°C. However, a significant increase in the aging response of this alloy was observed at 620°C (Fig.VIII.2). The iH_c increased with aging time and reached a more or less constant value after about 300 hours of aging. The iH_c value increased from the initial (before aging) value of ~ 20 Oe to 1180 Oe (> 50 fold increase) after 300 hours of aging. After 300 hours, a stable iH_c value was obtained. The σ_s value for this alloy was found to remain unchanged with change in aging temperature or time. The aged alloy, after 350 hours of aging, was examined by metallography and XRD. No apparent change could be noticed in the XRD pattern or microstructure of the alloy after aging [245]. The reproducibility of aging behaviour of alloy C_{11} was checked for different batches of alloy and the results are given in Fig.VIII.2 and Table VIII.2. The data show that the remarkable magnetic hardening of alloy C_{11} persist in all the

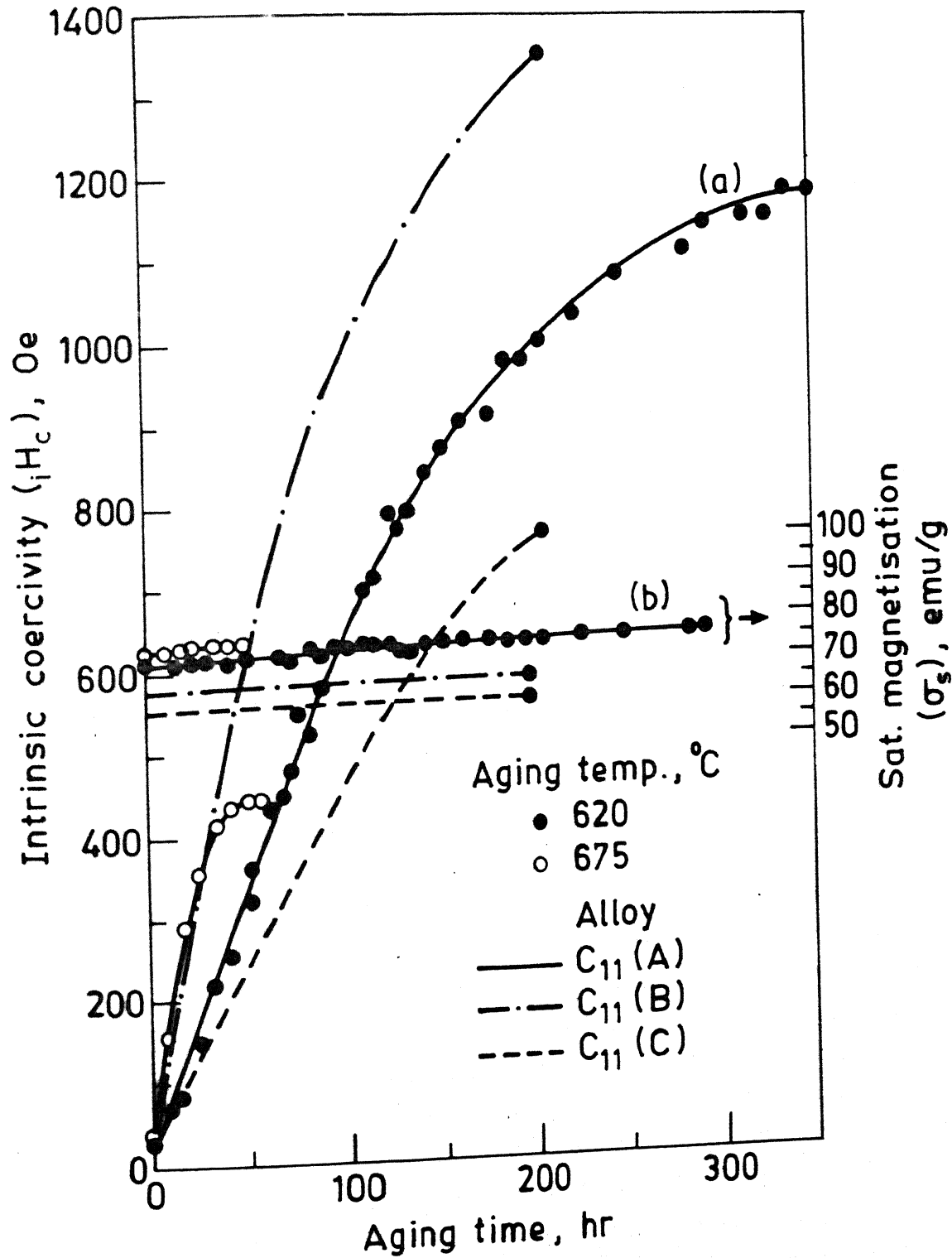


Fig.VIII.2 Aging behaviour of solid annealed specimens of alloy C_{11} [$RE(Co_{0.76}Fe_{0.13}Cu_{0.09}Zr_{0.02})_6$] at different temperatures ($C_{11}(A)$, $C_{11}(B)$ and $C_{11}(C)$ indicates different batch of alloy C_{11})

Table VIII.2: $\mu_0 H_c$ and σ_s Values for Different Batch of Alloy C_{11} After Aging at 620 °C

Batch	Aging Time (hrs.)	Magnetic Properties		
		$\mu_0 H_c$ (Oe)	σ_s (emu/g)	σ_r (emu/g)
(A)*	205	1000	75	11
(B)	210	1350	61	13
(C)	200	700	56	10

most of the results in Figs.VIII.1 and VIII.2 refers to this particular batch.

Alloys of C_{11} composition. The value of magnetic properties obtained was, however, found to vary from one batch of alloy to other. Hence, different batch of alloy C_{11} will be identified as $C_{11}(A)$, $C_{11}(B)$ and $C_{11}(C)$ as indicated in Table VIII.2.

1.1.3 Intrinsic Magnetic Properties of the N Phase

The intrinsic magnetic properties, used to assess the potential of an intermediate phase for permanent magnet fabrication, are Curie temperature (T_c), saturation magnetization (σ_s), anisotropy field (H_A) and direction of easy magnetization. The N phase ($T_c \sim 740$ °C) was characterized in terms of σ_s , H_A and direction of easy magnetization using the resin bonded pellets (see section 4.3.2.2 for fabrication method) prepared from one hour milled powder of alloy $C_{11}(C)$ annealed at 1100 °C for 48 hours and aged at 620 °C for 200 hours. VSM was used for the measurement of σ_s and H_A (section 4.3.3.2), and the technique of RD (section 4.2.2) was employed to determine the direction of easy magnetization.

Saturation Magnetization (σ_s)

Since the maximum available magnetic field in the VSM, i.e. 1 kOe, was insufficient to saturate the solid bulk alloy specimen of N phase, resin bonded pellet of alloy $C_{11}(C)$ was used to estimate the σ_s of the N phase. The magnetization (σ) of the resin bonded pellet was measured as a function of applied magnetic field (H) and plotted on a graph as shown in Fig.VIII.3. The σ_s value is taken as the value of σ at the highest available field strength. From the given curve, the value of saturation magnetization for the N phase was found to be ~ 90 emu/g.

Magnetocrystalline Anisotropy Field (H_A)

The basic origin of the high coercivity, necessary for good permanent magnet properties, is a high magneto-crystalline anisotropy. Different experimental definition of anisotropy field have been proposed [37]. Most workers [37] base it on the magnetization curves determined with the applied magnetic field parallel and perpendicular to the easy axis of magnetization of a single crystal or magnetically aligned resin bonded powder sample. The anisotropy field H_A is then defined as the field strength at which the hard-axis magnetization approaches the easy-axis magnetization value.

Magnetization measurements (σ vs. H) on resin bonded magnet, prepared from N phase alloy $C_{11}(C)$, were carried out for two different directions, namely, the parallel and the perpendicular to the magnetic alignment direction of the resin bonded magnet. Magnetization versus applied field curves for a resin bonded magnets are shown in Fig.VII.4.

Direct estimation of anisotropy field (H_A) from σ - H curve shown in Fig.VIII.4 is not possible because the available field strength for the electromagnet used was low. The magnetization curves, both in parallel and perpendicular directions, require extrapolation. Non-linear nature of the curves, particularly for the perpendicular direction, makes the extrapolation of curves difficult. Thus it is possible only to determine a very approximate value of H_A . The value seems to be ≥ 25 kOe.

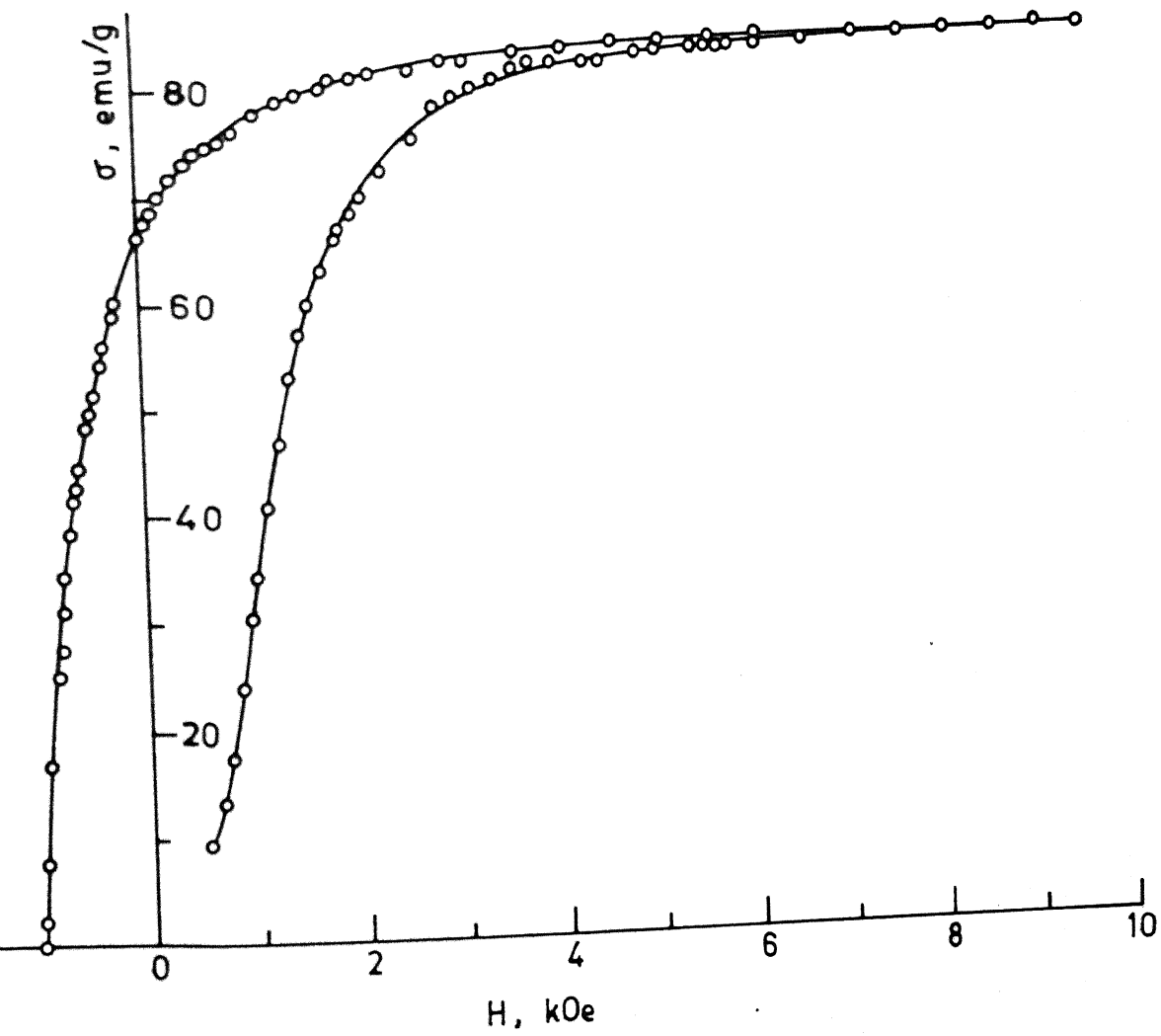


Fig. VIII.3 Magnetization (σ) vs. applied field (H) curves for a resin bonded pellet of alloy C₁₁(C)

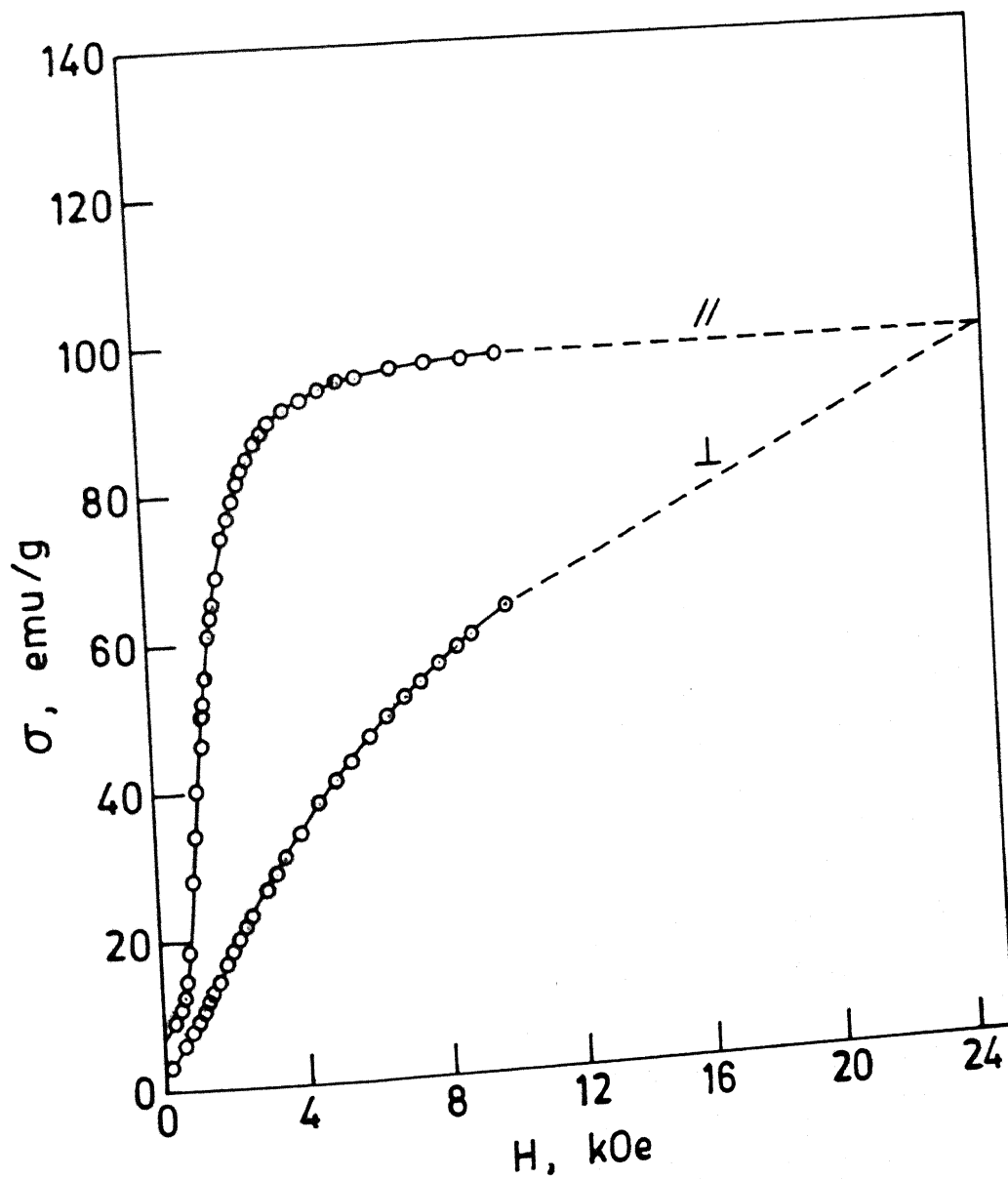


Fig.VIII.4 Magnetization (σ) vs. applied field (H) curves for a resin bonded pellet of alloy $C_{11}(C)$ (at room temperature) measured parallel and perpendicular to the magnetic alignment direction

Easy Axis of Magnetization for the N-Phase

The resin bonded sample fabricated for the purpose of determining the easy axis of magnetization was cylindrical in shape and 1 cm in diameter. During the preparation of resin bonded magnets, the particles are expected to align with their easy axis of magnetization parallel to the alignment field direction, i.e. in the present case perpendicular to the circular surface of the cylindrical sample. Thus the comparison of XRD patterns, from a randomly oriented powder sample and a magnetically oriented sample surface, can provide useful information regarding the preferentially oriented crystal plane (parallel to sample surface) and the easy axis of magnetization. Zhou et.al.[253] have used a technique, based on the above principle, to determine the crystallographic alignment of several Nd-Fe-B magnets. Similar method, as used by Zhou et al, was followed to determine the easy axis of magnetization of the N phase.

Fig.VIII.5 shows the XRD patterns obtained for alloy $C_{11}(C)$ with powder randomly oriented and in the magnetically aligned resin bonded condition, respectively. For the resin bonded sample, there is a very large increase in the intensity of the reflection with $d = 2.042 \text{ \AA}$ and the intensity of all other reflections drastically decreased. The reflections (110) and (200) completely disappear in the case of the oriented sample, whereas, the reflection (105), (104), (115) and (205), although detectable, occur with very much reduced intensity. The reflection for $d = 2.042 \text{ \AA}$ can be assigned the indices (0,0,10) and (203) (see Table V.3). Thus the easy axis of magnetization may be either normal to the (0,0,10) plane (i.e. c-direction) or normal to the (203) plane. If the easy axis of magnetization is normal to the (203) plane then a complete disappearance of the (110) and (200) reflections is quite unlikely. Preferential orientation of particles along the $\langle 001 \rangle$ direction is expected to influence the (hk0) type of reflections most significantly. For $\langle 001 \rangle$ easy axis of magnetization the disappearance of (110) and (200) reflections is predictable. Thus c-axis appears to be the easy axis magnetization for the N phase.

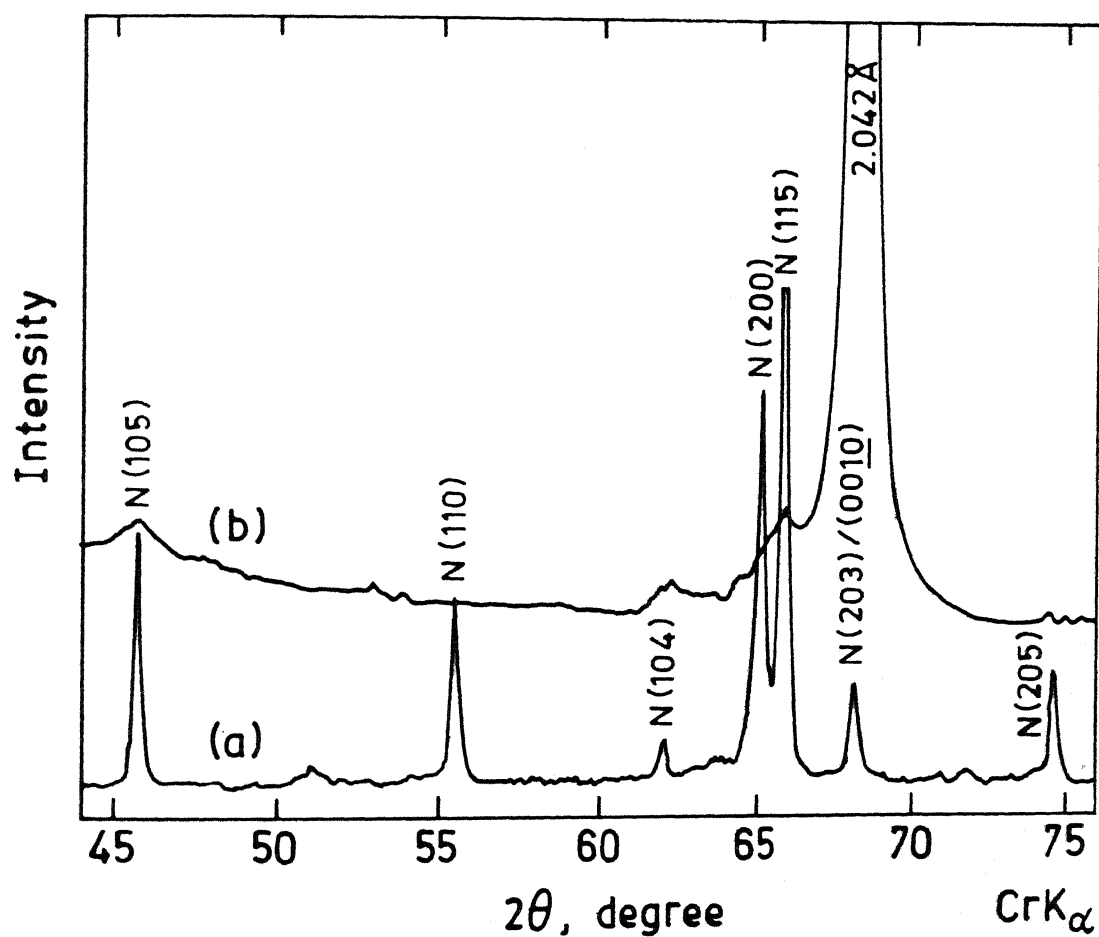


Fig.VIII.5 XRD patterns of alloy $\text{C}_{11}(\text{C})$: (a) randomly oriented powder sample; and (b) magnetically aligned cylindrical resin bonded sample (XRD pattern from the surface perpendicular to the magnetic alignment direction)

8.1.1.4 Resin Bonded Magnets

The alloys of C_{11} composition were used to explore the possibility of fabricating resin bonded magnets. The experimental procedure used for making the resin bonded magnets is given in section 4.3.2. Resin bonded pellets were prepared from the coarse as well as the milled alloy powders. The effect of the following processing variables on magnetic properties was studied : (a) milling time or particle size; and (b) aging treatment. The magnetic characterization of the pellets, in terms of intrinsic coercivity (iH_c), saturation magnetization (σ_s) and remanence (σ_r), was done by a VSM (section 4.3.3.2). The particle size of coarse powders was found out by sieve analysis. The average particle size and size distribution of milled powders were determined using an optical microscope fitted with an image analyzer (section 4.3.2.1). Morphological features of particle were examined by SEM.

8.3.1.4A Resin Bonded Magnet of Coarse Powders

Coarse powders of alloy $C_{11}(B)$, produced by mortar grinding, were size fractionated using 52 mesh (300 μm), 100 mesh (150 μm), 150 mesh (106 μm) and 250 mesh (63 μm) ASTM sieves. Each size fraction was made into two parts. One part from each size fraction was sealed in quartz tube under vacuum. Ti chips were used as getter during vacuum sealing to remove traces of oxygen from the ampule containing the alloy powder (vide section 4.3.2.2 for detail). The sealed powders were aged at 620°C for 200 hours and quenched in water. Aged and unaged powders were separately set in epoxy resin under 9 kG magnetic field to make the resin bonded pellets. Table VIII.3 shows the particle size and magnetic properties of pellets. Both aged and unaged coarse powders show considerably high σ_s value (90-106 emu/g) as compared to the unaged bulk alloy $C_{11}(B)$ (~ 60 emu/g). The σ_s value, however, was found to decrease with decrease in particle size (Table VIII.3). Although the aged powders show only marginally higher σ_s values as compared to the unaged powders, the increase in (σ_r/σ_s) and iH_c values are quite pronounced. For the aged powders, there is a

Table VIII.3: Magnetic Properties* of Oriented Resin Bonded Coarse Powders of Alloy C₁₁(B) (Annealed at 1100°C, 48 hrs) Before and After Aging at 620°C for 200 hrs.

Nominal Particle Size, μm	Before Aging				After Aging			
	σ_s	σ_r	iH_c	σ_r/σ_s	σ_s	σ_r	iH_c	σ_r/σ_s
300-150	101	6.8	24	0.07	106	47.4	740	0.45
150-106	100	8.8	27	0.09	106	60.0	820	0.57
106-63	99	9.6	30	0.10	104	60.7	850	0.59
< 63	90	8.7	45	0.10	99	58.8	900	0.59

* Units : σ - emu/g ; iH_c - Oe

gradual increase in iH_c value from 740 to 900 Oe as the particle size decreases from 300 μm to less than 63 μm ; the corresponding increase in (σ_r/σ_s) value is from 0.45 to 0.6.

8.3.1.4B Resin Bonded Magnet of Milled Powders

Two different sets of experiments were carried out with the milled powders. In the first set of experiments, to study the effect of milling time on the magnetic properties of resin bonded pellets, a homogenized (1100 °C, 48 hours) unaged alloy was used for making the powders. Combined effect of milling and aging treatment was studied in the second set of experiments. Aging treatment (620 °C, 200 hours) was carried out on the milled powders, prepared from a homogenized (1100 °C, 48 hours) alloy, or the solid piece of homogenized bulk alloy used for milling.

(i) Effect of Milling Time on the Magnetic Properties

To study the effect of milling time, -100 mesh powders of annealed alloy C₁₁(A) and C₁₁(B) were milled for different lengths of time upto 10 hours and used for making resin bonded magnets. Magnetic properties of these magnets were studied as a function of milling time. For the two different batch of alloys, magnetic properties, iH_c and σ_s , at different milling time are given in

Fig.VIII.6. The H_c value increases with increase in milling time. Typically, for alloy $C_{11}(A)$ the H_c increased from the initial value of 45 Oe (H_c of the -100 mesh powder used for milling) to 620 Oe, after about 8 hours of milling, and approached a constant value. σ_s value remains more or less constant during milling except for a small decrease at the highest milling time. Up to about 6 hours, for the milled powders of alloy $C_{11}(A)$ and $C_{11}(B)$, the σ_s values are 81 and 88 emu/g, respectively. The typical values of σ_r/σ_s for these magnets are of the order of 0.6.

Particle size distribution, obtained by plotting image analyser's statistical particle count data, is given in Figs.VIII.7(a)-(d) for the 2, 5, 7 and 10 hours milled powders of alloy $C_{11}(B)$. The fraction of particles in the 0-10 μm range appear to increase with increase in milling time; the increase is more pronounced between 2 and 5 hour of milling.

Fig.VIII.8(a) shows a typical SEM micrograph of particles [alloy $C_{11}(B)$] milled for 5 hours. The particles are often elongated and irregularly shaped. The shorter dimension of particles is 1 μm or less, the other dimension appears to fall in the range 1-4 μm . SEM micrograph of powders milled for 5 hours and after alignment in magnetic field and setting in epoxy resin is shown in Fig.VIII.8(b). The micrograph is recorded from the surface perpendicular to the alignment direction. The irregularly shaped particles appear to be somewhat rounded after magnetic alignment and setting in the resin [Fig.VIII.8(b)] due to preferential orientation. Contrary to SEM observation (Fig.VIII.8) the image analyzer particle size distribution (Fig.VIII.7) shows a larger number of particles with size greater than 5 μm . A larger fraction of particles with size greater than 5 μm is due to the inability of the optical microscope to distinguish between single particle and agglomerate of small particles.

(ii) Combined Effect of Milling and Aging Treatment

Two different kinds of experiments were performed to study the combined effect of milling and aging treatment and to know how these two operations should be sequenced during the fabrication of

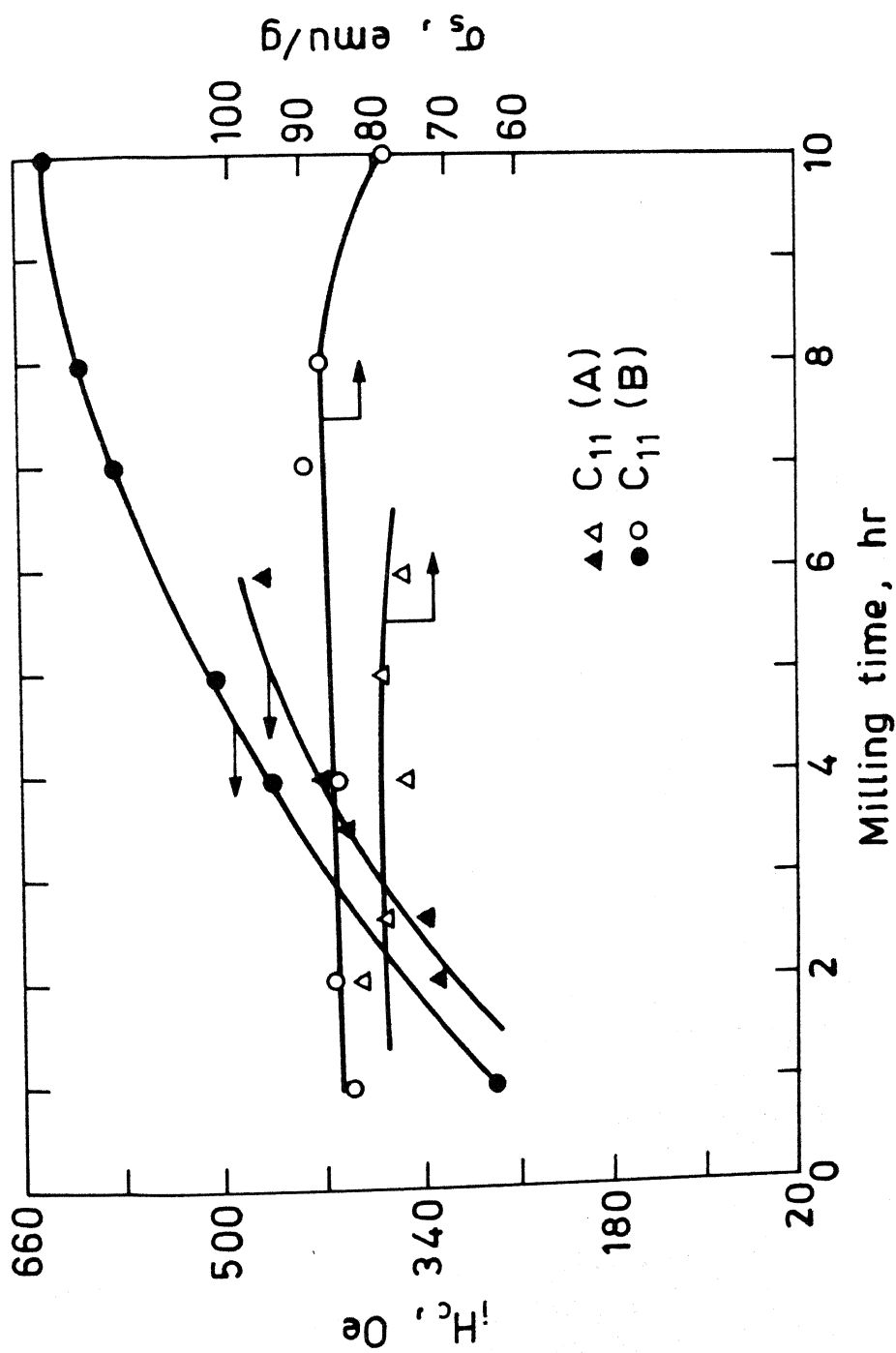


Fig. VIII.6 Effect of milling time on the magnetic properties of two different batches of alloy C₁₁ (annealed at 1100 °C for 48 hours)

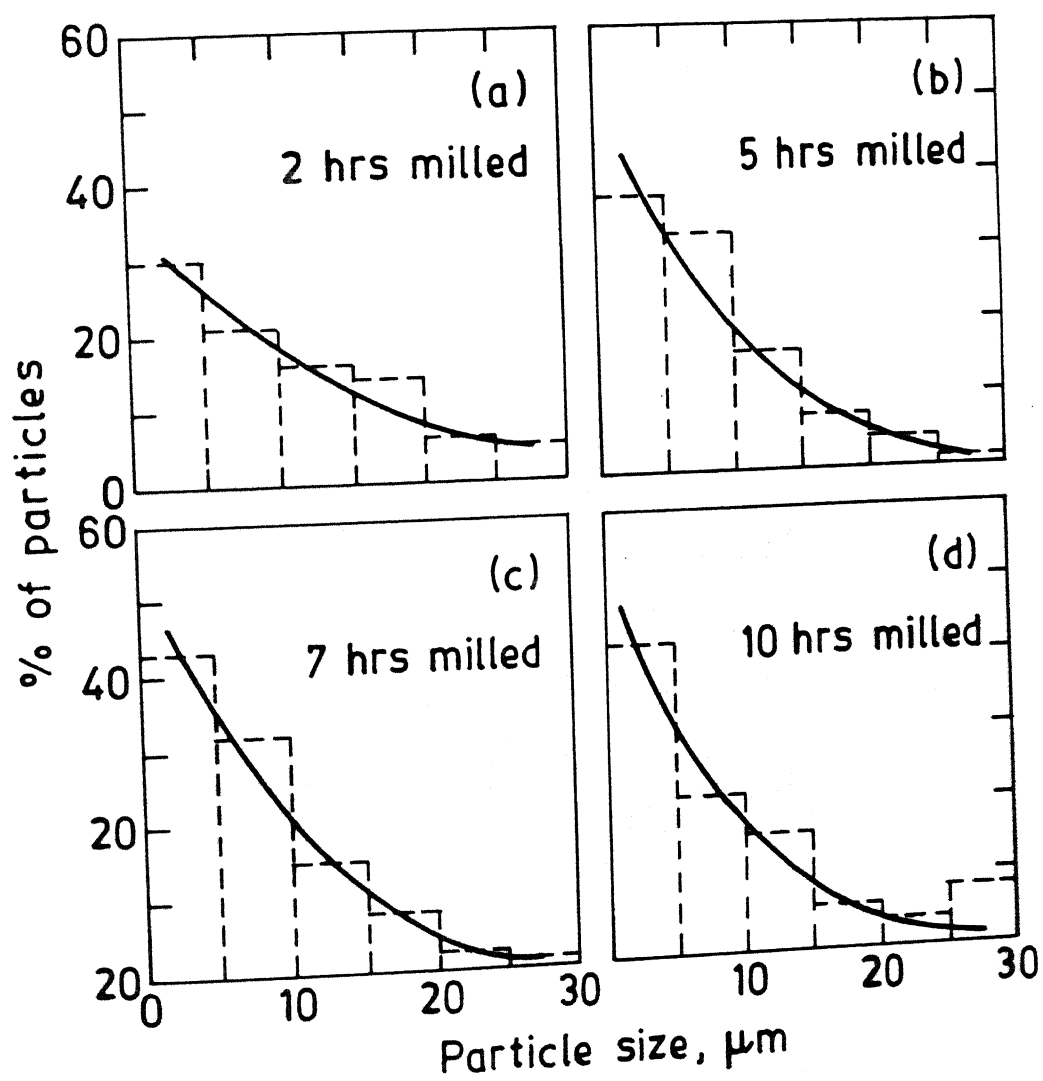
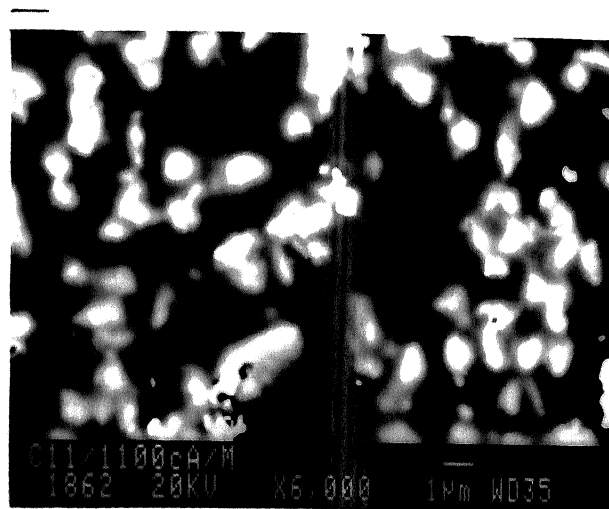
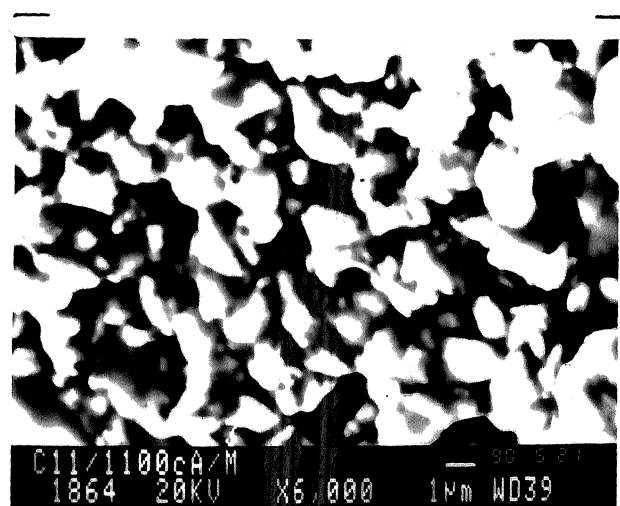


Fig.VIII.7 Particle size distribution at different milling periods for alloy $C_{11}(B)$



(a)



(b)

Fig.VIII.8 SEM (SE-mode) micrographs of 5 hours milled powder of alloy $C_{11}(B)$: (a) milled powder; and (b) milled powder after magnetic alignment and setting in epoxy resin (photomicrograph in (b) is recorded from the sample surface perpendicular to the magnetic alignment direction)

magnets.

In the first case, the homogenized alloy $C_{11}(C)$ was milled upto 2 hours and the powders collected at different intervals of time were dried, sealed under vacuum in quartz ampules (vide section 4.3.2.2 for the detail of sealing procedure) and aged for 200 hours at $620^{\circ}C$ before making the resin bonded magnets. The resin bonded pellets were characterized in terms of H_c , σ_s and σ_r , and the results for the different milling time are given in Fig.VIII.9(a). The H_c and σ_r shows a sharp drop with increase in milling time; typically the values were 950 Oe and 45 emu/g, respectively, after 0.5 hours of milling and decreased to 240 Oe and 22 emu/g after 2 hours of milling.

The results in Fig.VIII.9(b) are for the second case in which the alloy was first aged at $620^{\circ}C$ for 200 hours and then milled for the different lengths of time upto 7 hours. In this case, the H_c increased to about 1150 after 3 hours of milling and then it became more or less constant upto 7 hours of milling. The σ_r showed only a small decrease with increase in milling time and for the 3 hours milled powder its typical value was 60 emu/g. The particle size distribution of milled powders prepared from the aged alloy was also examined, for 1 hour and 5 hours milled powders, using SEM as well as optical microscope fitted with an image analyzer. The results are shown in Fig.VII.10(a)-(d). A majority of particles appear to fall in 1-6 μm size range even after 1 hour of milling [Fig.VIII.10(a),(b)]. There appears to be an increase in the proportion of finer particles (0-2 μm range) after prolonged milling for 5 hours [Fig.VIII.10(c),(d)].

8.1.1.5 Sintered Magnets

4 to 5 mm diameter and 4 to 6 mm height magnetically aligned green pellets (green density $4.5-5 \text{ g/cm}^3$) were made, vacuum degassed (at $200^{\circ}C$ for 10 minutes), sealed and sintered between 900 and $1100^{\circ}C$ for different lengths of time. One set of pellets was magnetized in a pulse magnetizer at 60 kOe magnetic field after sintering. Other set of pellets was subjected to post

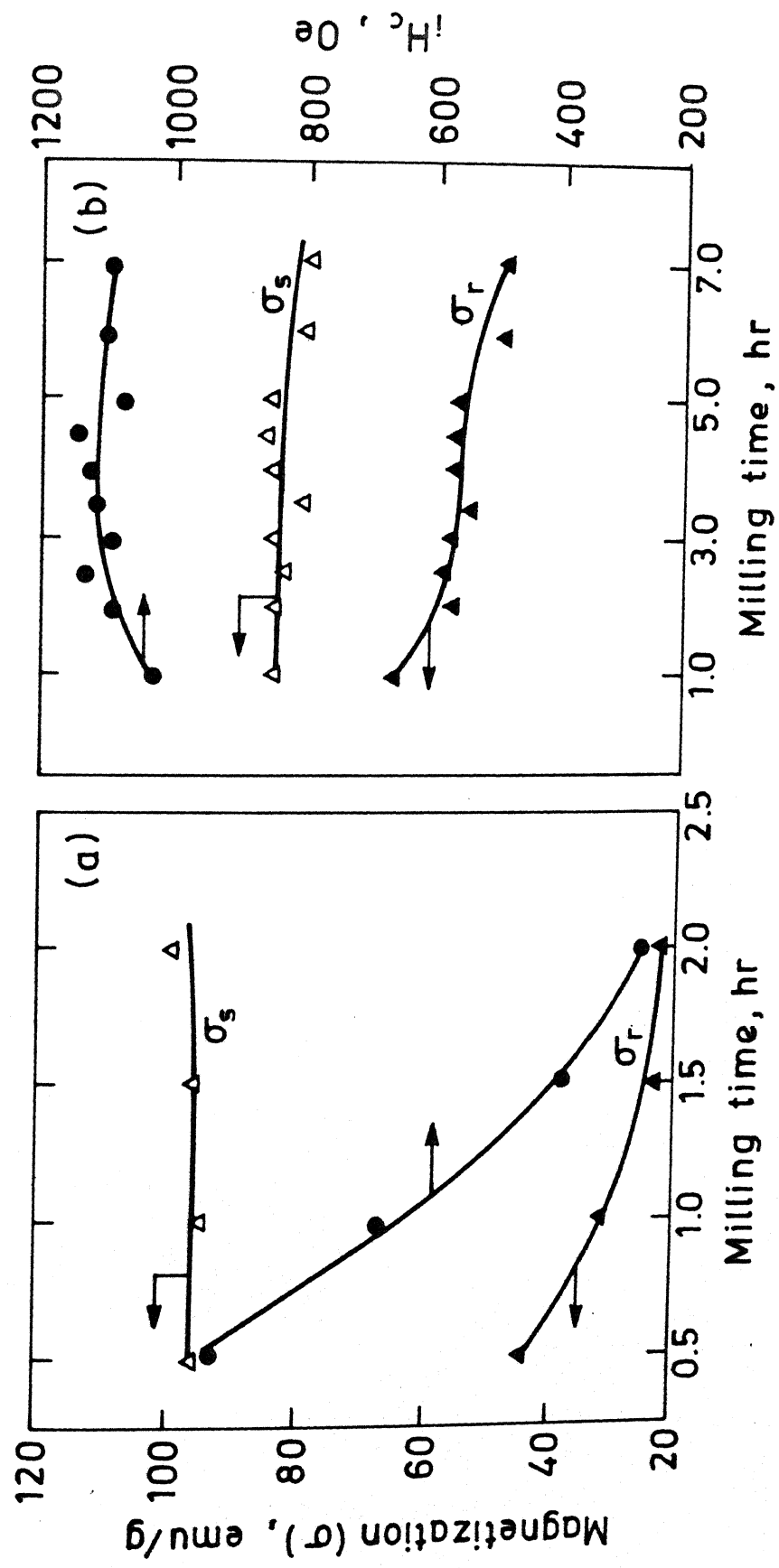


Fig.VIII.9 Effect of milling time on the magnetic properties of resin bonded magnets prepared from alloy $C_{11}(C)$ (annealed at $1100^{\circ}C$ for 48 hours) after different aging schemes : (a) milling followed by aging at $620^{\circ}C$ for 200 hours; (b) aging at $620^{\circ}C$ for 200 hours followed by milling

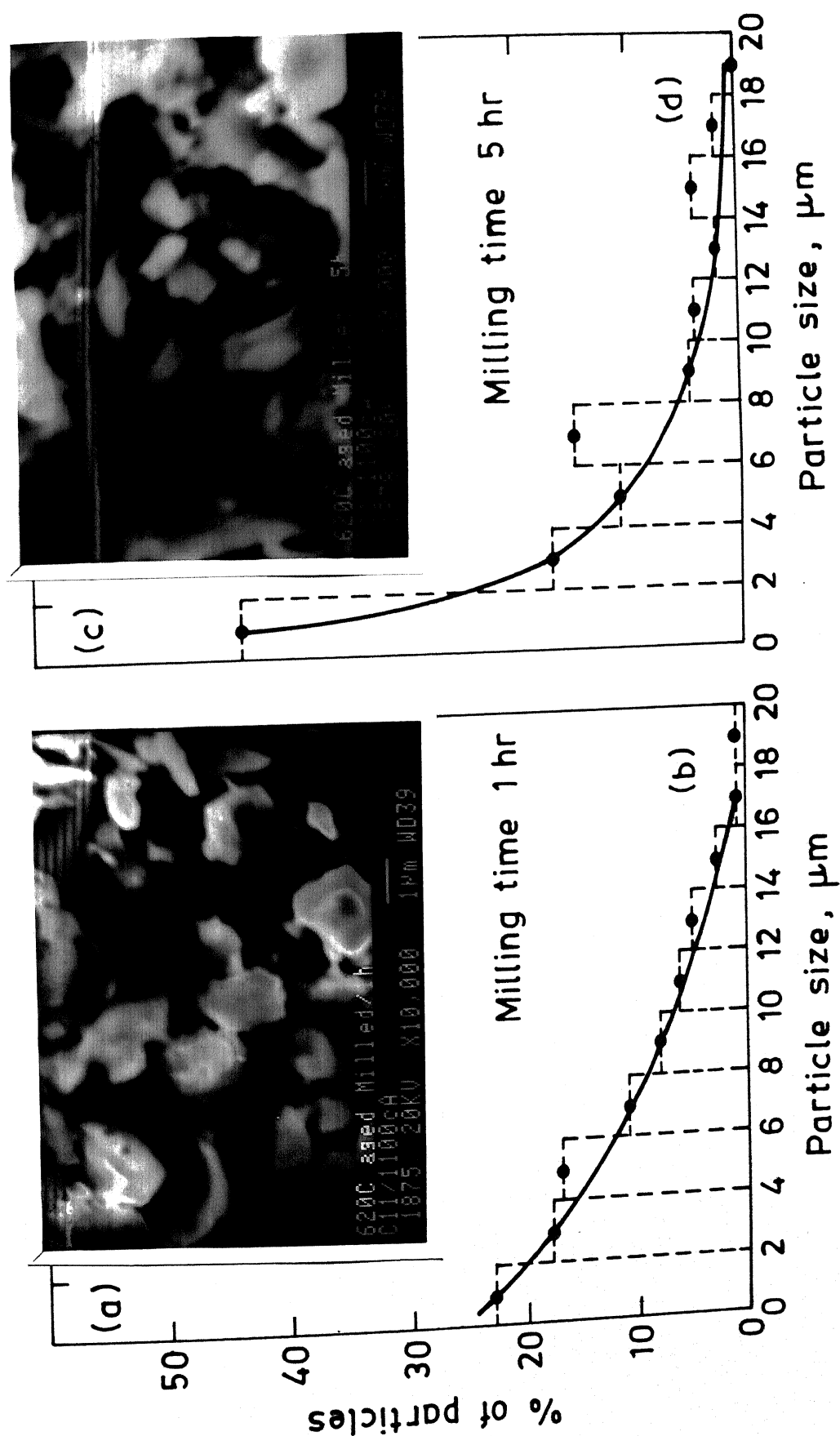


Fig.VIII.10 Particle size distribution for 1 hr and 5 hours milled powders of alloy C₁₁(C) : (a),(c) SEM micrographs; and (b),(d) image analyzer statistical particle count data

sintering aging treatment between 580-620°C for different lengths of time. Typical cycle of operation is schematically represented in Fig.VIII.11. The magnetic properties of the samples were measured using VSM.

Characterization of Sintered Pellets

The initial exploratory studies on sintered pellets were made using the alloy $C_{11}(C)$. The sintering was carried out at 1100, 1000, 950 and 900 °C for different lengths of time from 0.3 to 1 hour. The magnetic properties of these sintered samples are given in Table VIII.4 for the different sintering conditions. The magnetic properties, H_c , and M_r/M_s , of the sintered samples are very low. The H_c observed is only in the range of 80-125 Oe and (M_r/M_s) value is less than 0.1. Depending upon the sintered density of the pellets, $4\pi M_s$ value varied between 9.1-10.3 KG, more dense pellets showing higher values.

In order to investigate the reasons for the poor coercivity and remenance of sintered pellets prepared using alloy $C_{11}(C)$, the phases present in the green and the sintered pellets were examined by XRD, and the results are given in Fig.VIII.12. The XRD patterns in Fig.VIII.12 indicate that the N phase present in the green pellet changes to U+N phases after sintering. Since in the RE-Co-Fe-Cu-B phase diagram (Fig.V.9), the U+N+L phase region occur towards the lower RE content side of the N+L phase region, the nature of phase change suggest that there is loss of RE possibly due to oxygen pick up during various stages of processing, e.g. milling, sintering etc. As indicated before, the N phase appears to be more important from the magnetic point of view. To compensate for the loss of RE and get the desired N phase microstructure, several alloys with higher RE content were prepared in the close vicinity of alloy C_{11} . The composition of alloys prepared is schematically shown in Fig.VIII.13. One set of alloys was prepared with the same amount of Fe as in alloy C_{11} but with increasing RE content from 15 at.pct. to 20 at.pct., e.g. alloy $C_{34}(b)$, C_{27} , C_{28} and C_{31} [alloy of composition $C_{34}(b)$ is prepared by blending powders of alloy C_{11} and C_{27}]. In another set of alloys, e.g. $C_{35}(b)$, C_{30} , C_{33} , $C_{33}(b)$ [alloy $C_{35}(b)$ and $C_{33}(b)$

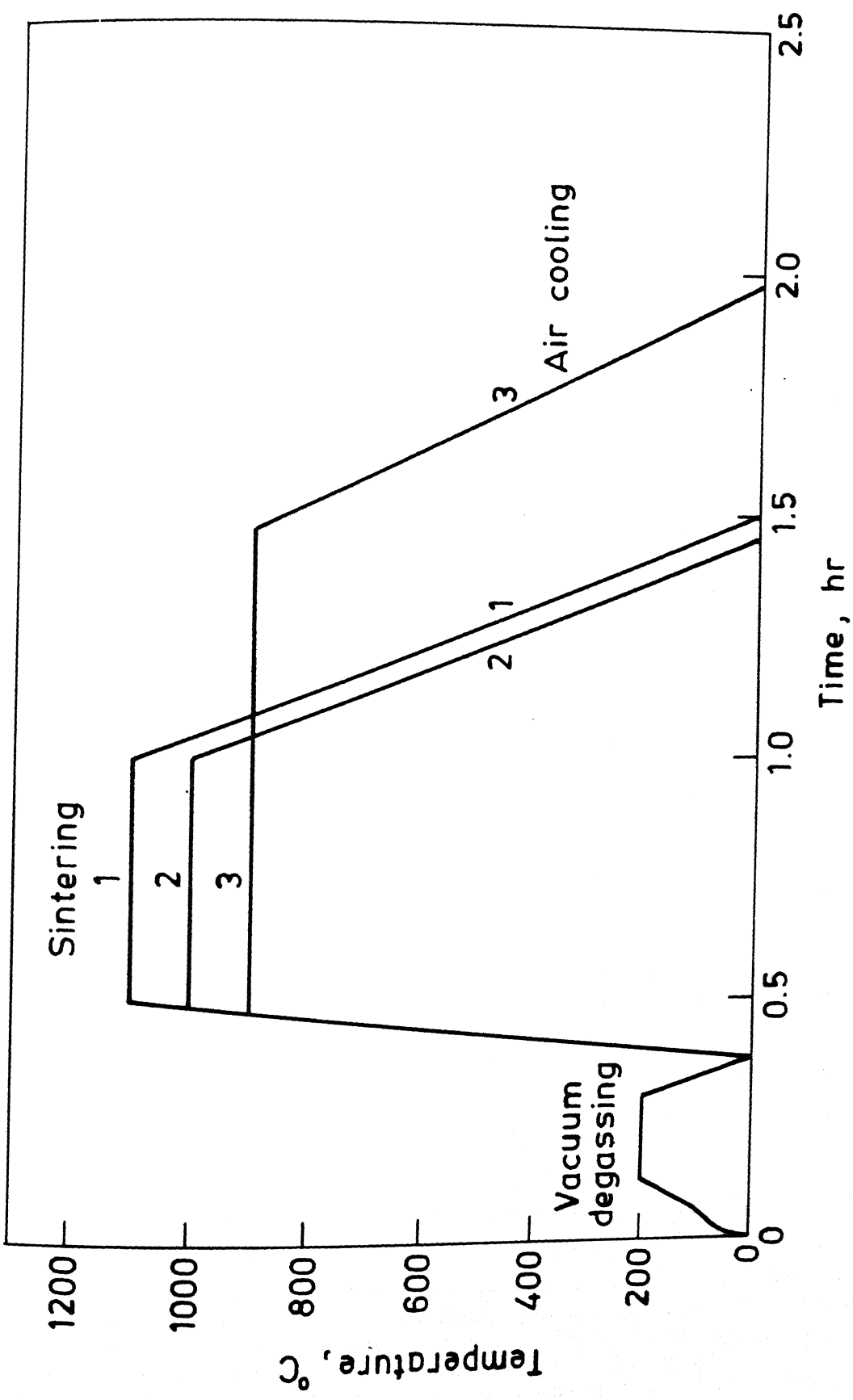


Fig.VIII.11 Heat treatment cycle for some of the sintering operations used in the RE-Co-Fe-Cu-Zr system

Table VIII.4: Physical and Magnetic Properties of the Sintered Pellets of RE-Co-Fe-Cu-Zr Alloys

Alloy Code (C _i) i	Composition at.pct.	Sintering		Density g/cc		4πM _s kG	H _c Oe	M _r /M _s	Phases* Identified by XRD
		Temp. °C	Time h	Green	Sintd.				
11	Fe = 13.0	900	0.5	4.74	9.87	10.3	127	0.06	U,N,L'
	RE = 14.2	900	1.0	-	9.41	9.7	132	0.06	U,N,L'
	Co = 62.8	950	0.3	-	9.20	9.1	129	0.05	U,N,L'
		950	0.5	-	9.94	10.2	119	0.05	U,N,L'
		950	1.0	-	8.99	9.4	118	0.05	U,N,L'
		1000	0.5	-	9.47	9.8	125	0.04	U,L',N
		1100	0.5	-	8.48	9.5	80	0.04	U,L',N
34(b)#	Fe = 13.0	1000	0.5	5.11	10.03	8.9	172	0.06	N,U,L'
	RE = 15.2	1050	0.5	-	8.34	7.3	132	0.05	N,U,L'
	Co = 61.8	1100	0.5	-	8.82	8.3	125	0.04	U,N,L'
27	Fe = 13.0	1000	0.5	-	8.60	6.9	204	0.09	N,U,L'
	RE = 16.2	1100	0.5	-	8.71	7.1	161	0.06	U,N,L'
	Co = 60.8	1100	1.0	-	9.22	7.8	133	0.05	U,N,L'
28	Fe = 13.0	950	0.5	-	9.53	7.2	240	0.13	N,U,L'
	RE = 17.2	1000	0.5	-	8.78	6.5	210	0.10	N,U,L'
	Co = 59.8	1100	0.5	-	9.14	7.4	154	0.06	U,N,L'
29	Fe = 13.0	1000	0.5	-	8.57	5.6	191	0.09	N,L'
	RE = 18.2	1100	0.5	-	9.72	7.0	158	0.07	U,N,L'
	Co = 58.8								
31	Fe = 13.0	1100	0.5	-	8.89	5.3	92	0.04	U,N,L'
	RE = 20.0								
	Co = 57.0								
35(b)#	Fe = 12.5	900	0.5	4.78	9.47	8.9	192	0.10	U,N,L'
	RE = 15.5	900	0.5	-	8.01	8.4	107	0.04	U,N,L'
	Co = 62.0	1100	0.2	-					
		950	0.5	-	8.80	7.9	168	0.06	U,N,L'
		1000	0.5	-	8.37	7.8	153	0.06	U,N,L'
		1100	0.5	-	9.46	9.4	110	0.03	U,N,L'
30	Fe = 12.0	1100	0.5	-	9.27	8.6	126	0.04	U,N,L'
	RE = 16.0								
	Co = 62.0								
33	Fe = 12.0	900	0.5	5.07	8.87	6.4	280	0.11	N,U,L'
	RE = 16.8	1000	0.5	-	9.04	6.4	170	0.08	N,L'
	Co = 61.2	1100	0.5	-	9.64	7.4	143	0.04	U,N,L'
33(b)#	Fe = 12.0	1000	0.5	4.49	-	-	-	-	N,U,L'
	RE = 16.8	1100	0.5	-	-	7.0	142	0.06	U,N,L'
	Co = 61.2								
32	Fe = 12.0	1100	0.5	-	9.11	6.0	116	0.04	U,N,L'
	RE = 18.5								
	Co = 59.5								
15	Fe = 10.8	1100	0.5	-	8.11	8.7	61	0.03	U,N,L'
	RE = 16.0								
	Co = 63.5								

* phases present in the sintered pellets; arranged in order of their decreasing amount; Δ phase present in all the cases; all the green pellets showed N+L'+Δ phases in their XRD patterns.
 # alloy made by blending -200 mesh powders of other nearby alloys.

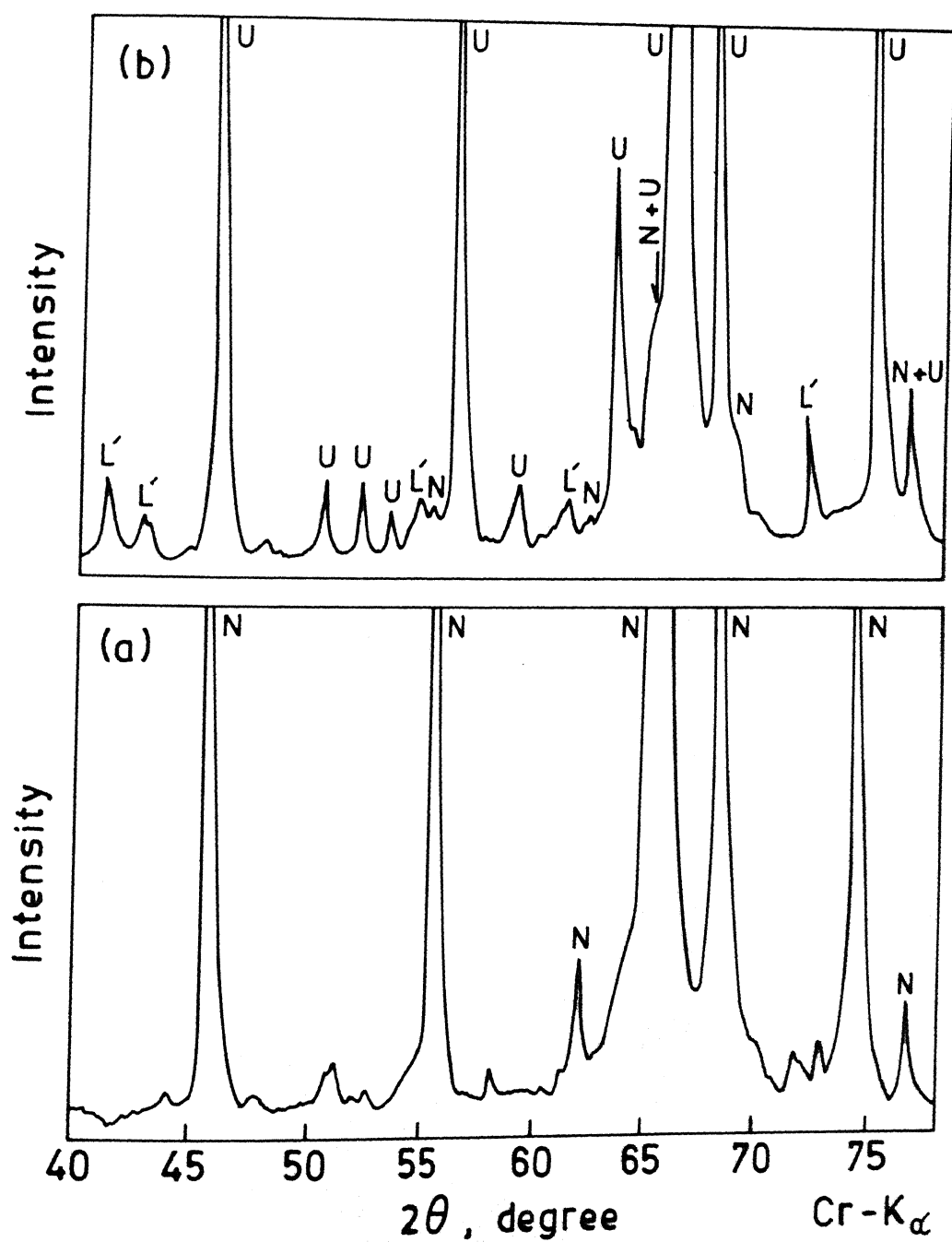


Fig.VIII.12 X-ray powder diffraction patterns for alloy C_{11} : (a) green pellet; and (b) 1100 °C sintered pellet

are prepared by blending alloy (C_{31}, C_{30}) and (C_{32}, C_{33}), respectively], a combination of somewhat higher RE (15.5-18.5 at.pct.) and lower Fe content (12.0-12.5 at.pct.) was tried. The alloy C_{15} was prepared with still lower Fe i.e. 10.75 at.pct. and 16.0 at.pct. RE. Besides chemical composition adjustment, the influence of sintering temperature was also explored in a bid to get the desired N phase microstructure which was expected to result in desirable good magnetic properties.

H_c , $4\pi M_s$ and (M_r/M_s) data for the sintered pellets, prepared from alloys of modified composition, are compiled in Table VIII.4 together with additional information regarding the phases present in the sintered pellets and the density of green and sintered pellets. For the alloy C_{33} , sintered at 900°C for half an hour, the maximum value of H_c (~ 280 Oe) was observed; the corresponding values of $4\pi M_s$ and M_r/M_s were about 6 kG and 0.1, respectively. The compiled data indicate that there is an increase in H_c with decrease in sintering temperature; e.g. for alloy C_{33} the H_c increased from 143 Oe to 280 Oe with decrease in the sintering temperature from 1100°C to 900°C . For all the high RE containing alloys the value of $4\pi M_s$ is less than the alloy C_{11} (C), the minimum value of 5.3 kG is observed for the alloy C_{31} containing highest (20 at.pct.) RE content (Table VIII.4). The value of M_r/M_s is only of the order of ~ 0.1 or below for all the sintered pellets prepared from the alloys of modified composition.

Examination of XRD data for the sintered pellets, prepared using alloys of modified compositions, revealed the following :

- (i) It has been possible to get N phase as the major constituent, together with small amount of U phase, in several sintered pellets (Table VIII.4). These include half hour sintered pellets of alloy C_{33} (sintered at 900°C); C_{28} (950°C); $C_{34}(b)$, C_{27} , C_{28} , $C_{33}(b)$ (1000°C); and $C_{34}(b)$ (1050°C).
- (ii) The alloys C_{29} (13 at.pct. Fe, 18.25 at.pct. RE) and C_{33} (12 at.pct. Fe, 16.8 at.pct. RE) contained only N phase with some liquid after sintering at 1000°C for half an hour
- (iii) Alloys sintered at 1050°C and 1100°C showed the presence of

U+N+L phases. N and U occur as major phases at 1050 and 1100°C, respectively (Table VIII.4).

Aging Behaviour of Sintered Pellets

Post sintering aging studies were performed on most of the sintered pellets. Aging treatments were carried out at 580, 600 and 620°C for different lengths of time. Figs.VIII.14 to 16 show the aging behaviour of pellets sintered at 1100, 1000 and 950°C. Complete iH_c and $4\pi M_s$ data for sintered and aged pellets of alloy C₃₃, which appeared to be the most promising from the point of view that in this alloy only (N+L) phases were present at 1000°C, are compiled in Fig.VIII.17.

Intrinsic coercivity (iH_c) shows a slow but continuous increase for all the 1100°C sintered samples (Fig.VIII.14) even after prolonged (e.g. 250 hours for C₃₂) aging. The sintered pellets used for aging study contained U as the major phase (Table VIII.4) with large amount of liquid phase as illustrated in Fig.VIII.18(a) for alloy C₃₄(b). The $4\pi M_s$ values do not show any significant change with aging time (Fig.VIII.14). The (M_r/M_s) value ranges from 0.1 to 0.2.

The aging behaviour of alloys sintered at 950 and 1000°C (Fig.VIII.16, VIII.15) differ considerably from the alloys sintered at 1100°C (Fig.VIII.14). The coercivity values in the case of 950 and 1000°C sintered pellets increase more rapidly, reach a maximum value and then start to decrease. As illustrated in the micrograph of alloy C₃₄(b) [Fig.VIII.18(b)], the amount of liquid phase formed decreases at the lower sintering temperatures. The aging behaviour of alloys (Figs.VIII.14-VIII.17) correlates well with the relative amount of the N phase and the second phase (U) present in the sintered pellets. For example, more pronounced aging response of 950°C sintered alloy C₂₈ and 1000°C sintered alloy C₂₉ compared to alloy C₁₁ (Fig.VIII.16) and C₃₄(b) (Fig.VIII.15), respectively, appears to be related to the higher amount of N phase being present in their sintered pellets as illustrated in the XRD patterns shown in Fig.VIII.19 and Fig.VIII.20. In general, the results of aging of sintered pellets

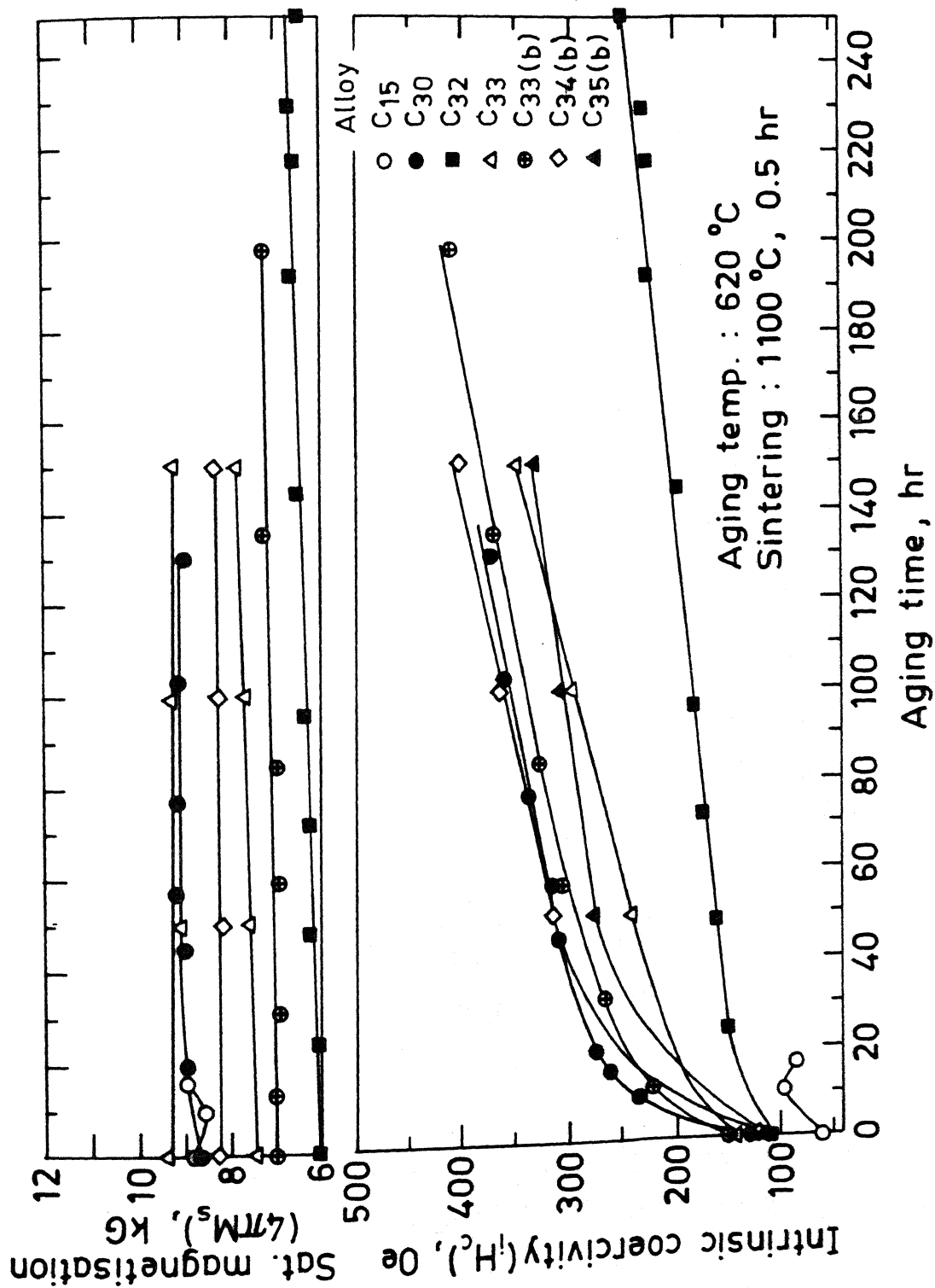


Fig.VIII.14 Aging behaviour of 1100 °C sintered pellets of alloy C₁₅, C₃₀, C₃₂, C₃₃, C₃₃(b), C₃₄(b) and C₃₅(b) at 620 °C

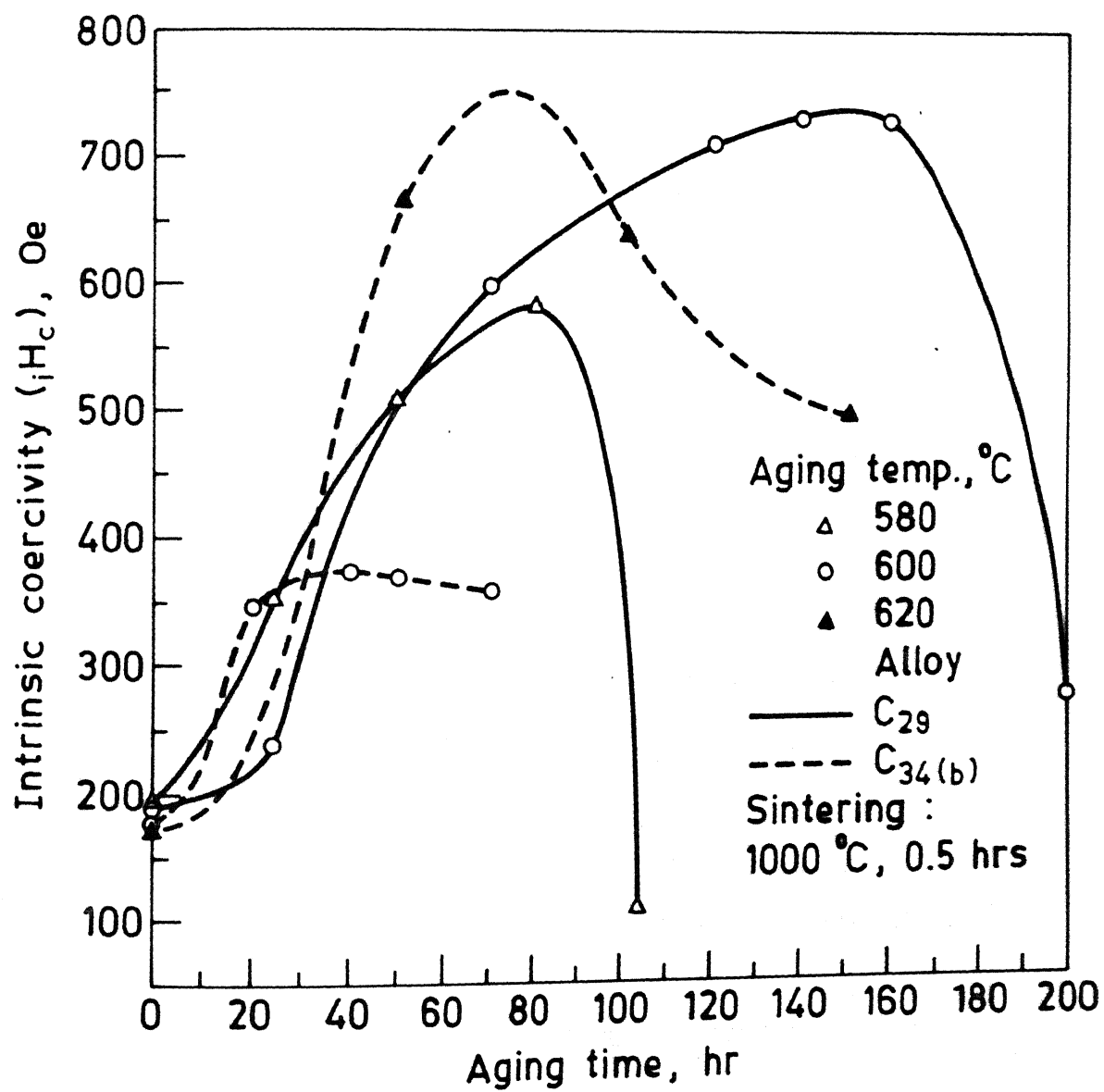


Fig.VIII.15 Aging behaviour of 1000 °C sintered pellets of alloy C₂₉ and C_{34(b)} at different temperatures

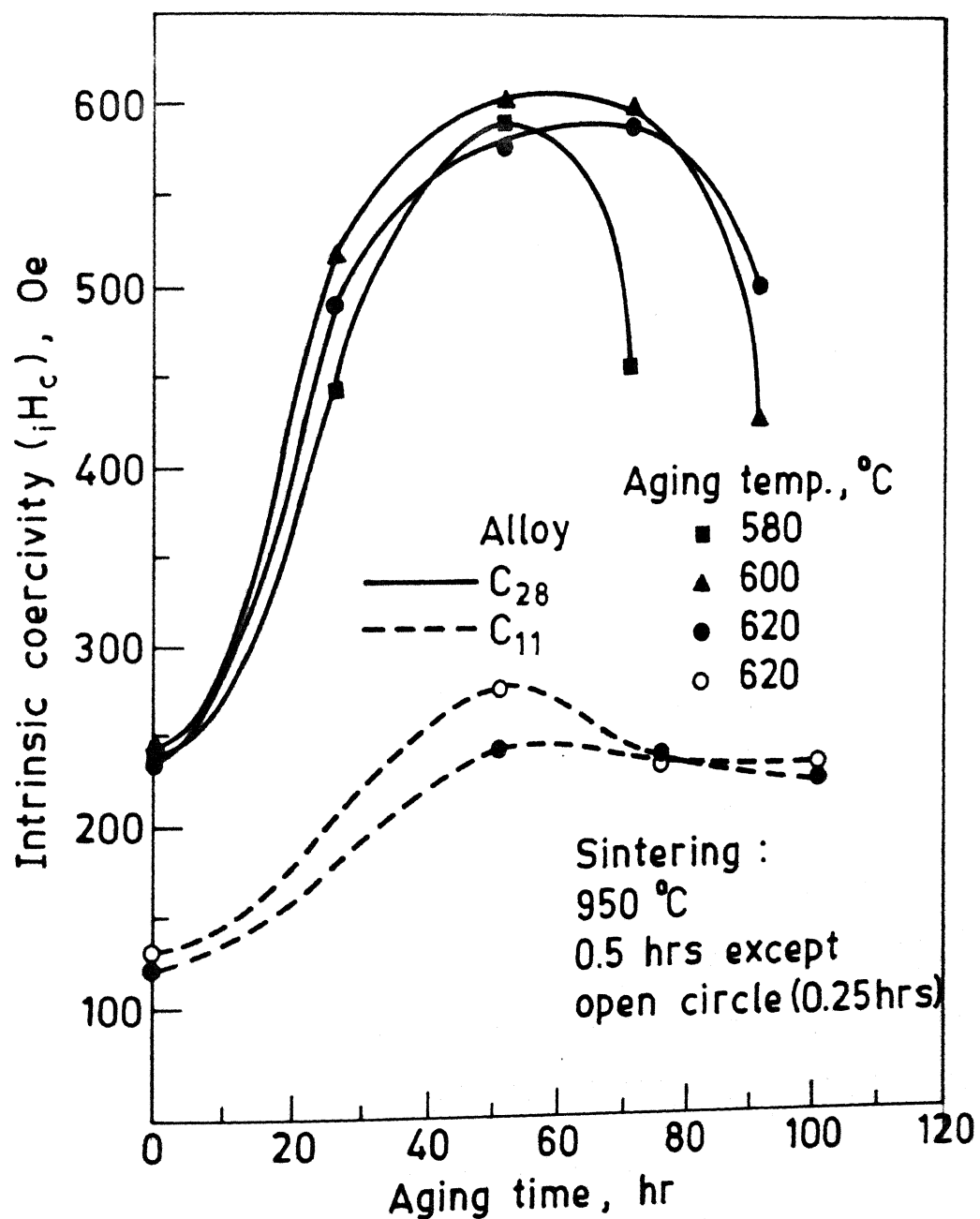


Fig.VIII.16 Aging behaviour of 950°C sintered pellets of alloy C_{28} and C_{11} at different temperatures

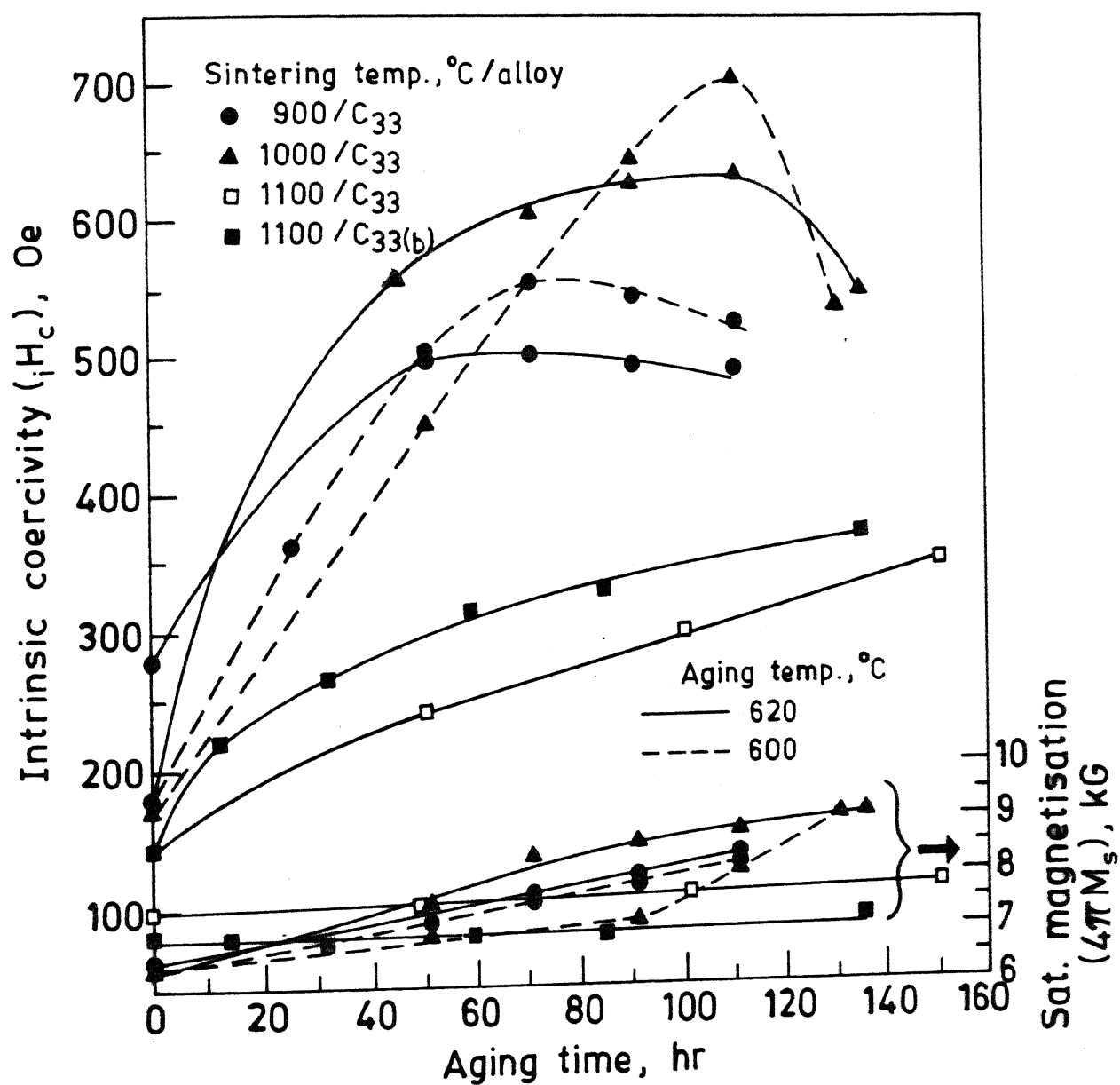
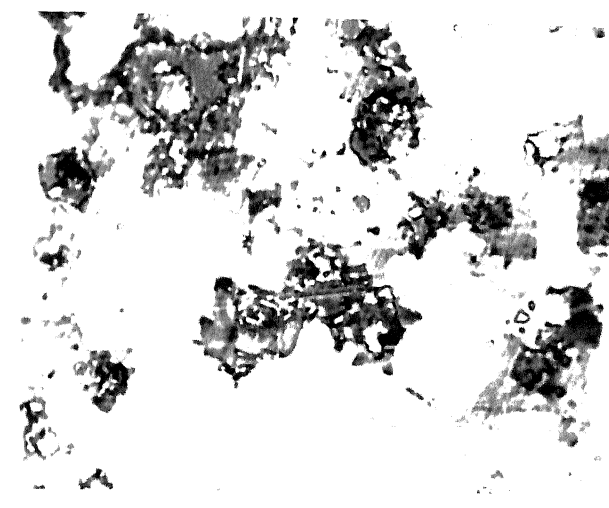
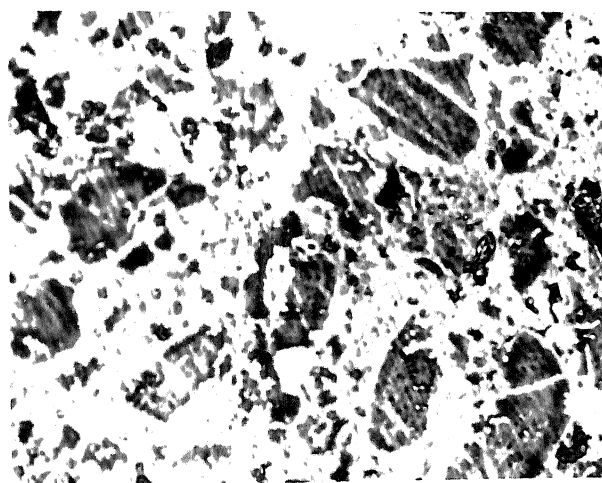


Fig.VIII.17 Variation of magnetic properties with aging time (at 620 and 600 °C) for the sintered pellets of alloy C₃₃ after sintering at different temperatures



(a)



(b)

Fig.VIII.18 Optical micrographs illustrating formation of liquid phase, grey regions, during sintering of green pellets of alloy $C_{34(b)}$ at different temperatures : (a) 1100 °C; and (b) 1000 °C
[Mag. 400x]

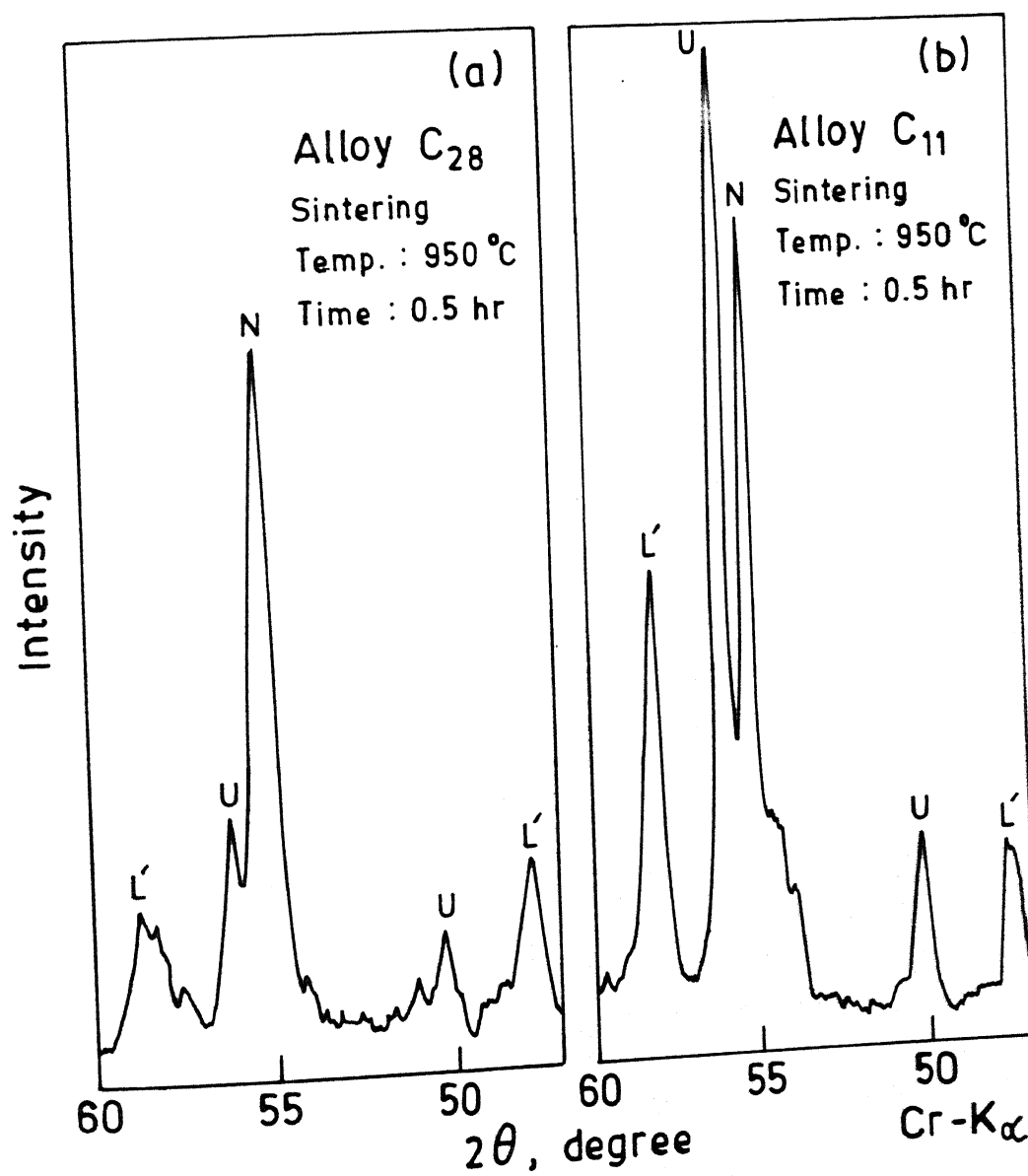


Fig.VIII.19 XRD patterns of the 950 °C sintered pellets of (a) alloy C₂₈ and (b) alloy C₁₁ illustrating relative amounts of the N and U phases

appear to be superior for the 620°C aged samples. The alloy C_{33} , sintered at 1000°C , shows somewhat superior aging behaviour at 600°C (Fig.VIII.17).

Sintered pellets of alloy C_{29} and C_{33} (sintering conditions : 1000°C , 0.5 hours) consist of mainly N phase. Although these alloys show the best aging response, the results are far below expectation. The maximum value of H_c is only of the order 750 Oe (Figs.VIII.15 and VIII.17). The results for alloy C_{33} in (Fig.VIII.17) do not show any remarkable feature. Aging of 900 and 1000°C sintered pellets of alloy C_{33} at 620°C results in ~ 20 pct. increase in $4\pi M_s$ after about 110 hours, the corresponding increase in (M_r/M_s) is from <0.1 to 0.3 .

8.1.2 Discussion

8.1.2.1 Aging Behaviour of the N Phase Alloys

A solid N phase alloy C_{11} $[\text{RE}(\text{Co}_{0.73}\text{Fe}_{0.15}\text{Cu}_{0.09}\text{Zr}_{0.02})_6]$ has shown remarkable magnetic hardening response to aging treatment between 675 – 620°C . Although the coercivity developed after 8 days of aging at 620°C was only about 1 kOe, 40 to 60 fold increase in coercivity was interesting.

Wide variations in the intrinsic coercivity and saturation magnetization are observed from one batch of alloy C_{11} to another after aging at 620°C for a fixed period (Table VIII.2). For the different batches of alloy C_{11} (with same alloy composition and very similar melting losses) the variation in the magnetic properties could not be correlated with their microstructures and XRD patterns which were found to be very similar for each batch of the alloy prepared. Since all these alloys were multiphase and contained a large amount of liquid phase, which gave rise to phases produced under non-equilibrium condition, it may be possible that these non-equilibrium phases may have a role to play in producing high and low coercivity and variation in saturation magnetization. This will require a more thorough investigation of the microstructure using TEM.

Devi [245] observed no apparent change in microstructure and XRD pattern of alloy C_{11} after aging at 620°C . SEM examination of the aged sample also did not give any indication regarding precipitation of a new phase. These observations suggest that precipitates formed are possibly very fine in nature. In precipitation hardenable $\text{Sm}(\text{Co}_{0.87}\text{Cu}_{0.13})_{7.8}$ and $\text{Sm}(\text{Co}_{0.74}\text{Cu}_{0.13}\text{Fe}_{0.13})_{7.8}$ magnets, Melton et.al.[252,253] also failed to detect by TEM the fine precipitates formed during aging. Only in highly overaged samples the precipitates could be identified by TEM. No attempt was made in this investigation to study the microstructural features by TEM. Future TEM studies on the aged and unaged sample may shed some light on the nature of change brought about during the aging treatment.

8.1.2.2 Intrinsic Magnetic Properties of the N Phase

The resin bonded pellets, prepared from the alloys of composition close to C_{11} , showed higher value of σ_s compared to the solid alloy specimen confirming that the maximum available field (10 kG) is not sufficient to saturate the sample in the bulk state.

The N phase XRD pattern indicated that it is possibly structurally related to the 1:5 stoichiometry phase. The T_c of N phase ($\sim 740^{\circ}\text{C}$) is reasonably higher than the MMCo_5 phase ($T_c \sim 500^{\circ}\text{C}$) and comparable with the SmCo_5 phase ($T_c \sim 747$) (Table II.2). For the MMCo_5 phase and the SmCo_5 phase the values of H_A observed are 185-195 kOe and 210-290 kOe, respectively. H_A of the N phase (≥ 25 kOe) is about 8-10 times less compared to the MM and Sm based 1:5 phase. However, in comparison with the H_A of the $\text{Sm}_2\text{Co}_{17}$ phase ($H_A \sim 75$ kOe) the H_A of N phase is moderate. The N phase has c-axis as the axis of easy magnetization which is desired for the fabrication of permanent magnet.

Thus, the overall magnetic properties of the N phase appeared to be moderate for the fabrication of resin bonded and sintered magnets.

8.1.2.3 Resin Bonded Magnets

Effect of Size Reduction on the Magnetic Properties of Unaged Alloys

The H_c of N phase alloy $C_{11}(B)$ responded favourably to size reduction. The H_c of the resin bonded magnet sample prepared using less than $63\ \mu\text{m}$ coarse powder of unaged alloy $C_{11}(B)$ is about 45 Oe (Table VIII.3) as compared to the bulk alloy coercivity of about 20 Oe (Table VIII.1). The increase in coercivity is small because particles are of considerably larger size than single domain particle size.

More pronounced increase in coercivity upto 20 fold of bulk alloy coercivity is observed for the finer milled powders (Fig.VIII.6). With increase in milling time the particle size decreases [see Fig.VIII.7(a)-(d)] and tends towards single domain particle size, consequently, resulting in an increase in coercivity. Contrary to SEM observations (Fig.VIII.8), a large number of particles show particle size greater than $5\ \mu\text{m}$ in the particle size distribution plots (Fig.VIII.7) prepared using image analyser's statistical particle count data. This is because the fine magnetic particles have a tendency to attract each other and form bigger agglomerates of particles which are difficult to break. In the microscope it is difficult to distinguish between a single large particle and an agglomerate of fine particles. Measurement on agglomerate results in apparently larger particle size. An increase in the fraction of finer particles with milling time is observed (Fig.VIII.7). However, with prolonged milling less pronounced increase in H_c and decrease in saturation magnetization occur (Fig.VIII.6). This is because finer particles are more prone to oxidation and also the chances of damage to particles surface increase with prolonged milling [2.11].

Effect of Size Reduction on the Magnetic Properties of Aged Alloys

It was thought that beneficial effect of both aging as well as size reduction, on the magnetic properties of alloy C_{11} , could

be utilized in the fabrication of resin bonded magnets. Sequencing of aging and size reduction step appeared to be an important consideration. Resin bonded pellets, prepared using powders which were subjected to aging treatment after milling, showed very low value of iH_c and σ_r ; typical values of σ_r , (σ_r/σ_s) and iH_c for 2 hours milled powders were 22 emu/g, 0.24 and 250 Oe [Fig.VIII.9(a)]. Resin bonded pellets prepared from coarse aged powder showed better magnetic properties; typical values for less than 63 μm coarse powder were $\sigma_r = 58.8$, $(\sigma_r/\sigma_s) = 0.59$ and $iH_c = 900$ Oe (Table VIII.3). These results clearly indicate that the poor magnetic properties for the milled and the aged powders are related to oxidation of fine powder due to large specific surface area of the milled particles. The oxidation could not be avoided by vacuum sealing of powder even after using heated Ti chips as a getter to remove traces of oxygen from the vacuum sealed capsule. On the other hand, when the alloy was first aged and then milled, much superior magnetic properties were observed. Typical values of σ_r , (σ_r/σ_s) and iH_c in this case, for 2 hours milled powder, were 60 emu/g, 0.68 and 1130 Oe, respectively [Fig.VIII.9(b)]. These observations suggest that aging treatment needs to be carried out in bulk form of the alloy before milling.

Resin bonded pellets prepared from the powder obtained after milling an aged (at 620°C for 200 hours) alloy for 2.5 hours showed the following magnetic properties; $iH_c = 1170$ Oe, $\sigma_s = 83$ emu/g, and $\sigma_r = 59$ emu/g [Fig.VIII.9(b)]. Since no published information could be found on the magnetic properties of similarly prepared MM based resin bonded magnets, the properties obtained were compared with the commercially available Zr containing Sm based 2:17 magnets. The σ_s and σ_r values mentioned above for the magnets prepared using 2.5 hours milled powder are comparable to the commercially available Sm based 2:17 magnets. However, the iH_c value of the MM based magnet is 6-10 times lower. The factors responsible for the low iH_c of the MM based magnet are difficult to pin point, however, the reasons could be the low H_A of N phase and also the mechanism responsible for coercivity development in the MM based magnet may be different from the Sm based magnets.

8.1.2.4 Sintered Magnets

The initial efforts to fabricate sintered magnets using the composition of alloy C_{11} resulted in quite low values of iH_c and M_r for the unaged as well as the aged sintered pellets. The inferior magnetic properties may be due to a small shift in the composition resulting in a microstructure consisting of both U and N phases [Fig.VIII.12(a), (b)]. It was felt that sintered pellets with N phase microstructure may result in better magnetic properties. In order to obtain the desired N phase microstructure, sintered pellets were prepared using alloys of modified chemical composition with higher RE content or higher RE and lower Fe contents (to compensate for any composition shift during processing, see Fig.VIII.13) and different sintering temperature between 900 to 1100°C. The U+N+L microstructure was obtained in all the alloys of modified composition after sintering at 1100°C (Table VIII.4). This does not appear to be surprising because the N phase region is very narrow (vide RE-Co-Fe-Cu-Zr phase equilibria at 1100°C; Fig.V.9), and alloys of modified composition can very easily enter into the U+N+L phase region due to any composition shift during processing. Only two alloys C_{29} (13.0 at.pct. Fe, 18.25 at.pct. RE) and C_{33} (12.0 at.pct. Fe, 16.8 at.pct. RE) showed N+L microstructure after sintering at 1000°C. It was found that the N+L microstructure in alloy C_{29} and C_{33} changed to the U+N+L microstructure (as observed in the 1100°C sintered sample, Table VIII.4) after the 1000°C sintered sample was annealed at 1100°C [Fig.VIII.21(a)(b)]. This sequence of heat treatment suggests that the N phase region possibly shifts towards the Co-Fe side of the RE-Co-Fe-Cu-Zr phase diagram as the temperature is lowered, i.e. the narrow N phase region may have a tilt in the composition temperature space so that the same alloy composition produces N+L phase at 1000°C and N+U+L phases at 1100°C.

The values of iH_c and M_r/M_s obtained for 1000°C sintered and 620°C aged pellets of alloy C_{29} and C_{33} , which showed N+L microstructure, were only of the order of 750 Oe and 0.1, respectively (Table VIII.4). The reasons for the low values of iH_c

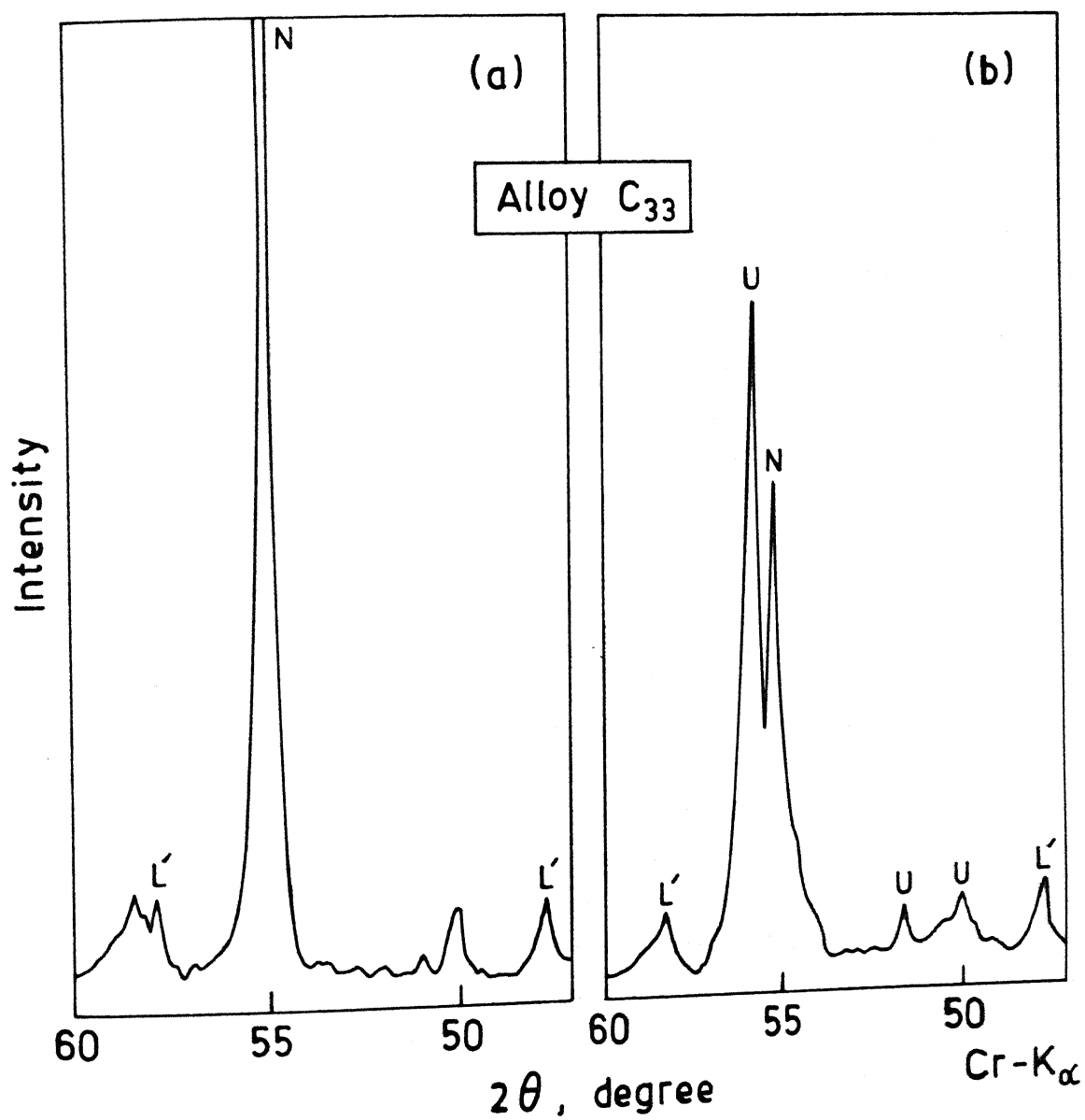


Fig.VIII.21 XRD patterns of sintered pellets of alloy C₃₃ : (a) sintered at 1000 °C for 0.5 hour; and (b) sintered at 1000 °C for 0.5 hour and annealed at 1100 °C for 0.25 hour

and M_r for the sintered pellets of these N phase alloys are not well understood. The composition of N phase in these alloys is not expected to be the same as that of the alloy C_{11} . It is not known whether the magnetic properties depend on the N phase composition. Since all the alloys were multiphase, and no single phase alloy could be produced, the possible dependence of magnetic properties of the N phase on alloy composition could not be studied. The presence of Δ phase [possibly $Zr(Co,Fe,Cu)_3$] in the microstructure of sintered magnet may be important from the point of view of low iH_c and σ_r observed. Ivanova et.al.[181] have reported that $Zr(Co,Fe,Cu)_3$ phase is soft magnetic phase and its presence is detrimental for coercivity development. Harmful effect of low coercivity $(Co,Fe)Zr$ phase (unknown stoichiometry) in Sm-Co-Fe-Cu-Zr magnets has also been observed by Hadjipayanis [182]. More detailed investigation on processing and microstructure aspects is required to pinpoint the precise cause of low coercivity and remanance observed.

8.1.2.5 Future Prospects

In a multicomponent system, such as RE-Co-Fe-Cu-Zr, several possibilities in terms of composition, microstructural features and process variables can be explored for the development of permanent magnets. Number of such possibilities is further compounded when various heat treatment options are taken into account. The present investigation has mainly focused on the alloys containing N phase as the major phase formed at $1100^\circ C$ or below down to $900^\circ C$, in a very narrow composition region with fixed Cu and Zr levels and limited heat treatment options. Thus the result of this study can at best be labelled 'preliminary' in this respect.

From the available results, the prospect of fabricating N phase based sintered magnets does not appear to be quite promising. For resin bonded magnets, based on C_{11} alloy composition [typical properties : $iH_c = 1170$ Oe, $\sigma_s = 83$ emu/g and $(\sigma_r/\sigma_s) = 0.68$], a two (or more) fold increase in coercivity is highly desirable. In order to improve iH_c , studies on the effect

of homogenization temperature (around 1100°C) and step aging, as tried successfully for $\text{Sm}(\text{Co,Fe,Cu,Zr})_Z$ ($Z \sim 7$) magnets (vide section 2.3.1.2), on coercivity development needs consideration.

XRD studies on U phase have indicated that it may be structurally related to the 2:17. The curie temperature ($\sim 830^\circ\text{C}$) and σ_s (~ 100 emu/g for the bulk alloy) values of U phase are quite favourable. This phase needs to be further characterized, in terms of H_A and direction of easy magnetization, to assess its potential. Since the U phase is structurally related to the 2:17 phase, studies on the response of this phase to different heat treatment cycles (e.g. step aging), used in the development of coercivity in precipitation hardenable 2:17 magnets deserves attention.

Other possibilities which may be explored are as follows: (i) the effect of different homogenization temperatures on the aging characteristics of U and N phases; (ii) adjustment of Cu and Zr levels and their effect on the stability of U and N phases, elimination of Δ phase, and magnetic properties; (iii) effect of partial substitution of MM by Sm and its effect on the stability and magnetic properties of U and N phases; etc.

8.2 RE-Fe-B System

In the Nd-Fe-B system, $\text{Nd}_{15}\text{Fe}_{77}\text{B}_8$ has been found to be the most promising alloy composition for magnet fabrication (Section 2.3.2.1). Since the phase diagram of RE-Fe-B system is quite similar to that of the Nd-Fe-B system and the $\text{RE}_2\text{Fe}_{14}\text{B}$ (Γ) phase has a crystal structure which is analogous to the $\text{Nd}_2\text{Fe}_{14}\text{B}$ phase (see Section 6.2.2), magnet fabrication work was planned for the alloy composition, $\text{RE}_{15}\text{Fe}_{77}\text{B}_8$, which is the same as used for the fabrication of Nd-Fe-B magnets. As reported earlier, the Γ phase has a T_c value of $\sim 245^\circ\text{C}$ and the saturation magnetization for the Γ phase has been found to be about 125 emu/g (see section 8.2.1.2). Grossinger et.al.[64] have reported that in MM-Fe-B system $\text{RE}_2\text{Fe}_{14}\text{B}$ phase has c-axis as the easy direction of magnetization and a H_A value of about 40 kOe.

8.2.1 Results

8.2.1.1 Effect of Aging Treatment on the Magnetic Hardenability of Bulk Alloy

Alloy E_{26} of composition $RE_{15}Fe_{77}B_8$ was chosen to investigate whether it shows magnetic hardenability by low temperature heat treatment. A bulk alloy piece used in this study, annealed at $1000^{\circ}C$ for 3 days, had initial H_c and σ_s values of 60 Oe and 100 emu/g, respectively. Different pieces of alloy E_{26} were subjected to low temperature aging treatment at 600, 650, 700, 800 and $900^{\circ}C$ for different lengths of time; 10 and 25 hours at 600 and $650^{\circ}C$ respectively and 2 hours at higher temperatures. H_c and σ_s values were measured and the results are shown in Fig.VIII.22. It can be seen from the Fig.VIII.22 that H_c and σ_s values remain more or less unchanged with aging time.

8.2.1.2 Resin Bonded Magnets

Rod milled powders of alloy E_{26} were used for making resin bonded magnets. Magnetic properties, H_c , σ_s and σ_r were measured as a function of milling time and the results are shown in Fig.VIII.23. Optimum milling time was selected from the variation of H_c and σ_s with milling time. The intrinsic coercivity (H_c) value increases to a maximum value of ~ 1500 Oe after 4 hours of milling. The σ_s value is the highest (~ 125 emu/g) for the 1-2 hours milled powder (Fig.VIII.23). The σ_r/σ_s has the highest value for 2-3 hours milled powder and it decreases slightly with increase in milling time. At three hours milling time, the H_c is ~ 1400 Oe which is very close to the maximum value with only a small decrease in σ_s and σ_r . Hence, keeping all these properties in mind, the 3 hour milled powder was considered to be the best. A part of the hysteresis loop of a resin bonded magnet prepared with the 3 hours milled powder is given in Fig.VIII.24. The hysteresis curve is close to square in nature, which is desired for a permanent magnet. Since it was not possible to make an accurate estimation of density of resin bonded pellets, $(BH)_{max}$ value could not be deduced from the hysteresis curve.

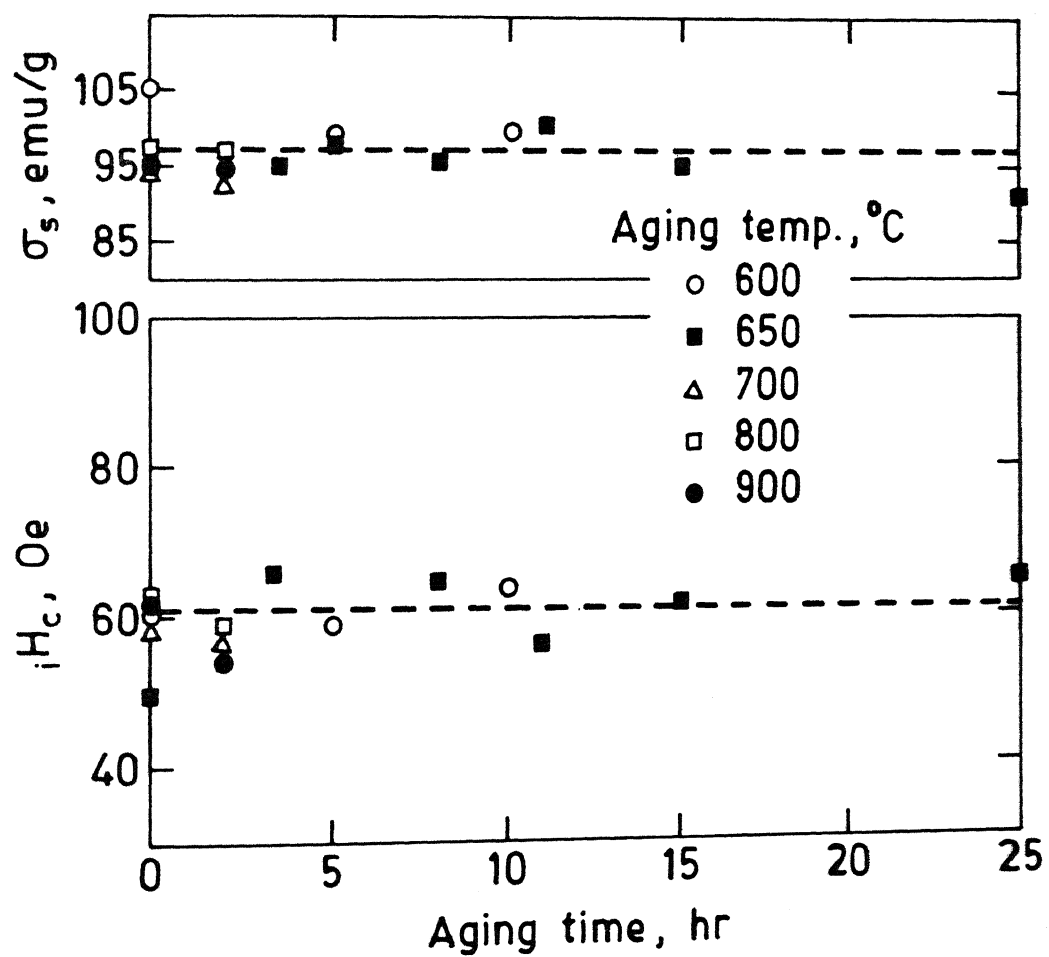


Fig.VIII.22 Effect of aging time on iH_c and σ_s of alloy E_{26} ($RE_{15}Fe_{77}B_8$) at different aging temperatures

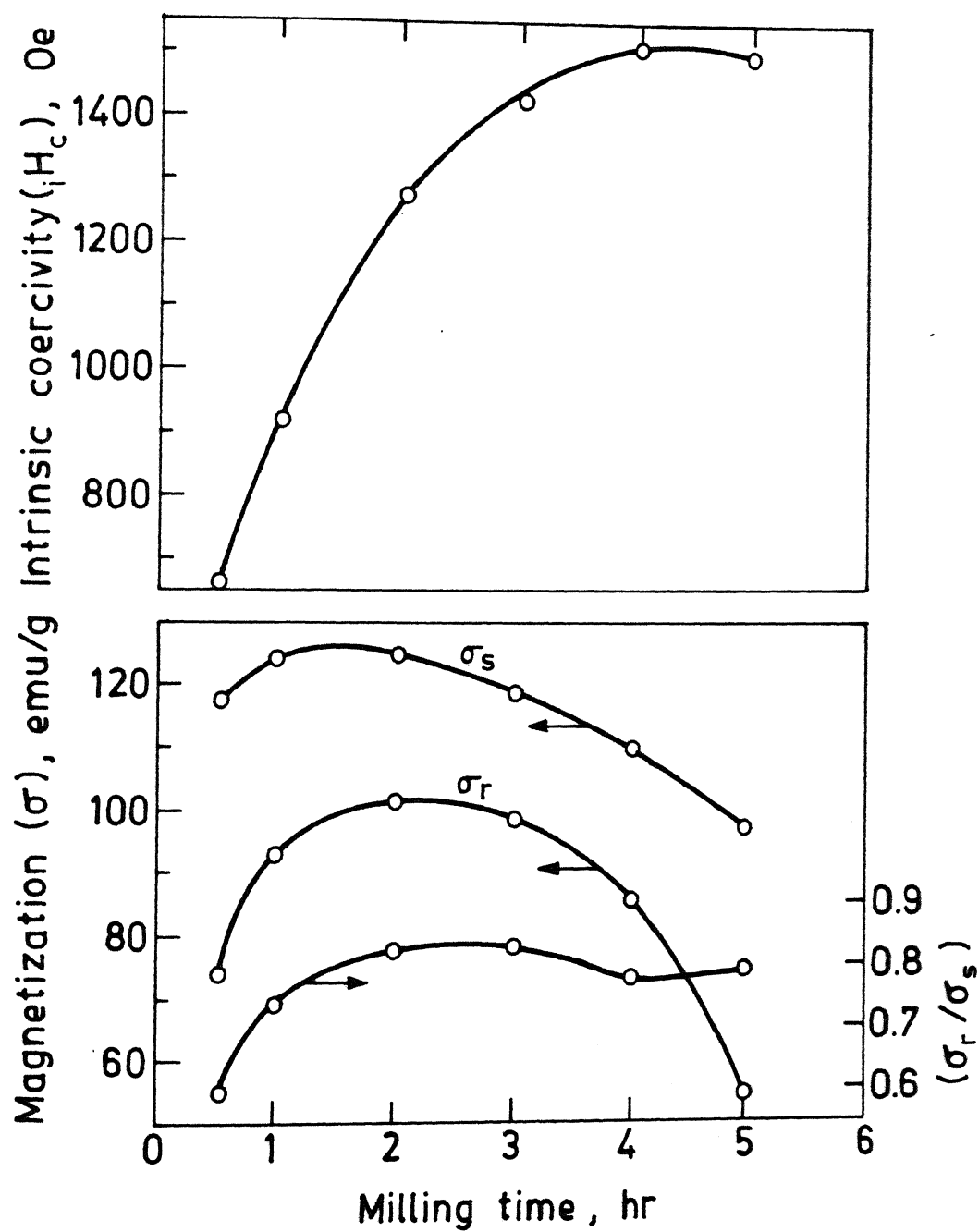


Fig.VIII.23 Effect of milling time on the magnetic properties of alloy E_{26} (measured on resin bonded oriented powder samples)

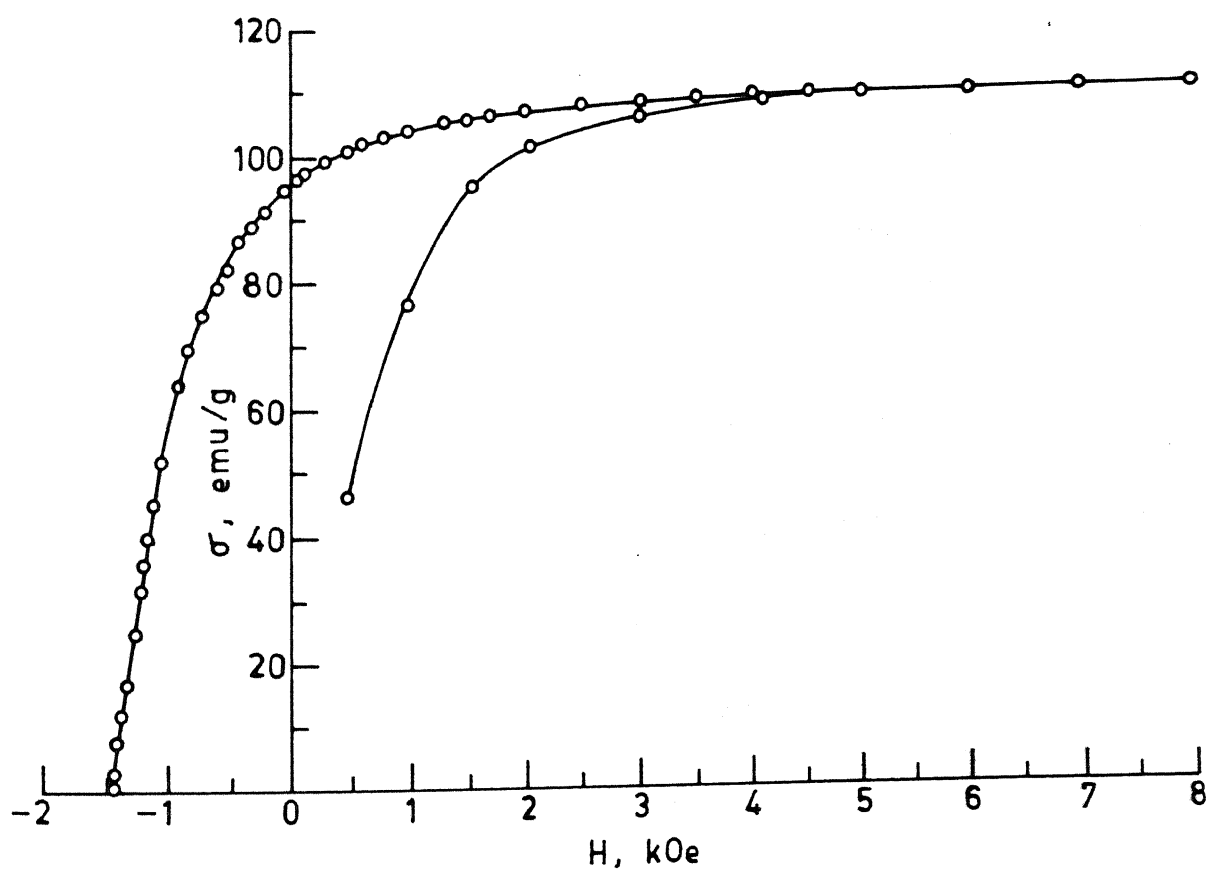


Fig.VIII.24 Half of the Hysteresis loop of a typical resin bonded pellet prepared from the 3 hours milled powder of alloy E₂₆

8.2.1.3 Sintered Magnets

Rod milled powders of alloy E_{26} , which were prepared for making resin bonded magnets, were used for the preliminary work of preparing sintered pellets. Magnetically aligned 3 mm diameter and 5-7 mm high green pellets were made using pulse magnetic field of 10 kG. The pellets were vacuum degassed at 200°C and sealed in fused silica tube under vacuum using Ti chips as a getter. Sintering of vacuum sealed pellets was carried out at different temperature from 1000 to 1100°C for 20-60 minutes (vide Section 4.3.2.3 for detail). The sintered pellets were magnetized in 10 kG magnetic field and their room temperature magnetic properties, H_c , σ_s and σ_r were measured. The microstructural and XRD studies were also carried out on the sintered pellets.

Magnetic properties for the sintered pellets of alloy E_{26} are given in Table VII.5. The sintered pellets show σ_s value in the range of 120-133 emu/g. Both H_c and σ_r/σ_s values are very low. H_c value is less than 360 Oe and σ_r/σ_s value is a meager 0.03-0.045. The microstructure of all the pellets showed very fine grains [Fig.VIII.25(a)]. XRD pattern showed the bcc α phase as the major phase indicating reasonable composition shift due to oxidation of the rare-earth component of the alloy during handling of alloy powders and sintering operation.

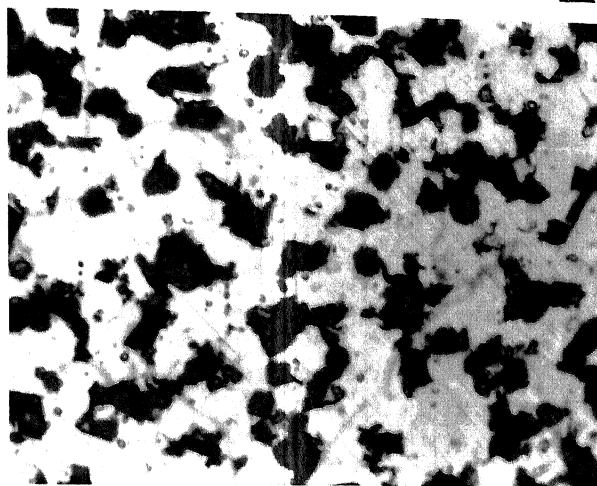
In order to tackle the composition shift problem, following measures were taken : (A) milling jar was evacuated and flushed with high purity argon gas several times before finally filling with argon gas, (B) fused CaCl_2 (preheated at 200°C for 30 minutes) was used in the vacuum desiccator for drying of alloy powder, and (C) five $\text{RE}_x\text{Fe}_{92-x}\text{B}_8$ alloys, E_{36} , E_{37} , E_{38} , E_{39} and E_{40} , were arc-melted with x increasing from 16 to 20 to compensate for the loss of RE during processing. All these measures led to an increase in the reactivity of alloy powder. The powders, after drying in vacuum desiccator, were bright and when brought in contact with atmosphere often caught fire. This problem was very serious when preheated CaCl_2 (200°C , 30 minutes) was used as a

Table VIII.5: Magnetic Properties of the Sintered RE-Fe-B Pellets Prepared Under Different Experimental Conditions

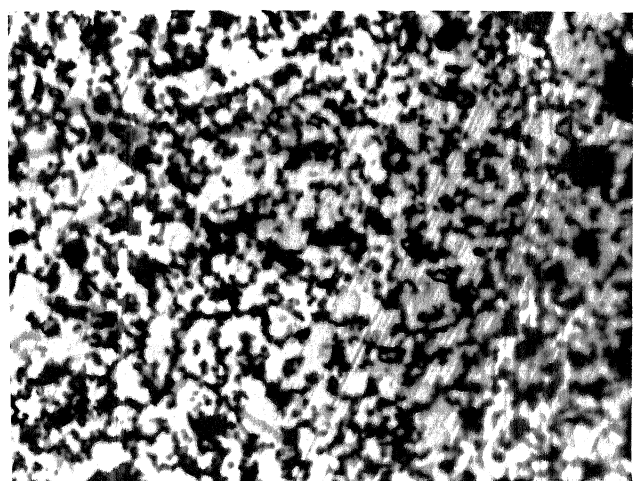
Alloy [#] No i	Milling Time of Powder Used, hr	Sintering Time and Temperature	Magnetic Properties			
			σ_s emu/g	σ_r emu/g	H_c Oe	σ_r/σ_s
26 RE=15* Fe=77 B=8	2	1100°C for 20 min taken into 600±10 °C for 20 min and air cooled	133	3.5	~ 360	0.03
	4	1150°C for 20 min other details as above	125	4.0	~ 250	0.03
	4	1050°C for 1 hr.	120	5.4	~ 250	0.05
	3	1000°C for 1 hr.	129	5.3	~ 265	0.04
36 RE=17 Fe=75 B=8	3	green pellet	70	-	-	-
	3	1050°C for 1 hr.	122	3.4	< 200	0.03
38 RE=19 Fe=73 B=8	1.5	1050°C for 1 hr.	80	5.4	~ 250	0.07
	1.5	1080°C for 1 hr.	85	1.4	50	0.02

Alloy designation E_i

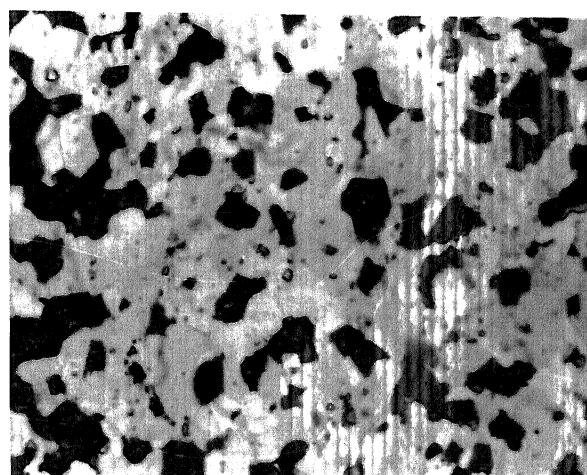
* Chemical composition of the alloy in at.pct.



(a)



(b)



(c)

Fig.VIII.25 Optical micrographs of sintered pellets of $RE_xFe_{92-x}B_8$ alloys : (a) alloy E_{26} ($x = 15$); (b) E_{36} ($x = 17$); and (c) E_{38} ($x = 19$) (Sintering conditions given in Table VIII.5; Microstructures Description : white phase often with scratch lines α , dull white phase without scratches Γ , grey or dark grey - liquid or oxide inclusions, 400x)

desiccant. Prolonged vacuum storage of the powder, even upto 24 hours, did not solve this problem. Attempts were also made to flush the desiccator with argon gas before taking out the powder, this also failed. Decrease in milling time to avoid generation of very fine powders also did not solve the problem.

In two cases (alloys E_{36} and E_{38}) it was found possible to save a part of the powders from oxidation. Pellets from these powders were made and sintered. The magnetic properties were found to be very poor. Fig.VIII.25(b),(c) and Fig.VIII.26 show the microstructures and XRD patterns of sintered pellets of alloy E_{36} and E_{38} . In the 1050°C sintered pellets, the alloy E_{38} shows more amount of Γ phase. However, the α phase appears to be the major one in both E_{36} and E_{38} sintered pellets (Fig.VIII.26). The RE-rich liquid phase show non-uniform spread around the grain boundaries. Since the oxidation problem could not be solved using the available facilities, further work on these alloys had to be abandoned.

8.2.2 Discussion

8.2.2.1 Intrinsic Magnetic Properties of the Γ Phase

The $\text{RE}_2\text{Fe}_{14}\text{B}$ (Γ) phase has shown a room temperature saturation magnetization (σ_s) value of ~ 125 emu/g for magnetically oriented resin-bonded powder sample of alloy E_{26} . The corresponding value for the $\text{Nd}_2\text{Fe}_{14}\text{B}$ phase, i.e. 140 emu/g [254], is somewhat higher than the Γ phase. According to available literature [64], the $\text{RE}_2\text{Fe}_{14}\text{B}$ phase has an H_A value of 40 kOe which is lower but moderate in comparison with the $\text{Nd}_2\text{Fe}_{14}\text{B}$ [1,2]. $\text{RE}_2\text{Fe}_{14}\text{B}$ has c-axis as the easy direction of magnetization [64]. Another important magnetic property is Curie temperature T_c . The Curie temperature of $\text{RE}_2\text{Fe}_{14}\text{B}$ has been found to be $\approx 245^{\circ}\text{C}$ in this investigation. Thus, the intrinsic magnetic properties of the $\text{RE}_2\text{Fe}_{14}\text{B}$ phase are inferior to that of the $\text{Nd}_2\text{Fe}_{14}\text{B}$ phase but are moderately high to qualify it as a suitable candidate for further consideration in the fabrication of low cost magnet with reasonably good magnetic properties.

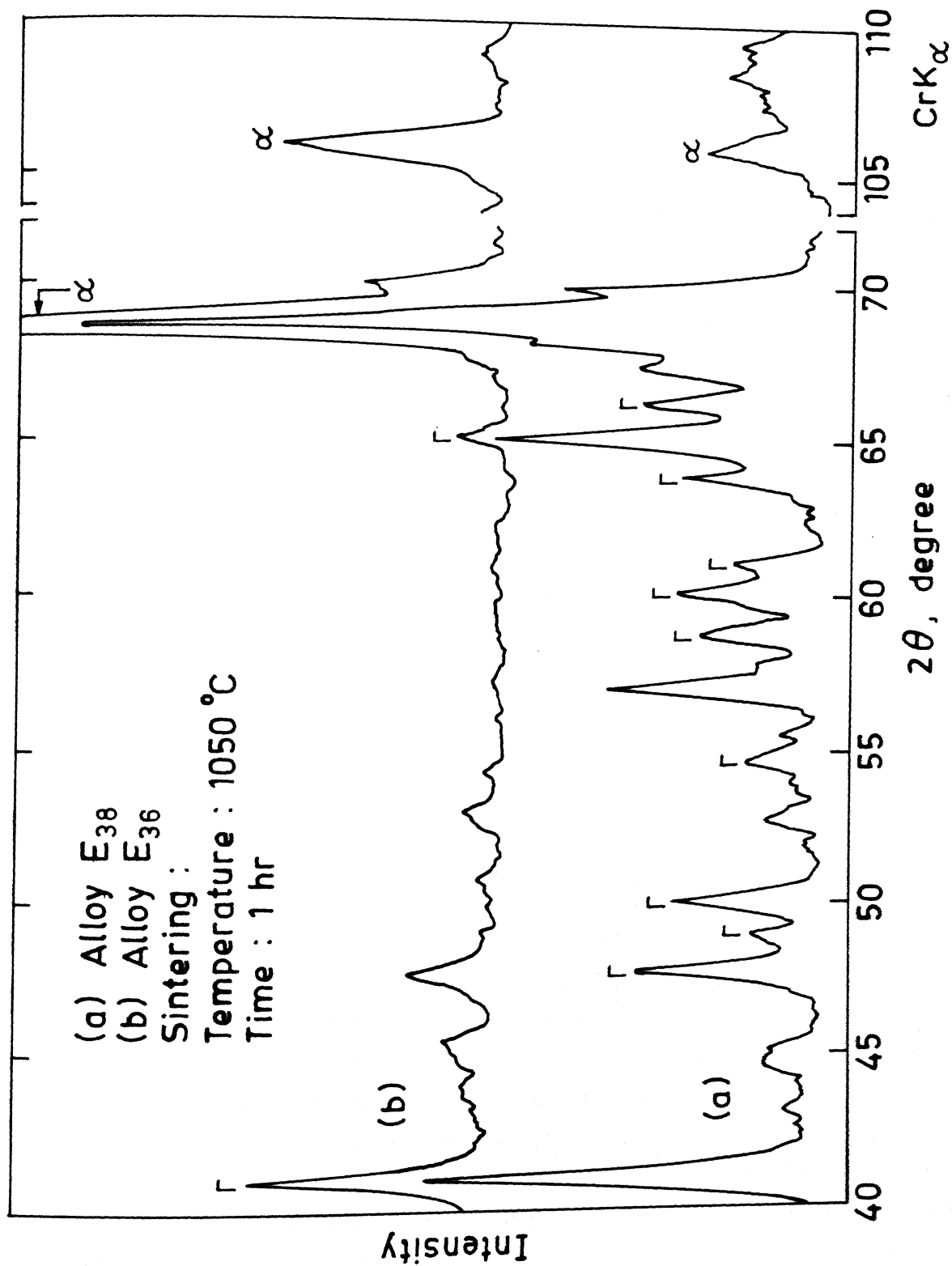


Fig.VIII.26 XRD patterns of 1050 °C sintered pellets of alloy (a) E₃₈ and (b) E₃₆

8.2.2.2 Aging Behaviour

Alloy E₂₆ of composition RE₁₅Fe₇₇B₈ did not show any response to the aging treatment between 600-800°C (Fig.VIII.22). Coercivity development during aging may result due to a combination of several factors, e.g. precipitation of second phase, composition readjustment, grain refinement etc.(vide literature review, section 2.3.1.2 and 2.3.2.3). Among these factors, the first factor is very important as observed in precipitation hardenable Sm-Co magnets; a large homogeneity region for the magnetic phase involved is essential. Poor response of alloy E₂₆ to aging treatment may be attributed to the very narrow homogeneity region of the Γ phase at 1000°C and its possible extension at lower temperatures without change in composition (Fig.VI.7). Since the bulk alloy is homogenized at 1000°C for 3 days in vacuum, there is little scope of any significant composition readjustment that could cause any significant change in coercivity.

8.2.2.3 Resin Bonded Magnets

There appears to be no information available regarding the resin bonded magnets produced using MM-Fe-B milled alloy powders. Yamasaki et.al.[216] reported the following magnetic properties for resin bonded magnets produced using melt spun ribbon of an alloy with MM₁₆Fe₇₅B₉ composition: $\sigma_s = 83.8$ emu/g, $\sigma_r = 64.9$ emu/g, $\sigma_r/\sigma_s = 0.77$ and $iH_c = 9.4$ kOe. The σ_s and σ_r values for the resin bonded magnet produced using RE₁₅Fe₇₇B₈ (alloy E₂₆) are superior (typical values for the 3 hours milled powder are $\sigma_s = 118$ emu/g, $\sigma_r = 97$ emu/g and $\sigma_r/\sigma_s = 0.82$ (Fig.VIII.23) however, iH_c value is comparatively quite low. The low value of iH_c may be attributed to larger grain size in milled alloy powders compared to the grain size produced in melt spun ribbon due to extremely fast cooling as well as the possible texture development in the melt spun ribbon.

8.2.2.4 Sintered Magnets

The properties developed by a sintered magnet depends on the intrinsic properties of basic magnetic phase and extrinsic microstructural factors which are governed by processing parameters. As indicated before, $\text{RE}_2\text{Fe}_{14}\text{B}$ (Γ) phase has sufficiently high intrinsic magnetic properties for the fabrication of low cost magnets with moderate magnetic properties. Thus inferior magnetic properties of the sintered magnets (Table VIII.5) may be related to the processing parameters and resulting microstructural factors. For the development of good magnetic properties in RE-Fe-B magnets, the microstructure should meet the following requirements (section 2.3.2.3): (a) large amount (80-90pct.) of the hard magnetic phase $\text{RE}_2\text{Fe}_{14}\text{B}$; (b) good magnetic insulation among the grain of hard magnetic phase i.e. uniform spread of RE-rich liquid phase around the grain of hard magnetic phase; (c) small grain size; and (d) no soft magnetic impurity phase should be present or the soft magnetic phase should not be in direct contact with the magnetically important phase. Thus the poor magnetic properties of sintered magnets (Table VIII.5) may be related to the presence of reasonably large amount of magnetically soft α phase, small amount of Γ phase and unevenly distributed RE-rich grain boundary phase (Fig.VIII.25 and VIII.26).

Alloys prepared for magnet fabrication are in the $\Gamma+\Delta+L$ region. The presence of large amount of α phase (Fig.VIII.26) in the alloys after sintering implies that due to loss of RE through oxidation the shift in composition is not simply a lateral one, i.e. in the $\Gamma+L+\Delta$ or $\Gamma+L$ regions, but towards $\alpha+\Gamma+L$ phase region (Fig.VI.9). Ormerod [11] has reported that in Nd-Fe-B magnet, significant oxidation during pre-sintering or sintering stage leads to the formation of the large amount of α -Fe phase and the resulting magnets show coercivity value less than 200 Oe. It is quite likely that atmospheric oxidation problem, which is serious for Nd-Fe-B magnets [208-213], will be worse with MM-Fe-B magnets as indicated by the present investigation. Gong and Hadjipayanis [22] have also reported that MM substitution in Nd-Fe-B magnets leads to significant increase in reactivity.

8.2.2.5 Further Prospects

Development of RE-Fe-B magnets may succeed provided the problems of powder catching fire in air atmosphere, composition shift and the large α phase in the microstructure are sorted out. Possible approach to tackle these problems may involve processing of alloys in an inert atmosphere and/or alloying with other element/s which will make the alloy less susceptible to oxidation.

In the present investigation, only the alloys with increasing rare-earth content, i.e. increasing x in $RE_xFe_{92-x}B_8$, have been explored to avoid the formation of large α phase in the microstructure of sintered magnets. As indicated by the RE-Fe-B phase equilibria at 1000 °C, the formation of α phase in the microstructure of sintered magnets may possibly be suppressed by using the alloys containing the combination of higher RE and B contents in the three phase $\Gamma+\Delta+L$ region, and this requires further investigation.

X-ray studies by Wan et.al.[24] on $(Nd,Pr)_{9.5}MM_{6.5}(Fe_{1-y}Al_y)_{77}B_7$ ($y = 0.05$) sintered magnets have indicated that Al addition suppresses the α formation. In recent studies, Gong et.al.[22] have also observed beneficial effect of Al addition on iH_c in $MM_{22}Fe_{70-x}Al_xB_8$ ($x = 2$ to 3) magnets. No information regarding the effect of Al addition on microstructure was, however, provided. Al addition in La and Ce substituted Nd-Fe-B magnets have been found to result in uniform distribution of grain boundary liquid phase and an increase in coercivity [216]. Beneficial effect of Al in Nd-Fe-B magnets has been attributed to improved wettability of the Nd-rich grain boundary liquid phase and its uniform spread over the grain of basic hard magnetic phase [195,221]. Al addition in Nd-Fe-B magnets have also been found to improve the resistance of these magnets to air oxidation [212]. Thus, from the available information it appears that partial substitution of Fe by Al (or AlN [206,207]) in MM-Fe-B sintered magnet may be beneficial and requires further investigation.

Apart from Al, the other elements which could be considered are Co and Dy. Both these elements are known to enhance the corrosion resistance of Nd-Fe-B magnets [212,213] and may help in overcoming the higher reactivity problem in RE-Fe-B magnets. Co addition will also be beneficial from the point of view of raising the Curie temperature of the Γ phase. Dy addition can further, help in raising the H_A of the Γ phase. However, its addition may also have to be considered from the cost point of view. Some workers [22,24,92] have tried partial substitution of Nd by MM and produced magnets of moderate magnetic properties. Partial substitution of Nd by Mischmetal together with other additions, e.g. Al, Co, Dy etc, may also help in the production of low cost magnet with attractive magnetic properties.

CHAPTER IX

CONCLUSIONS AND SCOPE FOR THE FUTURE WORK

This thesis has focused on the determination of phase equilibria in RE-Co-Fe-Cu-Zr, RE-Fe-B and RE-Fe systems using instrumental techniques such as metallography, X-ray diffraction, thermomagnetic analysis, SEM-EDS etc. Limited attempts have also been made to carry out magnetic characterization of some of the phases in the above systems, and fabricate resin bonded and sintered magnets using a few promising alloys. India is richly endowed with rare-earth deposits. Since at present only Mischmetal is produced in metallic form from these deposits, the present study is especially relevant in the Indian context. The results obtained in this investigation are expected to help in chalking out future strategies of research on magnet fabrication using Mischmetal.

9.1 Conclusions

9.1.1 Phase Equilibria Studies

The phase equilibria in RE-Co-Fe-Cu-Zr system at 1100 °C and RE-Fe-B system at 1000 °C have been investigated in the magnetically important regions. The investigated composition region of RE-Co-Fe-Cu-Zr system lies around RE:T ratio of ~ 1:7 and is bounded by 5 to 19 at.pct. RE, 55 to 75 at.pct. Co, 7 to 20 at.pct. Fe, and Cu and Zr contents fixed at 2 and 8 at.pct., respectively. The Fe rich end of the RE-Fe-B system has been determined upto 40 at.pct. RE and 45 at.pct. B. The phase equilibria studies in RE-Fe system, which were undertaken as an extension of the RE-Fe-B system, were limited to Fe-rich end upto 33.3 at.pct. RE and between 700-1150 °C. Major conclusions for each of the investigated phase equilibria are listed below.

Phase Equilibria in RE-Co-Fe-Cu-Zr System

1. The stable intermediate phases in RE-Co-Fe system are not found in the RE-Co-Fe-Cu-Zr system at 1100 °C. Existence of two new phases U and N, located around RE:T ratio of ~1:7 and 1:6 respectively have been established.
2. The U and N phases, which appear to be structurally similar to the 2:17 and 1:5 phases, have lattice parameters (hexagonal cell) of $a = 8.452 \text{ \AA}$, $c = 24.57 \text{ \AA}$ and $a = 4.940 \text{ \AA}$, $c = 20.42 \text{ \AA}$, and $T_c \sim 830$ and $740 \text{ }^\circ\text{C}$, respectively.
3. Both the U and N phases are restricted in their composition limits. The U phase appears to have small solubility range.
4. Besides the intermediate phases the other phases which are found at 1100 °C include a cobalt rich fcc solid solution phase (γ) with lattice parameter $a = 3.567 \text{ \AA}$ and $T_c \sim 1045 \text{ }^\circ\text{C}$, a liquid phase and a Zr rich hard phase Δ which is possibly not in equilibrium with other phases.

Phase Equilibria in RE-Fe-B System

1. Like the Nd-Fe-B system, the RE-Fe-B system has two ternary intermediate phases, i.e. $\text{RE}_2\text{Fe}_{14}\text{B}$ (Γ) and REFe_4B_4 (Δ), existing at the iron rich side of the diagram.
2. Both the Γ and the Δ phases have tetragonal crystal structure with lattice parameters $a = 8.784 \text{ \AA}$, $c = 12.177 \text{ \AA}$ and $c/a = 1.39$ for the Γ phase, and $a = 7.106 \text{ \AA}$, $c = 17.011 \text{ \AA}$ and $c/a = 2.39$ for the Δ phase.
3. The T_c of the Γ phase is $\sim 245 \text{ }^\circ\text{C}$. The Δ phase also shows a peculiar magnetic transition between 240 and $440 \text{ }^\circ\text{C}$ and its magnetic behaviour is not well understood.
4. The Γ phase appears to have a small homogeneity region.
5. Besides the ternary intermediate phases Γ and Δ , the other phases observed are a bcc Fe solid solution phase (α), a Fe_2B (β) phase and a liquid. The α and β phases have practically no solubility of RE.
6. The bcc α phase possibly arises out of the transformation of the fcc γ solid solution phase when the alloys are quenched to room temperature after equilibration at $1000 \text{ }^\circ\text{C}$.

7. The phase equilibria at 1000 °C is quite similar to the Nd-Fe-B system except that no $\text{RE}_2\text{Fe}_{17}$ phase is observed in equilibrium with any of the ternary phases in the the RE-Fe-B system at 1000 °C.

Phase Equilibria in RE-Fe System

1. Like the R-Fe systems (R = Ce, Pr), the RE-Fe system has two intermediate phases, i.e. $\text{RE}_2\text{Fe}_{17}$ (R) and REFe_2 .
2. No $\text{RE}_5\text{Fe}_{17}$ phase was detected down to 700 °C even after prolonged annealing upto 30 days.
3. The lattice parameters of hexagonal unit cell of $\text{RE}_2\text{Fe}_{17}$ (R) phase are $a = 8.525 \text{ \AA}$, $c = 12.420 \text{ \AA}$ and $c/a = 1.46$, and the REFe_2 is a cubic Laves phase with lattice parameter $a = 7.299 \text{ \AA}$.
4. The $\text{RE}_2\text{Fe}_{17}$ (R) phase has a T_c between 40 and 45 °C.
5. The solubility of RE in Fe is less than 0.5 at.pct.
6. The RE-Fe system is quite similar to the R-Fe systems (R = Ce, Pr) except for the opening up of the two peritectic reactions into two broad three phase regions consisting of ($\gamma + \text{RE}_2\text{Fe}_{17} + \text{Liquid}$) and ($\text{RE}_2\text{Fe}_{17} + \text{REFe}_2 + \text{Liquid}$).
7. All the high iron containing alloys show the presence of a bcc Fe solid solution phase α even when quenched from a temperature higher than 912 °C and indicate that the fcc Fe solid solution phase γ can not be retained by quenching.
8. The transformation of the α phase into the γ phase at temperature slightly higher than 912 °C and the increase in transformation temperature with the RE content of the alloys suggest a peritectoid type reaction through a very narrow three phase region ($\alpha + \gamma + \text{RE}_2\text{Fe}_{17}$).

9.1.2 Magnetic Characterization and Fabrication

Magnetic characterization and fabrication studies on RE-Co-Fe-Cu-Zr system has mainly focused on the alloys containing N phase as the major phase, especially the alloys of composition $[\text{RE}(\text{Co}_{0.76}\text{Fe}_{0.13}\text{Cu}_{0.09}\text{Zr}_{0.02})_6]$ (alloy labelled as C_{11}). The

studies on the RE-Fe-B system has been carried out using the alloys of composition $\text{RE}_x\text{Fe}_{92-x}\text{B}_8$ ($x = 15-19$). Since a large number of possibilities, in terms of alloy compositions and heat treatments, can be explored in the investigated multicomponent system, the present studies are preliminary in nature. The major findings for some of the RE-Co-Fe-Cu-Zr and RE-Fe-B alloys are as follows.

RE-Co-Fe-Cu-Zr System

1. The N phase alloy of the composition $[\text{RE}(\text{Co}_{0.76}\text{Fe}_{0.13}\text{Cu}_{0.09}\text{Zr}_{0.02})_6]$ (alloy C_{11}) shows remarkable increase, more than 50 fold, in coercivity due to aging at 620°C ; the coercivity was found to increase from 20 Oe to 1180 Oe after about 300 hours of aging.
2. The intrinsic magnetic properties of the N phase are found to be as follows: $\sigma_s = 88$ emu/g, $H_A \geq 25$ kOe, $T_C \cong 740^\circ\text{C}$. The N phase has the desired uniaxial anisotropy.
3. Resin bonded pellets prepared from 2.5 hours milled powder of an aged (620°C , 200 hours) N phase alloy of C_{11} composition showed σ_s and σ_r values comparable with the commercially available Sm based 2:17 magnets, however, iH_C was 6-10 times lower; the typical value of magnetic properties were as follows: $iH_C = 1170$ Oe, $\sigma_s = 83$ emu/g, $\sigma_r = 59$ emu/g and $\sigma_r/\sigma_s = 0.71$.
4. Sintered magnets prepared using an alloy of C_{11} composition show a $4\pi M_s$ value of 9-10 kG, and very low values of iH_C , about 100 Oe, and $M_r/M_s (< 0.1)$ due to small loss of RE, during processing, resulting in a microstructure consisting of U and N phases.
5. Sintered magnets prepared using alloys containing somewhat higher RE than the alloy C_{11} , to compensate for composition shift during processing, and N phase microstructure also show very poor iH_C (~ 700 Oe) and σ_r (~ 0.1) values inspite of using several combination of sintering condition ($900-1100^\circ\text{C}$, 0.2 to 1.0 hour) and post sintering aging treatment (between $580-620^\circ\text{C}$ upto 240 hours). The reasons for the poor

value of magnetic properties observed for the N phase containing sintered magnets were not understood properly.

6. From the available results, the prospect of fabricating N phase based sintered magnets does not appear to be quite promising.

RE-Fe-B System

1. The intrinsic properties of the $\text{RE}_2\text{Fe}_{14}\text{B}$ (Γ) phase were moderate in comparison with the $\text{Nd}_2\text{Fe}_{14}\text{B}$ phase. The Γ phase was found to have $T_c \cong 245^\circ\text{C}$ and $\sigma_s \cong 125$ emu/g (for magnetically oriented resin bonded magnet of an alloy of composition $\text{RE}_{15}\text{Fe}_{77}\text{B}_8$).
2. The alloy of composition $\text{RE}_{15}\text{Fe}_{77}\text{B}_8$ do not show any response to the aging treatment between 600 - 800°C because of the very narrow homogeneity region of Γ phase at 1000°C and possibly its extension at lower temperatures without change in composition.
3. Fabrication of magnets using powders of $\text{RE}_x\text{Fe}_{92-x}\text{B}_8$ alloys ($x = 15$ - 19) is difficult because the powders are very reactive and invariably catch fire during handling in open air atmosphere.
4. A resin bonded RE-Fe-B magnet, produced using 3 hours milled powder of an alloy of $\text{RE}_{15}\text{Fe}_{77}\text{B}_8$ composition, showed the following properties: $H_c = 1400$ Oe, $\sigma_s = 118$ emu/g, $\sigma_r = 97$ emu/g and $\sigma_r/\sigma_s = 0.82$.
5. Very low value of H_c (~ 400 Oe) and σ_r/σ_s (≤ 0.1), observed for the sintered magnets prepared using alloys of $\text{RE}_x\text{Fe}_{92-x}\text{B}_8$ ($x = 15, 17, 19$) compositions, were found to be due to the presence of reasonably large amount of the magnetically soft α phase, small amount of the Γ phase and unevenly distributed RE-rich grain boundary phase in the microstructure of sintered pellets.

9.2 Scope for the Future Work

Based on the present investigation and some of the current literature available on the $\text{Sm}(\text{Co}, \text{Fe}, \text{Cu}, \text{Zr})_2$ and Nd-Fe-B magnets,

the following research problems are identified for future studies:

1. Chemical and magnetic characterization of non-equilibrium phases, present in the N phase containing bulk alloys and sintered pellets, to ascertain the role of these phases in coercivity development.
2. Detailed magnetic characterization of the U phase, in terms of anisotropy field and direction of easy magnetization, to assess its potential for magnet fabrication.
3. Studies on the effect of different homogenization temperatures on the aging (including step aging) characteristics of the U and N phases
4. Adjustment in Cu and Zr levels and to study its effect on the stability of U and N phases, elimination of Δ phase, and magnetic properties
5. To study the effect of partial substitution of MM by Sm on the stability and magnetic properties of U and N phases.
6. High temperature X-ray studies on high Fe containing RE-Fe-B and RE-Fe alloys to confirm the presence of fcc Fe solid solution phase γ at high temperature.
7. Lorentz electron microscopy and EDS studies on the REFe_4B_4 and NdFe_4B_4 containing alloys to explain the magnetic transition observed in some of the alloys containing these phases.
8. Fabrication of RE-Fe-B magnets in inert atmosphere to avoid the problem of fine alloy powder catching fire in open atmosphere and large amount of α phase in the microstructure.
9. Adjustment of B level in the alloy composition to attain the α phase free desired microstructure.
10. Studies on the partial replacement of MM and Fe :
 - (a) Partial replacement of MM by other rare-earths, e.g. Nd, Pr, Dy etc, to optimize between the cost and the intrinsic magnetic properties of the hard magnetic phase $\text{RE}_2\text{Fe}_{14}\text{B}$.
 - (b) Partial replacement of Fe by Co (to improve T_c), Al or AlN (to reduce reactivity of the powders and suppress the formation of the α phase).

REFERENCES

1. Wallace, W.E., Progr. in Solid State Chem., 16 (1985) 127-162.
2. Buschow, K.H.J., Material Science Reports, 1 (1986) 1-64
3. Strnat, K.J., IEEE Trans. Mag., MAG-23, 5(1987) 2094-2099
4. Kumar, K., J. Appl. Phys., 63(6) (1988) R13-45.
5. Bran, W., In: Proceedings of the Eighth International Workshop on Rare-Earth Magnets and their Applications, K.J.Strnat (Editor) (University of Dayton, Ohio, 1985) 1-14
6. Warlimont, H., IEEE Trans.Mag., 26(5) (1990) 1313-1321.
7. Strnat, K.J., Hoffer, G., Olson, J. and Ostertag, W., J. Appl.Phys., 388 (1967) 1001.
8. Das, D.K., IEEE Trans. Mag., 5 (1969) 214.
9. Buschow, K.H.J., Nastepad, P.A. and Wastendorp, F.F., J.Appl. Phys., 40 (1969) 4029.
10. Benz, M.G., and Martin, D.L., Appl. Phys. Letter, 17 (1970) 176.
11. Ormerod, J., J. Less Comm. Met., 111 (1985) 49-69.
12. Ervens, W., In : Proceedings Second Congress-Cobalt Metallurgy and Uses (Cobalt Development Institute, London, 1986) 224.
13. Tawara, Y., and Senno, H., Jap. J. Appl. Phys., 12 (1973) 761.
14. Nagel, H., Perry, J., and Menth, A., J. Appl. Phys., 47 (1976) 2662.
15. Ojima, T., Tomizawa, S., Yoneyama, T., and Hori, T., Jap. J. Appl. Phys., 16 (1977) 671.
16. Ervens, W., Goldschmidt Informiert, 48(2) (1979) 3.
17. Mishra, R.K., Thomas, G., Yoneyama, T., Fukuno, A., and Ojima, T., J.Appl. Phys., 52 (1981) 2517.
18. Liu, S., and Ray A.E., IEEE Trans. Mag., 25(5) (1989) 3785.
19. Sagawa, H., Fujimura, S., Togawa, N., Yamamoto, H., and Matsuura, Y., J. Appl. Phys. 55 (1984) 2083.
20. Croat, J.J., Herbst, J.F., Lee, R.W., and Pinkerton, F.E., J.Appl. Phys., 55 (1984) 2076.

21. Sagawa, M., Hirose, S., Yamamoto, H., and Matsuura, Y.,
Jap. J. Appl. Phys., 26 (1987) 785.
22. Gong, W., and Hadjipanayis, G.C., J. Appl. Phys., 63(8) (1988)
3513.
23. Greinacher, E., and Reinhardt, K., In: Chem. Technologie,
Vol.2, K.Winnacker (Ed.) (Carl Hanser Verlag, Munich and
Vienna, 1982) 683.
24. Wan, Y., Wu, P., Jin, Y. and Gu, Ya, In : Proceedings of the
IXth International Workshop on Rare-Earth Magnets and their
Applications, C.Herget and R. Poerschke (Editors), Part-I
(DPG-GmbH, FRG, 1987) 561.
25. Chegwiddden, J., In: Proceedings of IXth International
Workshop on Rare-Earth Magnets and their Applications, C.
Herget and R. Poerschke (Editors), Part-I (DPG-GmbH, FRG,
1987) 711.
26. Culity, B.D., Introduction to Magnetic Materials
(Addison-Wesley Publishing Co., Massachussetts, 1972) 556.
27. Becker, J.J, J. Appl. Phys., 441 (1970) 1055.
28. Livingston, J.D., AIP Conf.Proc., 10 (1973) 643.
29. Buschow, K.H.J., Rep. Prog. Phys., 40 (1977) 1179.
30. Buschow, K.H.J., In: Ferromagnetic Materials, Vol.1, E.P.
Wohlfarth (Eds.) (North-Holland, Amsterdam, 1980) 197.
31. Lee, R.W., J.Appl. Phys., 52 (1981) 2549
32. Rabenberg, L., Mishra, R.K., and Thomas, G., J.Appl. Phys.,
53 (1983) 2389.
33. Fidler, J., Proceedings of Second Congress - Cobalt
Metallurgy and Uses (Cobalt Development Institute, London,
1986) 393.
34. Fidler, J., In : Proceedings of the IXth International
Workshop on Rare-Earth Magnets and their Applications, C.
Herget, H.Krönmüller and R. Poerschke (Editors), Part-II
(DPG-GmbH, FRG, 1987) 363.
35. Leupold, H.A., Potenzioni, E., Tauber, A., and Mildrum, H.F.,
J. Appl. Phys., 55 (1984) 2097.
36. Ray, A.E., In : Soft and Hard Magnetic Materials with
Applications, J.A.Salsgiver et.al. (Editors) (American
Society for Metals, Metals Park, OH, 1986) 105.

- Applications, K.J. Strnat (Editor) (University of Dayton, 1985) 423.
38. Livingston, J.D., In : Soft and Hard Magnetic Materials with Applications, J.A. Salsgiver et.al. (Editors) (American Society for Metals, Metals Park, OH, 1986) 71.
 39. Strnat, K.J., In : Soft and Hard Magnetic Materials with Applications, J.A. Salsgiver et.al. (Editors) (American Society for Metals, Metals Park, OH, 1986) 63.
 40. Bohlmann, M.A., In : Proceedings of the IXth International Workshop on Rare-Earth Magnets and their Applications, C. Herget and R. Poerschke (Editors) (DPG-GmbH, FRG, 1987) 233.
 41. Adler, E., Reppel, G.W., Rodewald, W., and Warlimont, H., Int. J. Powder Met., 25(4) (1989) 319.
 42. Croat J.J., IEEE Trans. Mag., 25(5) (1989) 3550.
 43. Higuchi, A., and Hirose, S., IEEE Trans. Mag., 25(5) (1989) 3555.
 44. Wallace, W.E., Rare Earth, Intermetallics (Academic Press, New York, 1973).
 45. Nesbitt, E.A., Wernick, J.H., Rare Earth Permanent Magnets (Academic Press, New York, 1973).
 46. McCaig, M., Permanent Magnets in Theory and Practice (Pentech Press, 1977) 374 pp.
 47. Subbarao, E.C., and Wallace, W.E. (Eds.) Science and Technology of Rare Earth Materials (Academic Press, New York, 1980) 439 pp.
 48. Andriessen, F., and Terpestra, M., Rare Earth Metals Based Permanent Magnets - A Literature Study (Elsevier Applied Science, London, 1989) 146 pp.
 49. Proceedings of the International Workshops on Rare-Earth Permanent Magnets and Their Applications
 - a) 2nd Workshop, K. Strnat (Editor), Dayton, OH (1976).
 - b) 3rd Workshop, K. Strnat (Editor), San Diego, CA (1978).
 - c) 4th Workshop, H. Kaneko and T. Kurino (Editors), Hakone, Japan (1979).
 - d) 5th Workshop, K. Strnat (Editor) Roanoke, VA (1981).
 - e) 6th Workshop, J. Fidler (Editor), Baden, Austria (1982)
 - f) 7th Workshop, X. Pan, W. Ho and C. Yu (Editors), Beijing, China, (1983).
 - g) 8th Workshop, K. Strnat (Editor), Dayton, OH (1985).
 - h) 9th Workshop, Part-I : C. Herget and R. Poerschke (Editors); Part-II: C. Herget, H. Krönmüller, and R. Poerschke (Editors), Bad Soden, FRG (1987).

50. Mitchel, I.V. (Editor) Nd-Fe-B Permanent Magnets: Their Present and Future Applications (Elsevier, London, 1985).
51. Becker, J.J., IEEE Trans. Mag. MAG-4 (1968) 239.
52. Durst, K.D., and Krönmüller, H., Loc cit 49(e), 725.
53. Smithells, C.J., Metals Reference Book, 5th Ed. (Butterworths, London, 1976).
54. Hume-Rothery, W., and Raynor, G.V., The Structure of Metals and Alloys (The Institute of Metals, London, 1954).
55. Stadelmaier, H.H., and Henig, E.-Th., J. Metals, 43(2) (1991) 32-35.
56. Kou, X.C., Grössinger, R., and Buschow, K.H.J., J. Magnetism and Magn. Materials, 88 (1990) 1-6.
57. Coey, J.M.D., and Sun, H., J. Magnetism and Magn. Materials, 87 (1990) L251-254.
58. Croat, J.J., IEEE Trans Mag., 6 (1982) 1442.
59. Hirosawa, S., Matsuura, Y., Yamamoto, S., Fujimura, Sagawa, M., and Yamauchi, H., J. Appl. Phys., 59 (1986) 873.
60. Strnat, K.J., Hoffer, G., Olson, J. Ostertag, W., and Becker, J.J., J. Appl. Phys., 38 (1967) 1001.
61. Strnat, K.J., IEEE Trans. Magn., MAG-6, 2 (1970) 182.
62. Velge, W.A.J.J., and Buschow K.H.J., J. Appl. Phys., 39 (1968) 1717.
63. Benz, M.G., Laforce, R.P., and Martin, D.L., AIR Conf. Proc., 18 (1974) 1173.
64. Grössinger, R., Sun, X.K., Eibler, R., and Kirchmayr, H.R., Loc cit 49 (g), 553.
65. Sagawa, M., Fujimura, S., Yamamoto, H., Matsuura, Y., Hirosawa, S., and Hiraga, K., Loc cit 49 (g), 587.
66. Boltich, E.B., Ostwald, M.Q., Huang, S., Hirosawa, S., Wallace, W.E., and Burzo, E., J. Appl. Phys., 57(1), (1985) 4106.
67. Abache, C., and Oesterreicher, H., J. Appl. Phys., 57(1) (1985) 4112.
68. Wallace, W.E., and Pedziwiatr, A.T., Loc cit 49(h), Part-II, 31.
69. Nakagawa, Y., Kido, G., Hiroyoshi, H., Kato, H. Yamada, M.,

- Hirosawa, S., and Sagawa, M., Loc cit 49(h), Part-II, 87.
70. Wallace, W.E., and Narasimhan, K.S.V.L., Loc cit 47, 393.
 71. Narasimhan, K.S.V.L., In: Soft and Hard Magnetic Materials with Applications, J.A. Salsgiver et.al. (Editors) (American Society for Metals, Metals Park, OH, 1986) 131.
 72. Buschow, K.H.J., Loc cit 49(h), Part-I, 453.
 73. Narasimhan, K.S.V.L., and Wallace, W.E., AIP Conf. Proc., 18 (1974) 1212.
 74. Lee, R.W., IEEE Trans. Magn., MAG-15 (1979) 1762.
 75. Wallace, W.E., Fujii, H., Satyanarayana, M.V., and Hirosawa, S., Loc cit 49(e), 537.
 76. Wallace, W.E., Merches, M., Shenoy, G.K., and Viccaro, P.J., J. Phys. Chem. Solids, 43 (1982) 55.
 77. Willman, C.J., and Narasimhan, K.S.V.L., IEEE Trans. Magn., MAG-21 (1985) 1976.
 78. Jiahai, W., and Ke Chang, Loc cit 49(h) 411.
 79. Koo, J.C., IEEE Trans. Magn., MAG-20 (1984) 1593.
 80. Akioka, K., Ikuma, K., and Shimoda, T., J. Japan Soc. Powder and Powder Met., (1988) 584.
 81. Liu, S., Ray, A.E., and Mildrum, H.F., IEEE Trans. Magn., 26(5) (1990) 1382.
 82. Perkins, R.S., Strassler, S., and Menth, A., AIP Conf. Proc., 29 (1976) 610.
 83. Ray, A.E., and Strnat, K.J., IEEE Trans. Magn., MAG-8 (1972) 516.
 84. Schaller, H.J., Craig, R.S., and Wallace, W.E., J. Appl. Phys., 43(1972) 3161.
 85. Narasimhan, K.S.V.L., IEEE Trans. Magn., MAG-12 (1976) 1009.
 86. Narasimhan, K.S.V.L., and Wallace, W.E., IEEE Trans. Magn., MAG-13 (1977) 1333.
 87. Satyanarayana, M.V., Wallace, W.E., and Craig, R.S., J. Appl. Phys., 50 (1979) 2324.
 88. Buschow, K.H.J., In : Ferromagnetic Materials, Vol.4, E.P. Wohlfarth and K.H.J. Buschow (Editors) (Elsevier, Amsterdam, 1988) 23.

89. Sun, X.K., Grössinger, R., Eibler, R., and Kirchmayr, H.R., *Physica (B&C)*, 130 (1985) 300.
90. Jurczyk, M., and Wallace, W.E., *J. Magn. Mater.*, 59 (1986) L182.
91. Yang, Y.C., Chen, H.Y., Liu, Z.X., Liao, B., Xing, F., and Ho W.W., *J. Appl. Phys.*, 57(1) (1985) 4115.
92. Maocai, Z., Deqing, M., Xiuling, J., and Shiqiang, L., *Loc cit* 49(g), 541.
93. Buschow, K.H.J., *MRS Symp. Proc.*, 96 (1987) 3.
94. Bolzoni, F., Leccabue, F., Pareli, L., and Sanchez, J.L., *J. Phys. (Paris)* 46 (1985) C6.
95. Liu, N.C., Stadelmaier, H.H., and Schneider, G., *J. Appl. Phys.*, 61 (1987) 3574.
96. Lemaire, R., *Cobalt*, 32 (1966) 132.
97. Foner, S., McNiff, E.J. Jr., Martin, D.L., and Benz, M.G., *Appl. Phys. Lett.*, 20(11) (1972) 447.
98. Tsui, J.B.Y., Mildrum, H.F., Strnat, K.J., and Shanley, C.W., *AIP Conf. Proc.*, 10 (1973) 623.
99. Mittal, R.C., M.Tech. Thesis, IIT, Kanpur (1977).
100. Satyanarayana, M.V., M.Tech Thesis, IIT, Kanpur (1977).
101. Gupta, K.P., *Loc cit* 47, p.77.
102. Durst, K.D., Krönüller, H., and Schneider, G., *Loc cit* 49(h), Part-II, 209.
103. Leonowicz, M., *IEEE Trans. Magn.*, 26(5) (1990) 2628.
104. Krönüller, H., In: *Proceedings of the Second International Symposium on Magnetic Anisotropy and Coercivity in Rare-Earth - Transition Metal Alloys*, K.J. Strnat (Ed.), (University of Dayton, OH, 1978) 1.
105. Menth, A., and Nagel, H., *ibid*, p.65.
106. Velicescu, M., *Loc cit* 49(e), 341.
107. Fidler, J., *Loc cit* 49(d), 407.
108. Leamy, H.J., and Green, M.L., *IEEE Trans. Magn.*, MAG-9 (1973) 205.
109. Nesbitt, E.A., Chin, G.Y., Sherwood, R.C., Green, M.L. and Leamy, H.J., *IEEE Trans. Magn.*, MAG-9 (1973) 203.

110. Livingston J.D., and Martin, D.L., J. Appl. Phys., 49 (1977) 2064.
111. Grössinger, R., Kou, X.C., Krewenka, R., Kirchmayr, H.R., and Tokunaga, M., IEEE Trans. Magn., 26(5) (1990) 1954.
112. Sagawa, M., Tenaud, P., Vial, F., and Hiraga, K., IEEE Trans. Magn., 26(5) (1990) 1957.
113. Ray, A.E., IEEE Trans. Magn., MAG-20 (1984) 1614.
114. Clegg, A.G., Coulson, I.M., Hilton, G., and Wong, H.Y., IEEE Trans. Magn., 26(5) (1990) 1942.
115. Moffat, W.G, The Handbook of Binary Phase Diagrams (Genium Publishing Corporation, N.Y. 1986).
116. Massalski, T.B., Murray, J.L., Bannett, L.H., and Baker, H. (Eds.) Binary Alloy Phase Diagrams (American Society for Metals, Ohio, 1986).
117. Buschow, K.H.J., Van der Goot, A.S., J. Less Common Metals, 14 (1968) 323.
118. Williams, K.L., Bartlett, R.W., and Jorgensen, P.J., J. Less Common Metals, 37 (1974) 174.
119. den Broeder, F.J.A., and Zijlstra, H., J. Appl. Phys., 47 (1976) 2688.
120. Perry, A.J., J. Less Common Metals, 51 (1977) 153.
121. Ray, A.E., Cobalt, 1 (1974) 13.
122. Khan, Y., and Feldmann, D., Z. Metall., 64 (1973) 853.
123. Khan, Y., J. Less Common Metals, 34 (1974), 191.
124. Gschneidner, K.A., Jr., Rare Earth Alloys (D. Van Nostrand Co., Inc., New York, 1961).
125. Koch, C.C., J. Less Common Metals, 22 (1970) 149.
126. Schafer, G., and Spyra, W., Entwicklung von Dauer magneten auf der Basis von Seltenerd-Kobalt-Legierungen Forschungbericht T76037, Zentralstelle für Luft-und Raumfahrt-dokumentation und information, Munich, Oct.1976.
127. Herget, C., Goldschmidt Informiert, 48(2) (1979) 72.
128. Velu, E.M.T., Subbarao, E.C., Gupta, H.O., Gupta, K.P., Kaul, S.N., Majumdar, A.K., Mittal, R.C., Sankar, T.A.P., Sarkar, G., Satyanaryana, M.V., and Subramanyam, J., J. Less Common Metals, 71 (1980) 219-234.

129. Nishida, I., and Uehara, M., J. Less Common Metals, 34 (1974) 285.
130. Ray, A.E., Strnat, K.J., Harmer, R.S., and Hartings, M.S., AIP Conf. Proc., 10 (1973) 613.
131. Mittal, R.C., Satyanarayana, M.V., Gupta, K.P., Gupta, H.O., Kaul, S.N., Majumdar, A.K., Prasad, K.S., Sankar, T.A.P., Subbarao, E.C., Velu, E.M.T., J. Less Common Metals, 78 (1981) 245.
132. Laha S., Uresekhar, P.M., Pandian, S., Gupta, K.P., Mazumdar, A.K., Sankar, A.T.P., Ramakrishna, U., Subbarao, E.C., and Velu, E.M.T., J. Less Common Metals, 124 (1986) 211-218
133. Morita, Y., Umeda, T., and Kimura, Y., IEEE Trans. Magn., 23(5) (1987) 2702.
134. Chin T.S., Chang, W.C., Chang, R.T., Hung, M.P., and Lee, H.T., IEEE Trans. Magn., 25(5) (1989) 3782.
135. Kubaschewski, O., Iron-Binary Phase Diagrams (Springer-Verlag, Berlin, 1982).
136. Landgraf, F.J.G., Schneider, G.S., Villas-Boas, V., and Missell, F.P., J. Less Common Metals 163 (1990) 209-218.
137. Chuang, Y.C., Wu, C.H., and Shao, Z.B., J. Less Common Metals, 136(1) (1987) 147.
138. Ray, A.E., Acta Crystallogr., 21 (1966) 426.
139. Buschow, K.H.J., J. Less Common Metals, 11 (1966) 204.
140. Gebhart, J.M., Etter, D.E., Tucker, P.A., Conf. Preprints, 6th Rare Earth Research Conference, Gatlinburg, Tenn., 1967, p.452.
141. Johnson, G., Wood, D.H., Smith, G.S., and Ray, A.E., Acta Crystallogr., Sect. B, 24 (1968) 274.
142. Jepson, J.O., and Duwez, P., Trans. ASM, 47 (1955) 543.
143. Nassau, K., Cherry, L.V., and Wallace, W.E., J. Phys. Chem. Solids, 16 (1960) 123.
144. Buschow, K.H.J., Van Wieringen, J.S., Phys. Stat. Solidi, 42 (1970) 231.
145. Moreau, J.M., Paccard, L., Nozieres, J.P., Missell, F.P., Schneider, G., and Villas-Boas, V., J. Less Common Metals 163 (1990) 245-251.
146. Schneider, G., Henig, E.-Th., Petzow, G., and Stadelmaier, H.H., Z. Metallkd. 78 (1987) 694

147. Terekhova, V.F., Maslova, E.V., and Savitsky, Ye.M., Russ. Metall., 6 (1965) 50.
148. Kuz'ma, Yu B., Bilonizhko, N.S., Mykhalenko, S.I., Stepanchikova, G.F., and Chaban, N.F., J. Less Common Metals, 67(1) (1979) 51.
149. Rogl, P., Handbook on the Physics and Chemistry of Rare-Earths, Vol.6, K.A. Gschneidner and L. Eyring (North-Holland, Amsterdam, 1984) 335.
150. Schneider, G., Henig, E.Th., Petzow, G., and Stadelmaier, H.H., Z. Metallkde 77(11) (1986) 755.
151. Chaban, N.F., Kuz'ma, Yu.B., Bilonizhko, N.S., Kachmar, O.O., and Pelrov, N.V., Dopov. Akad. Nauk URSS Ser.A.: Fiz-Mat. Tekh. Nauki, 10 (1979) 873 (Russian).
152. Stadelmaier, H.H., El-Masry, Liu, N.C., and Cheng, S.F., Mater. Lett., 2 (1984) 411.
153. Buschow, K.H.J., Mooij, D.B.De, Daams, J.L.C., and Van Noort, H.M., J.Less Common Metals, 115 (1986) 357.
154. Shoemaker, C.B., Shoemaker, D.P., and Fruchart, R., Acta Cryst., C40 (1984) 1665.
155. Givord, D., Li, H.S. and Moreau, J.M., Solid State Commun., 50 (1984) 497.
156. Herbst, J.F., Croat, J.J., Pinkerton, F.E., and Yelon, W.B., Phys. Rev., B29 (1984) 4176.
157. Boller, H., and Oesterreicher, H., J. Less Common Metals, 103 (1984) L5.
158. Tsai, D.S., Chin, T.S., Hsu, S.E., and Hung, M.P., IEEE Trans. Magn., MAG-23, 5 (1987) 3607.
159. Bezinge, A., Braun, H.F., Muller, J., and Yvon, K., Solid State Commun., 55(1985) 131.
160. Braun, H.F., Pelizonne, M., and Yvon, K., Proc.Int.Conf. Transition Metal Compounds, Grenoble, June, 1982, Vol.2B, p.11.
161. Givord, D., Morecau, J.M., Tenaud, P., Solid State Commun., 55(4) (1985) 303.
162. Matsuura, Y., Hirose, S., Yamamoto, H., Fujimura, S., Sagawa, M., and Osamura, K., Japan J. Appl. Phys., 24 (1985) L635.
163. Grieb, B., Henig, E. Th., Martinek, G., Stadelmaier, H.H.,

- and Petzow, G., IEEE Trans, Magn., 26(5) (1990) 1367.
164. Grieb, B., Henig, E. Th., Schneider, G., and Petzow, G., Loc cit 49(h), 395.
 165. Chuang, Y.C., Wu, C.H., and Wang, F.H., Loc cit 49(h), 439.
 166. Grieb, B., Schneider, G., Henig, E.-Th., and Petzow, G., Z. Metallkd., 78(1987) 694.
 167. Hadjipanayis, G.C., Loc cit 49(e), p.609.
 168. Nesbitt, E.A., Willens, R.H., Sherwood, R.C., Buehler, E., and Wernick, J.H., Appl. Phys. Lett., 12 (1968) 361.
 169. Tian-duo, S., Loc cit 49(e) 433.
 170. Shimoda, T., Okonogi, I., Kasai, K., and Teraishi, K., IEEE Trans., MAG-16 (1980) 991.
 171. Ray, A.E., Mildrum, H.F., and Krupar, J.B., IEEE Trans. Magn., MAG-19 (1983) 2044.
 172. Fidler, J., Bernardi, J., Ohashi, K., and Tawara, Y., IEEE Trans. Magn., 26(5) (1990) 1385.
 173. Tawara, Y., and Kaneko, Loc cit 49(e), p.499.
 174. Sun, D., Yi, Q, Hong, H., He, C., and Jin, X., Loc cit 49(f), p.477.
 175. Rothwarf, F., Tawara, Y., Ohashi, K., Fidler, J., Skalicky, P., Grossinger, R., Kirchmayr, H., Liu, S., and Strnat, K.J., Loc cit 49(e), p.576.
 176. Rabenberg, L., Mishra, R.K., Thomas, G., Loc cit 49(e) 599.
 177. Fidler, J., and Skalicky, P., J. Magn. Magn. Mater., 27, (1982) 127.
 178. Fidler, J., Skalicky, P., and Rothwarf, F., IEEE Trans. Magn., MAG-19 (1983) 2041.
 179. Kianvash, A., and Harris, I.R., J. Mater. Sci., 19 (1984) 353.
 180. Tsai, D.S., Ho, K.S., Chin, T.S., Chang, Y.H., and Tsai, W.T., J. Appl. Phys., 61 (1987) 3772.
 181. Ivanova, G.V., Popov, A.G., Magat, L.M., Maykov, V.G., Shchegoleva, N.N., and Shur, Y.S., Phys. Met. Metallogr. (USSR) 57 (1984) 49.
 182. Sochen, C., Run, W., and Guanfei, Loc cit 49(e), 693.

203. Doser, M., and Keeler, G., J. Appl. Phys., 64 (1988) 5311.
204. Knoch, K.G., Schneider, G., Fidler, J., Henig, E. Th., and Krön Müller, H., IEEE Trans. Magn., MAG-25 (1989) 3426.
205. Kim, A.S., J. Appl. Phys., 64 (1988) 5571.
206. Chen, S.K., Chin T.S., Heh, S.J., and Lin, K.D., IEEE Trans. Magn., 26(5) (1990) 2634.
207. Heh, S.J., Lin, K.D., Jain, Y.M., King, F.D., Lee, F.J., and Chin, T.S., IEEE Trans. Magn., 26(5) (1990) 2637.
208. Jacobson, J., and Kim, A., J. Appl. Phys., 61 (1987) 3763.
209. Willman, C.J., and Narasimhan, K.S.V.L., J. Appl. Phys., 61 (1987) 3766.
210. Minowa, T., Yoshikawa, M., and Honshima, M., IEEE Trans. Magn., MAG-25 (1989) 3778.
211. Bala, H., Szymura, S., and Wyslocki, J.J., IEEE, Trans. Magn., 26(5) (1990) 2646.
212. Kim, A.S., Camp, F.E., and Dulis, E.J., IEEE Trans. Magn., 26(5) (1990) 1936.
213. Tenaud, P., Vial, F., and Sagawa, M., IEEE, Trans., Magn., 26(5) (1990) 1930.
214. Shouzeng, Z., Lin, L., Lidong, Z., and Qin, H., J.M.M.M., 54/57 (1986) 521.
215. Okada, M., Sugimoto, S., Ishizaka, C., Tanaka, T., and Homma, M., J. Appl. Phys., 57 (1985) 4146.
216. Weizhong, T., Shouzeng, Z., and Run, W., Loc cit 49(h), Part-I, p.574.
217. Yamasaki, J., Private Communication, 1985.
218. Yamasaki, J., Soeda, H., Yanagida, M., and Mohri, K., Japan IEE Meeting on Magn., Sendai, Sept. 1985, p.11.
219. Schneider, G., Henig, E.Th., Stadelmaier, H.H., and Petzow, G., Loc cit 49(h) Part-II, p.347.
220. Ramesh, R., Chen, J.K., and Thomas, G., J. Appl. Phys., 61 (1987) 2993.
221. Pastuschenkow, P., Durst, K.D., and Krön Müller, H., Phys. Stat. Sol. (a), 104 (1987) 487.
222. Shuming, P., Hongcheng, J., Yushuang, L., Ruzhang, M., and Jueyun, P., Loc cit 49(h), Part-II, 419.

223. Lemarchand, D., Vigier, P., and Labulle, B., IEEE Trans. Magn., 26(5) (1990) 2649.
224. Ma, B.M., and Krause, R.F., Loc cit 49(h), Part-II, 141.
225. Fujii, H., Saga, M., Takeda, T., Kamura, S., Okamoto, T., Hirose, S., Sagawa, M., IEEE Trans. Magn., MAG-23 (1987) 3119.
226. Elbicki, J.M., Wallace, W.E., and Korabely, V., IEEE Trans. Magn., 25(5) (1989) 3567.
227. Sankar, S.G., J. Metals, 43(2) (1991) 30.
228. Cech, R.E., J. Met., 26 (1974) 32.
229. Herget, C., and Domazet, H.G., Goldschmidt Informiert, 35 (1975) 3.
230. Li, D., Liu, J., Xu E., Hua, G., and Su, X., Loc cit 49(d), 571.
231. Zhou, S.X., Li, D., and Shuai, R.J., Loc cit 49(h), Part-I, p.339.
232. Rozendaal, E., Ormerod, J., McGuinness, P.J., and Harris, I.R., Loc cit 49(h) 275.
233. Okada, M., and Homa, M., Loc cit 49(g), 507.
234. Hamano, M., Loc cit 49(h), Part-I, 683.
235. Shimoda, T., Loc cit 49(h), Part-I, 651.
236. Hopstock, D.M., Loc cit 49(h) Part-I, 667.
237. Stäblein, H., and Bran, W., Technische Mitteilungen Krupp Forschungsberichte, 43(3) (1985) 43-58.
238. Bonda, N.R., M.Tech. Thesis, IIT, Kanpur (1981).
239. Velu, E.M.T., Ph.D. Thesis, IIT, Kanpur (1981).
240. Augustin, H., Goldschmidt Informiert, 48(2) (1979) 64
241. Klug, H.P., and Alexander, L.E., X-ray Diffraction Procedures for Polycrystalline and Amorphous Materials, 2nd Edition (John Wiley and Sons, New York, 1974).
242. Barret, C., and Massalski, T.B., Structure of Metals, 3rd Edition (McGraw Hill, 1968) 140
243. Manuja, V., Devi, U.M., and Gupta, K.P., In: Progress in Metallurgical Research - Fundamentals and Applied Aspects,

- S.P. Mehrotra and T.R. Ramachandran (Eds.) (Tata McGraw Hill, New Delhi, 1986) 415.
244. Devi, U.M., Gupta, K.P., and Velu, E.M.T., loc cit 49(h), Part-II, p.461.
245. Devi, U.M., M.Tech. Thesis, IIT, Kanpur, 1985.
246. Devi, U.M., and Gupta, K.P., J. Less Common Metals, 159(1990) 13-21.
247. Laha, S., M.Tech. Thesis, IIT, Kanpur (1981).
248. Narita, K., and Yamamoto, Kyushu University, Japan (Personal Communication, E.C. Subbarao, 1979).
249. Zhou, S.Z., Zhou, Y.X., and Graham, C.D.Jr., J. Appl. Phys. 63(8) (1988) 3534.
250. Velu, E.M.T., Subbarao, E.C., Bonda, N.R., Goel, D.K., Gupta, K.P., Majumdar, A.K., Sankar, T.A.P., and Subramanyam, J., J. Appl. Phys., 51(6) (1980) 3322
251. JCPDS X-ray data file 3-1053.
252. Melton, K.N., and Perkins, R.S., J. Appl. Phys., 47 (1976) 4115.
253. Melton, K.N., and Nagel, H., J. Appl. Phys., 48(1977) 2608.
254. Yang, Y.C., Chen, H.Y., Liu, Z.X., Liao, B., Xing, F., Ho, W.W., J. Appl. Phys., 57(1) (1985) 4115.

APPENDIX-A

Relation Between Various Units

Gaussian, cgs, emu		Factor	SI	
flux density	B (G)	$\times 10^{-4}$	flux density	B (T)
field strength	H (Oe)	$\times 10^3/4\pi$	field strength	H (A/m)
magnetization	M (G) or (Oe)	$\times 10^3$	magnetization	M (A/m)
magnetization	M (G) or (Oe)	$\times 4\pi/10^4$	magnetization polarization	J (T)
magnetization	$4\pi M$ (G) or (Oe)	$\times 10^3/4\pi$	magnetization	M (A/m)
magnetization	$4\pi M$ (G) or (Oe)	$\times 10^{-4}$	magnetic polarization	J (T)
magnetization	σ (emu/g)	$\times 1$	magnetization	σ (A m ² /kg)
demagnetization	N	$\times 1/4\pi$	demagnetization	N
factor (dimensionless)			factor (dimensionless)	
energy product	BH_{\max} (MG Oe)	$\times 10^2/4\pi$	energy product	BH_{\max} (kJ/m ³)
anisotropy constant	K (erg/cm ³)	$\times 10^7$	anisotropy constant	K (MJ m ⁻³)

APPENDIX-B

Indexed X-ray Diffraction Pattern of U Phase (Alloy C₁₈) and N Phase (Alloy C₁₆) as reported by Devi et.al.[244]

U Phase

Unit cell		a		c		c/a	
Hexagonal		5.907 Å		33.324 Å		5.64	
Relative Intensity*	d _{obs} Å	hkl	d _{calc} Å	Relative Intensity	d _{obs} Å	hkl	d _{calc} Å
vw	3.340	0010	3.332	w	1.571	1118	1.569
vvw	3.056	0011	3.029	w ₊	1.488	3011	1.486
m	2.942	111	2.942	w ₊	1.472	222	1.471
vvw	2.702	115	2.700	vw	1.430	226	1.427
vw	2.621	116	2.608	vw ₊	1.410	227	1.410
vvw	2.559	200	2.558	w ₊	1.330	1218	1.337
m	2.439	1012	2.441	w	1.300	1123	1.301
vvw	2.293	1013	2.292	vvw	1.292	3017	1.287
vvw	2.256	207	2.253	vyw	1.290	1311	1.285
vw	2.219	0015	2.222	w ₊	1.262	2120	1.262
m	2.189	208	2.180	w ₊	1.261	2023	1.261
m	2.113	1111	2.115	w ₊ →	1.235	407	1.235
vvs	2.096	209	2.105	w ₊	1.221	3019	1.222
m	2.051	1015	2.038	w ₊ →	1.220	2024	1.220
w ₋	1.944	1113	1.936	w ₋	1.194	4010	1.194
m	1.878	2012	1.881	m			
vw ₊	1.845	0018	1.851				
w ₊	1.787	217	1.791				
vvw	1.645	305	1.652				

* Relative intensity scale : vvs- very very strong, m- medium, w- weak, vw- very weak, vvw- very very weak

→ Reflections used for the lattice parameters calculation

N Phase

Unit cell	a	c	c/a
Hexagonal	4.997 Å	20.698 Å	4.14

Relative Intensity [#]	d _{obs.} Å	hkl	d _{cal.} Å
s	2.956	007	2.957
s	2.469	111	2.480
w	2.225	108	2.221
vs	2.139	115	2.139
vvs	2.112	202	2.118
s	2.042	109	2.031
s	1.895	117	1.908
vw	1.843	206	1.833
vw	1.629	211	1.631
w ₋	1.574	209	1.576
m ₋	1.503	1,1,11	1.503
m	1.477	0,0,14	1.478
		216	1.478
w	1.426	302	1.429
vw	1.413	303	1.412
vw	1.362	305	1.362
m	1.347	2,0,12	1.349
vw ₋	1.298	307	1.296
m ₋	1.234	→ 2,1,11	1.234
s	1.192	→ 312	1.192

Relative intensity scale : vvs - very very strong, vs - very strong, s - strong, m - medium, w - weak, vw - very weak, vvw - very very weak

→ Reflections used for the lattice parameters calculation